

Vrije Universiteit Brussel



Faculteit Wetenschappen en Bio-ingenieurswetenschappen
Vakgroep Fysica

Search for direct stop quark pair production at the LHC with the CMS experiment

Alexis Kalogeropoulos

Promotor

Prof. Dr. Jorgen D'Hondt

Proefschrift ingediend met het oog op het behalen van
de academische graad Doctor in de Wetenschappen

December 2013

Doctoral examination commission

Chair: Prof. Dr. N. Van Eijndhoven (Vrije Universiteit Brussel)

Supervisor: Prof. Dr. J. D'Hondt (Vrije Universiteit Brussel)

Secretary: Prof. Dr. F. Blekman (Vrije Universiteit Brussel)

Prof. Dr. F. De Proft (Vrije Universiteit Brussel)

Prof. Dr. K. Mawatari (Vrije Universiteit Brussel)

Prof. Dr. S. Lowette (Vrije Universiteit Brussel)

Prof. Dr. J Alcaraz (CIEMAT/Madrid)

Prof. Dr. F. Maltoni (Université Catholique de Louvain)

© 2013 Alexis Kalogeropoulos

All rights reserved. No parts of this book may be reproduced or transmitted in any form or by any means, electronic, mechanical, photocopying, recording, or otherwise, without the prior written permission of the author.

Contents		v
I Preamble		1
1 Introduction		3
II Theoretical Framework		5
2 The Standard Model		7
2.1 Introduction		7
2.2 The fundamental forces of nature		8
2.3 The Standard Model and its building blocks		10
2.4 Quantum Field Theory approach of the SM		11
2.5 Quantum Electrodynamics (QED)		12
2.6 The Electroweak sector		13
2.7 Quantum Chromodynamics (QCD)		14
2.7.1 Asymptotic freedom		15
2.7.2 Confinement		17
2.8 The Brout-Englert-Higgs (BEH) mechanism		17
2.9 Shortcomings of the SM and the need for extensions		20
2.9.1 Hierarchy and the fine tuning problem		21
2.9.2 Dark Matter		21
2.9.3 Dark Energy		22

3	Supersymmetry	23
3.1	Introduction	23
3.2	Minimal Supersymmetric Standard Model (MSSM)	25
3.2.1	Breaking models	27
3.2.1.1	Gravity Mediated Supersymmetry Breaking (mSUGRA)	29
3.2.1.2	Gauge Mediated Supersymmetry Breaking (GMSB) . .	30
3.2.2	Decays of s-particles	32
3.3	Mixing of 3^{rd} generation fermions in the MSSM	34
3.4	Production of 3^{rd} generation stop quarks	35
3.5	Decay modes of 3^{rd} generation stop quarks	37
3.5.1	Two-body decays	38
3.5.2	Three-body decays	39
3.5.3	Four-body decays	39
3.6	Simplified Models Spectrum	40
3.6.1	Top-Down vs Bottom-Up (SMS) approaches	41
3.7	Direct stop quark pair production as a SMS model	43
3.7.1	Direct stop quark pair production and final state topology	44
3.7.2	Current experimental constraints	46
4	Simulating collision events	47
4.1	Introduction to Monte Carlo techniques	47
4.2	General characteristics of event generators	48
4.3	Anatomy of an event in collider physics	49
4.4	Hard subprocesses and the use of Matrix Elements	52
4.5	Parton Showers	55
4.5.1	Parton branchings	57
4.5.2	Sudakov Form Factor	58
4.6	Combining the Matrix Element and the Parton Showering	59
4.7	Used event generators and Parton Showers	60
4.8	Underlying Event, Beam-Beam Remnants, Multiple Parton Interactions and Pile-Up	63
4.9	Hadronization	64
III	Experimental Setup	67
5	Experimental Setup	69
5.1	Introduction	69

5.2	The Large Hadron Collider (LHC)	71
5.2.1	The LHC at work	72
5.3	The Compact Muon Solenoid (CMS) experiment	76
5.3.1	Coordinate system and variables	77
5.3.2	The CMS sub-detectors and components	78
5.3.3	The main Solenoid	79
5.3.4	The Silicon Tracker (TK)	79
5.3.4.1	The Silicon Pixel Tracker (SPT)	80
5.3.4.2	The Silicon Microstrips	81
5.3.4.3	Performance of the Silicon Tracker	82
5.3.5	The Electromagnetic Calorimeter (ECAL).	82
5.3.6	The Hadronic Calorimeter (HCAL).	84
5.3.7	The Muon System	86
5.3.8	The Trigger	87
5.3.8.1	Level-1 Trigger (L1-Trigger)	88
5.3.8.2	The High Level Trigger (HLT)	88
5.3.9	The Trigger efficiency scale factors	89
5.3.10	Data Quality Monitoring (DQM)	89
5.4	Computing and Software	90
 IV Analysis		 91
6	Reconstruction of physics objects	93
6.1	The need for object reconstruction	93
6.2	The Particle Flow (PF) method reconstruction	94
6.3	Primary Vertices (PV)	95
6.4	Muon reconstruction	96
6.4.1	Classification of Muon candidates	96
6.4.2	Reconstruction of Standalone and Tracker Muons	97
6.4.3	Reconstruction of Global Muons	98
6.4.4	Performance of Muon reconstruction	99
6.5	Jets and \cancel{E}_T	99
6.5.1	Jet input types	100
6.5.2	Jet algorithms	100
6.5.3	Jet-energy corrections	101
6.5.4	Identification of b -jets	106

6.5.4.1	The b -tagging algorithms	106
6.5.4.2	Performance of the b -tagging algorithms	111
6.5.5	Missing Transverse Energy (\cancel{E}_T)	112
7	Datasets and event selection	115
7.1	Recorded data	115
7.2	Generation of simulated datasets	116
7.2.1	Generation of SUSY signal simulated datasets	117
7.2.2	Generation of background simulated datasets	120
7.2.3	Variation and control of the matching parameters	125
7.2.4	Parton Showering and hadronization	127
7.3	Selection of the event topology	127
7.3.1	Trigger	128
7.3.1.1	Turn-on curves	128
7.3.2	Event cleaning	130
7.3.3	Event selection criteria	130
7.3.4	Muon selection	130
7.3.5	Jets and \cancel{E}_T selection	132
7.3.6	Applying b -tagging in the event selection	134
7.4	Corrections to simulated datasets	134
7.4.1	PU treatment	135
7.4.2	Jet Energy Resolution (JER)	135
7.4.3	B -tagging scale factors	136
7.4.4	Lepton scale factors	137
7.5	Efficiency and event yields	137
7.6	Comparison of data with expectation	140
7.6.1	Reconstruction of the top quark pair event topology	140
8	Selection of Observables and Multivariate Analysis Techniques	147
8.1	Selection of variables	147
8.1.1	Variables with discriminating power	148
8.2	Ranking of variables	148
8.3	Tools for Multivariate Analysis (MVA)	155
8.3.1	MVA introduction	155
8.3.2	Determining the optimal MVA method	157
8.3.3	The Receiver Operating Characteristics (ROC) curve	158
8.3.4	Checks for overtraining	159

9	Systematic Uncertainties	161
9.1	Experimental uncertainties	161
9.2	Theoretical uncertainties	166
9.3	Effect of systematic uncertainties on MVA distributions	167
10	Fitting Template Analysis	175
10.1	Statistical Tools	176
10.1.1	Construction of the Likelihood function in HistFactory	176
10.1.2	Systematics in HistFactory	177
10.1.3	The CLs method	179
10.1.4	The Asymptotic CLs method	180
10.2	Building the template histograms	180
10.3	Closure Tests	183
10.3.1	Interpretation of the α_i coefficients	183
10.3.2	χ^2 tests	188
10.3.3	Signal injection test	192
11	Results, conclusions and perspectives	193
11.1	Experimental Results	193
11.2	Conclusions and comparison with other searches	196
11.2.1	Comparison with other published results	196
11.2.2	Comparison with a cut-and-count method	198
11.3	Overview and future perspectives	204
V	Appendices	207
A	Pythia parameters	209
	Appendices	209
B	List of Variables	211
C	Various MVA techniques	215
C.0.1	Artificial Neural Networks (ANN)	215
C.0.2	The MultiLayer Perceptron (MLP) method	215
C.0.3	Boosted Decision Trees (BDT)	218
C.0.4	Comparison of ANN vs BDT	219
C.0.5	Other MVA methods	220

Bibliography	223
List of Figures	237
List of Tables	247
VI Epilogue	249
Summary	251
Samenvatting	253
Acknowledgements	255

Part I

Preamble

The evolution of particle physics during the last century has radically changed our understanding of nature and the universe. The Standard Model (SM) which is based on *Quantum Field Theory* (QFT) has taken shape over the last 50 years and embeds our current knowledge how the fundamental particles interact with each other. The Standard Model is one of the most successful theories ever constructed and has passed with flying colors an abundant number of experimental tests during the second half of the last century.

Physicists were struggling for decades to detect the only missing particle predicted by the *Brout-Englert-Higgs* mechanism the so-called Higgs particle which is responsible for the generation of the masses of fundamental particles. Finally, in the summer of 2012 the ATLAS and the CMS collaborations at CERN announced its discovery. Although this is a major scientific breakthrough which will help scientists to understand even better the mechanism of the electroweak symmetry breaking among other things, there are strong indications that the Standard Model is not the ultimate theory of nature but is merely an effective field theory at low energies. However, physicists have been wondering what this more fundamental theory is that can give answers where the SM fails. For instance, although the masses of the matter particles can be measured directly or indirectly, they appear to be arbitrary. That means that currently, there is no established set of rules that allows the direct calculation of these masses. Other questions, like how we can explain large differences between the masses of the elementary particles or what is the nature of the dark matter and that of the dark energy, are still to be answered. Even more, we do not know if the fundamental forces unify at a common

scale at very high energies and what the role of gravity is in this regime.

One of the more appealing theories that gives answers to many of the shortcomings of the Standard Model is *Supersymmetry* (SUSY) which has been proposed as an extension to it. Supersymmetry predicts a completely new spectrum of particles and it has attracted the attention of many experimentalists over the last decades, and therefore it is one of the main ingredients of the physics program of the LHC. Many supersymmetric models have been proposed, like the *natural SUSY* scenario, where due to the large mixing of the 3^{rd} generation supersymmetric quarks (squarks), they can be the lightest of all supersymmetric quarks and even accessible at the LHC. However, due to the fact that supersymmetric theories typically have many free parameters, therefore performing a generic search is a rather cumbersome task. For this exact reason, during the last years some simplified approaches have been employed, resulting in new models known as *Simplified Models Spectrum* (SMS). These models are favored by experimentalists as the phenomenology of a considered supersymmetric model is still preserved, while at the same time they remain simple enough to design dedicated searches at colliders.

The main topic of this thesis, is a search for pair produced 3^{rd} generation top-squarks at the LHC adopting a SMS approach. In the first chapter of this thesis, the Standard Model is briefly presented along with its shortcomings and the need to introduce new theories. Supersymmetry is introduced in Chapter 3, while also the appropriate SMS for the purposes of this thesis is defined. One of the key elements for modern high-energy physics analyses is the usage of simulation techniques which are elaborated in Chapter 4. This chapter is followed by Chapter 5, describing the experimental setup of the LHC and that of the CMS experiment. Aspects of the reconstruction of the final state objects proton-proton collisions are described in Chapter 6 with an emphasis on the objects that are used for this analysis. In Chapter 7 the details of the generation of the simulated datasets along with the selection of the collision events with signatures including a muon in multi-jet events are discussed, followed by the presentation of the developed method incorporating Multi-variate Analysis techniques in Chapter 8. The systematic uncertainties are discussed in Chapter 9, whereas in Chapter 10 the used statistical tools, the adopted fitting template analysis strategy and several closure tests are discussed. This thesis closes with Chapter 11 presenting the final experimental results and the future prospectives.

Part II

Theoretical Framework

*Once you can accept the universe as
matter expanding into nothing that is
something, wearing stripes with plaid
comes easy.*

A.Einstein

CHAPTER 2

THE STANDARD MODEL

2.1 Introduction

Particle physics is the adventurous quest to unravel and understand the fundamental principles and the nature of matter. The Standard Model (SM) is a very elegant theory trying to explain the connection between fundamental particles and forces. With no doubt, it can be regarded as one of the most quantitatively and successful scientific construction the human mind has ever assembled, with an almost excellent agreement between prediction and observation. Indeed, the SM has been extensively tested during the past decades and has been tremendously successful describing experimental data [1–3]. For instance, the anomalous magnetic moments of the muon and that of the electron are amongst the most precise predictions that matched the experimental measurements in the history of physics [4, 5].

Recently, on July 4th 2012, both the CMS and the ATLAS experiments at CERN, announced the discovery of the predicted particle by the *Brout-Englert-Higgs* mechanism the so-called *Higgs* particle [6, 7], which has been evading detection since its prediction for almost five decades [8, 9]. This could be the last missing piece of the SM, but even if the observed particle is indeed the missing Higgs boson, there are some very well defined problems and shortcomings that the SM cannot successfully address. This leads to the strong belief that SM is only an effective theory at the currently accessible energies, but is not suited to describe physics above the TeV scale. However, new the-

ories extending the SM have been proposed. These theories do not aim to abolish the SM rather than to provide a more coherent theoretical framework to describe matter and its interactions at (or even above) the TeV scale. This chapter presents only a brief overview of the successes of the SM as well as its limitations, followed by a chapter describing Supersymmetry as a proposed theory beyond it solving some of its shortcomings.

2.2 The fundamental forces of nature

There are four fundamental forces in nature, namely *the strong*, *the electromagnetic*, *the weak* and *the gravitational* force. Together they account for all the interactions between the fundamental building blocks of matter.

Until the 1930s, it was believed that almost all natural phenomena were connected to two forces, *gravity* and *electromagnetism*. Both of them were described with the help of *Classical Field Theory* (CFT) and considered to have an infinite range. Also, the source of the forces were respectively the mass and the electric charge which were thought to be the building blocks of matter. All that was of course perfectly consistent with the principles both of general relativity and classic electromagnetism, but as newly subatomic phenomena started to puzzle the physicists of that time, it became obvious that two more forces had to be introduced, namely *the weak* and *the strong* force.

The Strong force was introduced due to the necessity to understand the stability of the nucleus. Indeed, as we know today, the strong force is responsible for binding quarks together in nucleons (e.g. protons and neutrons) in a very confined space ($\approx 10^{-15}$ m), as well as binding nucleons together to make the nucleus of the atom.

The Weak force on the other hand, was needed in order to explain the conversion of a neutron in the nucleus to a proton during the slow process of what is known as *beta decay* ($n \rightarrow p e \bar{\nu}_e$), allowing neutrons to convert into protons and vice versa. The weak force also manifests in the decays of the muon and the pions and is also believed to have played a crucial role in the formation of the heavy elements during the Big Bang nucleosynthesis and in stellar cores. Further, newer astronomical observations indicate that in general, fusion power cycles in stars depend on this force as well.

The electromagnetic force is responsible for the attraction or repulsion of charged particles (depending on their charge), and is manifesting in phenomena like electromagnetic radiation. This force also stabilizes the atoms and the molecules.

The gravitational force is by far the weakest one of all four. Although it has a negligible effect on nuclear and sub-nuclear particle phenomena, it is of great importance at the scale where classical physics is valid. As SM is a quantum theory, the gravitational force is not described by it. This is one of the remaining problems of particle physics, the incorporation of a quantum theory of gravity and its embedding into the SM, something that could lead us a *theory of everything*.

The four forces are propagated by gauge particles which carry spin. The strong force is mediated by massless spin-1 gluons, the weak force by massive spin-1 W^\pm and Z^0 bosons, the carrier of the electromagnetic force is the spin-1 photon, while gravity is believed to be mediated by the spin-2 graviton. It is worth noting that the coupling strength and the range of each force varies drastically. For the forces with massless gauge bosons, (except for the special case of the gluon), their potential energy falls as $\frac{1}{r}$. The weak interaction has an extra exponential factor due to the mass of its force carriers resulting in a potential energy falling $\propto e^{-mr}/r$. This means that the weak force cuts off sharply beyond $r \sim 10^{-16}$ cm $\approx 1/M_W$. The potential energy of the strong force deviates from the expected $1/r$ behaviour due to the effect of colour. The properties of the forces and its carriers are summarised in Table 2.1¹.

Force	Strong	Electromagnetic	Weak	Gravity
Carrier	gluon	photon	W/Z boson	Graviton
Symbol	g	γ	W^\pm, Z^0	G
Charge	0	0	$\pm 1, 0$	0
Spin	1	1	1	2
Mass (GeV)	0	0	80.4/91.2	0
σ at 1 GeV (mb)	10^1	10^{-1}	10^{-11}	10^{-77}
Interaction Time (s)	10^{-23}	10^{-21}	10^{-6}	stable
Relative strength	$\alpha_s = g_s^2 \approx 1$	$\alpha = e^2 \approx \frac{1}{137}$	$G_F m_p^2 \approx 10^{-5}$	$G_N m_p^2 \approx 10^{-38}$

Table 2.1: Summary of the fundamental forces and its properties

¹Throughout this thesis we adopt the *Natural Units* notation [10] where c, \hbar are set to unity.

2.3 The Standard Model and its building blocks

The twelve particles of the SM that constitute the matter can be divided into two categories: those that interact with the strong force (like quarks) and those that do not (like leptons). Those particles carry half-integer spin and are called *fermions* (f) as they obey Fermi-Dirac statistics. Each matter particle f has its corresponding anti-matter particle \bar{f} , which has the very exact same quantum numbers except that it carries opposite electric charge. Both leptons and quarks, are grouped into three distinct families, formally known as *generations*.

For the quarks, the first generation is comprised of the up quark (**u**), and the heavier down quark (**d**) and carry electric charges of $+\frac{2}{3}$ and $-\frac{1}{3}$ respectively. The next two generations include more massive particles and they always consist of a doublet of an "up"-type and a "down"-type quark. The second generation consists of the charm quark (**c**) and strange quark (**s**), while the third generation includes the top quark (**t**) being the heaviest quark of all, and the bottom quark (**b**). Stable free quarks have never been isolated or observed directly, since they are confined inside bound states like the hadrons. An example of a hadron is the proton (neutron) where two (one) "up" and one (two) "down" quarks are bound together.

We have to note however, that all the atoms in our universe are made exclusively from the fermions of the first generation. All the other fermions, although they can be produced at accelerators, (or even while cosmic rays cascade while entering Earth's atmosphere) do not hold an important role in our macroscopic life, at least, not to our current knowledge.

Similarly to the three quark families, equal number of families also exist for the leptons. Each lepton family consist of a doublet with an electrically charged lepton (electron, muon, tau) and a corresponding *neutrino* without electric charge. For many decades the neutrinos were considered to be massless, however observations of neutrino flavour oscillations from solar, atmospheric, reactor and long-baseline accelerator experiments have shown that neutrinos must carry some small mass [11]. Table 2.2 summarises the three generations of fermions together with their electric charge Q , their mass M , and the forces that they are subject to.

Quarks						Leptons					
Symbol	Q	M (GeV)	Weak	E/M	Strong	Symbol	Q	M (GeV)	Weak	E/M	Strong
u	2/3	0.002	✓	✓	✓	e	-1	5.11×10^{-4}	✓	✓	×
d	-1/3	0.005	✓	✓	✓	ν_e	0	$< 2 \times 10^{-9}$	✓	×	×
c	2/3	1.3	✓	✓	✓	μ	-1	0.1057	✓	✓	×
s	-1/3	0.1	✓	✓	✓	ν_μ	0	$< 1.9 \times 10^{-4}$	✓	×	×
t	2/3	172	✓	✓	✓	τ	-1	1.776	✓	✓	×
b	-1/3	4.8	✓	✓	✓	ν_τ	0	$< 1.82 \times 10^{-2}$	✓	×	×

Table 2.2: The three generations of fermions in the context of the SM with their electric charge (Q), mass (M) and the forces they "feel" [12].

The Higgs-boson is not included in Table 2.2, which according to the SM gives mass to the other particles. At the time that this thesis was written, there are strong indications that the observed BEH-like particle at ~ 125 GeV is indeed the predicted scalar particle in the mechanism of Brout, Englert and Higgs, whereas its spin-parity appears to be 0^+ [13–15]. Further, also its production cross-section as observed in specific production and decay modes is in agreement with the predictions of the SM [16, 17].

2.4 Quantum Field Theory approach of the SM

The appropriate theoretical framework to coherently describe the strong and the electroweak interactions is the relativistic *Quantum Field Theory* (QFT). In general, a local gauge theory is a field theory where its Lagrangian remains invariant under a group of local transformations. Further, the gauge bosons and their couplings are realised as a result of the local gauge invariance (or gauge symmetry) applied to the fields. However, an exact gauge invariance requires massless gauge bosons. The symmetry group of the underlying theory is determined by the symmetry group of these local gauge transformations. The SM is gauge invariant and it is described by the symmetry group:

$$SU(3)_C \otimes SU(2)_L \otimes U(1)_Y \quad (2.1)$$

This symmetry group describes the interactions of spin- $\frac{1}{2}$ particles whereas the forces are mediated by spin-1 gauge bosons. The C subscript stands for the colour-charge, the L subscript stands for the weak interaction between the left handed particles and the

Y subscript stands for the hyper-charge. In some more details, the strong interaction is described by the symmetry group $SU(3)_C$ embedded in the *Quantum Chromo Dynamics* (QCD) theory, whereas the electromagnetic interaction is described by the $U(1)_{EM}$ symmetry of *Quantum Electrodynamics* (QED), while the electroweak (EW) interaction is described by the unified $SU(2)_L \otimes U(1)_Y$. However, we should note that the last symmetry has to be spontaneously broken by the BEH mechanism so that the bosons to acquire mass (Section 2.8).

2.5 Quantum Electrodynamics (QED)

The first formulated gauge theory, was the *Quantum Electrodynamics* (QED). QED is an Abelian² gauge theory with the symmetry group $U(1)_{EM}$ which describes the interaction between charged fermions and the massless photon γ . Its Lagrangian density (\mathcal{L}_{QED}) describes the interaction of a spin $-\frac{1}{2}$ charged fermion field ψ with the gauge field A_μ and is of the form :

$$\mathcal{L}_{QED} = \bar{\psi}_e(i\mathcal{D}_{QED} - m_e)\psi_e - \frac{1}{4}F_{\mu\nu}F^{\mu\nu} \quad (2.2)$$

where $F^{\mu\nu} = \partial^\mu A^\nu - \partial^\nu A^\mu$ stands for the field strength tensor, while ψ_e denotes the field of mass (m_e) and charge (e), while the covariant derivative is defined as :

$$\mathcal{D}_{QED}\psi \equiv \gamma^\mu D_\mu\psi \equiv \gamma^\mu(\partial_\mu + ieA_\mu)\psi \quad (2.3)$$

The Lagrangian \mathcal{L}_{QED} , must remain invariant under the gauge transformations:

$$\psi \rightarrow \psi' \equiv e^{ie\chi}\psi, \quad (2.4)$$

$$A^\mu \rightarrow A'^\mu \equiv A^\mu - \partial^\mu\chi \quad (2.5)$$

where $\chi = \chi(x,t)$ is in general a function of space-time. Omitting the field A^μ , the Lagrangian would not be invariant under the local transformation of the field ψ alone. Indeed, the transformation of the term $\bar{\psi}\gamma^\mu\partial_\mu\psi$ under Eq. (2.4):

$$\bar{\psi}\gamma^\mu\partial_\mu\psi \rightarrow \bar{\psi}e^{-ie\chi}\gamma^\mu\partial_\mu(e^{ie\chi}\psi) = \bar{\psi}(\gamma^\mu\partial_\mu + ie\gamma^\mu(\partial_\mu\chi))\psi \quad (2.6)$$

²An Abelian group is defined as a group which the generators commute i.e. $[\tau_i, \tau_j] = 0$.

which is not invariant, unless we make use of the covariant derivative, which introduces A_μ in order to cancel out the extra term :

$$\begin{aligned}\bar{\psi}\gamma^\mu D_\mu\psi &\rightarrow \bar{\psi}e^{-ie\chi}\gamma^\mu D_\mu(e^{ie\chi}\psi) = \bar{\psi}(\gamma^\mu\partial_\mu + ie\gamma^\mu A_\mu - ie\gamma^\mu(\partial_\mu\chi)\psi + ie\gamma^\mu(\partial_\mu\chi))\psi \\ &= \bar{\psi}\gamma^\mu D_\mu\psi\end{aligned}\quad (2.7)$$

Thus, in order to satisfy the invariance of the Lagrangian (and consequently also the equations of motion) under local $U(1)_{EM}$ transformations, the existence of a *gauge field* A^μ is required. This field corresponds to the electromagnetic field and hence to the photon.

2.6 The Electroweak sector

Fermi first proposed the weak theory in the 1930s in order to explain the β -decay [18]. Although the Feynman diagrams using the weak theory describe this interaction very well at tree-level, it was not the case while trying to include higher order diagrams. That was happening as Fermi's interaction was not renormalisable, thus infinities would not cancel out. It was only in the late 1960's when Glashow, Salam and Weinberg unified the electromagnetic with the weak interaction [19–21] that this problem was solved. The underlying idea was to incorporate these two fundamental interactions into the same theoretical framework, hence they should be considered as the manifestations of the same principal interaction. Furthermore, the strength of the weak interaction given by Fermi's constant (G_F) was five orders of magnitude smaller than the coupling constant of the electromagnetic force. But as it turned out, attributing large masses on the weak's force carriers could explain this difference.

The symmetry group of the unified electroweak force is the $SU(2)_L \otimes U(1)_Y$. The first part has three generators which remain gauge invariant under the $SU(2)$. Therefore a new quantum number known as the *weak isospin* (T_3) and three gauge fields, namely W_μ^a with $a = 1, 2, 3$ are introduced. The weak isospin is associated to the different spin-like multiplets, whereas the third component of the T_3 , the electric charge Q and the weak-hypercharge Y are related by :

$$Q = T_3 + Y/2 \quad (2.8)$$

On the other hand, the gauge invariance under the Abelian group $U(1)_{EM}$ introduces a single field B_μ . The covariant derivative which ensures the gauge invariance of the

Lagrangian is :

$$D_\mu = \partial_\mu - ig \frac{\tau^a}{2} W_\mu^a - ig' \frac{Y}{2} B_\mu \quad (2.9)$$

where g, g' stand for the coupling constants of the $SU(2)_L$ and of the $U(1)_{EM}$ respectively, while the τ^a with $a = 1, 2, 3$ are Pauli matrices. Moreover, as the $SU(2)_L$ is not a Abelian group, the W_μ^a fields couple only to left-handed fermions, something that is compatible with the parity violating character of the weak interactions. The gauge fields are then :

$$W_\mu^\pm = \frac{1}{\sqrt{2}} (W_\mu^1 \mp iW_\mu^2) \quad (2.10)$$

$$Z_\mu = W_\mu^3 \cos \theta_W - B_\mu \sin \theta_W \quad (2.11)$$

$$A_\mu = W_\mu^3 \sin \theta_W + B_\mu \cos \theta_W \quad (2.12)$$

where W_μ^\pm, Z_μ are associated with the physical W^\pm, Z^0 boson particles, while A_μ represents the photon field and θ_W is the Weinberg mixing angle defined as :

$$\tan \theta_W = \frac{g'}{g} \quad (2.13)$$

Finally, the electron charge e and the Fermi constant G_F can be expressed as :

$$e = g \sin \theta_W \quad (2.14)$$

$$G_F = \frac{\sqrt{2}}{8} \frac{g^2}{m_W^2} \quad (2.15)$$

2.7 Quantum Chromodynamics (QCD)

The *Quantum Chromodynamics* (QCD) is the theory that describes the strong interaction and it is defined by the $SU(3)_C$ gauge group which is non-Abelian. The eight massless gauge bosons are the generators of this group, also known as *gluons* which are vector particles, carry spin-1 and are responsible to mediate the force. Also, the three dimensions of the groups corresponding to the three types of colour charge, that is red, blue, and green (R, B, G). For each colour charge, there is an anti-colour charge, namely anti-red, anti-blue and anti-green ($\bar{R}, \bar{B}, \bar{G}$) carried by an anti quark.

Since all hadrons are colour neutral (i.e. carry *white* colour) we know that in baryons, all three quarks carry different colour charge, while in mesons the anti quark carries

the anti-colour of the quark. The Lagrangian of QCD is given by :

$$\mathcal{L}_{\text{QCD}} = -\frac{1}{4}G_{\mu\nu}^\alpha G_{\alpha}^{\mu\nu} + \sum_n \bar{\psi}_n^a (i\mathcal{D}_{\text{QCD},\mu} - m_n)\psi_n^a \quad (2.16)$$

where $\mathcal{D} = \gamma^\mu D$, whereas the gluon field is given by $G_{\mu\nu}^\alpha$ with $\alpha = 1\dots 8$ and the quark field of mass m_n is represented as ψ_n^α . The different flavours are denoted by the n subscript, which can take six values, namely $n = (u, d, c, s, t, b)$ while the colour charge is denoted by $a = 1, 2, 3$. However, QCD has an approximate flavour symmetry as the gluon field does not have a flavour index. This symmetry is broken by the difference in quark masses. In order to maintain local $SU(3)_C$ gauge invariance, the following term is necessary :

$$D_{\text{QCD},\mu} = \partial_\mu + ig_s A_\mu^\alpha \lambda_a \quad (2.17)$$

where g_s is the interaction strength and λ_a stands for the $SU(3)_C$ group generators. The commutator of the generators is proportional to the antisymmetric structure constant of $SU(3)_C$, $f^{\alpha\beta\gamma} = f_{\alpha\beta\gamma} = f_{\alpha\beta}^\gamma$:

$$[\lambda_\alpha, \lambda_\beta] = if_f^{\gamma\alpha\beta} \lambda_\gamma \quad (2.18)$$

Exactly because of the non-Abelian character of the above relation, the self-interaction of the gluon fields is allowed. This leads to a very different behaviour of the strong interaction compared to the electromagnetic interaction.

2.7.1 Asymptotic freedom

Quarks and gluons interact via the strong force as they carry colour charge. Additionally, the gluons are allowed to interact with themselves as a consequence of the non-Abelian nature of the strong force. Also the strength of the interaction force increases over distance and for large distances the dynamic potential is given by $V(r) \propto \lambda r$, with $\lambda = \text{const}$ (Figure 2.1 [24]). The strong coupling constant is defined as :

$$\alpha_s \equiv \frac{g_s^2}{4\pi} \quad (2.19)$$

Nevertheless, perturbative calculations depend on the small value of the strong coupling constant. Furthermore, its numerical value decreases as the renormalization scale μ_R increases :

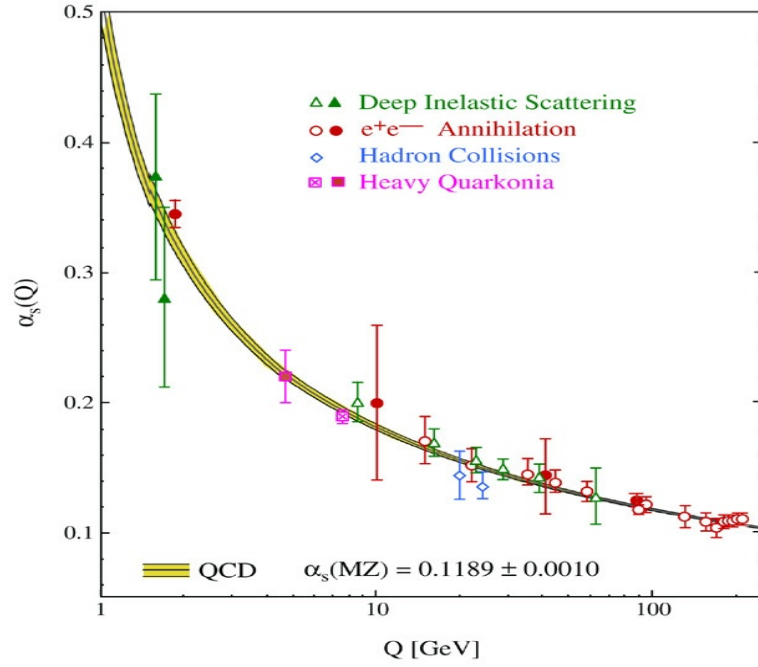


Figure 2.1: Summary of various measurements of α_s as a function of the energy scale Q . Open symbols denote (resummed) NLO, and filled symbols stand for NNLO QCD calculations. The curves stand for the QCD predictions for the combined world average value of $\alpha_s(M_{Z^0})$ [24].

$$\mu_R \frac{\partial g_s(\mu)}{\partial \mu} = - \left(11 - \frac{2N_F}{3} \right) \frac{g_s(\mu)^3}{16\pi^2} + \mathcal{O}(g_s(\mu)^5) \quad (2.20)$$

where N_F is the number of flavours which is 3 for the SM. This feature of QCD where the coupling strength decreases at large energies (or short distances), is known as *asymptotic freedom*. This yields non-perturbative effects at distances of $\mathcal{O}(\Lambda_{QCD}^{-1})$, where Λ_{QCD} is given by:

$$\Lambda_{QCD}^2 = \mu^2 \exp \left(\frac{-12\pi}{(33 - 2N_F)\alpha_s(\mu)^2} \right) \quad (2.21)$$

and the strong coupling constant can be written as :

$$\alpha_s \equiv g_s^2/4\pi = \frac{12\pi}{(33 - 2N_F)\ln(\mu^2/\Lambda_{QCD}^2)} + \mathcal{O} \left(\frac{1}{\ln(\mu^2/\Lambda_{QCD}^2)^2} \right) \quad (2.22)$$

The actual value of Λ_{QCD} is not predicted by theory since it is a free parameter, but it has been experimentally measured to be $\Lambda_{QCD} \approx 0.21$ GeV. When $\mu^2 \sim \Lambda_{QCD}^2$, then $\alpha_s \approx 1$, thus perturbation theory is no longer valid. The value of Λ defines the range

of the strong interactions, hence we could say that the Λ_{QCD} "sets" the boundaries between the semi-free quarks and their bound states like protons, mesons etc.

2.7.2 Confinement

After a hard scattering, the produced quarks form stable combinations called *hadrons* and *mesons*. This is the direct effect of colour confinement present in the strong interactions since only colourless (white) "clusters" are allowed to be created.

Indeed, if quarks are separated by a very energetic process, this will cause the initial quarks to eventually create even more quarks. This is the case because if two quarks move away from each other, the force between them starts to increase, eventually leading to conditions that favour the production of a new quark-antiquark pair. This process is formally known as *hadronization* and has direct experimental consequences at a hadron collider. That is why final state quarks and gluons are not observed as single particles, but in objects called "jets", a composition of many colourless hadrons. However, the top quark is an exception to the above rule, since it has a very small life time of $\sim 10^{-15}$ s, much smaller than the scale of QCD. Hence, the top quark decays before it can hadronize, and this is how "bare" top quarks can be observed [?].

2.8 The Brout-Englert-Higgs (BEH) mechanism

Strong and electroweak interactions can be combined into a single Lagrangian, invariant under $SU(3)_C \otimes SU(2)_L \otimes U(1)_Y$ transformations, but this invariance is broken when the weak W^\pm and Z bosons acquire mass leading to a non-renormalisable theory [26]. To tackle this problem, the *Brout-Englert-Higgs* (BEH) mechanism had to be introduced which handles elegantly this problem [8, 9]. Practically, the BEH mechanism allows for the generation of mass terms via the spontaneous breaking of the electroweak symmetry. For this, the complex scalar field (BEH field) Φ is introduced which transforms as a doublet under $SU(2)_L$ defined as :

$$\Phi = \frac{1}{\sqrt{2}} \begin{pmatrix} \phi_1 + i\phi_2 \\ \phi_3 + i\phi_4 \end{pmatrix} = \begin{pmatrix} \phi^+ \\ \phi^0 \end{pmatrix} \quad (2.23)$$

And the BEH Lagrangian reads :

$$\mathcal{L}_{\text{BEH}} = (\partial_\mu \phi)^\dagger (\partial^\mu \phi) - \mu^2 \phi^\dagger \phi - \lambda (\phi^\dagger \phi)^2 \quad (2.24)$$

with ϕ^0 being also a complex scalar fields expressed by :

$$\langle \phi_0 \rangle = \frac{1}{\sqrt{2}} \begin{pmatrix} 0 \\ v \end{pmatrix} \quad (2.25)$$

with

$$v = \frac{-\mu^2}{\lambda}, \quad \mu^2 < 0 \quad (2.26)$$

where μ^2 and λ represent respectively a mass parameter and the strength of the field's self interaction. As is demonstrated in Figure 2.2, if one chooses $\mu^2 < 0$ and $\lambda > 0$ the potential has a minimum for :

$$\Phi^\dagger \Phi = -\frac{\mu^2}{2\lambda} \quad (2.27)$$

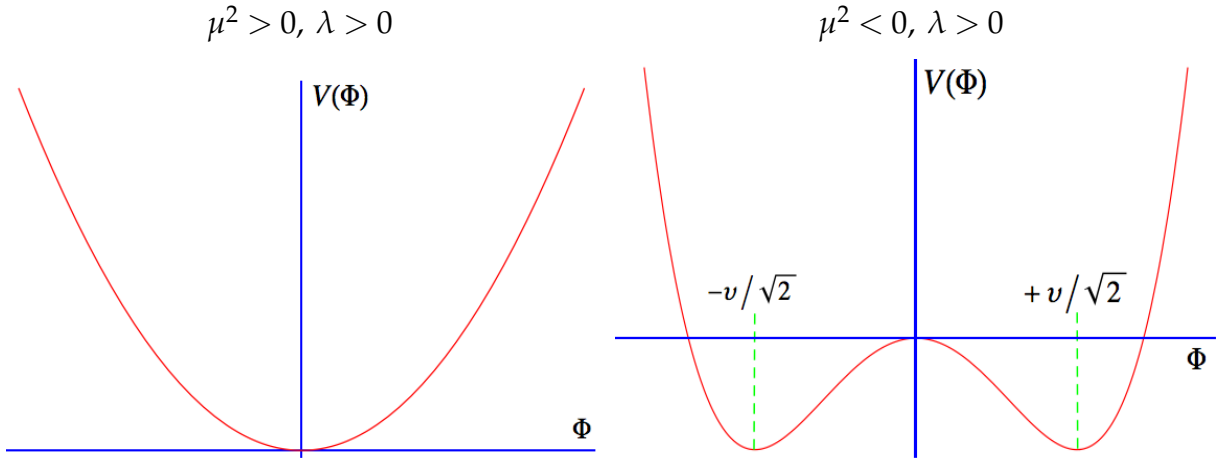


Figure 2.2: The potential of the BEH mechanism for $\mu^2 > 0, \lambda > 0$ (left) and $\mu^2 < 0, \lambda > 0$ (right) where is minimised at $-\mu^2/(2\lambda)$.

That means, that the field Φ has a non-zero VEV like :

$$\langle 0 | \Phi | 0 \rangle = \frac{v}{\sqrt{2}} \neq 0 \quad (2.28)$$

According to the Goldstone theorem, fields that acquire a VEV *must* have an associated massless Goldstone boson, which will disappear transforming to the longitudinal component of a new massive gauge boson. Taking this into account and since the photon is massless, the symmetry is chosen so that it can be broken while only the fields with zero electric charge (thus the ones that cannot couple to the electromagnetic interaction) acquire a vacuum expectation value VEV. Then, and after expanding around

the true minimum of theory, the complex field Φ becomes equal to :

$$\Phi = \frac{1}{\sqrt{2}} e^{(i\vec{\zeta}(x))} \begin{pmatrix} 0 \\ v + h(x) \end{pmatrix} \quad (2.29)$$

where $\vec{\zeta}(x) = 0$ stands for the motion through the degenerated minima in the $SU(2)$ space, but as the Lagrangian is locally gauge invariant, one can safely choose $\vec{\zeta}(x) = 0$ without losing generality. However, $h(x)$ is the only gauge invariant degree of freedom, and being a complex scalar field carries four degrees of freedom; three of them are gauged away to give masses to the W^\pm and the Z bosons via the spontaneous symmetry breaking mechanism, while the remaining degree of freedom is assigned to a new massive scalar particle, the famous *BEH*-boson which counts for the quantum fluctuations of the field Φ around the chosen minimum. The masses of the aforementioned particles are given by the relations :

$$M_H = \sqrt{2\lambda v^2} \quad (2.30)$$

$$M_W = \frac{1}{2}vg \quad (2.31)$$

$$M_Z = \frac{1}{2}v\sqrt{g'^2 + g^2} = \frac{M_w}{\cos\theta_W} \quad (2.32)$$

$$M_\gamma = 0 \quad (2.33)$$

$$(2.34)$$

The VEV can be determined experimentally from weak interactions, and it yields :

$$\frac{G_F}{\sqrt{2}} = \frac{g^2}{8M_W^2} = \frac{1}{2}v^{-2} \quad (2.35)$$

thus, the electroweak scale is :

$$v = (\sqrt{2}G_F)^{-1/2} \approx 246 \text{ GeV} \quad (2.36)$$

Also, the measured masses of the weak W^\pm and Z bosons are 80.39 GeV and 91.18 GeV respectively [12].

Except the prediction of the existence of the *BEH*-boson, luckily enough, the *BEH* mechanism also provides a formalism for fermions to acquire mass [21]. The non-zero VEV grants the vacuum the ability to emit or even absorb neutral colourless Higgs-bosons that carry isospin. By adding gauge invariant couplings between the fermions

and the Higgs-boson field, the latter can acquire mass through the so-called Yukawa couplings, adding also a term in the Lagrangian :

$$\mathcal{L}_{\text{Yuk}} = -\lambda_f(\bar{\psi}_f\Phi\psi_f) \quad (2.37)$$

This forces us to introduce a new series of coupling constants for each fermion f denoted by the λ_f in the last equation. These terms are subject to the masses of the fermions. Since the Yukawa couplings are unknown, theory cannot predict fermion masses directly, hence they remain free parameters within the SM.

2.9 Shortcomings of the SM and the need for extensions

The SM has been verified and profoundly tested experimentally during the last decades. But despite its success, it cannot provide answers to many open questions of particle physics. Further, there are conceptual and phenomenological hints that the SM is not nature's most fundamental theory. For instance, we do not yet have a satisfactory answer why the SM contains at least 19 free parameters, that is counting the couplings, the masses and the mixings [10, 27]. These parameters cannot be predicted by theory and their values must be acquired from direct experimental observations. So, questions like *why three generations of matter, why the masses of the elementary particles are so different, why four forces exist, or how to interpret neutrino oscillations* cannot be satisfactorily explained with our current knowledge of nature. Even more importantly, the SM cannot incorporate gravity and it also cannot explain various astrophysical observations like the nature of the Dark Matter and the Dark Energy, or even the baryon asymmetry of the universe. Another problem of the SM, is the unification of the gauge couplings of the three forces. Each of the three gauge groups in the SM has an associated coupling strength. These are considered to be *running couplings* as they change value depending on the energy scale of the interaction. Unification of the forces requires these to be identical at some large energy scale (the *Grand Unified Theory* (GUT) scale), whereas they differ at lower energy scales due to spontaneous symmetry breaking. Current extrapolations towards higher energies however show that these couplings do not intersect at a common point, and hence do not unify.

All of the above strongly indicate that the SM has to be just an effective theory, that is the "low energy" limit of a more fundamental theory. This leads to the question of up to which energy scale the SM remains valid. This cut-off is considered to be the *Planck Scale* ($\Lambda_{\text{Planck}} \approx 10^{19}$ GeV provided that there is another theory at lower scales) where

quantum effects of gravity become strong while the forces unify. Below we elaborate about those problems that are more likely to be solved if new physics exists above the electroweak scale.

2.9.1 Hierarchy and the fine tuning problem

An important pathology of the SM is the so-called *hierarchy problem*. The problem arises from the fact that the SM predicts that the Higgs-boson acquires large radiative corrections to its mass from one-loop diagrams from top quarks, gauge bosons and the Higgs-boson itself, something that leads to *quadratic divergences*. These contributions are proportional to the squared Planck scale (Λ_{Planck}^2), with the contribution coming from the top quark bearing a minus sign, while the corrections from the gauge and Higgs-boson being positive. The Higgs-boson mass is then given by :

$$M_{\mathcal{H}} = (M_{\mathcal{H}})_0^2 - \frac{\lambda_f^2}{16\pi^2} + \left[2\Lambda_{cut}^2 + \mathcal{O} \left(m_f^2 \ln \left(\frac{\Lambda_{cut}}{m_f} \right) + \dots \right) \right] \quad (2.38)$$

where λ_f stands for Yukawa coupling of the fermion f , while Λ_{cut} is the ultraviolet cut-off scale up to which theory is valid. Of course, we could choose to tweak the bare mass of the Higgs-boson in a fashion where the renormalised Higgs-boson mass would be of the order of the weak scale. But this approach implies that a fine tuning on the bare mass of the Higgs-boson of the order of $\frac{M_W^2}{M_{GUT}} \approx 10^{-26}$ would be needed which is regarded as unphysical [28]. In other words, if the SM is valid up to the Planck scale, meaning $\Lambda_{GUT} \equiv \Lambda_{Planck}$, then the Higgs-boson should have a mass of that order (i.e. without fine tuning). But recent experimental data shows that this is not true, and the Higgs-boson is ~ 125 GeV [6, 7]. Hence, the cut-off scale has to be much smaller, i.e. $\Lambda_{cut} \ll \Lambda_{Planck}$ which would imply the existence of a new theory at a larger scale.

2.9.2 Dark Matter

Since the early 1930 astronomical measurements of the moving patterns of certain clustered galaxies strongly indicate that the universe must be filled with large quantities of non-radiating, weakly interacting (if at all) material. The latest prediction estimates that the so-called *Dark Matter* [29] must consist $\sim 83\%$ of the total matter in the universe. The rest $\sim 17\%$ must be formed by baryonic matter. Nevertheless, the SM does not predict a suitable candidate for Dark Matter. Supersymmetric theories on the other

hand, can fill that gap with the prediction of the *Lightest Supersymmetric Particle* (LSP) as an excellent candidate [28] for it.

2.9.3 Dark Energy

The more appealing evidence concerning the existence of *Dark Energy* comes from supernovae observations, implying that our universe still expands with the help of Dark Energy that permeates all of space [30]. The very nature of the Dark Energy is even a greater mystery compared to the Dark Matter, as Dark Energy is thought to contribute to about 70% of the energy density of the Universe, while Dark Matter makes up about 27%. If we would count for all of the ordinary mass we know of, i.e. every massive quantity on Earth and everything massive object ever observed with all of our instruments, all these would add up to about 3%.

One possible explanation for Dark Energy is included in Einstein's cosmological constant. He was the first person to realise that empty space is not literally empty as it can possess its own energy. Because this energy is a property of the space itself, it would not be diluted as space expands. This form of energy would cause the universe to expand with an accelerating rate.

We can get some answers to all of the above questions by introducing new theoretical models. These include *Supersymmetry* (SUSY), *Extra Dimensions* (ED) or *Technicolour*. The most attractive and most popular is SUSY which is also the framework of this thesis. The next chapter focuses on its basic concepts, and how helps to solve some of the problems discussed above.

*I learned very early the difference
between knowing the name of something
and knowing something.*

R. Feynman

CHAPTER 3

SUPERSYMMETRY

3.1 Introduction

Supersymmetry (SUSY) [31], [32] is a very attractive theory which has been proposed as an extension to the SM. SUSY basically postulates the existence of an underlying -yet fundamental- symmetry between bosons and fermions. SUSY manifests once the operator Q acts and a symmetry between bosons and fermions appears :

$$Q|boson\rangle = |fermion\rangle \quad (3.1)$$

$$Q|fermion\rangle = |boson\rangle \quad (3.2)$$

The SUSY has to be a space-time symmetry, as its algebra resides on the fact that (Q, Q^\dagger) are fermionic operators (with spin-1/2). But as the SM's left and right-handed fermions transform differently under the gauge symmetries, the possibility of parity-violating interactions exists. It follows that the (Q, Q^\dagger) operators must satisfy some commutational and anticommutational algebraic relations so that :

$$\{Q, Q^\dagger\} = P^\mu \quad (3.3)$$

$$\{Q, Q\} = \{Q^\dagger, Q^\dagger\} = 0 \quad (3.4)$$

$$[P^\mu, Q] = [P^\mu, Q^\dagger] = 0 \quad (3.5)$$

where P^μ denotes the four-momentum generator of space-time translations. The idea of adding an extra symmetry provides a framework to solve many of the problems of the SM, whereas according to SUSY, all currently known particles have a *superpartner*, the so-called *s-particles*. Hence, the already observed SM particles can be placed in super multiplets with the new postulated s-particles from which they differ by spin- $\frac{1}{2}$, while they share all of the other quantum numbers (electric charge, weak isospin, colour, etc.).

Currently, there are neither indications nor direct or indirect experimental results that support the existence of SUSY. Therefore it is true that strictly speaking and for the time being, SUSY is "just" a very appealing theory, but if it is found, it could help us tackle some long-standing problems of modern particle physics. Indeed, if SUSY is realized in nature, it could then provide a solution to the *hierarchy* problem which implies the presence of new physics around the TeV scale [33]. Also, the unification of the gauge-couplings of the SM close to the Planck scale would be then feasible (as illustrated in Figure 3.1). Further, it is important to note, that a weakly-interacting massive particle (WIMP) whose properties are associated with the presence of physics at the TeV scale, could help us understand the nature of the Dark Matter [34]. Remarkably, SUSY predicts the existence of the *Lightest Supersymmetric Particle* (LSP), which is also an excellent WIMP candidate [35].

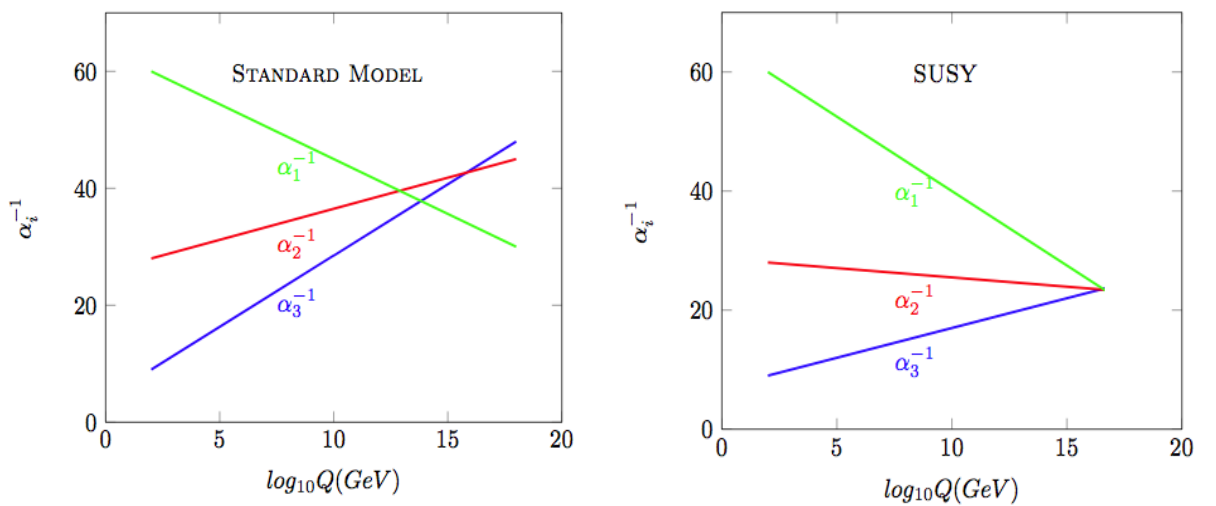


Figure 3.1: The running gauge couplings in the SM (left) and their unification in the context of its minimal SUSY extension (right), assuming *s*-particle masses at the electroweak scale.

However, SUSY is not an exact symmetry of nature. Had it been one, SM particles and their superpartners would have to be degenerate in mass. Since superpartners have

not been observed so far, SUSY *must* be a broken symmetry. Practically, breaking SUSY implies that the masses of the s-particles are unconstrained, thus we cannot predict their exact numerical values unless if a SUSY breaking mechanism is defined first. However, if we want SUSY to solve the hierarchy problem, the masses of the s-particles are required to be at the region of the weak scale. The coupling constants of a SM particle and its superpartner must be the same, whereas SUSY provides an additional "negative" sign loop correction for each of the SM quantum corrections coming from f_L and f_R . This is very important, since the quadratic divergencies are cancelled and we are left only with a logarithmic term, something that solves the hierarchy problem as advertised.

The only side-effect is that the baryon and the lepton numbers are violated, which can result in the process ($p \rightarrow \pi^0 e^+$). This can be tackled by introducing a new quantum number *R-parity* defined as :

$$R \equiv (-1)^{3(B-L)+2S} \quad (3.6)$$

where B , S and L stand for the baryon, the spin and the lepton numbers respectively. All SM particles have $R = 1$ while all s-particles have $R = -1$, meaning that s-particles must be produced or destroyed in pairs, implying that the LSP must be stable. If the LSP is the neutralism it does not interact via the strong nor the electromagnetic force and this qualifies it as a perfect Dark Matter candidate.

Since SUSY cannot possibly predict the exact masses of the SUSY particles after symmetry breaking, the generic SUSY model introduces a large number of free parameters. In order to constrain these, some assumptions can be made leading to some simpler models. One of these models, the *Minimal Supersymmetric Standard Model* (MSSM) is introduced in the next section.

3.2 Minimal Supersymmetric Standard Model (MSSM)

The *Minimal Supersymmetric Standard Model* (MSSM) introduces the minimum set of free parameters that are needed in order to get a consistent supersymmetric theory while the *R-parity* is conserved. The used naming scheme of the MSSM makes some conventions. For example, the superpartners of the SM fermions, are attributed with a "s" in front of the corresponding SM name. For instance, the partner of the top quark is then called *stop* quark. Briefly, within the MSSM the SM fermions are incorporated into

chiral super multiplets expressed with the use of super scalars. Also, the SM gauge bosons are expressed with vector (gauge) super multiplets along with an additional fermion, meaning that each super multiplet must contain an equal number of fermionic and bosonic degrees of freedom. The chiral (matter) super multiples contain three generations of left and right-handed quarks and lepton fields, along with their scalar SUSY partners, that is squarks and slepton fields.

Especially the Higgs-boson, needs some special treatment and must be part of a chiral super multiplet [28] as it has spin-0. On top, the MSSM introduces two complex Higgs-doublets and their associated superpartners. The extra doublets are necessary not only to cancel some gauge anomalies, but also to ensure that we get Yukawa couplings between the Higgs-boson and both the "up" and "down"-type quarks [36, 37].

The naming scheme is chosen so that the spin- $\frac{1}{2}$ superpartner is appended with an "ino" at the end of the corresponding SM name. This way, we get the *higgsinos*, being the fermionic superpartners of the SM scalar Higgs particle. Since the electric charge depends on the third component of the weak isospin (T_3) and the $U(1)$ hypercharge (Y), the chiral super multiplet H_u is realized when $Y = 1/2$ which generates the "up"-type quarks, while the "down"-type quarks and charged leptons are generated from the H_d chiral super multiplet when $Y = -1/2$. Further, the ratio of the vacuum expectation values v_u and v_d of the aforementioned Higgs-doublets is expressed as :

$$\tan \beta = \frac{v_u}{v_d} \quad (3.7)$$

and it is a free parameter of the MSSM. However, the supermultiplet H_d has the same SM gauge quantum numbers as the left-handed leptons and sleptons. But if a scalar BEH-particle and a neutrino were superpartners, this would simply mean that the sneutrino and the Higgs-boson are one and the same particle. Consequently, this would imply that the lepton number would not be conserved, whereas at least one of the neutrinos should be massive. In a similar fashion, when it comes to the vector bosons of the SM, the nomenclature is the same as in the case of the Higgs-doublets, thus they get appended with an "ino" as well. Thus, a colour octet partner is formed known as the *gluino*, which has spin- $\frac{1}{2}$.

Also, the electroweak (EWK) gauge symmetry $SU(2)_L \times U(1)_Y$ is associated with the spin-1 gauge bosons, namely the W^\pm the W^0 and the B^0 , while their superpartners with spin- $\frac{1}{2}$ are the *winos* ($\tilde{W}^\pm, \tilde{W}^0$) and the *bingo* (\tilde{B}^0) respectively. After the EWK symmetry breaking, the bino and the winos mix with the higgsinos to form linear combinations (mass eigenstates), like the four *neutralinos* ($\tilde{\chi}_k^0$ with $k = 1, 2, 3, 4$), or the two

charginos ($\tilde{\chi}_l^\pm$ with $l = 1, 2$). The convention is that both the charginos and the neutralinos are ordered according to their mass like :

$$M_{\tilde{\chi}_1^+} < M_{\tilde{\chi}_2^+} \quad (3.8)$$

$$M_{\tilde{\chi}_1^0} < M_{\tilde{\chi}_2^0} < M_{\tilde{\chi}_3^0} < M_{\tilde{\chi}_4^0} \quad (3.9)$$

Similarly, the W^0 and the B^0 gauge eigenstates can mix resulting to the mass eigenstates of the Z^0 and of the γ , whereas the corresponding gauging mixtures of the \tilde{W}^0 and of the \tilde{B}^0 are the *zino* (\tilde{Z}^0) and the *photino* ($\tilde{\gamma}$) respectively.

From the eight total degrees of freedom because of the SM Higgs-doublets (each doublet bears four degrees of freedom), three of them are absorbed in the EWK symmetry breaking so that the W^\pm , Z bosons acquire mass. The remaining degrees of freedom form five physical Higgs-bosons, which are the H^\pm, h^0, A^0, H^0 . These BEH-fields are categorised into chiral supermultiplets and have a total of four fermionic superpartners. Tables 3.1 & 3.2 summarise the s-particle content of the MSSM.

Particles Names	spin-0	spin- $\frac{1}{2}$	SU(3)	SU(2)	U(1)
sleptons/leptons	$(\tilde{e}^-, \tilde{\nu})_L$	$(e^-, \nu)_L$	1	2	-1
	\tilde{e}_R^-	e_R^-	1	1	-2
squarks/quarks	$(\tilde{u}, \tilde{d})_L$	$(u, d)_L$	3	2	1/3
	\tilde{u}_R	u_R	3	1	4/3
	\tilde{d}_R	d_R	3	1	-2/3
Higgs / higgsinos	H_u^+, H_u^0	$\tilde{H}_u^+, \tilde{H}_u^0$	1	2	+1
	H_d^0, H_d^-	$\tilde{H}_d^0, \tilde{H}_d^-$	1	2	-1

Table 3.1: The chiral supermultiplets in the MSSM along with their $SU(3)_C \times SU(2)_L \times U(1)_Y$ quantum numbers. For simplicity, only one generation of quarks and leptons is listed. However, for each of the quarks, leptons or BEH supermultiplet, there exists a corresponding anti-particle multiplet including the charge conjugate fermions with their associated scalar partners.

3.2.1 Breaking models

If SUSY is spontaneously broken, then a Goldstone fermion which is called *goldstino* ($\tilde{G}_{1/2}$) must exist. Furthermore, since the goldstino is massless, it will be playing the role of the LSP. But if SUSY is a local symmetry, then gravity has to be incorporated, which leads to theory of *supergravity* [38]. In the context of such a framework, the

Particles Names	spin- $\frac{1}{2}$	spin-1	SU(3)	SU(2)	U(1)
gluino/gluon	\tilde{g}	g	8	1	0
winos/W-bosons	$\tilde{W}^\pm, \tilde{W}^0$	W^\pm, W^0	1	3	0
bino/B-boson	\tilde{B}^0	B^0	1	1	0

Table 3.2: The gauge supermultiplets in the MSSM along with their $SU(3)_C \times SU(2)_L \times U(1)_Y$ quantum numbers.

goldstino is "eaten" by the gravitino which then acquires mass [39]. This mechanism is formally known as the *super Higgs* mechanism and is the analogous mechanism that occurs in the context of ordinary gauge theories. However, the goldstino possesses "physical" degrees of freedom only if SUSY is broken spontaneously.

Although MSSM is a nice theory, it introduces 105 new parameters on top of the SM ones [39], which is simply too much if one targets to test the MSSM experimentally. In order to tackle this, some theoretical assumptions can be made concerning the way SUSY is broken. No matter what, if we expect SUSY to provide an elegant solution to the naturalness problem, only terms with specific characteristics (i.e. *Soft Supersymmetry Breaking* (SSB) terms) are allowed to cancel the quadratic divergences of the Higgs-boson mass correction. To satisfy this condition, we need to make the assumption that two sectors exist, a *hidden* and a *visible* one. The visible sector consists of the particles of the MSSM, whereas the hidden of those that are completely neutral with respect to the SM gauge group. It is the hidden sector that has to be responsible for the breaking of SUSY, which is then propagated to the MSSM by some kind of *messenger* sector. The exact values and nature of the parameters at a high scale are determined by the choice of the SSB and the mediation mechanisms. Theoretical and experimental considerations restrict the scale to the rather extensive range of $10^4 \text{ GeV} < M_{SSB} < M_{Planck}$. As a natural consequence, the exact s-particle masses, or even their couplings (in cases mixing occurs), fully rely on the exact details of the SSB mechanism under question. Following a bottom-up approach, if these low energy values of s-particle properties can be measured, this could point to the scale where new physics phenomena manifest, which would reveal the underlying SUSY breaking mechanism.

We therefore have a set of different models that could be responsible for the SUSY breaking mechanism. The most theoretically studied are the *Gravity-Mediated Supersymmetry Breaking* (GMSB) and the *Gauge-Mediated Supersymmetry Breaking* (GMSB) which are summarised below.

3.2.1.1 Gravity Mediated Supersymmetry Breaking (mSUGRA)

This category refers to the minimal SuperGRAvity (mSUGRA) [31, 40] and the constrained MSSM (cMSSM) models, where gravity is believed to play the role of a messenger of the SUSY breaking back to the MSSM fields [41, 42]. The underlying idea is that the Gravity Mediated Breaking (GMB) mechanism could have a more universal character, exactly due to the uniform character of gravity, whereas the SUSY breaking must be mediated by effects of gravitational strength (suppressed by inverse powers of \mathcal{M}_{Planck}).

The difference between mSUGRA and cMSSM lies in the fact that the former fixes the higgsino mixing mass parameter by demanding the radiative breaking of the EWK symmetry, while the latter leaves it as a free parameter. On the other hand, they both assume universality of the scalar masses and gaugino masses at the high scale and the presence of a universal cubic coupling at some mass (M_X). These models have always an extra scalar mass parameter which needs to be fine-tuned so that the s-particle exchange does not generate large Flavour Change Neutral Current (FCNC) effects. What is important here, is that the breaking of the symmetry must occur at $\mathcal{O}(10^{10})$ GeV or even higher, but the gravitino acquires a mass of the order of the electroweak scale. What makes the mSUGRA approach very attractive, is that under certain assumptions we end up with only five free parameters, namely :

1. $m_{1/2}$: The universal gaugino mass at the GUT scale. Assuming that the SM gauge couplings unify at the GUT scale (Figure 3.1), the one-loop renormalization group equations (RGE) for the three gauginos are given by [28] :

$$\frac{M_1}{\alpha_1} = \frac{M_2}{\alpha_2} = \frac{M_3}{\alpha_3} = m_{1/2} \quad (3.10)$$

where $M_1 = \tilde{B}^0$, $M_2 = \tilde{W}$, $M_3 = \tilde{g}$. The bino, the wino and the gaugino are related like :

$$M_1 = \frac{5}{3} \tan^2 \theta_W M_2 \quad (3.11)$$

$$M_3 = \frac{\alpha_s}{\alpha} \sin^2 \theta_W M_2 \quad (3.12)$$

$$M_3 = \frac{3}{5} \frac{\alpha_s}{\alpha} \cos^2 \theta_W M_1 \quad (3.13)$$

Assigning numerical values for $\alpha_s = 0.118$, $\alpha = 1/128$, $\sin^2 \theta_W = 0.23$ then the following relation is anticipated to be true at the EWK scale [28].

$$M_1 : M_2 : M_3 \approx 1 : 2 : 6 \quad (3.14)$$

meaning that the gluino must be much heavier than the charginos or the neutralinos.

2. m_0 : The universal mass of the scalars, that is the squarks and the sleptons.
3. A_0 : The (soft) universal breaking trilinear coupling between the sfermions and the BEH-scalars at the GUT. The assumption here is that all trilinear coupling constants have the same value.
4. $\tan\beta$: This parameter was defined in Eq 3.7 as the ratio of the H_u and the H_d which stand for the vacuum expectation values of the SUSY Higgs-bosons that give masses to the "up" and "down"-type fermions.
5. μ : The μ parameter corresponds to the Higgs-boson mass parameter in the SM and can be written like : $|\mu| = \pm \sqrt{-0.5M_Z^2 - M_{H_u}^2}$. We want μ to take the value that gives the correct Z-boson mass. Hence, only the sign of μ is a free parameter, since its value at the GUT scale is fixed. The absolute appears here as in the GUT case μ must be a real number.

The evolution of the RGE of the $m_0, m_{1/2}$ is illustrated in Figure 3.2 [28]. It can be also shown that according to these RGE, the gauge couplings can unify at a common scale, in contrast with the SM, where this is not possible (Figure 3.1).

The fact that there are only five free parameters in the mSUGRA model makes it a very appealing and a favourable framework for experimental searches as the mSUGRA spectrum can lead to very clear and distinct experimental signatures. The SUSY mechanisms in the context of the mSUGRA include pair production, namely $\tilde{q}\tilde{q}, \tilde{q}\tilde{q}, \tilde{g}\tilde{q}, \tilde{g}\tilde{g}$. Typically in experimental mSUGRA searches, one fixes the $A_0, \tan\beta$ and $sgn(\mu)$ and this way the s-particles phenomenology and the mass spectrum with the corresponding branching ratios are obtained, as well as the corresponding decay rates and production cross sections while surveying the $(m_0, m_{1/2})$ mass plane. Recently, the CMS collaboration has published results based on mSUGRA searches in various topologies, constraining the remaining available phase space significantly. These limits are demonstrated in Figure 3.3 [43, 44].

3.2.1.2 Gauge Mediated Supersymmetry Breaking (GMSB)

According to the GMSB, the SSB is propagated to the supersymmetric SM through gauge interactions. However, unlike the MSSM, in the so-called *direct gauge mediation*

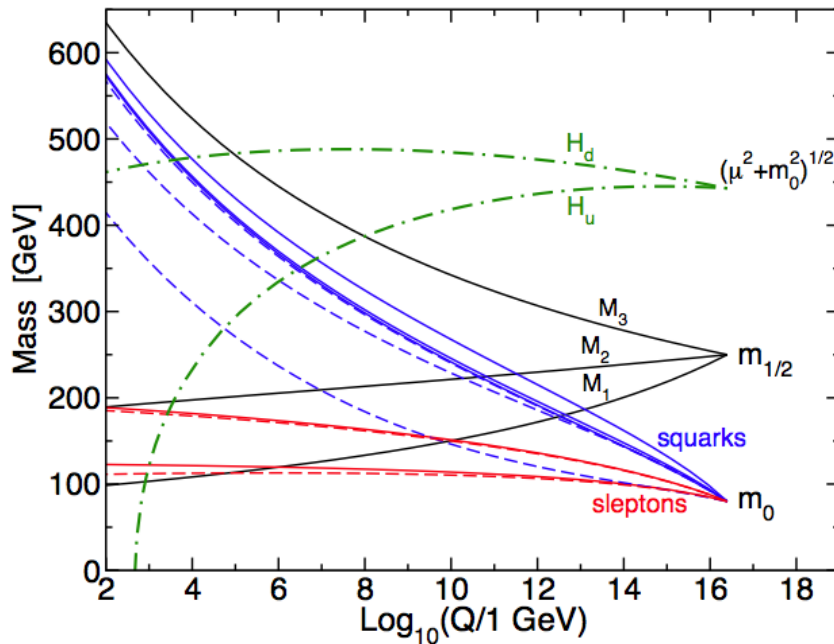


Figure 3.2: The evolution of the renormalization group equations (RGE) of the $m_0, m_{1/2}$ mass parameters in the MSSM in $mSUGRA$ with inspired boundary conditions imposed at $Q_0 = 2.5 \times 10^{16} \text{ GeV}$. The parameter $\mu^2 + m^2 H_u$ gets negative, provoking electroweak symmetry breaking [28].

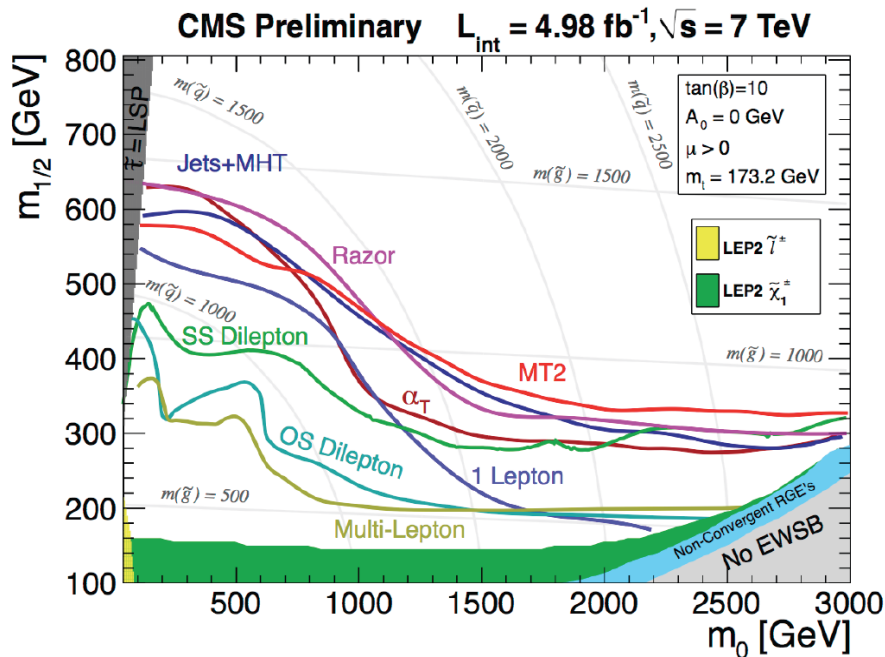


Figure 3.3: The CMSSM exclusion limits in the $(m_0, m_{1/2})$ plane by the CMS collaboration obtained by using data corresponding to an integrated luminosity of 4.98 fb^{-1} at $\sqrt{s} = 7 \text{ TeV}$ Center of Mass Energy (C.M.E)[43, 44].

models there is no need for a separate messenger sector [32]. These models by definition keep flavour violations small, hence FCNC are not a problem, while the gravitational effects are also suppressed and they do not involve any scalar mass parameter. Also, if SUSY gets broken this way, this has to happen at much lower scales compared to the gravity-mediated scenarios, typically at a scale of $\mathcal{O}(10^5)$ GeV, while the gravitino plays the role of the LSP being really light with a mass of the $\mathcal{O}(\text{keV})$, hence it is a potential Dark Matter candidate. On the other hand, for most of the phase space it is either the lightest neutralino ($\tilde{\chi}_1^0$) or the stau ($\tilde{\tau}$) that becomes the *next-to-lightest-superpartner* (NLSP). There is also the possibility for small mass splittings leading to degenerate sleptons, something that is usually referred to as *co-NLSP scenarios*. This kind of models also characterize the case when the neutralino and stau are the co-NLSPs.

The CMS collaboration has performed various searches considering the bino and the wino-like neutralino scenarios while scanning the parameters of squark and gluino masses [45]. The bino-like neutralino can decay dominantly according to $\tilde{\chi}_1^0 \rightarrow \gamma \tilde{G}$, while the decay to $\tilde{\chi}_1^0 \rightarrow Z \tilde{G}$ is suppressed. Phenomenologically, a $\tilde{\chi}_1^0$ that lives long enough to decay outside the detector, can lead to the peculiar SUSY signature of large missing energy plus leptons and/or jets. On the other hand, if the decay $\tilde{\chi}_1^0 \rightarrow \gamma \tilde{G}$ is realized inside the detector, the experimental signature would contain photons. In the case of a wino-like NLSP neutralino, the neutral wino would decay according to $\tilde{\chi}_1^0 \rightarrow Z \tilde{G}$ dominantly. Since the splitting between the neutral and the charged winos becomes small, the charged wino becomes a co-NLSP which then decays directly to a gravitino LSP and a W-boson. Finally, there is also the possibility that the NLSP may be a charged particle like slepton, which would result in a multi-lepton experimental signature.

3.2.2 Decays of s-particles

In the context of MSSM and assuming that R-parity is conserved, several decay paths can be realized. In what follows we adopt the notation $k = 1, 2, 3, 4$ and $l = 1, 2$.

Squarks provided that is kinematically allowed, they can decay into a two-body final state including a quark and a gluino :

$$\tilde{q} \rightarrow q \tilde{g} \quad (3.15)$$

Otherwise, the squarks can decay into a quark and a chargino/neutralino :

$$\tilde{q} \rightarrow q \tilde{\chi}_I^\pm \quad (3.16)$$

$$\tilde{q} \rightarrow q \tilde{\chi}_k^0 \quad (3.17)$$

The coupling of a squark to charginos strongly depends on the handedness of the SM partner of the squark. In general, the left-handed squark (\tilde{q}_L) can couple both to charginos and neutralinos, while the couplings of the right-handed squarks (\tilde{q}_R) are suppressed. In general, the coupling depends on the mixing parameters of the charginos and the neutralinos.

The decay products will further decay, until a final state containing a LSP is achieved. That implies that the cascade path can be very long incorporating many particles, but the kinematically allowed path will be the dominant one. One feature of the phenomenology of squarks, is that also decays to lighter squarks and a SM gauge boson or even the Higgs-boson are possible. While these decays are rather suppressed, they cannot be completely neglected. Experimentally that means, that a light stop squark can decay according to $\tilde{t} \rightarrow \tilde{b}W$ provided that the sbottom quark is lighter than the stop squark.

Sleptons can give two-body and three-body decays involving leptons, charginos and neutralinos :

$$\tilde{l} \rightarrow l \tilde{\chi}_k^0 \quad (3.18)$$

$$\tilde{l} \rightarrow \nu \tilde{\chi}_I^\pm \quad (3.19)$$

$$\tilde{\nu} \rightarrow \nu \tilde{\chi}_k^0 \quad (3.20)$$

$$\tilde{\nu} \rightarrow \ell^\mp \tilde{\chi}_I^\pm \quad (3.21)$$

Gluinos decay via the strong coupling to a quark squark final state :

$$\tilde{g} \rightarrow q \tilde{q} \quad (3.22)$$

If the two-body decays are kinematically not allowed, then a three-body decay can take place involving off-shell quarks and neutralinos :

$$\tilde{g} \rightarrow q \tilde{q}^* \rightarrow qq \tilde{\chi}_k^0 \quad (3.23)$$

Charginos and neutralinos can decay into a fermion and its superpartner :

$$\tilde{\chi}_I^\pm \rightarrow \tilde{l}\nu, l\tilde{\nu}, q\tilde{q}' \quad (3.24)$$

$$\tilde{\chi}_k^0 \rightarrow \tilde{l}l, \tilde{\nu}\nu, \tilde{q}q \quad (3.25)$$

In addition, since charginos and neutralinos inherit the gaugino/gaugino/vector boson and the gaugino/higgsino/Higgs-boson couplings of their components, they can decay into a lighter chargino/neutralino and a Higgs/gauge -boson :

$$\tilde{\chi}_l^\pm \rightarrow W^\pm \tilde{\chi}_k^0 \quad Z^0 \tilde{\chi}_{l' < l}^\pm \quad h^0 \tilde{\chi}_{l' < l}^\pm \quad [A^0 \tilde{\chi}_{l' < l}^\pm \quad H^0 \tilde{\chi}_{l' < l}^\pm \quad H^\pm \tilde{\chi}_{l' < l}^0] \quad (3.26)$$

$$\tilde{\chi}_k^0 \rightarrow Z^0 \tilde{\chi}_{k' < k}^0 \quad W^\pm \tilde{\chi}_l^\mp \quad h^0 \tilde{\chi}_{k' < k}^0 \quad [A^0 \tilde{\chi}_{k' < k}^0 \quad H^0 \tilde{\chi}_{k' < k}^0 \quad H^\pm \tilde{\chi}_l^\mp] \quad (3.27)$$

The decay channels between brackets are suppressed since h^0 is the lightest Higgs-boson. However if the two-body decays are not allowed, the charginos and neutralinos can give three or even more body decays into two fermions and a lighter neutralino or chargino via off-shell squarks.

$$\tilde{\chi}_l^\pm \rightarrow f \bar{f}' \tilde{\chi}_k^0 \quad (3.28)$$

$$\tilde{\chi}_2^\pm \rightarrow f \bar{f}' \tilde{\chi}_1^\pm \quad (3.29)$$

$$\tilde{\chi}_k^0 \rightarrow f \bar{f}' \tilde{\chi}_{k' < k}^0 \quad f \bar{f}' \tilde{\chi}_l^\pm \quad (3.30)$$

where f denotes a SM or its superpartners fermion, \bar{f} its antiparticle and f' denotes the other fermion belonging to the same generation. For example if $f = u$, then $\bar{f} = \bar{u}$, $f' = d$ and hence $\bar{f}' = \bar{d}$.

3.3 Mixing of 3rd generation fermions in the MSSM

Chiral fermions have two degrees of freedom, and hence the MSSM contains two spinless superpartners for each SM fermion. Although usually they are referred to as *left* and *right*-handed sfermions, in reality they have no standard handedness or chirality. Since they share the same colour and charge, thus they can mix, resulting in mixing states between squarks and/or sleptons. However, the mixing depends on the mass of the SM fermion under question, thus the 3rd generation sfermions mix more strongly. In what follows, we consider only the case of stop quarks, but similar relations can be derived for the sbottom quarks. Taking into account the MSSM Lagrangian, the mass matrix of the stop quarks in the basis of $(\tilde{t}_L, \tilde{t}_R)$ can be expressed with the matrix :

$$\mathcal{M}_t^2 = \begin{pmatrix} M_{\tilde{t}_L}^2 & \alpha_t M_t \\ \alpha_t M_t & M_{\tilde{t}_R}^2 \end{pmatrix} \quad (3.31)$$

with M_t being the mass of the top quark and α_t

$$\alpha_t = (A_t + \mu \cot \beta) \quad (3.32)$$

where the A_t denotes the soft SUSY breaking trilinear coupling of Higgs-scalars and sfermions. The mass eigenvalues then read :

$$M_{\tilde{t}_{1,2}}^2 = \frac{1}{2} \left[M_{\tilde{t}_L}^2 + M_{\tilde{t}_R}^2 \mp \sqrt{(M_{\tilde{t}_L}^2 - M_{\tilde{t}_R}^2)^2 + (2\alpha_t M_t)^2} \right] \quad (3.33)$$

The used convention here is that $M_{\tilde{t}_1} < M_{\tilde{t}_2}$. Furthermore, the mixing angle $\theta_{\tilde{t}}$ can be written as :

$$\tan 2\theta_{\tilde{t}} = \frac{2\alpha_t M_t}{M_{\tilde{t}_R}^2 - M_{\tilde{t}_L}^2} \quad (3.34)$$

The last relation implies that the mixing angle is proportional to the mass of the top quark. Consequently, the corresponding mixings for other generation of squarks will be very small as a direct result of their small masses. The mixing angle $\theta_{\tilde{t}}$ helps to parametrize the mass eigenstates which are obtained after diagonalising the matrix $\mathcal{M}_{\tilde{t}}^2$:

$$\begin{pmatrix} \tilde{t}_1 \\ \tilde{t}_2 \end{pmatrix} = \begin{pmatrix} \cos\theta_{\tilde{t}} & \sin\theta_{\tilde{t}} \\ -\sin\theta_{\tilde{t}} & \cos\theta_{\tilde{t}} \end{pmatrix} \begin{pmatrix} \tilde{t}_L \\ \tilde{t}_R \end{pmatrix} \quad (3.35)$$

The mass splitting between the two mass eigenstates \tilde{t}_1 and \tilde{t}_2 can be written :

$$M_{\tilde{t}_1}^2 - M_{\tilde{t}_2}^2 = \frac{2M_t(A_t - \mu \cot\beta)}{\sin 2\theta_{\tilde{t}}} \quad (3.36)$$

Looking at the above relation, one can notice that due to the big top quark mass and consequently the large top Yukawa coupling, the mass splitting can be large, hence one of the stop quark mass eigenstates can be much lighter compared to the other squarks.

3.4 Production of 3^{rd} generation stop quarks

Since this search focuses on stop quarks only and not sbottom quarks, we thus elaborate only on the production of the "up"-type 3^{rd} generation squarks, but similar discussions hold for the "down"-type squarks. Also, we have to note that in hadron colliders both \tilde{t}_1 and \tilde{t}_2 stop quarks can be produced, but we will focus only on the phenomenology of the former assuming that $M_{\tilde{t}_1} < M_{\tilde{t}_2}$. In case R-parity is conserved and the stop

quarks are relatively light, there are two main production mechanisms at hadron colliders. One way is via quark-antiquark annihilation while the other is via gluon fusion. The corresponding cross section can be expressed as [46]:

$$\sigma\{q\bar{q} \rightarrow \tilde{t}_1\bar{\tilde{t}}_1\} \propto \frac{\alpha_s^2}{s} \beta_{\tilde{t}_1}^3 \quad (3.37)$$

$$\sigma\{gg \rightarrow \tilde{t}_1\bar{\tilde{t}}_1\} \propto \frac{\alpha_s^2}{s} \log\left(\frac{1 - \beta_{\tilde{t}_1}}{1 + \beta_{\tilde{t}_1}}\right) \quad (3.38)$$

where $\beta_{\tilde{t}_1} = \sqrt{(1 - 4m_{\tilde{t}_1}^2/s)}$ and \sqrt{s} is the partonic center of mass energy (C.M.E). Those two production mechanisms are illustrated in Figure 3.4.

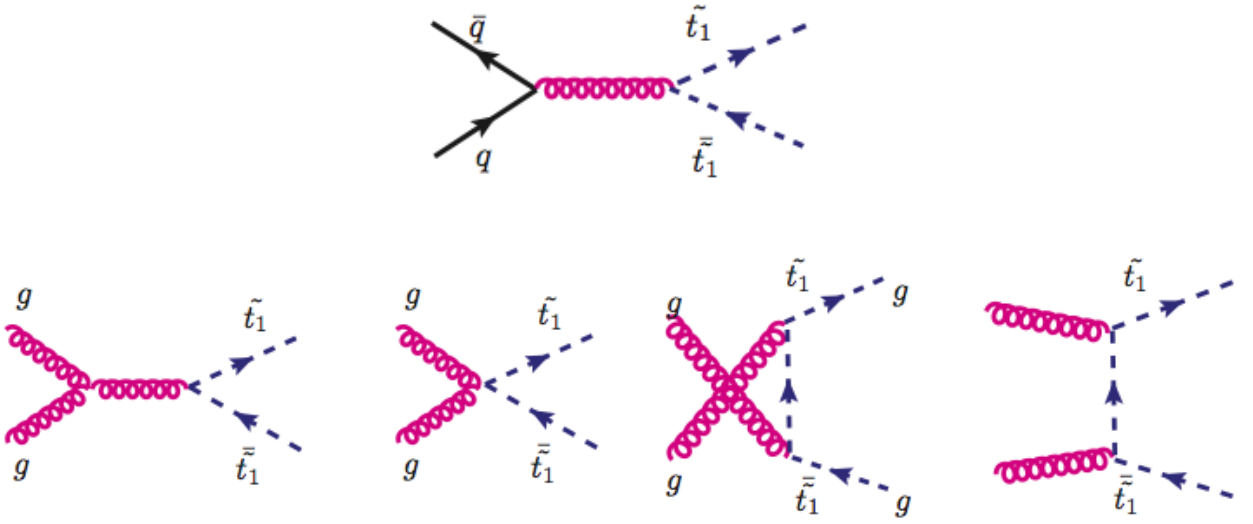


Figure 3.4: First order Feynman diagrams of stop quark pair production via $q\bar{q}$ annihilation (top) and gluon fusion (down).

Furthermore, there is also a third mechanism involving gluinos ($\tilde{g} \rightarrow \tilde{t}_1 t$) which dominates if it is kinematically allowed :

$$m_{\tilde{g}} \geq m_{\tilde{t}_1} + m_t \quad (3.39)$$

whereafter the gluino decays according to :

$$\tilde{g} \rightarrow \tilde{t}_1 t \quad (3.40)$$

When the two-body decay of the gluino is kinematically not allowed, it will decay to a three-body or even four-body decay. But if the stop quark is heavier than the gluino,

the decay mode of a gluino to a top quark pair (or a bottom quark pair, or mixed top-bottom pair) can still be realized if the stop quark is lighter than the other squarks via a virtual emitted squark :

$$\tilde{g} \rightarrow \bar{t} t \tilde{\chi}_1^0 \quad (3.41)$$

Finally, the cross section of the $pp \rightarrow \tilde{t}_1 \tilde{t}_1$ process at $\sqrt{s} = 7$ TeV is shown in Figure 3.5 [47].

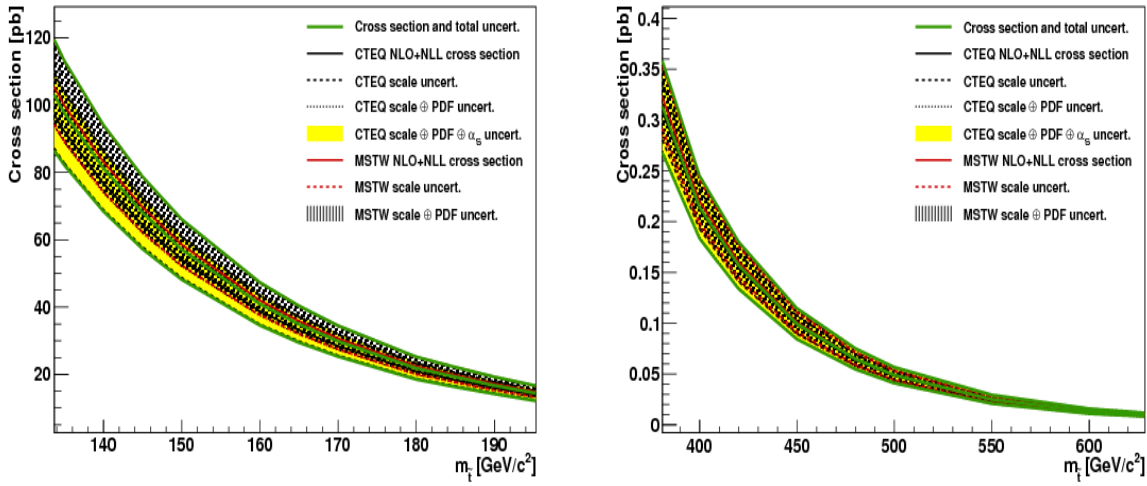


Figure 3.5: The NLO+NLL production cross section of the $\tilde{t}_1 - \tilde{t}_1$ as a function of the stop quark mass at $\sqrt{s} = 7$ TeV for different ranges. The black (red) lines correspond to the cross section and scale uncertainties by using the CTEQ (MSTW) PDF set. The yellow (dashed black) band corresponds to the total CTEQ (MSTW) uncertainty. The green lines show the total cross section and uncertainty [47].

3.5 Decay modes of 3rd generation stop quarks

In general, the accessible decay modes of stop quarks strongly depend on the SUSY particle mass spectrum, but we can separate it into two, three, or even four-body decays.

3.5.1 Two-body decays

1. Assuming that $m_{\tilde{t}_1} > m_t$ and if the stop quark particle is very heavy, it can decay via the strong interaction into top quarks and gluinos. If it holds :

$$m_{\tilde{t}_1} \geq m_t + m_{\tilde{g}} \quad (3.42)$$

then the stop quark decays according to :

$$\tilde{t}_1 \rightarrow t \tilde{g} \quad (3.43)$$

2. On the same context, assuming the presence of the top quark then if :

$$m_{\tilde{t}_1} > m_{\tilde{\chi}_k^0} + m_t > m_{\tilde{\chi}_k^0} + m_b + m_W \quad (3.44)$$

then the following mode dominates :

$$\tilde{t}_1 \rightarrow \tilde{\chi}_k^0 t \quad (3.45)$$

3. Another accessible decay if $m_{\tilde{t}_1} \geq m_{\tilde{\chi}_l^+} + m_b$ is :

$$\tilde{t}_1 \rightarrow \tilde{\chi}_l^+ b \quad (3.46)$$

If the chargino is the lightest one ($l=1$), then it can further decay into five possible ways, provided that they are kinematically allowed :

$$\tilde{\chi}_1^+ \rightarrow \tilde{\chi}_1^0 (H^+ / W^+) \quad (3.47)$$

$$\tilde{\chi}_1^+ \rightarrow \tilde{u}_L \bar{d} \quad (3.48)$$

$$\tilde{\chi}_1^+ \rightarrow \bar{\tilde{d}}_L u \quad (3.49)$$

$$\tilde{\chi}_1^+ \rightarrow \tilde{u}_R \bar{d} \quad (3.50)$$

where u (d) denotes "up" ("down")-type fermions.

4. If the above decay modes are suppressed and :

$$m_{\tilde{t}_1} \geq m_{\tilde{\chi}_k^0} + m_l \quad (3.51)$$

then the following decay is possible :

$$\tilde{t}_1 \rightarrow \tilde{\chi}_k^0 c \quad (3.52)$$

3.5.2 Three-body decays

Three-body decays are also possible if the two-body decays are kinematically not allowed. Hence decays to a lighter sfermion and a gauge or Higgs-boson are possible provided that the mass splitting is large enough.

$$\tilde{t}_1 \rightarrow \tilde{\nu}_\ell \ell^+ b \quad (3.53)$$

In fact, also decays involving sleptons are possible if $m_{\tilde{t}_1} \geq m_{\tilde{\ell}} + m_b$ and they also give three-body decays :

$$\tilde{t}_1 \rightarrow \tilde{\ell}^+ \nu_\ell b \quad (3.54)$$

In such a case, the subsequential decay of the slepton being the NLSP, results in final states with heavy flavour quarks (b-jets), leptons and missing transverse energy.

3.5.3 Four-body decays

In case sneutrinos and leptons are heavier than the stop quark, the following decay is also possible via :

$$\tilde{t}_1 \rightarrow \tilde{\chi}_k^0 (H^{+*}/W^{+*}) b, H^{+*}/W^{+*} \rightarrow f f' \quad (3.55)$$

Table 3.3 summarises the allowed decay modes of \tilde{t}_1 along with the kinematical conditions that have to be met.

Condition	Decay mode
$m_{\tilde{t}_1} \geq m_t + m_{\tilde{g}}$	$\tilde{t}_1 \rightarrow t \tilde{g}$
$m_{\tilde{t}_1} > m_{\tilde{\chi}_k^0} + m_t > m_{\tilde{\chi}_k^0} + m_b + m_W$	$\tilde{t}_1 \rightarrow \tilde{\chi}_k^0 t$
$m_{\tilde{t}_1} \geq m_{\tilde{\chi}_l^+} + m_b$	$\tilde{t}_1 \rightarrow \tilde{\chi}_l^+ b$
$m_{\tilde{t}_1} \geq m_{\tilde{\chi}_k^0} + m_l$	$\tilde{t}_1 \rightarrow \tilde{\chi}_k^0 c$
$m_{\tilde{t}_1} \geq m_{\tilde{\ell}^+} + m_b$	$\tilde{t}_1 \rightarrow \tilde{\ell}^+ \nu_\ell b$
$m_{\tilde{t}_1} \geq m_{\tilde{\nu}_\ell} + m_{\ell^+} + m_b$	$\tilde{t}_1 \rightarrow \tilde{\nu}_\ell \ell^+ b$
$m_{\tilde{t}_1} \geq m_{\tilde{\chi}_k^0} + m_{H^+/W^+} + m_b$	$\tilde{t}_1 \rightarrow \tilde{\chi}_k^0 f \bar{f}' b$

Table 3.3: The kinematical conditions that have to be satisfied for the specific decay modes of the \tilde{t}_1 .

3.6 Simplified Models Spectrum

One of the big challenges while drawing the strategy for an experimental SUSY search, is the treatment of the free parameters of the model(s) under consideration. Indeed, all currently existing SUSY models, are in general not much constrained due to the affluent degrees of freedom. At the end of the day, this results in numerous difficulties both while building the analysis, but also while trying to interpret the results as well. For instance, SUSY searches optimised for mSUGRA models have only five free parameters which define the exact topology. Although this gives a easy handled toy model, the strong assumptions that are made are always at the expense of inclusiveness, thus sensitivity is decreased. Even more, the results are typically quantified by using the statistical significance of the expected deviation from the background-null hypothesis. This procedure was reasonable for the first LHC data taking period as mSUGRA models were well-motivated and in the belief was that the generic SUSY models were out of reach during the low data statistics era [48]. But even if mSUGRA can predict some very clear and distinctive experimental final-state signatures, choosing a single SUSY model is restrictive by definition. This is a side-effect of the aforementioned assumptions which include the particles spectrum, their mass splittings, or even the branching ratios.

That said, performing a generic SUSY study while using all these assumptions looks a very tricky task, if feasible at all. More problems start to appear when the same production modes and decay channels contribute to the same final states, but the kinematics and shapes vary according to the choice of the model parameters at question. Hence, and given the potential of the LHC, it is obvious that a more coherent strategy must be used if we want to be as inclusive as possible and at the same time be able to translate the results to consistent theories.

During the last years, new models have been developed known as *Simplified Models Spectrum* (SMS) [49, 50]. In principle, the SMS are constructed by effective field theories bearing only the minimum needed SUSY particle parameters which give a specific final state of interest. The SMS are parametrized directly in terms of production cross sections, branching ratios for decays and masses of the involved s-particles. Moreover, usually there is more than one production mode and decay path that can contribute to the very same experimental final state (i.e. leptons or multiple jets and/or missing transverse energy). Therefore, it is necessary that the SMS is able of reproducing the kinematics, the shapes and the essential phenomenology of the mapped new physics models, which is depicted in various final state observables like the invariant mass

edges and endpoints for instance. In other words, what makes SMS that useful, is that by definition they are built from the simplest possible spectra which is still compatible with the full SUSY model. Thus, they represent a natural starting point if we aim to simplify new physics searches, since observations based on the phenomenology of the SMS can be read out as evidences (but not hard proofs) for the very existence of new physics phenomena.

In practice, the build-up of a SMS is based on a customized s-particle spectrum where some particles are decoupled from all others in order to simplify the experimental search. Therefore the natural choice is that the s-particles that are allowed to be "produced" are also the ones that are accessible to the experiment. As for the rest of the s-particles, the masses typically are set to be too high, thus not reachable. Furthermore, one allows only certain decay paths to be realized by setting the branching ratios so that only the topology (ies) of interest are allowed to be produced.

Given all the above, it comes as no surprise that the list of the SMS already covers a rather diverse topologies spectrum, covering the majority of production and decay mechanisms one can meet in SUSY. This allow us to interpret the results of a given SMS having only a minimum number of free parameters that characterize it. It is important to realize that employing SMS does not aim to replace the inclusive/generic signature searches. On the contrary, the intention is to steer these searches even better by providing bottom-up pragmatic models. For example, provided that we observe a deviation in the context of a given SMS, we can go back to the full physics model and focus better on that specific region of the phase space compatible with this exact signature of the utilized SMS model. Therefore, the SMS framework should be seen as a useful tool *complementary* to the generic/inclusive searches which could pinpoint us better where to look in case evidence for new physics arises.

3.6.1 Top-Down vs Bottom-Up (SMS) approaches

In this search we adopt a *bottom-up* approach using a SMS. In the already conducted BSM searches at the Tevatron, the LEP and the LHC as well, usually the so-called *top-down* approach was adopted which is better suited for inclusive searches. In this section we argue why the former was chosen and what are its advantages and disadvantages compared to the latter.

No matter what path one chooses, first a reference model has to be chosen. In the case of a top-down framework, the involved s-particles masses (like for example the

gaugino and squark ones) are ruled by high scale physics in contrast to the SM particles which are ruled by the weak scale. Although the weak scale parameters can be retrieved from renormalization group evolution, the chosen high scale parameters are not always very well defined. Consider for example, the *compressed spectrum scenarios*, the region where produced SUSY particles acquire mass close to the mass of the LSP. In that corner of the phase space things become complicated as the final state signatures are the result of the interplay between the neutralinos, the gluino and the squarks and all these reside in a phase space with large weak scale degeneracy.

On top, even the "simple" SUSY scenarios which follow a top-down approach (like mSUGRA), are not always suitable for experimental searches as they lack the ability to reproduce the compressed spectra coherently mainly due to the limited sensitivity there. One could argue, that this is somehow anticipated as the results typically are being interpreted in terms of high scale physics. For instance, the majority (if not all) of the results on mSUGRA models are interpreted in the $(m_0, m_{1/2})$ plane. And to make things even worse, these acquired results have to be re-interpreted in terms of weak scale physics, something not trivial at all. This is still a missing component in the current SUSY search strategies, where simplified models are needed to be employed. Thus and to obtain sensitivity in this restricted phase space where soft final-state signatures are produced, the development of a new strategy is required.

Mapping a given final state to a specific decay channel is usually a very tricky task. A simple example is the top quark final state signature, where it is a very difficult to differentiate between a top quark coming from a long SUSY cascade, a gluino-mediated prompt decay according to $\tilde{g} \rightarrow t\tilde{t}_1$, or even a SM process. Therefore, the top-down approach has to be tweaked carefully and the analysis strategy has to take into account the involved masses, the production cross sections and the branching ratios, all at the same time. That said, it is not difficult to see, that for many of the SUSY searches, the top-down approach is not the most optimal solution, as similar decay chains limit the sensitivity due to final state signatures that look alike. On the contrary, starting from a bottom-up model, one can easier trace back to the origin the most relevant contributing topology of a particular model.

Further, within a top-down approach there is also another side-effect caused by the probed result, where typically part of the phase space gets excluded in the absence of strong excesses. But while for the reference model this classification is perfectly sane, the problem comes while examining other "suppressed" models which in principle could result into similar final states, thus might get excluded or not. Now, if the same

initial model is used again as a reference point in a new optimisation/search "round", the already excluded region typically is usually ignored. Hence, there are models that are excluded while they should have not. And this happened, simply because the production and decay processes of these models were just concealed as the reference model was dominating. Clearly, the sensitivity to these models will be decreased or even lost, while there was a region still to be considered.

Given all the above arguments, a bottom-up approach incorporating a SMS offers the flexibility to model all the necessary weak scale parameters mapped up to high scale parameters. At the same time, all the unique characteristics of each production and decay mode under consideration can be still used. For example, the direct stop quark pair production and its decay down to a top quark pair and the LSP consists one simplified model, while gluino-mediated stop quark pair production with the same final state particles forms another. The former is the adopted model for this analysis.

3.7 Direct stop quark pair production as a SMS model

No matter if one works with a SMS model or not, the overall event topology depends on the kinematics and properties of the produced s-particles that come out of the hard-scattering. However, in the former case it is enough to just vary the masses of the considered s-particles of the model in order to build a full scan on the considered parameter space. Consequently, the derived results can be expressed in terms of the mass parameters alone, with no need to involve any other property of the s-particles. But if one wants to have a full SUSY model, meaning not working with a SMS, then adjusting for the branching ratios and for the cross sections at each point and for each considered topology is a necessity. The above arguments is just few of the reason why experimental physicists have grown so fond of the SMS during the last years.

In this search we consider the topology of direct stop quark pair production according to $pp \rightarrow \tilde{t}\tilde{t}$ decaying to a top quark and a neutralino (similar to Equation 3.45 with $k=1$, i.e. $\tilde{t}_1 \rightarrow \tilde{\chi}_1^0 + t$). The produced neutralino is also the LSP and assuming R-parity conservation it has to be stable. By setting the branching ratio of that particular decay mode of the stop quarks to be 100%, we thus ensure that our SMS model has only two free parameters, which are the masses of the stop and that of the LSP. Also, the rest of the squark masses and the gluino are decoupled, meaning that their masses have been set to high values, thus they are not produced at all. In the CMS collaboration, this SMS model is usually referred to as "T2tt".

The cross section of the T2tt SMS model depends only on the mass of the stop quark (Section 3.4). Recently, both the ATLAS and the CMS collaborations have agreed to use common tools to derive the cross section for various SMS scenarios [51]. These calculations include the resummation of soft gluon emission at the next-to-leading logarithmic accuracy whenever possible. In this search we make use of these tools to derive the production cross section of direct stop quark pair production. Figure 3.6 illustrates the direct stop quark pair cross section at a $\sqrt{s} = 8$ TeV along with the theoretical uncertainties.

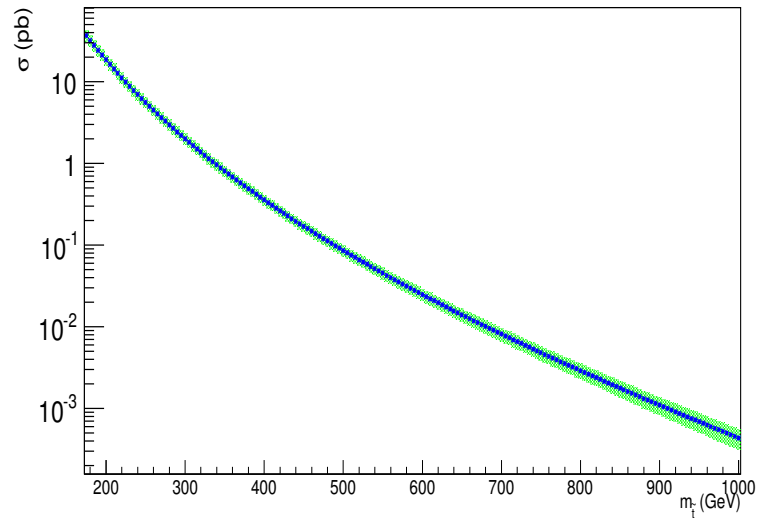


Figure 3.6: The NLO+NLL direct stop quark pair production cross section at $\sqrt{s} = 8$ TeV (blue line) with the theoretical uncertainties (green band). The values have been obtained from [51].

3.7.1 Direct stop quark pair production and final state topology

The top quarks decay almost exclusively to a b quark and a W-boson. Therefore, in our considered SMS model since each of the stop quarks decays always to a top quark and a neutralino. Hence, we can classify the events according to the W-boson decays. In the context of this thesis, we assume that the top quark decays always to a b quark and a W-boson, whereas the decay modes of the latter can be classified as :

1. **Fully Hadronic** : The branching ratio of a $t\bar{t}$ event where both the W-bosons decay hadronically is $\sim 4/9$. This $t\bar{t}$ results in six quarks, with two of them being b quarks while the remaining four are light ones. Since no leptons are produced, multi-jet production emerging from QCD is a source of abundant background making the signal not easily distinguishable, although its large rate compared to

the other decay modes. In any case, the signal rate is some orders of magnitude smaller than that of the background. This mode can be identified by requiring six relative hard jets. The extra requirement of at least one b-tagged jet, a minimum threshold on the scalar sum of the transverse momentum (p_T) of the jets and a minimum threshold on the missing transverse energy (E_T) will further help controlling the background contribution.

2. **Fully Leptonic** : This decay mode comprises $\sim 1/9$ of a $t\bar{t}$ event. Here, both W-bosons decay into a lepton with its neutrino, giving a final state with two opposite-sign leptons, two neutrinos and two b quarks. Experimentally, this mode can be identified by requiring two high p_T leptons, two jets and the presence of E_T . Further, requiring at least one b-tagged jet will help reducing the background, while putting a minimum threshold on the E_T will help controlling the contribution coming from the $W \rightarrow \ell\nu_\ell$ process which is a source of real E_T . Still, in this kind of topology although the SM backgrounds have a small contribution, the cross section of such signal processes is also very small in general.
3. **Single Lepton + Jets** : This decay mode comprises $\sim 4/9$ of a $t\bar{t}$ event. One of the W-bosons decays into a lepton and its neutrino, while the other decays hadronically. The final state consists of four jets with two of them being b quark jets and the other two being light jets, one neutrino and one charged lepton. Typically, this mode can be identified by requiring one high p_T isolated lepton, four jets and the presence of E_T . Similarly to the previous cases, posing a minimum threshold on the E_T and/or the H_T the contribution from background processes can be reduced.

For the three outlined decay modes, the SM $t\bar{t}$ consists an irreducible background source to the $\tilde{t}_1 \bar{\tilde{t}}_1$ production as the final states are very similar, with the exception of the presence of two neutralinos in the case of the latter. Furthermore, the neutrinos and the neutralinos of the final state do not interact with the detector, and as they escape direct detection they result in additional E_T as an experimental signature. In this search, stop quark pair production in the single lepton + jets decay mode will be studied, where the lepton is the muon. Therefore, our experimental signature is one muon, four jets where two of them originate from a b-quark, while we also expect large E_T due to the undetected neutralinos and neutrinos of the final state. Figure 3.7 illustrates the leading order Feynman diagram of this topology along with the mass spectrum in the context of the employed T2tt SMS model. We have to note, that although in the aforementioned plot the decay to a μ^+ is illustrated, all conjugate diagrams have been

considered as well.

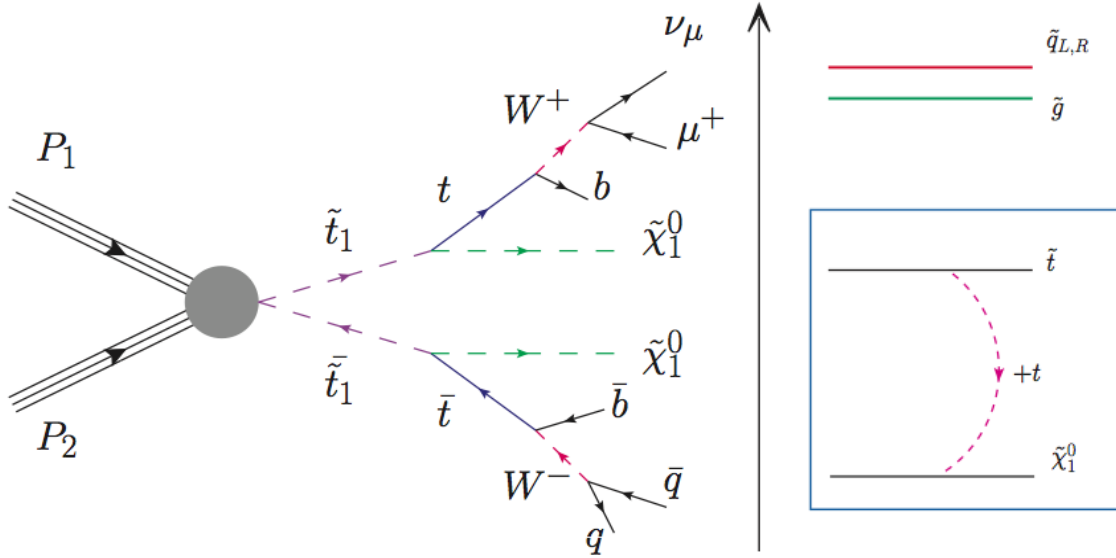


Figure 3.7: Left : The leading order Feynman diagram of the T2tt SMS model (direct stop quark pair production) that will be considered for this analysis, along with the decay according to $pp \rightarrow \tilde{t}_1 \bar{\tilde{t}}_1 \rightarrow b\mu^+\nu_\mu\tilde{\chi}_1^0 \bar{b} q\bar{q}\tilde{\chi}_1^0$, where also the charge conjugate diagrams are considered as well for this analysis. Right : The T2tt mass spectrum. Except the stop quark and the lightest neutralino, the rest of squarks and the gluino are considered to be much heavier, therefore decoupled and not participating in the production mechanism at all.

3.7.2 Current experimental constraints

Both the ATLAS and the CMS collaborations have performed studies considering the same SMS model as we do [52–54] but following different analysis strategies. All results have put upper limits on the $(m_{\tilde{t}_1}, m_{\tilde{\chi}_1^0})$ plane for the direct stop quark pair production. Briefly, at 95% C.L. stop quark masses up to 700 GeV when considering massless neutralinos have been excluded, while the excluded stop quark masses are up to 600 GeV for neutralino masses close to 240 GeV. In Section 11.2 we will discuss the existing exclusion limits in more details and make a full comparison with our obtained results.

The good thing about science is that it is true whether or not you believe in it.

Neil de Grasse Tyson

CHAPTER 4

SIMULATING COLLISION EVENTS

4.1 Introduction to Monte Carlo techniques

The events in high-energy collisions have usually a complex sub-structure, whereas the entities composing them cannot always be predicted from first principles. The majority of these events incorporate partons, either because the colliding particles are hadrons (like at the LHC which is a p - p colliding experiment) or just because they are present in the produced final state and therefore are used to define the observables. So, the need for accurate and robust theoretical predictions of the observable distributions at collider experiments is the main reason for developing Monte-Carlo (MC) event generators for high energy physics (HEP).

The backbone of MC algorithms is their integration routine. They use random numbers in order to calculate integrals numerically, usually over a multidimensional space. In physics however, we usually deal with theories that are formulated in terms of the equations of motion. These equations usually try to describe the relative or absolute change of variables with respect to system parameters, something that is even more challenging if one considers time-dependent systems [55, 56]. This chapter is organised as follows : Section 4.2 describes the basic workflow of event generators and in Section 4.3 the anatomy of a collision event in HEP is discussed, while the rest of the chapter describes the connection between an observable event in collider physics and the various steps involved in a full chain to generate the events.

4.2 General characteristics of event generators

Event generators, constitute a vital component of modern high energy physics experiments such as the LHC. An event generator can be seen as a program which aims to simulate individual and distinct events, rather than just depict the bulk properties of a physical process. At the same time it should allow the problem to be subdivided into smaller and more fundamental pieces. The event generators are capable of calculating the scattering Matrix Elements (ME) and use MC techniques in order to arrive at representative distributions of the processes involved. An event generator creates numerous events, each one being characterised by unique kinematic features encapsulated into its four-momentum, along with the particle type (proton, lepton, etc). However, nowadays there are many different event generators available, some of them being general-purpose ones (like Herwig [57] or Pythia [58]) while some others are specialised generating only a sub-range of the known physics processes. Further, other packages (like GEANT4 [59] or Delphes [60]) can mimic the detector's response to simulate the interaction of the particles with the detector's budget. Therefore, we see why event generators consist an inseparable part of modern HEP experiments. However, one should always have in mind that generators are far from being perfect and this can be seen for example while trying to describe a range of diverse physics processes. Some of these are better understood from first principles, while others are not. That means, that the event generators although they can be a very helpful tool in order to test any theoretical framework to see if it fits the experimentalists expectations, it may happen that they are not optimised for a specific class of physics processes in the first place. In such a case, we will need to make use of models tuned to data to cover this gap. Also, different implementations of the same physics processes have been implemented in various event generators, thus a given process may be better modelled in one generator compared to another. Of course, it is not always trivial to distinguish nor easy to quantify these differences.

However, it would not be possible carrying out physics analyses without the use of event generators, since a proper understanding of both the signal and background processes is first needed if we want to discriminate those two in the most efficient way. The main concept is that generators must provide an adequate description of the produced final state so at least ideally any experimental observable (or even their combinations), can be used to compare prediction against data. That implies that generators must be appropriate to be used at various stages of an experiment: while calibrating and commissioning the detector, while optimising its triggers, while estimating the sensi-

tivity to a given physics model, while setting and revising analysis strategies, when we need to evaluate acceptance and selection efficiencies etc. However, it is not the event generators that produce real events, rather than the "machine", like the LHC. From these events, the most interesting ones are stored with the help of the data acquisition (DAQ) system of the detector for further processing like for example the reconstruction of final state objects. But in principle, the same event reconstruction framework and workflows can to be used for both the real experiment output and the event generators "product" delivering robust final objects suitable for real analysis. Therefore, the MC techniques have to be bound to the physical process under study in such a way that a direct connection between phase space points and generated events can be made at the end. This can be achieved if the used MC methods are able to generate the so-called *unweighted* events.

The main argument of using MC event generators is that quantum mechanics are *probabilistic* and not *deterministic*. Hence, the underlying calculations can only provide the probability for different outcomes for a given measurement. That implies, that on an event-by-event basis, it is impossible to know *beforehand* what will happen: anything that is bearing probability above zero, is *allowed* to happen next. It is *only* when averaging over very large event samples which in theory, these should go to infinity, that the expected probability distributions emerge and come into place. In MC techniques, the use of (pseudo) random numbers is broadly used in order to reproduce as accurately as possible the real probabilities for different feasible outcomes of a given input process.

4.3 Anatomy of an event in collider physics

If we want to break down the structure of a real HEP hadron collision event in several steps, it could be summarised as follows [61] :

1. Initially, a collision between two hadrons happens. Each one of these hadrons is a collection of partons, that is quarks and gluons. Then, a parton from each side collides with another parton from the other side, and this composes the hard process of interest, like for example $gu \rightarrow gu, gg \rightarrow t\bar{t}$ etc. Also, the production of "resonances" such as the top quark, the BEH-boson or the W^\pm, Z^0 -bosons and their decays have to be considered as part of this process itself, since intrinsic properties like the spin correlations will be propagated from the production down to the final decayed particles.

2. Given the above, accelerated coloured particles such as quarks and gluons are involved in the collision. Although due to the confinement they cannot be measured directly, we do know that they can cause bremsstrahlung. Exactly because of this properly, the emissions that are associated with the two incoming colliding partons are commonly referred as *Initial-State Radiation* (ISR) and typically the *space-like* parton showers are used to describe it.
3. On the other hand, emissions that are associated with final state partons are formally known as *Final-State Radiation* (FSR) which can be approximated with the so-called *time-like* Parton Showers (PS).
4. The actual interaction between hadrons cannot be directly modelled from first principles. It is only the hard scattering between partons that can be calculated perturbatively. Due to the asymptotic freedom of QCD, the partons can be treated as free particles. Typically, the realised scattering processes involve large invariant momentum transfers, happening in a short time scales. If we take into account higher orders of the perturbation approach, infrared divergencies arise for both the virtual-loop correction and the real radiation. However, these divergencies must mutually cancel if we want to get an finite inclusive cross section [62, 63].
5. At this point, we have considered the interaction from only one parton from each incoming hadron that participates into the hard collision. However, the hadron is made up of more partons, meaning that more partons can collide with other partons from the other hadron, resulting in *multi-parton interactions* (MPI). We must distinct the MPI from the Pile-Up events where several hadron pairs collide during the bunch-crossing. Furthermore, it is obvious that each of these collisions can be coupled with ISR and FSR.
6. Partons participating in the collisions, carry only a sub-fraction of the total energy of the incoming hadrons, while much of the energy remains in the beam remnants. These remnants carry colour that levels for the colour that was taken away by the already collided partons and continue to travel essentially in the same direction as that of the original protons.
7. Once the coupling between the aforementioned partons becomes larger enough, new quark-antiquark pairs are produced from the vacuum and the partons form new hadrons. This phase is known as *hadronization* which results in colour neutral hadrons. These newly created hadrons are usually unstable, thus they will further decay. However, these decays take place at various timescales until sta-

ble particles are created which can be observed directly in the detectors provided that they are sufficiently long-lived. At this point, we have to match and combine the event-generator description to a detector- simulation framework. It is only from this point onwards that experimental information can be retrieved and used to reconstruct back the initially states and interactions.

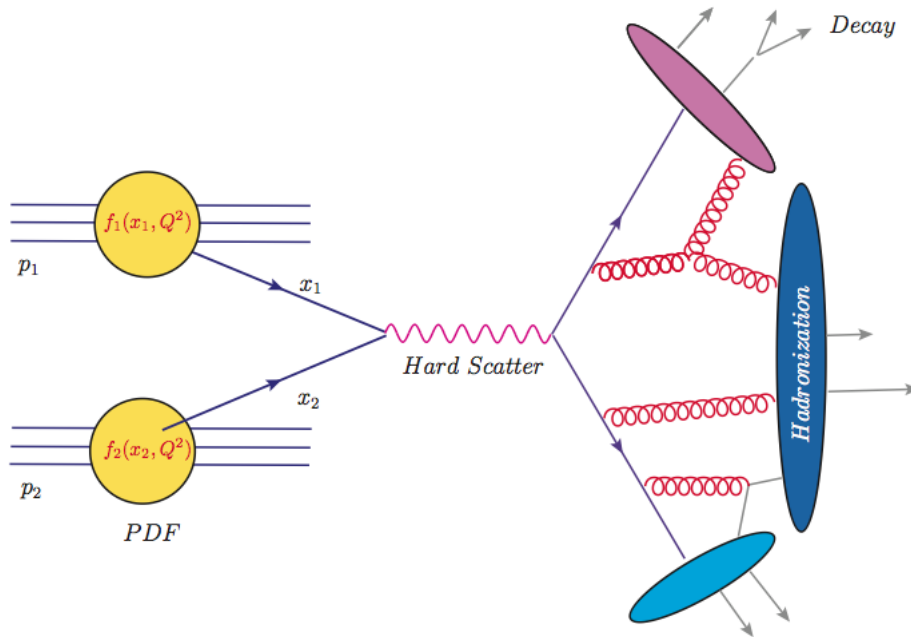


Figure 4.1: The general structure of an event generation starting from the hard interaction and the resulting fragmentation, hadronization, and decay.

The different steps mentioned above are illustrated in Figure 4.1 which sketches the evolution of a hadron-collider event while QCD bremsstrahlung and hadronization effects are included. Modern event generators allow all of the above steps to be considered sequentially. On top, we still have the freedom to define a set of rules that can be used as input to construct simple or more complex states, some of these resulting to hundreds of particles travelling to many different directions of the phase space. In any case, the core piece of the event simulation is provided by the hard process, which can be calculated with fixed order perturbation theory and can be handled by computations based on the *Matrix Elements* (ME). Typically, the calculation of the ME is either hard-coded in routines or it can be calculated analytically by specialised programs called *parton-level* or *Matrix Element* (ME) generators. The QCD evolution which can be described by *Parton Showers* (PS) is the connecting bridge between the hard scale of the created coloured parton with the hadronization scale where the transition to the colourless hadrons occurs.

The available event generator tools cover a very broad spectrum, from general-purpose ones to more specialised ones. In this thesis, MadGraph, PowHeg [64–66] and Pythia have been used for the simulated datasets while more details are given in Section 4.7.

4.4 Hard subprocesses and the use of Matrix Elements

From the Lagrangian that describes a theory, the ME can be calculated analytically with the use of the Feynman rules. If we also integrate the ME available phase space, the calculation of the production cross section is feasible. As an example we can take the scattering of quarks in the QCD framework, say $u_1 d_2 \rightarrow u_3 d_4$, a process very similar to the Rutherford scattering but with gluon exchange instead of photon. The Mandelstam variables [67] are therefore :

$$\hat{s} = (\mathbf{p}_1 + \mathbf{p}_2)^2, \quad \hat{t} = (\mathbf{p}_1 - \mathbf{p}_3)^2, \quad \hat{u} = (\mathbf{p}_1 - \mathbf{p}_4)^2 \quad (4.1)$$

where \hat{s} is the shared total energy, and \hat{u} , $\hat{t} = -\hat{s}(1 \pm \cos\hat{\theta}/2)$ with $\hat{\theta}$ being the scattering angle. The differential cross section can be expressed by :

$$\frac{d\hat{s}}{d\hat{t}} = \frac{4\pi}{9\hat{s}^2} \alpha_s^2 \frac{\hat{s}^2 + \hat{u}^2}{\hat{t}^2} \quad (4.2)$$

Similar expression can be obtained by varying the colour factors to obtain the differential cross section for other processes, like $qg \rightarrow qg$ or even gluon scattering $gg \rightarrow gg$ without neglecting some other QCD processes like $gg \rightarrow qq$, which however contribute less.

The next step is to get unweighted hard scattering events which are produced using the *hit-or-miss* method which was described in Section ??.

We denote the fraction of the momentum of the proton that a parton p_1 possesses at scale Q^2 as x_1 , while the momentum fraction distribution is given by $f_{p_1}(x_1, Q^2)$. For a hadron-hadron collision with incoming hadrons A, B the colliding partons p_1 and p_2 extracted from each hadron are carrying a fraction of the total momentum x_{p_1} and x_{p_2} respectively. The *Parton Density Function* (PDF) $f_i(x_i, Q^2)$ gives the probability of finding in the proton a parton of flavour i (gluon or quarks) carrying a fraction x of the proton momentum whereas Q stands for the energy scale of the hard interaction. The PDFs are obeying non-perturbative theory, and cannot be predicted from first principles. However, what we can derive, is the evolution of the equations for their scale-dependence [68].

In our case and for the p_1 parton for example, the exact equation describing the evolution of the PDF $f_{p_1}(x_{p_1}, Q^2)$ is given from what is formally known as the *Dokshitzer-Gribov-Lipatov-Altarelli-Parisi* [69–71] (DGLAP) equation and reads :

$$Q^2 \frac{\partial f_{p_1}(x_{p_1}, Q^2)}{\partial Q^2} = \sum_j \int_x^1 \frac{dz}{z} \frac{\alpha_s}{2\pi} P_{p_1, p_2}(z, \alpha_s) f_{p_2}(x_{p_1}/z, Q^2), \quad (4.3)$$

where the $P_{p_1, p_2}(z, \alpha_s)$ stands for the (regularised) splitting functions, and it is related to the probability that a parton p_1 emits a quark or a gluon and turns into a parton p_2 carrying a momentum fraction z .

Figure 4.2 illustrates the kinematic plane x - Q^2 that is covered by existing measurements and an extrapolation up to the kinematic regime of the LHC by using the DGLAP equation [72, 73].

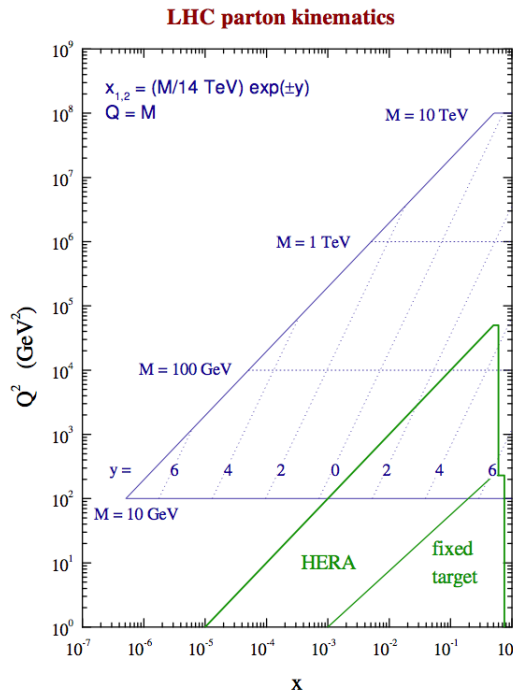


Figure 4.2: The kinematic x - Q^2 plane probed in the production for an object of mass M and rapidity y for the LHC nominal $\sqrt{s} = 14 \text{ TeV}$.

However, to derive the PDFs which are energy dependent, typically they are first measured at a given scale and then are fitted to experimental data. Such PDF sets are the MSTW [74], the HERAPDF [75], or the CTEQ [76]. Figure 4.3 shows the MSTW PDFs, for the gluon and different quark flavours at two different scales of Q^2 [74, 75].

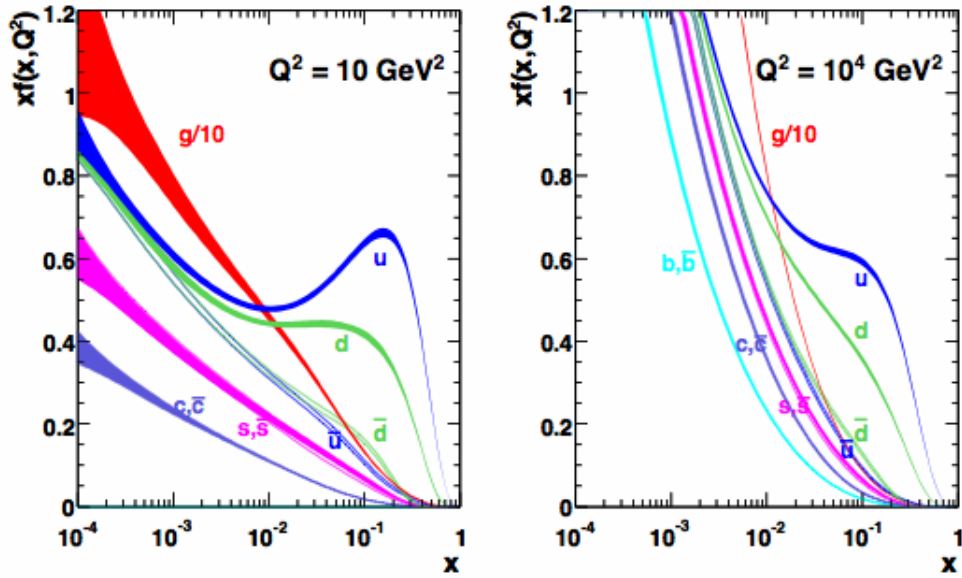


Figure 4.3: MSTW NLO PDFs for $Q^2 = 10\text{GeV}^2$ (left) and $Q^2 = 10^4\text{GeV}^2$ (right) [74, 75].

For lower values of the momentum fraction x , the gluon density dominates, while for large values the densities of up and down valence quarks are dominating. For the CMS MC production, mainly the CTEQ6L1 [77] PDF set was been used for most of the generation of the events utilized for this analysis.

Coming back to the cross section calculation of the hard-scattering, we can write :

$$\sigma = \sum_{p_1, p_2} \int \int \int dx_1 dx_2 f_{p_1}^A(x_1, \mu_F^2) f_{p_2}^B(x_2, \mu_F^2) d\hat{\sigma}_{p_1, p_2}(\mu_F, \mu_R) \quad (4.4)$$

where μ_F and μ_R stand for the relevant factorization and renormalization scales [68]. The renormalization scale is introduced in order to cure the Ultra-Violet (UV) divergencies of the theory. The factorization scale is the cut-off value where the perturbative QCD collapses, thus non-perturbative models are needed to describe the regime below that boundary which corresponds to the long-distance (low energy) part. Both renormalization and factorization introduce a somewhat arbitrary but still necessary scale dependence when it comes to distinguish the "hard" from the "soft" region. Usually, the μ_F^2 is chosen so that the scale dependance of the calculated quantities is minimised, but the exact dependance is actually an artefact of the finite order of the computation itself, which in any case can be mitigated by the inclusion of higher-order terms. Quite often though, the same choice for both factorization and renormalization scales is made meaning $\mu_F^2 = \mu_R^2 = Q^2$.

For the $2 \rightarrow 2$ and some of the $2 \rightarrow 3$ processes it is relatively easy to draw all contributing Feynman diagrams at tree-level and then derive the expression of the squared Matrix Element. Some examples are illustrated in Table 4.1. However, for more complex processes (for instance when we want to include ISR), this is very tricky and becomes unwieldy as well, as it requires specialised routines integrated in stand-alone programs which draw and then evaluate all relevant Feynman diagrams in a semi or fully-automated fashion.

Inclusive event properties including NLO calculations and the corresponding corrections lead to an improved accuracy of the predicted distributions. For more specialised and exclusive models, the cancellation of singularities boils down to the calculation of the contributions from virtual corrections. Still, if we only care about processes at LO it is possible to include up to something like ten partons in the final state. In such a case, the partons have to be kept well separated to avoid the phase-space regions where the divergencies become troublesome, and this can be controlled by the applied angular separation cuts. In addition, we need to make use of the parton showers to avoid the collinear regime.

4.5 Parton Showers

As explained earlier, the generation of events at parton level is usually not directly useful for experimental high energy physics searches. Instead, these parton level events should be bridged with a more universal hadronization model which manifests around a scale where α_s becomes large and perturbative methods collapse. The evolution of partons between the scale of the hard scattering and the hadronization scale is the task of the PS. Also, all other particles involved in the collision (except the incoming partons) which carry colour charge, will radiate via the strong interaction. That means, that quarks and gluons will radiate gluons which can further branch out to create new quark anti-quark pairs. Sometimes, collinear singularities may arise due to collinear emissions of the gluon, for instance in the $g \rightarrow qg$ branching. Thus, the main mission of the PS is to help factorize these collinear singularities with the use of a ME calculation, while evolving the initial PDF at scale Λ'_{QCD} down to a new scale $\Lambda_{QCD} < \Lambda'_{QCD}$. At this new scale, the initial parton should branch into two daughter partons while the PS will set their kinematic properties and flavours. Of course, the definition of a *scale* it is a bit ambiguous and the chosen scale will depend on the used PS scheme. The available PS methods use a different integrated functional form for a given scale. The

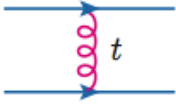
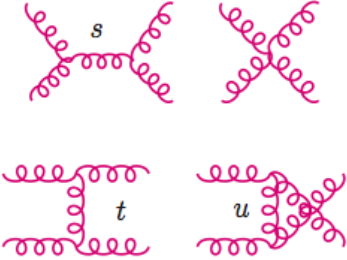
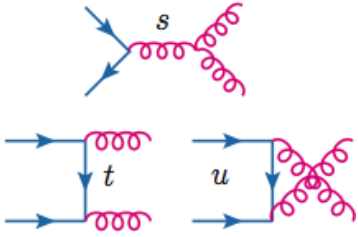
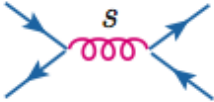
Process	Feynman Diagrams	$ \mathcal{M} ^2 / (4\pi\alpha_s)^2$
$qq' \rightarrow qq'$		$\frac{4}{9} \frac{s^2 + u^2}{t^2}$
$gg \rightarrow gg$		$\frac{27}{2} \left(1 - \frac{tu}{3s^2} - \frac{su}{3t^2} - \frac{st}{3u^2} \right)$
$qq \rightarrow qq$		$\frac{4}{9} \left(\frac{s^2 + u^2}{t^2} + \frac{t^2 + s^2}{u^2} \right) - \frac{8}{27} \frac{s^2}{tu}$
$q\bar{q} \rightarrow q\bar{q}$		$\frac{4}{9} \left(\frac{s^2 + u^2}{t^2} + \frac{t^2 + u^2}{s^2} \right) - \frac{8}{27} \frac{u^2}{st}$
$q\bar{q} \rightarrow gg$		$\frac{32}{27} \frac{u^2 + t^2}{tu} - \frac{8}{3} \frac{t^2 + u^2}{s^2}$
$q\bar{q} \rightarrow q'\bar{q}'$		$\frac{4}{9} \frac{u^2 + t^2}{s^2}$

Table 4.1: Some of the $2 \rightarrow 2$ QCD parton scatterings at tree-level along with the expression for the $|\mathcal{M}|^2$ using the Mandelstam variables.

scale is usually associated to the invariant mass of the branching i.e. $\Lambda_{QCD} \sim M^2$, but can also incorporate other variables, like the angle between the partons, or the transverse momentum of the daughter partons for example. In any case, these branchings are applied recursively down to the chosen hadronization scale and at the end we have the "full" evolution of the parton's branchings at hand.

The machinery behind the PS allows the combination of branchings like $g \rightarrow q\bar{q}$, $q \rightarrow qg$ or $g \rightarrow gg$. Thus, more complex multiparton final states are built. Furthermore, the PS makes use of the so-called *Sudakov Form Factor* which provides a physical way to handle the cancellations of the divergencies. Of course none of the above simplifications is exact, but their cumulative description provides a relatively good approximation concerning the sub-structure of emissions at both the soft and the collinear regimes [61].

4.5.1 Parton branchings

QCD perturbative calculations at NLO are far from trivial, as the complexity of the calculations increases factorially with the order. However, there are cases where a collinear parton emission from either an incoming or outgoing parton forbids us from to obtain a fixed order calculation. This is where the PS comes into play, when for example we need to map a complex $2 \rightarrow n$ process into a more simple core process, like $2 \rightarrow 2$ convoluted with showers. At this point there are two approaches that one can use. The particles are either treated as being always on-shell while the uncertainty relation allows the energy to be violated for a very short time. In the other approach, (which nowadays tends to be more commonly used) the representation of Feynman graphs requires the conservation of the 4-momentum at each vertex, but the intermediate "propagator" particles are still allowed to be off-shell.

So, the incoming quarks in the aforementioned scattering can radiate progressively harder and harder gluons, while the outgoing ones softer and softer gluons. Of course, we need to define what "hard" or "soft" means, and one convenient definition of hardness is how much off-shell the quarks are, or by how much the 4-momentum is violated [61]. With respect to the ISR of the process, these virtualities are considered to be space-like when $p^2 < 0$, while the FSR is characterised by time-like virtualities, when $p^2 > 0$. Both cases are illustrated in Figure 4.4.

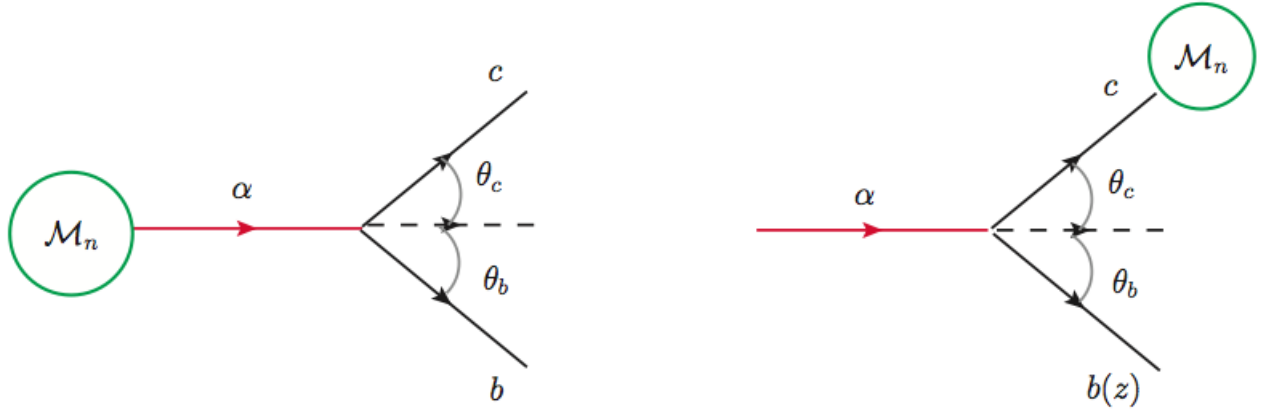


Figure 4.4: Left : The kinematics of time-like branching where an outgoing parton from a n -body Matrix Element \mathcal{M}_n emits partons c, b at angles θ_b and θ_c . Right : The kinematics of space-like branching. An incoming parton α branches into partons b, c . Parton b carries a fraction z of α 's momentum.

4.5.2 Sudakov Form Factor

The Sudakov form factors [78, 79] are related to the intrinsic properties of the loop diagrams, but more generally we can think about it as a direct consequence of the conservation of the total probability that a branching has either to happen or not :

$$\mathcal{P}(\text{no - branch}) = 1 - \mathcal{P}(\text{branch}) \quad (4.5)$$

If no branching occurs upon time T with $T_i = \frac{i}{n}T$ and $0 \leq i \leq n$, it then holds :

$$\begin{aligned} \mathcal{P}_{\text{no-branch}}(0 < t \leq T) &= \lim_{n \rightarrow \infty} \prod_{i=0}^{n-1} \mathcal{P}_{\text{no-branch}}(T_i < t \leq T_{i+1}) \\ &= \lim_{n \rightarrow \infty} \prod_{i=0}^{n-1} (1 - \mathcal{P}_{\text{branch}})(T_i < t \leq T_{i+1}) \\ &= \exp \left(- \lim_{n \rightarrow \infty} \sum_{i=0}^{n-1} \mathcal{P}_{\text{branch}}(T_i < t \leq T_{i+1}) \right) \\ &= \exp \left(- \int_0^T \frac{d\mathcal{P}_{\text{branch}}(t)}{dt} dt \right) \end{aligned} \quad (4.6)$$

equivalently we can write :

$$d\mathcal{P}_{\text{first}}(T) = d\mathcal{P}_{\text{branch}}(T) \exp \left(- \int_0^T \frac{d\mathcal{P}_{\text{branch}}(t)}{dt} dt \right) \quad (4.8)$$

So, the probability for *something to occur* for the *first* time at time T equals the probability for this to happen, *times* the probability that this did not yet happen.

For a shower the analogous of the time scale is $1/Q$. Therefore, an evolution of time corresponds to an evolution to smaller scales of the hard interaction scale Q^2 . Hence, the DGLAP equation can be written as :

$$d\mathcal{P}_{a \rightarrow bc} = \frac{\alpha_s}{2\pi} \frac{dQ^2}{Q^2} P_{a \rightarrow bc}(z) dz \exp \left(- \sum_{b,c} \int_{Q^2}^{Q_{\max}^2} \frac{dQ'^2}{Q'^2} \int \frac{\alpha_s}{2\pi} P_{a \rightarrow bc}(z') dz' \right) \quad (4.9)$$

where the exponential term is what we have precluded as the *Sudakov form factor*.

The introduction of the Sudakov form factor provides a way to deal with the divergencies of both the real and the virtual emissions while incorporating them in the Matrix Elements calculation.

Using this prescription the implementation of a cascade evolution looks sane. Having started from a simple process, its constituents are individually evolved downwards from some initial Q^2 scale until they further branch out into daughter particles. Once the branching is realised, the mother particles disappear and the daughter partons take their place, which in their turn will behave similarly i.e. evolve downwards in Q^2 and finally branch until the lower cut-off scale has been reached.

4.6 Combining the Matrix Element and the Parton Showering

Coming again to the use of the ME and the PS, they both have different goals and virtues and are bounded by different applicability limits. The ME basically allows a systematic expansion in powers of α_s , offering a higher precision. As long as tree-level calculations are concerned, these can be performed up to several partons (8-10) in the final state. However, we cannot neglect the fact that tree-level calculated cross sections have divergencies in the soft and collinear regions, while higher order calculations are much more difficult to get. Therefore, the ME cannot be used to explore the structure of a jet, and it is even more difficult to match the ME to hadronization models. Given that jets are the experimental observed final state objects, the necessity for accurate fragmentation models becomes clear. The use of bare ME partons would mean that experiments would have to tune these models for each centre of mass energy. While

this is not impossible, this would limit their applicability and that of the raw ME calculations. On the other hand, a PS makes approximations, thus cannot provide a guaranteed level of precision for well separated jets in the phase space. Still, on the bright side the PS is based on a universal and better understood theoretical framework.

In other words, the ME are always good for well separated jets, while the PS are good to provide insights for the structure inside jets. Clearly, these two have to be combined and to achieve this one needs to make sure that double-counting or even neglecting important graphs does not happen. This is far from trivial and several approaches have been developed over the years. Given the diversity of final state objects one can find at the LHC, the different PS implementations could be classified by the multiplicity of jets or even the relevance of correlations between the final state objects themselves, for example those between leptons and jets.

Therefore, being able to include higher order effects into the PS is a necessity, and practically we could say that one could follow two approaches : One tries to address the question how to correct the total cross section by including the QCD NLO terms, which has led to the MC@NLO [80] and PowHeg packages. The alternative approach tries to incorporate the tree-level multi-leg ME into the simulation directly and different implementations of this kind are the CKKS [81, 81], the CKKW-L [82], the MLM [83, 84] and the WHIZARD [85, 86] algorithms.

4.7 Used event generators and Parton Showers

To date, there are event generators that offer the possibility of generating processes at LO or even at NLO by including both real and virtual corrections as well. This is something that affects both the total cross sections and the shape distributions of the observables. Since it is clear that NLO event generators are crucial tools to give us the full control while exploiting the scale dependence of NLO calculations, it makes sense to combine them with the PS. In this section we briefly present the event generators and the parton showering programs that have been used for this thesis, while avoiding to go into too much detail.

MadGraph

The MadGraph package is capable of calculating the ME at tree-level for any Lagrangian-based model while it can also incorporate automated NLO computations of the real corrections with the appropriate subtractions in an automatic fashion. Hence, it is able to describe well separated parton configurations up to a given order in perturbation theory. At the same time, several generator level cuts can be incorporated to constrain the phase-space in case that fits certain experimental or analysis needs, while both ISR and FSR are also calculated at ME level. That means that it gives the option to include additional partons to serve as ISR, which is calculated separately. This way, both SM and BSM processes can be accurately simulated, while removing double counting diagrams whenever appropriate. Practically, this helps avoiding to use the same element of the phase space more than once while the associated parton generated at ME level gets showered. MadGraph has been extensively used for the simulation of pp and $p\bar{p}$ collisions. In addition, it is also the work-horse event generator of the CMS experiment since it is used for most of the physics processes.

Once the events are generated, they are interfaced to other programs for the showering / hadronization to obtain a complete generated event. This can be done either at LO (with the use of Pythia for example) or at NLO order (via MC@NLO or PowHeg) as well.

Pythia

Pythia [58] is a LO multi-purpose event generator which was first implemented in the 1970s and has been extensively used since then. It can be used for the complete event generation, namely from the calculation of the cross section down to the unweighting, showering and hadronization of the events. It is also capable of simulating the vast majority of the SM processes as well as many BSM ones, analytically. However, the Matrix Elements can be calculated only at LO, whereas the jets in the final state can be only calculated with the use of its integrated parton showering routines. In the context of this thesis, Pythia has been used for the showering and hadronization for the majority of both the SM and the SUSY simulation datasets. Further, in order to simulate coherently the decays of the τ -leptons while taking into account the spin correlations and the relative QED corrections, the TAUOLA [87] package has been interfaced with Pythia for all of the simulated datasets used in this analysis.

MC@NLO

The MC@NLO [80] package is a rather ambitious effort of combining the NLO ME with the PS. The underlying idea relies on the fact that since NLO results are recovered upon expansions in the strong coupling α_s , the ME should be used to generate the hard emissions, while collinear and soft ones should be taken care of by the PS. Within MC@NLO, the ME is generated with NLO accuracy including both the n -particle virtual as well as the $n + 1$ -particle real corrections. Next, the branchings from n -particles are calculated numerically. Also, as the ME and the PS must agree in the limit of the soft region, the singularities must mutually cancel giving us a finite cross section at the end. Finally, both the n and $n + 1$ -body topologies are showered. Special attention must be paid that the ME populates the region above the linear / collinear regime, something that is not guaranteed a priori. To achieve that a relative small fraction of events with negative weights is allowed.

To summarise, the MC@NLO event generator is becoming popular very fast in the experimental community, since it can provide the NLO cross section making it a very useful tool for many precision tests.

PowHeg

The *Positive Weight Hardest Emission Generation* (PowHeg) method was proposed as a solution to the negatively-weighted events generated by MC@NLO. The underlying idea, is that the full ME at NLO accuracy is used to produce the hardest emission and it should result only into positively-weighted events. This method has the advantage that a priori, does not depend on the exact PS. But it is not uncommon though, that in MC event generators like HERWIG++ which work with angular-ordered showers, the first emission is not the hardest one. Practically, that implies that by using PowHeg, another approach is needed (i.e. p_T ordered showers), to ensure that the next to first emissions is softer than the previous. Finally, in order to restore the logarithm accuracy of the shower, some extra soft radiation must be generated.

4.8 Underlying Event, Beam-Beam Remnants, Multiple Parton Interactions and Pile-Up

After the hard partonic interaction has taken place, also secondary collisions can still happen. The CDF collaboration during Run I and Run II provided clear experimental evidence that this is happenings [88]. It was clearly demonstrated that an accurate description of such processes at hadron level typically involves particle multiplicities with jet activity, which can be modelled with the help of event generators. That said, it is clear that final states from hadronic interactions are composed of several ingredients : The products of the partonic hard scattering with the highest p_T (including ISR/FSR), the hadrons produced in additional *Multiple Parton Interactions* (MPI) and the *Beam-Beam Remnants* (BBR) emerging from the hadronisation of the partonic scattering remnants. Contributions from MPI and BBR form the *Underlying Event* (UE). The description of the UE usually involves several parameters that are not constrained by the model and have to be tuned. In a nutshell, all of the above cannot be described from first principles, but the underlying idea relies on the calculation of the probability distribution of these processes with multiple scatterings.

The first strong experimental evidence for the existence of the UE came from the CERN ISR experiment from measurements of the momentum imbalance [89]. The UE encloses all the emerged activity from the primary hadronic collision that cannot be associated with the colliding partons of the hard process. In a broader sense, ISR and FSR could also be considered as UE, but usually for coherence reasons they are associated to the hard process itself. The UE becomes important while measuring jet properties since the UE by definition originates from the extra scatterings that follow the hard one. The fact that a jet clustering algorithm sums all energy deposits residing in a given cone, therefore, the UE can swift the energy and sub-structure of the formed jets. The models describing the UE are based on phenomenological arguments with the simplest one treating UE as an additional hadronic activity with softer spectra [90]. In another more recent approach, the UE is considered to be composed from "almost" independent partonic interactions which are described by simple $2 \rightarrow 2$ QCD scattering, provided that the interaction contains at least one hard jet and that is properly showered [91]. The latter approach is able to describe the *jet-ish* characteristics of the UE.

Although the UE is not understood from first principles, within *Pythia*, a primordial transverse momentum k_T is used to describe the fragmented proton, while the rem-

nants are considered to be its recoil. This primordial k_T distribution is taken as a Gaussian with the width given by the $\sigma(k_T)$ parameter. Furthermore, an upper threshold k_T^{max} for the primordial is being used.

For the MPI treatment, within Pythia an empirical lower threshold p_T^{min} is introduced of about 2 GeV. Below this cut-off value the perturbative cross section is taken to be zero. A varying impact parameter and a hadronic matter overlap are used, which are modelled by a double Gaussian matter distribution given by :

$$\rho(r) \propto \frac{1-\beta}{a_1^3} \exp\left(-\frac{r^2}{a_1^2}\right) + \frac{\beta}{a_2^3} \exp\left(-\frac{r^2}{a_2^2}\right) \quad (4.10)$$

where a_2 is the radius of a small cone which contains a fraction β of the total hadronic matter; a_1 stands for a larger hadron of radius a_1 which embeds a_2 . Also, the values of p_T^{min} and the regularisation scale p_T^0 are used. The former accounts for an MPI to occur, while the latter is used for the continuous degrading of the cross section. The above parameters have been determined at a reference energy scale \sqrt{s}^{ref} taken to be equal to the center of mass energy of the Tevatron experiment. The energy rescaling is assumed to be proportional to $(\sqrt{s})^{x_{scale}}$, where x_{scale} was tuned to Tevatron data.

In this analysis, the Tune Z2* was used to describe the UE and the MPI [92]. This tune is a variation of the Z2 tune (which was basically studied at CDF) and gives the best agreement between data and simulation for CMS. In Appendix A the used values are listed that were used in the context of this analysis as well for the treatment of the MPI within Pythia.

On the other hand, in high luminosity environments, more than one $p-p$ interaction can occur while the bunches cross. These additional proton collisions are known as *Pile-Up* (PU) and give additional background events that look like "noise". About 20-25 $p-p$ interactions per bunch crossing are anticipated at the nominal luminosity of LHC i.e. $10^{34} cm^{-2} s^{-1}$ [93–95]. Finally, it is worth saying that the PU depends on the luminosity in contradiction with the UE [93–95].

4.9 Hadronization

The hard subprocess combined with the PS will produce a big collection of partons coming from the original colliding partons. Still, the hard scatter can be associated

with even heavier resonances (heavy quarks, gauge bosons or new heavy particles) which would then decay in their own right.

After the PS stage the *hadronization* happens where all the showered partons end up forming hadrons of a typical 1 GeV mass scale corresponding to a low momentum, but long-distance regime. This region of the phase space is non-perturbative and cannot be described from first principles. Instead, phenomenological models like the *string* and the *cluster fragmentation* [55, 56] have to be used for that. These models are based on the existence of parton-hadron dualities, which link the momentum transfer between the hadronic and partonic levels giving us the advantage to compare the theoretical parton-level estimation with real data.

In any case, in the aforementioned models the free parameters are assigned values based only on phenomenological arguments. This is somehow expected, given the fact that there are practically hundreds of known hadron species that need to be considered, each one with its own quantum numbers, mass, width, coupling, decay properties etc or every other property that could actually interfere with the structure of the final observable hadronic state. The parameters for the hadronization of the simulated datasets used in this thesis are summarised in Appendix A.

Part III

Experimental Setup

Never worry about theory as long as the machinery does what it's supposed to do.

Robert A. Heinlein

CHAPTER 5

EXPERIMENTAL SETUP

5.1 Introduction

Between the borders of France and Switzerland located at CERN, the **Large Hadron Collider** (LHC) [93–95] is the biggest and most powerful machine human kind ever constructed. The LHC embeds unprecedented technological achievements, both from the mechanical engineering but also from the particle accelerator physics perspective. Its installation was completed in 2008, while its main goal is to accelerate, bend and collide proton beams inside a $\approx 100\text{m}$ underground tunnel of about 27 km circumference. Its nominal energy is 14 TeV at the centre of mass energy (C.M.E.), while at four locations around the accelerator ring the collisions are collected at a high rate by its main experiments, namely *ALICE*, *ATLAS*, *CMS* and *LHCb*. The expected reach of the LHC while working at the nominal luminosity is at the TeV scale, where the production of rare processes (cross sections of a few femto-barn) becomes feasible. Figure 5.1 illustrates the SM cross section predictions for both the LHC and the Tevatron experiments [96].

Two main reasons drove the decision of building an hadron collider instead of an electron-positron one: The first one was related to the need of reaching and exceeding the energies that LEP was able to peak at. The second one was related to the amount of synchrotron radiation ultra-relativistic particles emit at each revolution while be-

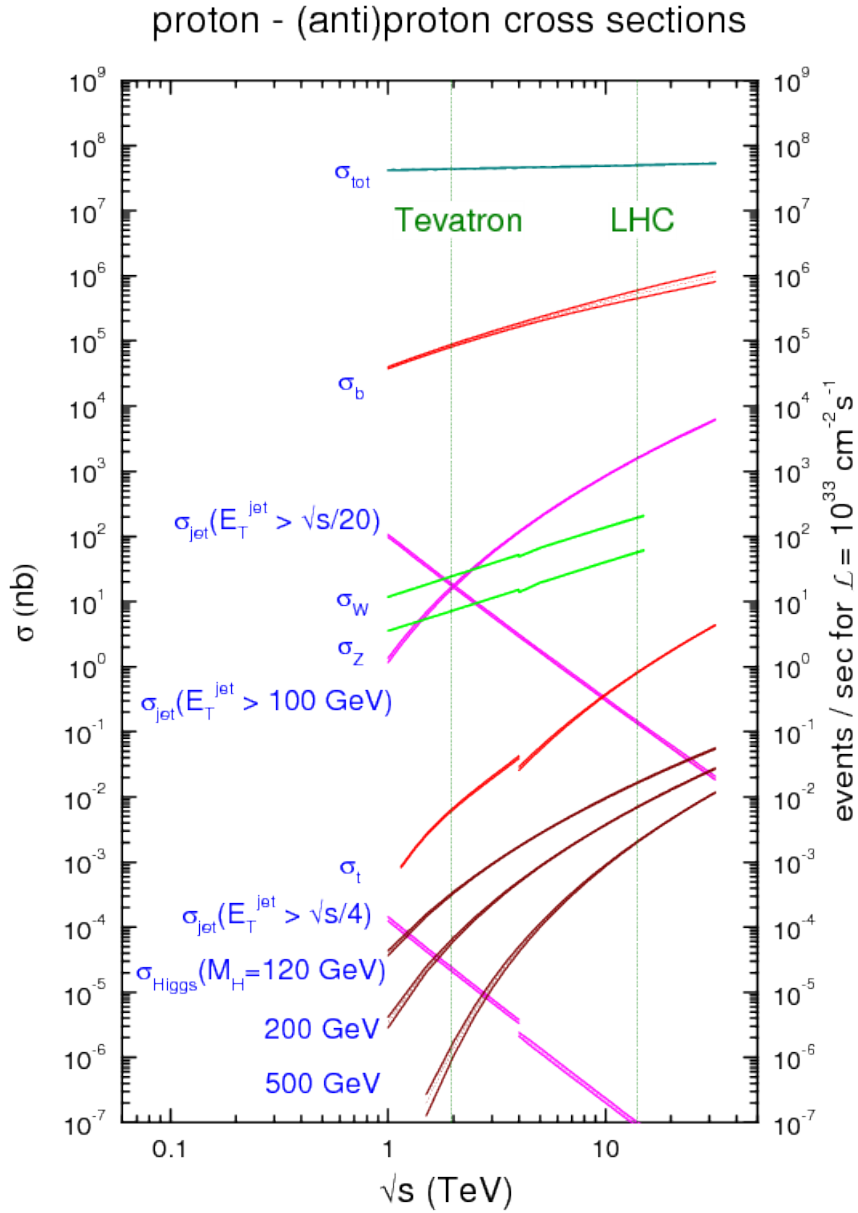


Figure 5.1: The Standard Model cross section predictions for the Tevatron and the LHC [96].

ing accelerated in a curved path of radius R . This radiation is inverse proportional to the radius and inverse proportional to the fourth power of the mass of the accelerated particle :

$$\Delta E \propto \frac{E^4}{Rm^4}, \quad (5.1)$$

thus, the ΔE losses for circulated protons are a factor of $\mathcal{O}(10^{12})$ less compared to the one from electrons.

Furthermore, as protons are composed from fundamental particles, they can provide access to uncharted energy regimes, which is crucial on the quest for new physics. Questions like what is the nature of the electroweak symmetry breaking, what makes things heavy or how does the origin of mass connects with other phenomena in the universe, are still to be answered. Still, the LHC is not only pushing the current energy frontiers, but is already setting new records for the instantaneous luminosity in hadron colliders [97]. At the same time, while LHC will be working at its design energy, the interaction points will become the hotter places on earth since the temperatures will go up to 500,000 times hotter than the centre of the sun. Furthermore, the superconducting magnets which are responsible to bend the beams, are kept at 1.9 K [93], making them the cooler place on the universe, since this temperature is even lower than the one of the Cosmic Microwave Background. Also, the pressure of the beam pipe vacuum is 10^{-13} atmospheres, which is also lower compared to the inter-planetary space value.

5.2 The Large Hadron Collider (LHC)

The idea of reusing the already existing underground tunnel which was hosting the LEP collider was already on the table since the late 1980's. But as the Superconducting Super Collider (SSC) project was still open at the time, many countries opposed on the idea of having two large colliding experiments, since this would be financially disastrous for the participating parties. But when in the early 1990's the SSC was cancelled, the LHC idea was revived. The initial proposal was to build the machine within the next 10 years in order to become operational in the first years of the new millennium. Nevertheless, it was not until the 2008 when the LHC was became reality.

CERN's main mission is to transact many physics programs at the same time in order to cover the widest range of particle physics possible. Thus, a rather diverse spectrum of physics searches is covered, from cosmic rays to pions, and from SM to SUSY and Exotic signatures. Furthermore, in order to reduce the costs and also exploit the existing facilities on their full potential, the LHC makes use of the already built accelerator

complex, while some of its components have been put in operation for more than 4 decades now. The LHC alone has seven experiments [93–95] which are :

- **The ATLAS and the CMS** experiments which are general-purpose detectors with a very similar hermetic, symmetrical and cylindrical structure. They were designed to search not only for the BEH-boson but also for hints that would point to new physics phenomena. The existence of two detectors which are ran and operated by two big distinct collaborations is vital for cross-confirmation of any possible new discovery.
- **The ALICE and the LHCb** experiments are focusing on studies of specific phenomena. The former one, being a detector designed to study heavy-ion collisions focuses on strongly interacting matter at extreme energy densities where a phase of matter called quark-gluon plasma forms. The latter experiment searches for differences between matter and antimatter by studying b quark physics focusing on CP violation.
- **The LHCf and the TOTEM** are two smaller experiments at the LHC and focus on searches of the so-called "forward particles" which are protons or even heavy ions that merely "meet" while head-on collisions take place. TOTEM makes use of installed detectors on either side of the CMS interaction point (IP) while LHCf is made up of two detectors sitting along the LHC beam-line, distanced by 140 metres from either side of the ATLAS IP.
- Finally, **the MoEDAL** experiment uses detectors near LHCb searching a still-hypothetical particle known as the "*magnetic monopole*".

5.2.1 The LHC at work

The sequence up to the point where the two proton beams are circulating inside the LHC tunnel is as follows : Initially, protons are created from ionised hydrogen atoms in an electric field. Then, several particle accelerators increase progressively the energy of the proton beams. Protons are first accelerated with a linear accelerator (the *LINAC2*) reaching energies of 50 MeV. Then, an additional boost is applied by two circular accelerators (the *BOOSTER complex*) to 1 GeV. The next step is to enter the *Proton Synchrotron* (PS) where they are accelerated to 26 GeV. The *Super Proton Synchrotron* (SPS) follows next, where protons reach the energy of 450 GeV. This chain is shown schematically in Figure 5.2.

CERN's accelerator complex

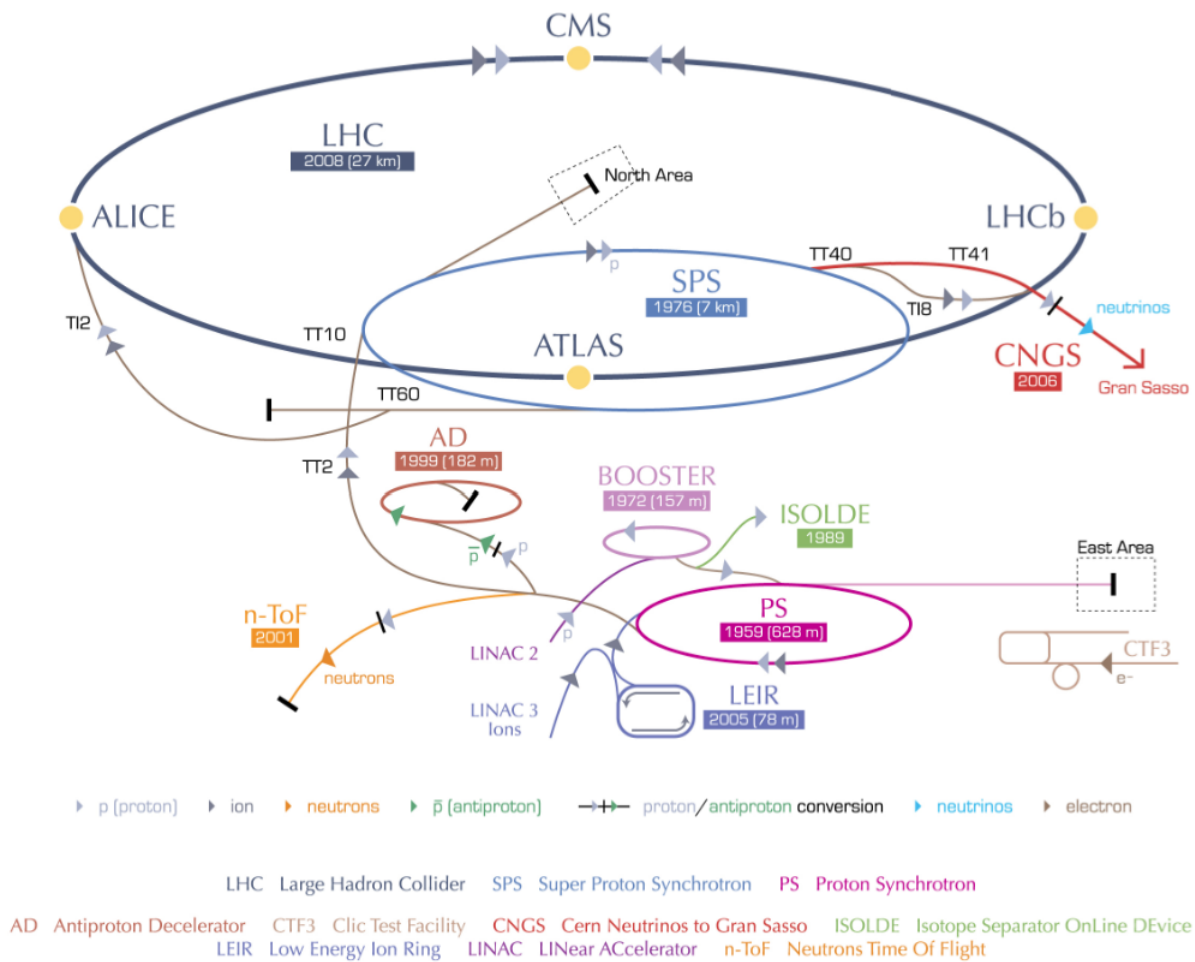


Figure 5.2: The CERN accelerator complex

The LHC is responsible for both the acceleration and the collision the proton bunches at the different experimental sites, around the 26.7 km underground tunnel. The acceleration is achieved with the help of 16 radio frequency (RF) cavities, whereas the circulation of the beams is steered from the 9.300 superconducting magnets. A liquid-helium cryogenics system is used for the magnet's cooling while operational. The largest and most important magnets are the dipole ones with the mission to bend the beam along its trajectory. Each one of these 1232 dipole magnets is 15 m long and is kept at a temperature of 1.9 K, while they weigh more than 27 tons in total. At each dipole, a current of ≈ 12 kA is used to obtain the 8.33 T magnetic field. On the other hand, the 858 quadrupole magnets are responsible for the beam focusing. Historically, and given the limited available diameter of the tunnel which is no more than 4 m, the installa-

tion of two completely separated rings each one holding dipole magnets was out of the question. A mechanical breakthrough was needed, and for this, the "two-in-one" solution was developed which practically embeds 2 beam lines in the same support structure with separate super-conducting coils surrounding them. This is shown in Figure 5.3.

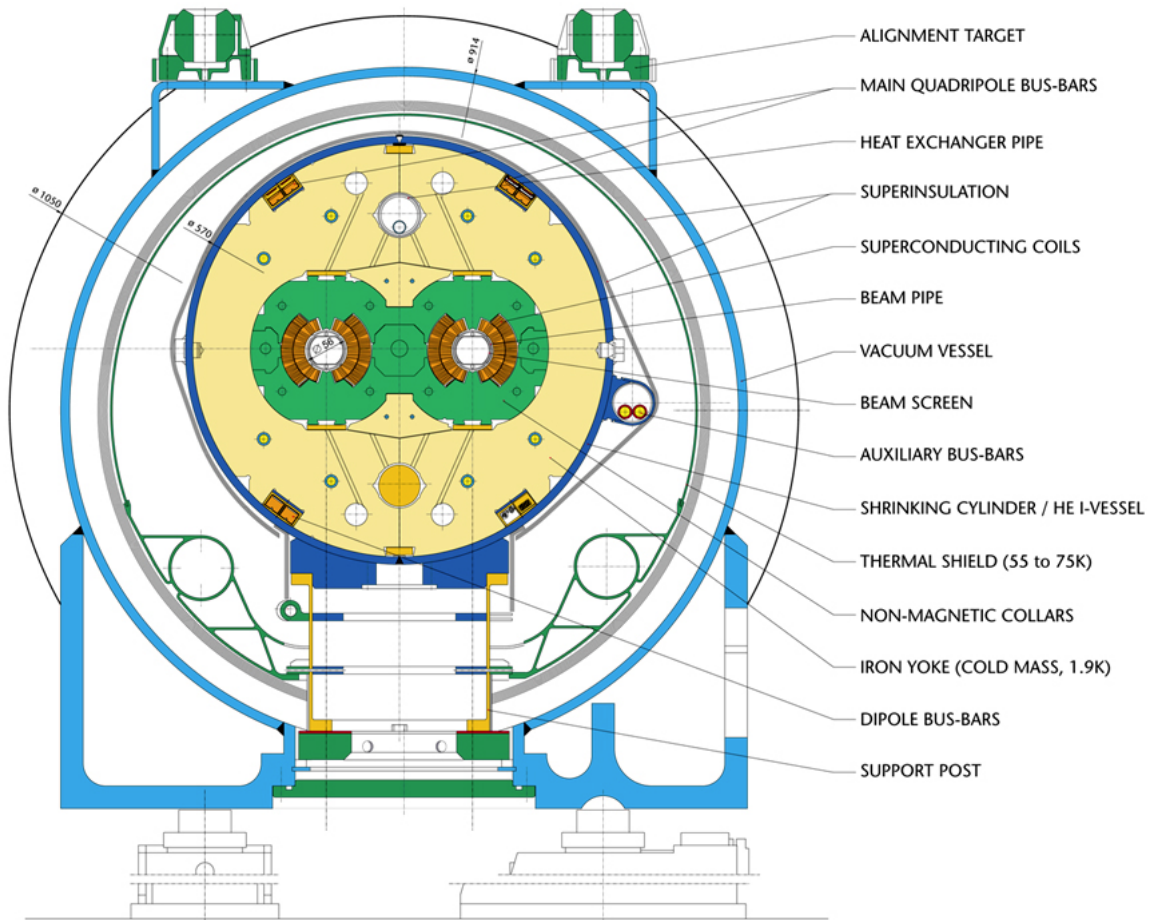


Figure 5.3: The cross section of a LHC dipole magnet

The rest of the magnets are of different types, like sextupoles, octupoles, decapoles etc. which are also directly involved in the final beam shaping and guidance.

While the beams are injected in the LHC, they have a large transverse and longitudinal momentum which translates in low-rate collisions. At this point, and before the beams are accelerated, an oscillating electric field is applied to the beam's direction. Its oscillation frequency is a multiplicative of the revolution frequency of the accelerator being $f_{osc} = n f_{revol}$, with $f_{osc} \approx 11$ kHz while $n = 35640$. Stable regions in momentum and phase of the oscillation are formed because of the imposed electric field. However, the

near-by protons are either accelerated or decelerated until they form stable bunches. Once this is done, the beams are considered to be "locked" and then, the magnetic field is increased adiabatically until it is stabilised at a certain value.

These stable regions also result in distinct spatial regions along the longitudinal direction of the proton beams. That means, that the previously described procedure changes the beam structure itself, and the newly created bunches of protons are characterised by reduced longitudinal extension (0.75 meters) centred around those stable regions produced by the synchrotron acceleration. The frequency of the oscillation is of course related to the actual number of these stable regions, and one small fraction around 10% (of the stable region of 0.75 m) can be filled effectively with protons. The LHC has the capability of filling 2808 of the 3564 available regions with 1.1×10^{11} protons per bunch, and these are organised in different "bunch trains" while the spacing between them is 25 ns, but this depends on the machine plans and status in a certain period.

When the beams reach the desired energy, the LHC declares "stable beams" something that signals experiments to be ready for data-taking. Due to the collisions, the intensity of the beams decreases over time and when the intensity drops below a certain value (typically a factor of e^{-1}), the beam is "dumped". Then, the whole procedure can start all over again, with this step known as "beam fill" which typically lasts several hours. Of course, the actual rate of the collisions also depends on the inclusive proton-proton cross section. The total proton-proton cross section (σ_{pp}) can be broken down in contributions from inelastic, single diffractive and elastic scattering. However, the cross section associated with the elastic scattering of the protons and diffractive events will not be seen by the detectors and it is only the inelastic scatterings that give rise to particles at sufficient high angles with respect to the beam axis [93]. All the parameters that have an impact on the rate of the collision are expressed with the instantaneous luminosity \mathcal{L} , so that the rate of collision \mathcal{R} can be simply written as :

$$\mathcal{R} = \sigma_{pp} \cdot \mathcal{L} \quad (5.2)$$

The luminosity then reads :

$$\mathcal{L} = f \frac{n_1 n_2}{4\pi\sigma_x\sigma_y} \quad (5.3)$$

where n_1 and n_2 stand for the number of particles in both beams, f is the collision frequency, whereas σ_x and σ_y are the transverse dimensions of the beams.

The first p - p collisions happened on November 23rd of 2009 with each beam's energy set at 450 GeV, while it reached 1.18 TeV a few days later providing the first collisions

at 2.36 TeV at the centre of mass energy. A few months later, and after only a month of beam commissioning at 30th of March 2010, the beam energies were raised to 3.5 TeV (the 2010 data taking run) while the beam intensities were gradually increased up to 368 bunches per beam, reaching a luminosity of $2.1 \times 10^{32} \text{cm}^{-2} \text{s}^{-1}$. The final integrated luminosity delivered by the LHC during the first year of its operation was $\approx 40 \text{pb}^{-1}$. One year later, the 13th of March 2011, the machine went to 3.5 TeV energy per beam reaching progressively 1374 bunches per beam resulting at more than $3 \times 10^{33} \text{cm}^{-2} \text{s}^{-1}$ of instantaneous luminosity while in 2012 the energy was set to 4 TeV per beam. Currently, the machine is not operating due to the programmed long shutdown which will last until late 2014 for scheduled upgrades and maintenance work. The CMS integrated luminosity during the 2010-2012 period is shown in Figure 5.4. The data used in this thesis was produced from the 8 TeV collision data recorded by the CMS experiment during 2012 which corresponds to an integrated luminosity of roughly 19fb^{-1} .

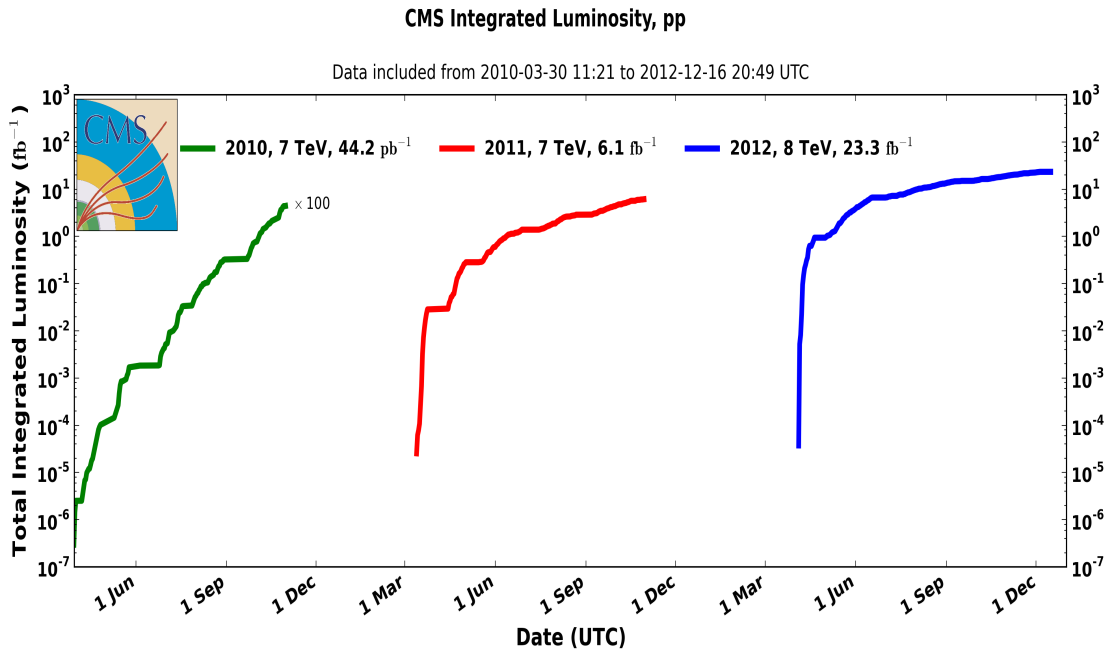


Figure 5.4: The delivered luminosity to CMS versus time for years 2010 (green), 2011 (red) and 2012 (blue) during stable beams and data taking periods.

5.3 The Compact Muon Solenoid (CMS) experiment

The Compact Muon Solenoid (CMS) experiment [98] is one of the two general purpose detectors at the LHC. It is located about 100m underground at the so-called Interaction

Point 5 (IP5). It is 21.6 m long and has a radius of 7.3 m, while with its total mass of 12500 tons it is the heaviest detector at the LHC. Its main feature is the strong superconducting solenoidal magnet which is able to produce a uniform magnetic field of 3.8 T, and the whole detector is having a cylindrical shape around the beam pipe. That said, it is easy to understand the in-to-out structure of the detector, consisting of several different cylindrical sub-detectors. The part of the detector coaxial to the beam direction is usually referred to as the "barrel region" while the closing discs at both ends perpendicular to the beam are referred to as "end-cap regions". A schematic view of the detector is shown in Figure 5.5.

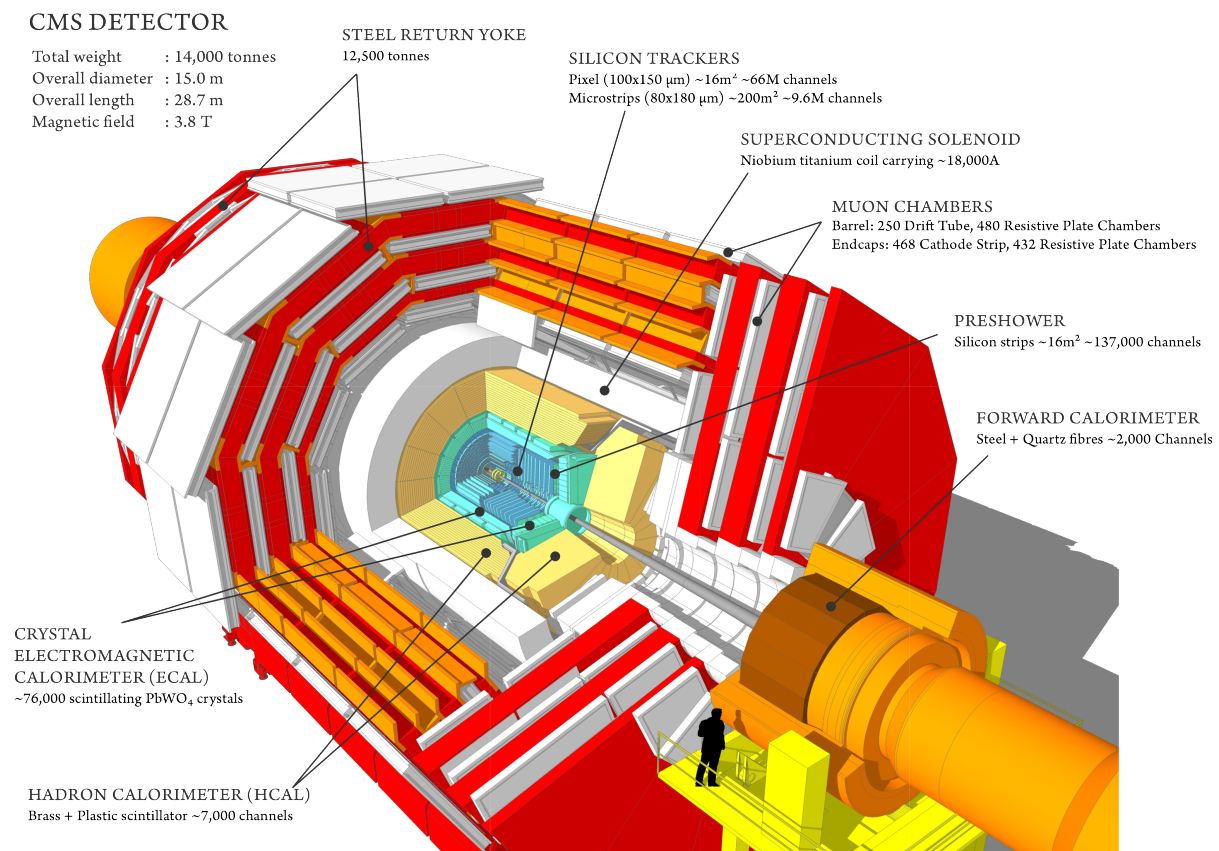


Figure 5.5: Schematic view of the Compact Muon Solenoid (CMS) detector.

5.3.1 Coordinate system and variables

The CMS uses a right-handed cartesian coordinate system, with the origin being the centre of the detector, the x -axis pointing towards the centre of LHC, the y -axis pointing vertically upwards and the z -axis being along the beam direction. Given the cylindrical

symmetry of the detector and the invariant description of p - p collisions, the use of a pseudo-angular reference is advised, defined by the (ρ, ϕ, θ) coordinates. In more details, the distance from the beam pipe (z -axis) is the ρ , while the azimuthal angle ϕ is measured from the x -axis in the x - y plane ($0 \leq \phi \leq 2\pi$), and the polar angle θ is measured from the $+z$ -axis and is defined as $\theta = \arctan(z/r)$ with $r = \sqrt{(x^2 + y^2)}$. Usually, instead of the polar angle θ , the *pseudorapidity* (η) is used, which is invariant under Lorentz boosts in the z -direction and is defined as :

$$\begin{aligned} \eta &= -\ln\left(\tan\left(\frac{\theta}{2}\right)\right) \\ &= \frac{1}{2} \frac{|\mathbf{p}| + p_z}{|\mathbf{p}| - p_z} \end{aligned} \quad (5.4)$$

The last relation indicates that the pseudorapidity can be expressed as a function of the momentum \mathbf{p} of a particle and its longitudinal component p_z . Other useful variables, are the transverse energy ($E_T = \sqrt{m^2 + \mathbf{p}_T^2}$) and the transverse momentum ($p_T = \sqrt{p_x^2 + p_y^2}$). Finally, due to energy and momentum conservation, the neutrinos (or the LSPs if SUSY exists) escape direct detection as they fly through the detector having not interacted at all, which leaves an negative imbalance on the total vectorial sum of the final measured transverse energy. This is quantified by the missing transverse energy.

5.3.2 The CMS sub-detectors and components

From the beginning, CMS was designed to host a high precision electromagnetic and hadronic calorimeter, a redundant muon tracking system and a high quality tracking system. Briefly, CMS is made up of four main sub detectors, namely :

1. **The Silicon Tracker (TK)** : It is composed mainly by two main parts, the *Silicon Pixel* vertex detector and the surrounding *Silicon Microstrip* detector. Both together have a total active area of about 215 m². Its main task is to reconstruct the charged particle vertices and tracks.
2. **The Electromagnetic Calorimeter (ECAL)** : The ECAL is used to give precise measurement of the electrons and photons energy and direction.
3. **The Hadronic Callorimeter (HCAL)** : The HCAL is used to measure the direction and energy deposited by hadrons and is mainly used for the detection of particles

that interact via the strong force, like quarks. Thus, the HCAL along with the TK are the cornerstone for the reconstruction of jets.

4. **The Muon Stations:** The CMS Muon System is a rather composite tracking system for muons. It consists of the *Cathode Strip Chambers* (CSC) installed in the end-cap regions and the *Drift Tube* (DT) that reside in the barrel. Also, a secondary system of *Resistive Plate Chambers* (RPC) is used both in the end-cap and the barrel regions helping with the triggering decisions.

With the exception of the Muon Chambers, every other sub-detector is located inside the magnetic coil. The Muon Chambers on the other hand, are placed in the magnet return yoke. A more detailed description of each sub-component follows next.

5.3.3 The main Solenoid

The CMS magnet encloses most of the detector's subcomponents (TK, ECAL, HCAL) and it is the most powerful and biggest ever built superconducting solenoid on Earth. The magnet being 12.5 m long and with a diameter of 6 m can achieve a magnetic field of 3.8 T, while the energy that can be stored can go up to 2.5 GJ when the magnet is fully operational. The superconductor is made of four layers of NbTi and if is needed, the magnet can flux its stored energy to resistors in about 200 ms. The field in the yoke reaches around half of the value of the field in the central volume. The magnet return yoke in the barrel is made up from 12-fold rotational symmetric pieces.

5.3.4 The Silicon Tracker (TK)

The TK is the innermost sub-detector of CMS. Its length along the z -direction is 5.5 m while it has a diameter of 2.4 m. Its main purpose is to measure the trajectories of the charged particles with great precision, covering the region $|\eta| < 2.4$. In particular, its main goal is to provide accurate measurements of the particles momentum and charge, while at the same time it must provide an accurate determination of the spatial coordinates of the secondary vertices via the reconstruction of the resulted intersection points of track originating from this vertex. To accurately reconstruct the trajectories of the particles and to ease pattern recognition, two requirements must be fulfilled:

1. The TK must have large hit redundancy, which is achieved by having a big number of subsequent detecting layers.

2. The TK must have a low detector occupancy, which can be accomplished with high granularity components.

The TK is divided into two sections as a function of radius. Starting from the interaction point to $r = 20$ cm where the particle flux is really high (at $r = 10$ cm this is $\approx 10^7 \text{ m}^{-2} \text{ s}^{-1}$), silicon pixels of $100 - 150 \mu\text{m}^2$ are used, resulting in an occupancy of $\mathcal{O}(10^{-4})$ per pixel per bunch crossing for nominal operation values. For the region following the pixel tracker ($20 < r < 55$ cm), the particle flux decreases significantly, something that allows us to use silicon microstrips ($10 \text{ cm} \times 80 \mu\text{m}$) instead. The farthest region has low enough particle flux, so that the use of microstrips with a cell size ($25 \text{ cm} \times 180 \mu\text{m}$) is advised. The TK gives an efficiency of roughly 100% in the central region, but the efficiency drops for the regions $2.1 < |\eta| < 2.5$ due to the fact that fewer modules are present there. A schematic view of the tracker is shown in Figure 5.6.

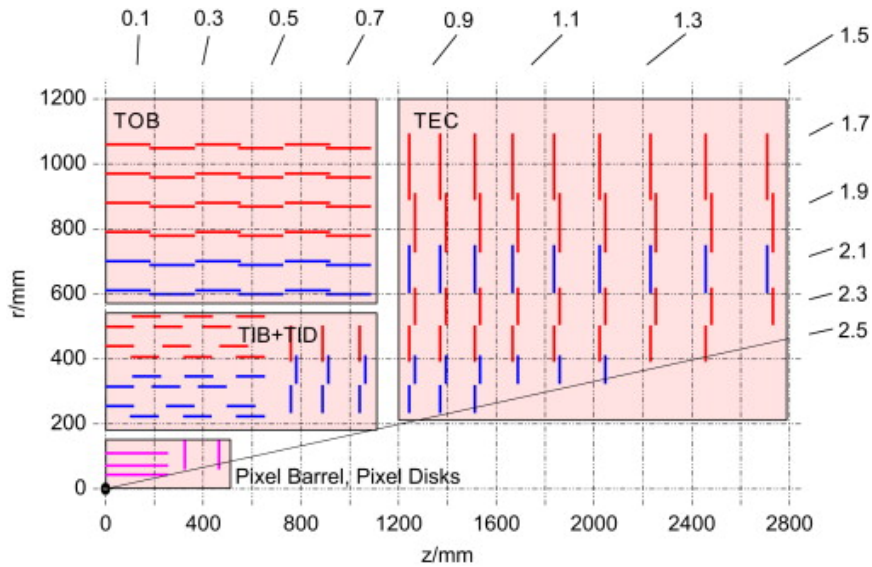


Figure 5.6: A view in $r - z$ of the CMS tracker structure.

5.3.4.1 The Silicon Pixel Tracker (SPT)

The SPT is very crucial for a precise measurement of the impact parameters of the tracks. Also, it is the starting point for the reconstruction of the charged particle tracks and can be subdivided into three layers, each one being around 53 cm long and positioned at $r = 4.4$ cm, $r = 7.3$ cm, $r = 10.2$ cm correspondingly. Also, two end-cap disks are placed at $|z| = 34.5$ and $|z| = 46.5$ with a diameter between 12 and 30 cm to

ensure at least two layers are crossed by each track originating from the centre of the detector covering the pseudorapidity region $|\eta| < 2.5$. On each layer, modular detector units are installed containing a sensor plate with $\approx 320 \mu\text{m}$ of thickness, with built-in highly precision readout units. In total, there are 66 M installed pixels shared on 1440 modules. In order to optimise the vertex reconstruction and impact parameters identification, the pixels are formed from rectangular shape subcomponents, each one being $100 \times 150 \mu\text{m}^2$ and with a hit-position spatial resolution of $10 - 20 \mu\text{m}$. A drawing of the Pixel Detector is shown in Figure 5.7.

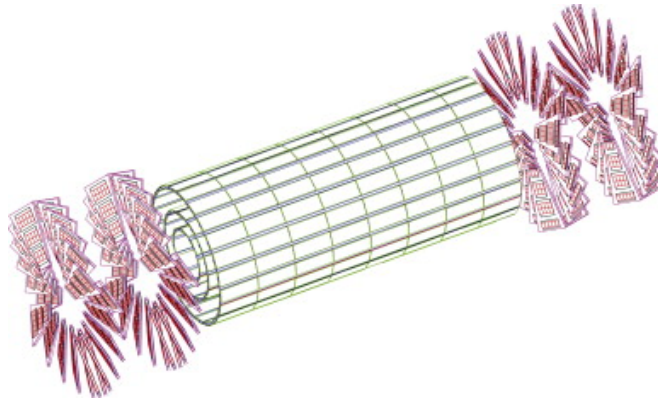


Figure 5.7: A schematic illustration of the CM Pixel Detector.

5.3.4.2 The Silicon Microstrips

Outside the SPT, the 5.4 m long Silicon Microstrips detector stands, covering a tracking volume of $r = 1.1 \text{ m}$ in total. It contains about 9.3 M strips placed on 15148 modules, which are divided into four subsystems, namely the *Tracker Inner Barrel* (TIB), the *Tracker Outer Barrel* (TOB), the *Tracker Inner Disk* (TID) and the *Tracker end-cap* (TEC). From these, the TIB and TOB are aligned in parallel to the beam line, while the TID and TEC modules are installed perpendicular to the beam pipe. The interspacing between the strip varies from $80 \mu\text{m}$ in the TIB up to $184 \mu\text{m}$ in the TEC side. The received analog signal from each strip, is transmitted to ADCs with the use of optical fibers while with these microstrip sensors it is possible to measure one coordinate and then determine the crossing position by interpolation of charge sharing between the adjacent involved strips. Nevertheless, due to the highradiation environment, the sensors get damaged over time. Therefore, the readout units and the micro-strip detectors need to be radiation hard. In order to limit the radiation damage due to high particles fluxes and prolong as much as possible the life of the tracker, it should operate at temperatures below -4 C° .

5.3.4.3 Performance of the Silicon Tracker

A small fraction of the total modules are defect. This amount is around $3\% \oplus 1\%$ (3% in the end-caps and 1% in the barrel), resulting in a somehow decreased performance of 98.4% for the Tracker [99]. Practically, the radiation length (X_0) corresponding to the tracker material is $0.4 X_0$ for $\eta = 0$, but this increases to $X/X_0 = 1.8$ at $\eta = 1.4$ [100]. The reconstruction of the tracks is performed with the use of a Combinatorial Track Finder (CTF) algorithm which implements a Kalman Filter (KF) [101] in order to assign hit seeds of the internal tracker extrapolated to the outer tracking layer. For this, all compatible hits from all layers are added to the trajectory in an iterative way by removing all unambiguous hits and then reconstruct those tracks with the remaining hits in a subsequent iteration. This keeps the mis-reconstruction at a small level.

During the first data taking period at C.M.E of 7 TeV, an almost perfect alignment was achieved [102], while for highly energetic tracks having a p_T of the $\mathcal{O}(100)$ GeV the momentum resolution is $\frac{\Delta p_T}{p_T} \approx 2\%$ for $|\eta| < 1.6$. The resolution becomes worse ($\approx 7\%$) for $|\eta| = 2.5$. The track reconstruction efficiency has been measured for muons with $1 < p_T < 100$ GeV and $|\eta| < 2.1$ to be greater than 95%, but this drops to $\approx 73\%$ for the region outside the Pixel acceptance. Yet, it reaches high values of $\approx 98.8\%$ for muons coming from J/Ψ [100]. The measured resolution of the Primary Vertex (PV) is found to be between $20 - 30 \mu\text{m}$ for ≥ 20 tracks [103]. Also for charged pions, the reconstruction efficiency of tracks having less than 100 GeV varies between 60% and 95% for increasing values of the η .

5.3.5 The Electromagnetic Calorimeter (ECAL).

The electromagnetic calorimeter (ECAL) [98, 100] covers the pseudorapidity region $|\eta| < 3$ and is composed of 75848 lead tungstate ($PbWO_4$) crystals. From these crystals, 61200 are installed in the central barrel while 7324 crystals are placed in each one of the end-caps. The lead tungstate crystals have a very good stopping power and radiation hardness as well as a high density of 8.28 g/cm^3 . In addition, their characteristics include a short radiation length ($X_0 \approx 0.9 \text{ cm}$) and a small Moliere radius ($r_m \approx 2.1 \text{ cm}$), hence the ECAL is more than 25 X_0 deep. Given the fact that $\approx 80\%$ of the deposited energy can be collected in 25 ns, it is ideal for the high collision rate of the LHC. The disadvantages of $PbWO_4$ crystals are the low light yield per MeV (≈ 10 photo-electrons/ MeV) something that is confronted with the use of photodetectors. A schematic view of the ECAL is shown in Figure 5.8.

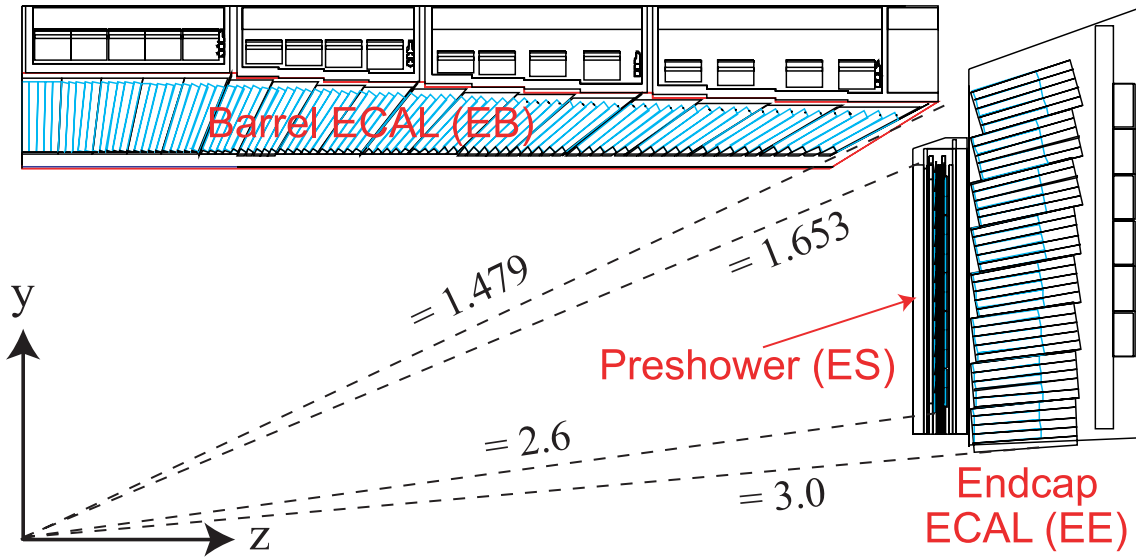


Figure 5.8: A schematic view of one quadrant of the CMS ECAL layout.

The ECAL barrel (EB) crystals are segmented by $\Delta\eta \times \Delta\phi = 0.0174 \times 0.0174$ with a cross section of $\approx 22 \times 22 \text{ mm}^2$ and are positioned in an angle of about 3° in both ϕ, θ directions with respect to the p - p IP axis. The ECAL end-cap (EE) covers a pseudorapidity region $1.479 < |\eta| < 3$ where the crystals are clustered in 5×5 segments ("supercrystals"), being arranged in different angles varying from 2° to 8° with respect to the p - p IP. Their total length is $\approx 24.8X_0 = 220 \text{ mm}$ while their cross section is $28.62 \times 28.62 \text{ mm}^2$ and $30 \times 30 \text{ mm}^2$ for the front and back side respectively.

As electrons and photons pass through the ECAL, their shower results in cascades giving rise to scintillations in the crystals. These signals are collected by two different types of photo-detectors. The EB crystals are read with the help of *avalanche-photodiodes* while *vacuum-photodiodes* are responsible for this task in the EE as they are more radiation resistant. At the end, more than 90% of the electromagnetic shower can be contained within a single crystal.

A 20 cm thick *Electromagnetic Preshower* (ES) sampling calorimeter detector is contained within the ECAL. It is made up of two layers of lead absorbers and silicon micro-strips, which are interleaved by two silicon strip detectors. It covers effectively the region $1.653 < |\eta| < 2.6$ and is situated between the TEC and the EE. Its main mission is to help the identification of π^0 in the forward region, and also to distinguish electrons from *Minimum Ionising Particles* (MIP), as the pions in that regions are so energetic that the photon resolution is diminished. The identification of π^0 is achieved as the first lead layer is about $2 X_0$, while the second one gives another X_0 before the second

sensor plate. This allows to differentiate between electrons and pions due to the fact that $\approx 95\%$ of the photons shower before the second silicon plane is reached, therefore providing discrimination against neutral pions. The ES operates at temperature of -5C° .

The energy resolution of the ECAL can be parametrized as :

$$\left(\frac{\sigma(E)}{E}\right)^2 = \left(\frac{S}{\sqrt{E}}\right)^2 + \left(\frac{N}{E}\right)^2 + C^2 \quad (5.5)$$

where E is the energy, S is a parametrized stochastic term including the contribution from fluctuations in the number of electrons being produced and collected, while N is the noise contribution and C is a constant term for the non-uniformity of the read-out units and mis-calibrations. Specifically for the S factor, the contribution can be described by poissonian distributions, meaning that $S \propto 1/\sqrt{n_{\gamma e}}$, where $n_{\gamma e}$ is the number of photo-electrons emitted per energy unit. Additional contributions must be considered from the efficiency of the light collection and from the multiplication processes taking place in the photo-detectors. The noise term N absorbs the electronic noise coming from the photodetector and the preamplifier, whereas the target value is $N = 0.12 \text{ GeV}$.

The resolution is evaluated as a function of E using electron beams. From measurements the values have been found to be $S = 0.028\sqrt{E}$ (while the target is $S = 0.027\sqrt{E}$), $N = 125 \text{ MeV}$ and $C = 0.003$ in the barrel region [100]. These values change for the end-cap region, that is $S = 0.05\sqrt{E}$ (whith target value $S = 0.057\sqrt{E}$), $N = 0.5 \text{ GeV}$ and $C = 0.003$.

At high energies, the C term becomes dominant, including contributions coming from the need for stable operating conditions, such as the stable high voltage, the temperature, the non-uniformal crystal yields, miscalibrations, presence of inactive (dead) material or the accumulated radiation damage of the components.

5.3.6 The Hadronic Calorimeter (HCAL)

The hadronic calorimeter (HCAL) [100, 104] is a sampling calorimeter, being 11 interaction lengths in depth, and is used complementary with the ECAL to measure the direction and energy of strongly interacting particles, including both neutral and charged hadrons, as well as to be able to calculate the \cancel{E}_T . It is made up of brass absorbers and

plastic scintillator layers, except in the forward region where quartz fibres and steel absorbers are needed as they are more radiation-hard materials.

It is composed mainly of two parts, the barrel (HB) and two end-caps (HE) where a sandwich of brass plates and plastic scintillator is used. The HB completely surrounds the ECAL and is located between the outer boundary of the ECAL at $r = 1.77$ m and the inner region of the solenoid coil at $r = 2.95$ m, covering a range up to $|\eta| < 1.3$ while the HE covers a range $1.3 < |\eta| < 3$. The HB tower granularity is $\Delta\eta \times \Delta\phi = 0.087 \times 0.087$, while the HE towers have varying tower dimensions, between $\Delta\eta \times \Delta\phi = 0.087 \times 0.08$ and $\Delta\eta \times \Delta\phi = 0.035 \times 0.08$. Figure 5.9 shows the CMS HCAL parts with its segmentation.

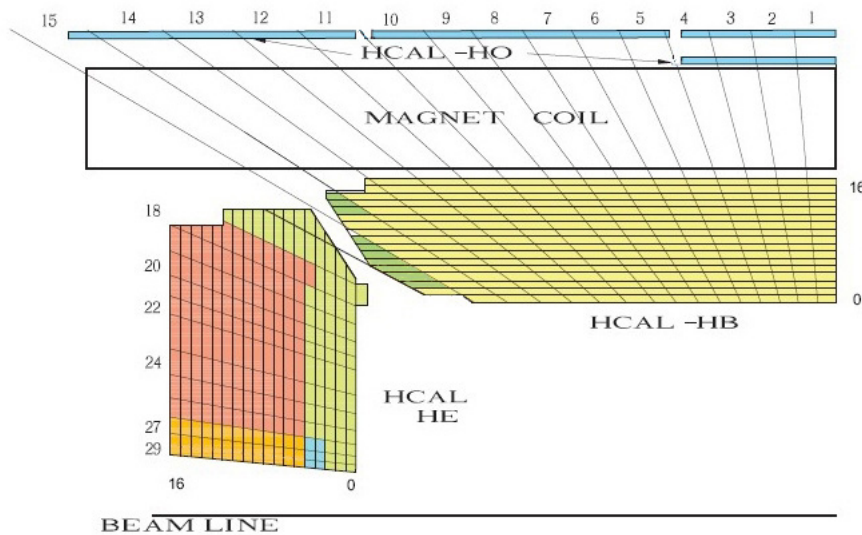


Figure 5.9: A schematic view of the one quadrant of the CMS HCAL layout.

When showers from hadrons are initialised while passing through the absorber layers, they produce scintillations in the surrounding tiles which are then read out by photodiodes assisted by wavelength shifting fibres. In order to achieve a better sampling in the region $|\eta| < 1.26$, another component namely the *Outer Hadron Calorimeter* (HO) is situated outside the solenoid, composed of a layer of scintillators that samples the remnants of highly energetic, thus penetrating, showers.

Finally, in the very forward region the HCAL Forward (HF) calorimeter, is made from steel absorber plates and quartz fibres serving as active material. The HF is positioned as far as 11.5 m away from the p - p IP, covering the region $3 < |\eta| < 5$. On this region, the rates of hadrons are really high, and the generated signal via Cherenkov light is

collected and then amplified by photo-multipliers. Due to the above choice of materials for the active medium, the HF is mainly sensitive to the electromagnetic fraction of a hadron shower. By sampling the energy deposits close to the front as well as to the back of the absorber, good discrimination is obtained for showers coming from e or γ and from hadrons, since the former ones usually deposit the bulk of their energy in the first set of fibres.

Due to the nature of the hadronic showers, the HCAL has a worse resolution compared to the ECAL while its granularity is coarser. Also, HCAL response is different for the hadronic and the electromagnetic parts of the hadron showers, something that leads to a non-linear overall energy response. It has been found, that 99.3% of the HB, the HE and the HF, and 95.5% of the HO channels are operational [105]. The combined energy resolution of the HCAL and ECAL can be described by :

$$\left(\frac{\sigma(E)}{E}\right)^2 = \left(\frac{S}{\sqrt{E}}\right)^2 + (C)^2 \quad (5.6)$$

Which is valid for energies $30 \text{ GeV} < E < 1 \text{ TeV}$. In Equation 5.6 S and C are constant terms. The values have been measured to be $S \approx 0.85\sqrt{E}$ and $C = 7.4\%$ [105]. The barrel and end-cap energy resolution is similar. The performance of the HCAL is usually determined by estimating the resolution on the E_T of jets reconstructed using the calorimeters only.

5.3.7 The Muon System

The Muon System (MS) is one of the most important components of the CMS detector. The muon chambers are positioned just outside the magnet coil, integrated within the magnet's return yoke. It covers the region $|\eta| < 2.5$ but the full muon reconstruction is heavily depending on the Tracker's measurements. The Muon System's working principle is based on wire chamber detectors. Since muons by nature do not interact via the strong force and yet are too massive to radiate enough via bremsstrahlung, the solution is to use ionised gas chambers. While muons are travelling through the detector, their hits are recorded when they ionise the gas of the detector. These hits are then combined with the information obtained from the TK and the muon paths are reconstructed while their momenta is measured. Being the outermost component of the detector, it covers an effective area of about 25.000 m^2 which can be further subdivided in a main barrel and two end-cap regions.

In total, three different types of gas chambers are in use (Figure 5.10). In particular, the DT chambers are sitting in the barrel region ($|\eta| < 2.1$) consisting of four layers. The CSCs are present in the end-cap disks ($0.8 < |\eta| < 2.4$) and are positioned perpendicular to the beam line arranged in four stations. Finally, the RPCs are mounted in both the barrel and end-caps and are operating in avalanche mode, while they practically serve as a complementary triggering system. As it has been measured, around 98.5% (96%) of the installed channels are functional in the DTs (CSCs) [106, 107]. The DTs give a position resolution of about $200 \mu\text{m}$ and a track resolution around 1 mrad along the ϕ direction. Although the RPCs perform worse for the position resolution compared to the DT, they have a faster response ($< 25 \text{ ns}$). This response is small enough to help associating the muon to a given bunch crossing.

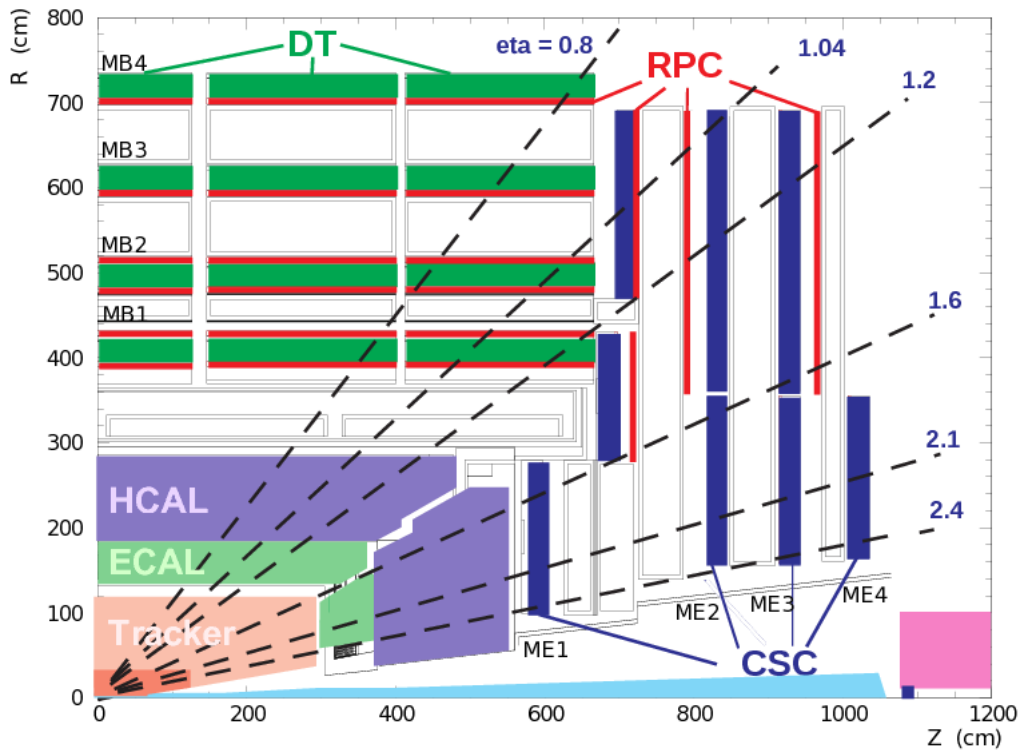


Figure 5.10: A quadrant of the CMS muon system.

5.3.8 The Trigger

The nominal rate of the p - p bunch crossings for the LHC is 40 MHz resulting in roughly 10^9 p - p collision events per second. However, recording all events is simply impossible and a two stage trigger decision is employed in order to reduce this rate down to ≈ 100

Hz so that the data volume becomes manageable [?]. These two stages are the *Level-1* (L1) Trigger which is a highly selective yet hardware-based decision which reduces the initial rate down to 100 kHz, while the second stage named the *High Level Trigger* (HLT) is software based and further reduces the event rate to the final 100 Hz or about $\mathcal{O}(100)$ events per second.

5.3.8.1 Level-1 Trigger (L1-Trigger)

The L1-Trigger processes data from every bunch crossing which is propagated from the muon chambers and the calorimeters with a latency time of $3.2 \mu\text{s}$. The L1-Trigger can be further subdivided in three components, *the Local, the Regional and the Global*, whereas up to the *Global Trigger* (GT) decision, information from the calorimeter and the muons can be treated independently.

The so-called *Trigger Primitive Generators* (TPG), are constructed from muon hits or calorimeter deposits above a given threshold and serve as seeds for the trigger decision. For this, the muon chambers and the calorimeters are read out with a reduced granularity; the calorimeters are clustered into trigger towers of $\Delta\eta, \Delta\phi = 0.087 \times 0.087$ up to $|\eta| < 1.74$, whilst the clusters are bigger for values beyond $|\eta| > 1.74$. Also, the energy information from the trigger tower is gathered out of the energies from both the HCAL and ECAL crystals. This primary information from the TPGs is then piped to the *Regional Calorimeter Trigger* (RCT). The RCTs are responsible to combine all received information by applying basic quality cuts and define the e/γ candidates while summing up the E_T contained in each one of the trigger tower regions. The third part, the *Global Calorimeter Trigger* (GCT) defines the total \cancel{E}_T , the number of jets in the event, or even their scalar sum (H_T). At this point, the L1-Trigger output rate can be narrowed down to 30 kHz, which is a factor of three smaller compared to the desired value of 100 kHz. However, the final decision to either accept or reject an event is taken by the GT, which is based on the information provided by the RCT and the GCT (that is jets, \cancel{E}_T , leptons, photons etc).

5.3.8.2 The High Level Trigger (HLT)

Assuming that the L1-Trigger took a positive decision, the data corresponding to this interesting event is transferred to the front-end units for further processing. The HLT partially reconstructs the event to finally determine if it will be stored or not. The decision of rejecting or accepting the event has to be taken as soon as possible by using

at first only basic information coming from the calorimeters and the muon system. This is done by a filter-farm which runs the necessary reconstruction algorithms. The processing of the event is done in parallel and the workload is shared among few thousands of CPUs. On average, it takes about 40 ms to reach a decision, and at the end, the desired rate of 100 Hz is achieved while the surviving events are written on tape.

5.3.9 The Trigger efficiency scale factors

Given the technical challenges CMS faces, and due to the limited rate of events that can be stored on tape, triggers are characterised by relative high threshold values for the transverse momentum of the of the final state objects. The exact values of these thresholds vary given the instantaneous luminosity, but in general, the rule is that the higher the luminosity, the higher the thresholds have to be. Nevertheless, it is still possible to have triggers with lower thresholds, or even build trigger paths using a combination of more than one trigger object, like for example a second or third jet, a second lepton etc. These trigger paths are referred to as *cross-triggers*. An example could be the trigger which looks for events with at least 3 jets with $p_T > 30$ GeV each, along with an isolated muon with $p_T > 25$ GeV. In order to lower the HLT output rate even further, a *prescale factor* (N_{pf}) can be applied when appropriate. Using a prescaled trigger, implies only one event every N_{pf} passes the trigger, thus the final output event rate is artificially reduced by a factor of $1/N_{pf}$.

5.3.10 Data Quality Monitoring (DQM)

Even if the event is recorded on tape, it does not mean that it is good to be used for a certain analysis. First, it has to be confirmed that all subcomponents of the detector were working properly and were functional at the time of the data taking. This is the mission of the *Data Quality Monitoring* (DQM) system, which harvests the recorded data and scans for potential detector or any other operational disfunctions while data was taken that could have affected the quality of it. This is done in two phases, the online and the offline phase [108].

In the online monitoring, the data is retrieved directly from the HLT and is projected into several control histograms, while events from a specialised DQM tape-stream are processed at a rate of $\approx 10 - 15$ Hz. If for example bad channels or noise at unaccept-

able rate is found, the event is rejected. The offline DQM deals only with fully reconstructed data, provided that all final state objects have been properly reconstructed. Given that a full reconstruction takes several weeks, the offline DQM runs at a much later stage after the data was collected. The offline DQM runs several cross-checks to ensure the sanity and robustness of the recorded data, and the results can be stored in a database accessible by the CMS analysers.

5.4 Computing and Software

During data taking periods, the output of the HLT is directly reconstructed at the so-called *Tier-0* which is located at CERN. Because of the huge amount of data that can be more than 1 Petabyte per year, the need to properly distribute both the collision as well as the simulation data, is of vital importance for the CMS collaboration. To achieve that, several Tier-1 and Tier-2 computing clusters have been accommodated in various institutes all over the world. Together they constitute the so-called *CMS computing infrastructure* [109] which is implemented on top of the *WorldWide LHC Computing Grid* (WLCG) [110], a very powerful network of computers which allows analysers to use the required computational resources for analysis. No matter if it is collision or simulated events, both can be accessed from any grid enabled machine using tools like *CRAB* [111]. The backbone is the CMS Software called CMSSW which is written in Python/C++ and it is the result of the combined efforts of thousands of CMS members over the past 15 years. This software, is a rather sophisticated mixture of various integrated software packages, which allows users to explore and use different tools. These can include the generation of simulated events, detector-level reconstruction, or even data analysis using of the reconstructed final objects.

Part IV

Analysis

There are in fact two things, science and opinion; the former begets knowledge, the latter ignorance.

Hippocrates

CHAPTER 6

RECONSTRUCTION OF PHYSICS OBJECTS

6.1 The need for object reconstruction

Particles are produced copiously at the LHC, literally hundreds of them arise after every p - p collision. Leptons, photons, neutrinos, charged and neutral hadrons are produced and interact in various ways with the detector's materials as they pass through it. Most of these particles have a rather low p_T , even when a big fraction of the momentum is transferred during the collision. Phenomenologically, the above hold for all type of particles, no matter if we consider a SM or a BSM model. In order to determine the exact production process, it is vital to identify and reconstruct the final state objects accurately. For this task, all information coming from the sub-detectors has to be combined into the form of charged particles trajectories, calorimeter deposits and muon tracks. These are the building blocks, the raw "elements" of the final reconstructed objects. In modern experiments such as the LHC, high reconstruction efficiency and low misidentification (fake) rates are a necessity, even in a high luminosity environment. In the CMS experiment, the *Particle Flow* (PF) event reconstruction method is utilised for this purpose (Section 6.2). Although the PF is able to reconstruct all the different final state particles, we will focus only on the ones related to this analysis, namely the reconstruction of the *Primary Vertex* (Section 6.3), the *muons* (Section 6.4), the *jets* and the *missing transverse energy* (Section 6.5).

6.2 The Particle Flow (PF) method reconstruction

The *Particle Flow* (PF) [112] event reconstruction method, aims to both identify and reconstruct the final state particles emerging after a p - p collision. The idea behind PF is to combine in the most efficient way all the information gathered from the different CMS sub-detectors in order to define the energy, direction and type of the particles involved in each event. Thus, the input information to the PF event reconstruction are the tracks, the clusters of energy deposits collected in the calorimeters and the hits from the Muon System. The response of the PF event reconstruction is a collection of particle candidates associated to each event. These candidates can be further classified in different collections such as electrons, muons, photons, charged and neutral hadrons. These particle collections are then used to reconstruct higher level physics objects, such as the jets, or to calculate the missing transverse energy (\cancel{E}_T). Compared to the plain calorimeter-based reconstruction methods, the PF event reconstruction has been found to be superior with respect to the spatial and energy resolution of the reconstructed jets, while it also gives a more accurate measurement of the \cancel{E}_T of the event [113, 114].

The PF machinery makes use of the information collected by the TK by using an *Iterative Tracking* approach [115] while applying relatively tight criteria to the seeds. This approach will result into a somehow limited tracking efficiency, but it will yield a very small fake rate as well. In the next step, the criteria are loosened, but the hits that were unambiguously related to the tracks found in the first step are removed. This increases the efficiency (the looser the criteria, the higher the efficiency), while the removal of the associated track hits keeps the fake rate at low levels as a result of reduced combinatorics. The method consist of five such iterations and at the end charged particles associated with at least three hits located inside a small cylinder around the beam pipe of $r \approx 25$ cm and having p_T as low as 150 MeV can be reconstructed [115].

The way the PF event reconstruction uses the information from the calorimeters is embedded in the so-called *clustering algorithm* which is composed of (at least) four steps :

1. Measurement of the energy and direction of stable neutral particles, such as neutral hadrons or photons.
2. Separation of the energy deposits in the calorimeters depending on the origin i.e. neutral or charged particles.

3. Reconstruction and identification of leptons (and possible bremsstrahlung photons) associated to the collision event.
4. In the case of low-quality or highly energetic tracks, measurement of the energy of the charged hadrons, if the track characteristics could not be determined accurately.

In order to perform the above, topological clusters are formed in the calorimeter by combining information from adjacent calorimeter cells after including seeds above some noise threshold. Typically, a given particle leaves an imprint in more than one of the sub-detectors, producing more than one element useful to the PF event reconstruction. For instance, a hadron can give a charged-particle track in the TK, deposit energy in the HCAL etc. Therefore, all of these "candidates" must be combined and connected to each other. This is done by a link algorithm, which aims to fully reconstruct a given particle, while rejecting possible double-counting effects. Since the CMS detector is a high granularity detector, each segmentation block contains only a limited number of elements, something that favours the PF identification algorithms.

6.3 Primary Vertices (PV)

The exact position of the interaction point consists is also referred to as the *Primary Vertice* (PV). The identification of its exact position is done by reconstructing all collision vertices in the event by using the charged particles trajectories in the TK [98]. The identification of the promptly produced particles (i.e. production of a particle at the PV) from those produced in subsequent decays of hadrons/photon conversions is important for the identification of the PV. Furthermore, we need to take into account the effects of PU where multiple p - p interactions happen during the same bunch crossing. In other words, we must be able to classify the hardest p - p scattering from interactions associated with the secondary collisions, or even distinguish its tracks from the ones associated with the decayed particles.

The PV is defined to be the vertex with the largest scalar sum of the transverse momentum squared from the associated tracks. The PV are reconstructed by building formations of two or more tracks spatially separated along the z - axis less than 1 cm, measured from their closest point of approach [103]. Next, PV candidates are formed which are made from the clustered tracks with the use of an appropriate algorithm. This algorithm evaluates the position of each vertex in 3D taking also into account the

disassociated tracks or mismeasured track errors. Each track is assigned with a weight which is zero (unity) for the less (most) compatible tracks with the fitted vertex position [116].

6.4 Muon reconstruction

The muons hold a special role in the discrimination of semi-muonic final states when compared to the huge multi jet rate coming mainly from background sources. Therefore, it is very important to properly reconstruct the trajectory of isolated muons to discriminate signal from background events. Due to its intrinsic properties, like its mass which is ~ 106 MeV (200 times heavier compared to electron, thus minimal energy loss because of bremsstrahlung), as well as its lifetime of $2.2 \mu\text{s}$, muons typically reach the outer layers of the detector where they are measured by the Muon System [12, 98]. Therefore, muons are relatively easy to isolate and reconstruct compared to electrons since they deposit a relatively small amount of energy in the inner sub-detectors.

6.4.1 Classification of Muon candidates

In general, several sources can give muon-like objects resulting in a high rate of fake muon candidates. We can however classify the muon candidates as follows :

Prompt muons. These are muons that can be associated directly with the IP and are coming from Drell-Yan processes, W-boson decays, or even promptly produced quarkonium states etc. Usually, the hits in the Muon System from this class of muons can be easily associated with the muon trajectory.

Muons from hadrons. These can be further separated between muons coming from heavy or light-flavours. The light-flavour category includes decays of in-flight pions or kaons, or even particles produced while interacting with the detector's material. In the case of heavy-flavours, the muon can come from a charmed hadron, a beauty one, or even from the hadronic decays of a τ -lepton.

Hadron punch-through. *Punch-through* denotes the remnants of a hadron shower that penetrates the calorimeter detector and make it to the Muon System. Thus, these misidentified "muon-like" particles give hits in the muon chamber resembling prompt muons hits, but in general, they are not associated with a track in the TK.

Duplicates. In case that during the reconstruction step several muons are reconstructed from one candidate, then we get a *duplicated muon* object. The reconstructed muon with the largest number of matched hits is kept, while all the others are rejected.

The reconstruction of the muons in CMS is done by using either one of the two following techniques, the *Local Reconstruction* (Section 6.4.2), or the *Global Muon Reconstruction* (Section 6.4.3). In the context of this analysis, the final state muons were reconstructed with the use of the Global Muon Reconstruction method.

In CMS we have three types of muons: standalone muons, built without any tracker input (serves mainly L1 trigger purposes); global muons, built from muon segment seeds, to which a tracker track is matched, and a global track is then fitted; and tracker muons, which use the tracker track as a seed, and look for matching muon segments (even if only 1, which would be insufficient for a global muon).

6.4.2 Reconstruction of Standalone and Tracker Muons

The Standalone muons are built without any input from the TK and seeds need to be found from the DT, the CSC and the RPC's as well. This is known as the *inside-out* approach and it is done in a complementary way in order to compensate for the limited spatial resolution of the RPCs. Also, information coming from the overlapping regions between the end-caps and the barrel has to be used. Once seeds are found from the combination of the direction, momentum and track positions, a combination of the candidates in the Muon System is performed to finally reconstruct the muons. However, if on top the TK seeds are matched with muon segments while all possible effects from energy losses, multiple scatterings and their associated uncertainties have to be considered when extrapolating a track in the TK to the Muon System i.e. when the muons travel from inside-out we then get the *Tracker Muons*. In any case, all necessary corrections have to be made every single time the muon crosses a different sub-detector. It is important to note however, that at least one hit is required to be present in the Muon System to allow the reconstruction of a tracker-associated muon. Finally, when the outermost layer is reached, a Kalman fit is applied in a reverse way to determine the parameters of the track in the Muon System, propagated down to the interaction point. This approach is more efficient than the Global muon reconstruction for muons with momentum less than 5 GeV.

6.4.3 Reconstruction of Global Muons

In the Global muon (or *outside-in*) approach the track of a muon reconstructed in the Muon System is attempted to be matched with compatible tracks coming from at least two reconstructed hits belonging to different layers of the Silicon Tracker. These tracks, are initially combined to build a first regional seed. A Kalman fit is performed on the tracks to determine its momentum. Similarly to the inside-out approach, effects of energy losses and multiple scatterings while the muon penetrates the detector, have to be considered. In case of remaining ambiguities, the Global Muon track is selected according to a χ^2 criteria of the track fit's response. This could happen for instance in case more than one global muon track candidate is present for the same stand-alone muon track. For muons with a high transverse momentum, the global fit is using only a subset of the TK and the innermost hits in the Muon System. The χ^2 of the two fitted tracks are compared in order to find significant energy losses due to multiple scatterings in the region between the Muon System and the Inner Tracker. For muons with $p_T \gtrsim 200$ GeV the global fit can further improve the momentum resolution, because the global fit procedure becomes more efficient if only a part of a track is required to be present in the muon chambers.

However, there can be several background sources mixing with the prompt muons, as it has been already elaborated in Section 6.4.1.

In general, the non-prompt muons do not match the properties of those produced at the PV (i.e. the prompt ones). So, in order to reject them it is usually sufficient to apply several muon identification (ID) selection requirements, which are based on the properties of the muon track itself. For example :

1. Requiring good quality global fits and small impact parameters of the involved muon tracks with respect to the PV will reduce the punch-through candidates.
2. Requiring a minimum number of hits inside the Pixel Detector, will suppress the in-flight decays occurring outside the pixel layers.
3. Applying isolation requirements when reconstructing muons, will control muon candidates from background sources like hadrons. This can be achieved by requiring to have little energy deposited in the calorimeter in a cone of radius R around the muon candidate, or by requiring that the sum of the transverse momentum of the tracks (apart from the muon track) in this cone to be small.

6.4.4 Performance of Muon reconstruction

The reconstruction efficiency is evaluated by reconstructing the $J/\psi \rightarrow \mu\mu$ for muons with $p_T < 20$ GeV and $Z \rightarrow \mu\mu$ for muons with $p_T > 20$ GeV. The efficiency yields 99% as can be seen in Figure 6.1 [117]. The charge mismeasurement seems to be very well controlled as its value is less than 0.01% for $p_T \sim 10$ GeV and about $\sim 1\%$ for $p_T \sim 500$ GeV.

The resolution of the muon momentum is $\sim 1\%$ for muons with $p_T > 100$ GeV, while it is worse, yielding $\sim 8\%$ for muons with $p_T \simeq 10$ GeV. In total, several measurements during the 2011 and 2012 gave results in very good agreement with simulated predictions [118].

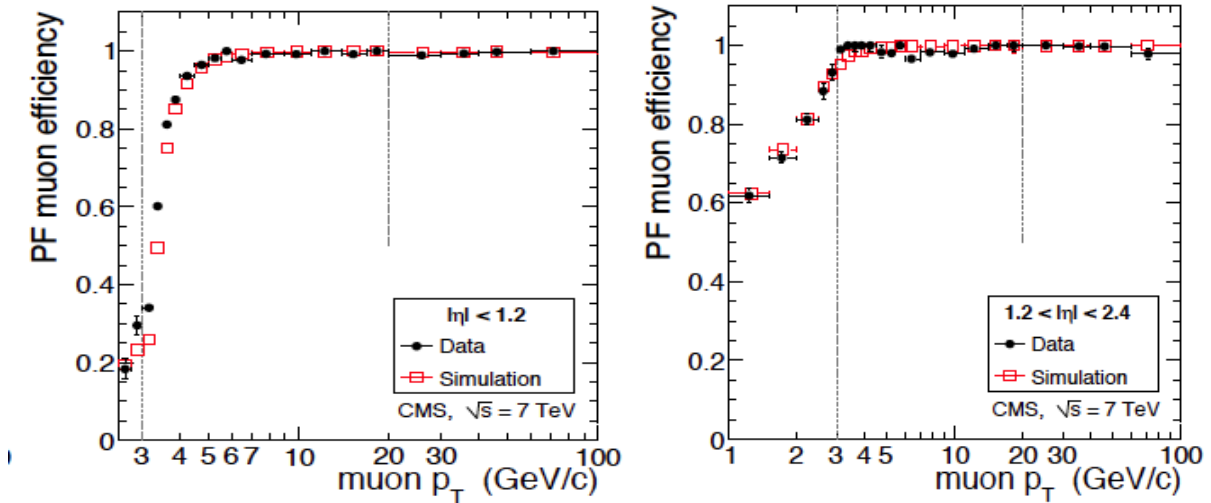


Figure 6.1: Muon efficiency results from $J/\psi \rightarrow \mu\mu$ for muons with $p_T < 20$ GeV and $Z \rightarrow \mu\mu$ for muons with $p_T > 20$ GeV using PF-Muons in the barrel and overlap regions (left) and in the end-caps (right) [117].

6.5 Jets and \cancel{E}_T

Jets are formed from the fragmentation of quarks and gluons produced during the hard scattering of partons in the events. As multi jets events have a huge cross-section, they vastly populate the high- p_T region at the LHC. Jets are important both for SM measurements as well as in the search for new physics, but they also are a very powerful tool to calibrate the various sub-detectors.

In modern HEP searches experimental signatures typically involve jets whether one is studying BEH-boson production, natural or split SUSY models, exotic models or compositeness. Usually, the sensitivity of these searches depends on a very fine reconstruction and precise measurement of the jets properties. Of course, this does not come without a price, since it is a long standing problem how to associate a jet with the originating parton. This is why, the understanding and calibration of the reconstructed jet energy to the physical quark energy using the *Jet Energy Scale* (JES) corrections is essential. In other words, this necessity is dictated by the need to minimise and estimate accurately the involved systematic uncertainties, while in parallel the discrimination of signal and background has to be achieved with the greater efficiency. Even more, the reconstruction of jets also serves as the stepping stone for the characterisation of the hadronic decays of τ -leptons and b -hadrons. The jets contain a diverse spectrum of different particle types which interact with the CMS detector in different ways. By the same token, the resolution of the missing transverse energy is closely related to the calorimeter jet energy response. Hence, just like for the jets reconstruction, the information from various parts of the detector has to be combined in order to get the most accurate reconstruction.

6.5.1 Jet input types

While reconstructing jets, several aspects have to be taken into account. For example, the detector's geometry and granularity, the size of the ECAL segmented crystals and the spatial resolution of the HCAL cells affect the performance of the jet reconstruction. During the last years the CMS experiment has used the *PF jet* collections, although also the *CaloJet* and *Track-Plus-Jets* collections have been exploited in the past [48, 112]. Also, the *GenJets* collection are made from the stable hadrons which are clustered directly after the hadronization process but before any interaction with the detector's materials. Practically, the GenJets can be made only from simulated samples and is a very useful tool when it comes to evaluate the various jet reconstruction methods or algorithms.

6.5.2 Jet algorithms

Due to the QCD colour confinement, partons cannot be isolated. Instead, we have to identify all the associated objects originating from quarks and gluons that were produced during the fragmentation and the hadronization steps. This task is performed by

the *Jet-Finding* algorithms, which can be thought as an approximate attempt to reverse-engineer the quantum mechanical processes of fragmentation and hadronization. This is the same to say, that the jet algorithms aim to reestablish the connection between the observed particles and the partons produced during the hard scattering process.

Historically, the first attempts of jet reconstruction algorithms were based on simple cones from the UA1 collaboration [119]. In the meantime, the accumulated experience gathered from the UA1, the UA2, the Tevatron, the LEP and the HERA experiments has resulted into more sophisticated techniques. In the CMS collaboration one main jet reconstruction algorithm is used, the anti- k_T algorithm, which was also used in this analysis.

The anti- k_T algorithm [120] is a sequential clustering one and basically it tries to combine near by entities noted here by i, j . The input to the jet-clustering routine is the collection of PF candidates of the event from which a list of pseudo jets is defined. These pseudo jets are recombined to form the final jets. For each one of the initial input particles from the PF candidates list the following quantities are calculated :

$$d_i = \frac{1}{k_{T_i}^2} \quad (6.1)$$

$$d_{i,j} = \min\left(\frac{1}{k_{T_i}^2}, \frac{1}{k_{T_j}^2} \frac{\Delta_{i,j}^2}{R^2}\right) \quad (6.2)$$

with k_T being the transverse momentum, while $\Delta_{i,j} = \sqrt{(\eta_i - \eta_j)^2 + (\phi_i - \phi_j)^2}$ is the angular distance between the two PF candidate objects and R gives the size parameter to weight the distances $d_{i,j}$. The anti- k_T is both *infrared* and *collinear safe*. Being *collinear safe*, means that all collinear splitting does not change the final output of the algorithm. Being *infrared safe* (IR) means that the presence of soft emissions should not change the structure of the jet. That means that for an IR-safe algorithm, the physical event with hadron jets should give almost the same response as a partonic event, while infinities have been cancelled. Finally, it has been found that the anti- k_T algorithm results in more regulated shapes of the jets compared to other algorithms [120]).

6.5.3 Jet-energy corrections

Since the reconstructed jets are affected by both the imperfections of the detector as well as the weaknesses of jet clustering algorithms, jet-energy corrections have to be

applied. These are needed to get the most accurate reconstructed object derived from the constituents of the jets. On average, they connect the measured jets to a more generic and universal jet definition, hence, independent of the detector's geometry and response. Problems arise since the theoretical definition of a jet can be very different compared to the final output of a given jet-algorithm, because of the interaction of particles with matter. Thus, one needs to calibrate and tweak the reconstructed jet energy to be a close match to the energy of the initial parton or the GenJet. In this section we discuss the various levels of jet corrections CMS has developed.

The Factorized approach

The adopted workflow for CMS is the so-called *factorized approach* where the jet-energy calibration can be divided into different levels as illustrated in Figure 6.2. Once this sequence of different levels of corrections is applied, a non-negligible reduction of the systematic errors and uncertainties is achieved. Each one of these, is studied in detail by dedicated working groups, which are trying to get a better understanding and control of the different sources of systematic uncertainties involved.

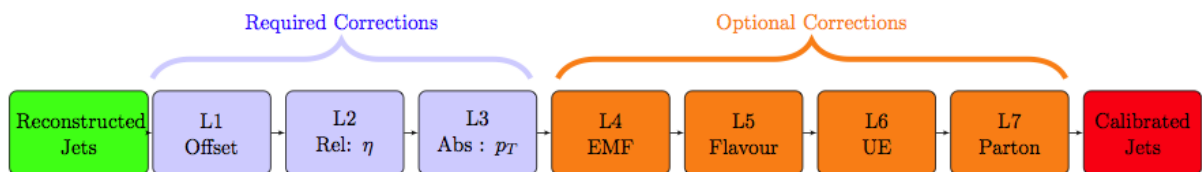


Figure 6.2: Sketch of the factorized approach to apply the jet-energy corrections.

This strategy was already employed at the Tevatron, where collider data was used to derive the necessary jet-energy scale corrections. Currently, the CMS collaboration derives the jet-energy corrections from both simulation and by using data-driven methods. The different correction levels are defined as :

1. *Offset correction* (L1)

Even when the jet energy has been measured, there are still sources that result in additional calorimeter energy deposits. These contributions are due to electronic noise and PU events. As a consequence, they cause an offset of the jet energy scale. The PU correction subtracts from the jet the average extra energy that was deposited from other vertices which were present in the event, but are not associated with the jet itself. The correction formula is parametrized as a function of the median jet energy [98], or alternatively of the number of primary

vertices N_{PV} . Currently, various methods are in use to get the L1 corrections, both at hardware and software level. Hardware (or detector-level) corrections are reflected on the choice of timing, threshold or any other relevant change that could reduce the actual level of PU contributions. On the other hand, software level corrections are applied after the reconstruction as the scaling of the p_T of the jet depends on the actual measured amount of PU. For this task, two main methods are in use, namely the *Average Offset* (AO) and *Jet Area* (JA) correction. The AO method is based on both MC and data-driven techniques and associates the extra average deposited amount of energy due to PU. The JA method uses a different parametrisation based on the FastJet algorithm [121] and takes as input the energy from PU on an event-by-event basis and on a jet-by-jet basis as well [122, 123]. Both these methods present a linear response while measuring the PU contribution as a function of the N_{PV} as shown in Figure 6.3 [124].

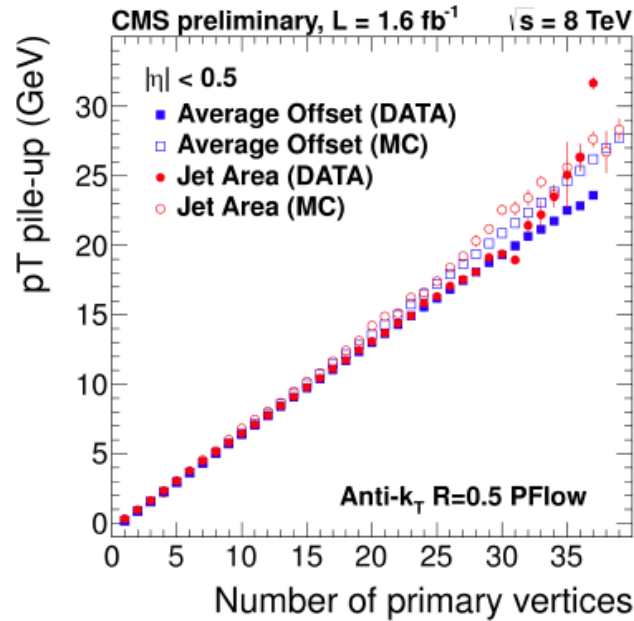


Figure 6.3: The PU measured in PF jets for the AO and JA methods. Both methods present a good linear behaviour of the p_T of the PU as a function of the number of Primary vertices in the event [124].

All the above has to be quantified and for this the response of the detector to the jets is expressed as the ratio of the p_T of the PF jet divided by the that of the matched GenJet, namely $R = \langle p_T^{cor} / p_T^{GEN} \rangle$ [125]. Provided that the corrections are perfect, the response of the jets has to be independent of N_{PV} . This would mean that the PU contributions are completely understood and controlled. However, before any correction, the response for low p_T jets is far from perfect as the

ratio strongly depends on the N_{PV} value (Figure 6.4 left plot). After the L1 corrections, it can be seen that this dependency has mostly disappeared (middle plot), while the response is significantly larger in the low p_T region before the corrections are applied. After the L1 corrections have been applied the response still deviates from 1 for low p_T jets, therefore additional corrections need to be applied to correct for the η and p_T dependence of the jet response (right plot).

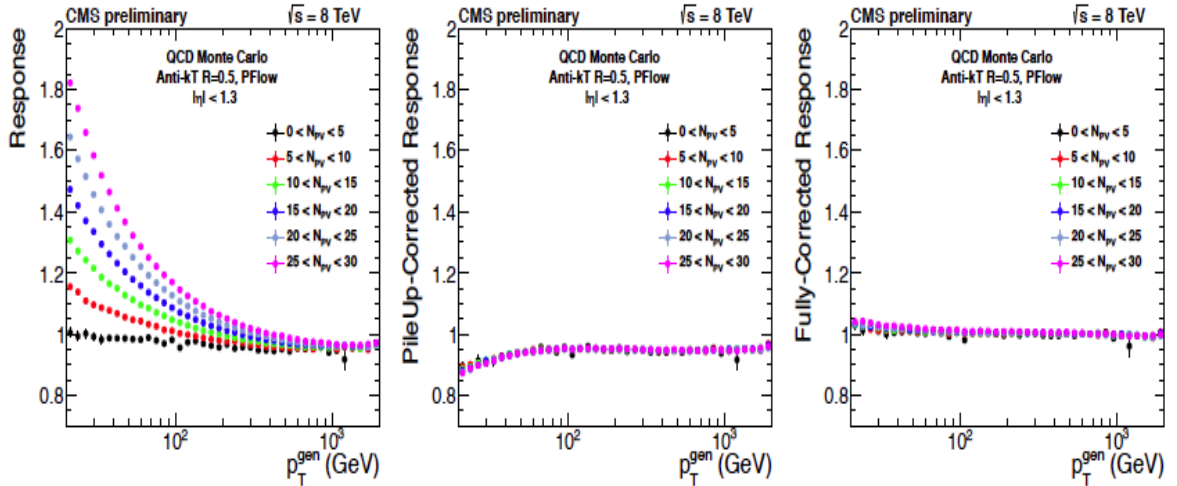


Figure 6.4: The PF jet response versus the p_T of GenJet. On the left (middle), before (after) applying any L1 correction and on the right after having applied the required MC correction chain [125].

2. Relative η dependence (L2)

The L2 correction aims to correct for the effects of the dependence of the jet energy response with the pseudo-rapidity. Studies based on MC [125] show a need for a correction at the level of 0.5 – 1.5% for jets with $p_T > 30$ GeV, depending on the flavour of the jet.

3. Absolute p_T dependence (L3)

The L3 correction aims to tweak the jet energy due to the non-uniform response of the detector as a function of their p_T and correcting back to the jet energy scale.

Figure 6.5 [126] demonstrates some of the relative uncertainty sources as a function of p_T and η for the PF jets collection.

4. Electromagnetic fraction (L4)

The electromagnetic fraction (EMF) of the jet (i.e. the fraction of energy deposited and measured in ECAL compared the total energy measured in both HCAL and ECAL), can result in a different jet energy scale. The L4 correction is the first of the

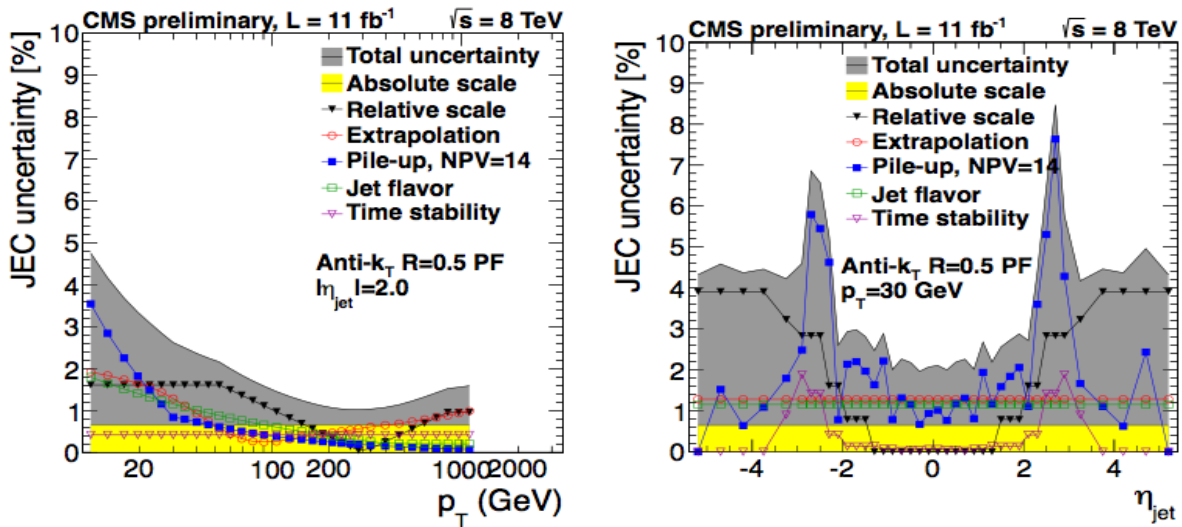


Figure 6.5: Relative uncertainties of the jet energy scale correction as a function of p_T (left) and of η (right) for various sources [126].

"optional" corrections and is depending on the EMF value. The L4 correction can be derived both from simulation studies or from a data driven approach [127].

5. Correction for the dependency on the jet flavour (L5)

Given the fact that jets originate either from gluons or (u,d,c,s,b) quarks, the jet energy scale can be different depending on the flavour of the jet as small differences are expected due to the way jets fragment depending on their the flavour. On top of that, gluons are responsible for the presence of extra radiation in the jet activity. The L5 corrections can be derived from simulation studies by matching the jet flavour to the GenJet. In the CMS experiment, the so called *algorithmic definition* is used [126]. Practically, the jet flavour is determined by using a spatial criterion between the GenJet and the final state partons. For example, for a jet to be tagged as a b/c jet, it has to reside within a cone of radius $\Delta R < 0.3$ of the corresponding GenJet object and then the jet is labeled as such. In the case a match is not found, the flavour of the highest p_T parton within this cone determines the jet flavour. However, there is a strong correlation between the flavour of the jet and the mean jet response. This can be explained on the basis of the different p_T spectrum with respect to the flavour of the jet. Still, these corrections assume a certain working hypothesis about the flavour of the originating parton related to the jet.

6. Correction for the underlying event (L6)

This correction accounts for the extra amount of energy that is attributed to a jet

due to the UE. Hence, the L6 correction aims to subtract this contribution which gives an extra hadronic activity that shifts the jet energy to higher values.

7. *Parton correction* (L7)

The L1-L6 corrections aim to correct the jet energy back to the energy of the Gen-Jet collection. The L7 calibration targets to correct the jet energy back to the energy of the originating parton. However, the connection between the jet p_T and the patron p_T , is far from trivial. Consequently, the correction strongly depends on the implementation and modelling of the UE and the MPIs in the MC generator. It also depends somehow from the choice of the used jet reconstruction algorithm and the details of the physics process in question.

However, more details on how the JEC are applied for this analysis are discussed in Chapter 7.

6.5.4 Identification of b -jets

Decays from b quarks are suppressed due to the small values of the corresponding CKM matrix elements. Consequently, b -flavoured hadrons have a long lifetime. Since the b quark is relative heavy compared to other quarks (with the exception of the top quark), their decay products usually have a large momentum hence they produce relatively wider jets compared to the jets originating from light quarks (i.e. u, d, c, s) or a gluon. These two characteristics allow us to separate b -jets from light-flavoured jets. This separation is vital for the CMS physics program which includes several SM precision measurements and many BSM searches that give experimental signatures explicitly involving b -jets in the final state.

6.5.4.1 The b -tagging algorithms

Three main b -tagging algorithms are used by the CMS collaboration. Basically, each algorithm combines one or more discriminating observables and a single discriminator value is provided by each jet. These specific observables are associated with the properties of the jet. For example, the impact parameter of a track is used in the *Impact Parameter significance* algorithm, while the information of the secondary vertices are used in the *Secondary Vertex* algorithm. Similarly, the kinematic properties of the lepton present in the jet are used in the *Soft Lepton* algorithm. In any case, a common

starting point is to first apply several quality cuts in order to ensure the robustness of the algorithm [128], such as:

1. Only well-reconstructed tracks with high purity are considered. Poorly reconstructed tracks are suppressed by requiring $p_T > 1$ GeV.
2. At least eight hits must be present in the Strip Tracker.
3. $\chi^2 / \text{number of degrees of freedom (n.d.o.f.)} < 5$.
4. At least two hits in the Pixel Detector.
5. A looser selection on the transverse ($|d_{xy}| < 0.2$ cm) and longitudinal ($|d_z| < 17$ cm) distances (i.e. the impact parameters) is applied. These requirements suppress the decayed products of long-lived particles (K^0 for instance).
6. A cone of $\Delta R < 0.5$ around the jet axis is used to associate tracks with the jet. The jet axis is defined by the PV and the direction of the jet momentum.
7. The distance of a track to the jet axis (as was defined above) has to be less than $700 \mu\text{m}$ to reject contributions from PU.
8. Point of closest approach of the above distance must be less than 5 cm of the PV.

In Figure 6.6 some track properties like the distance to the jet axis and the average track multiplicity are shown [128].

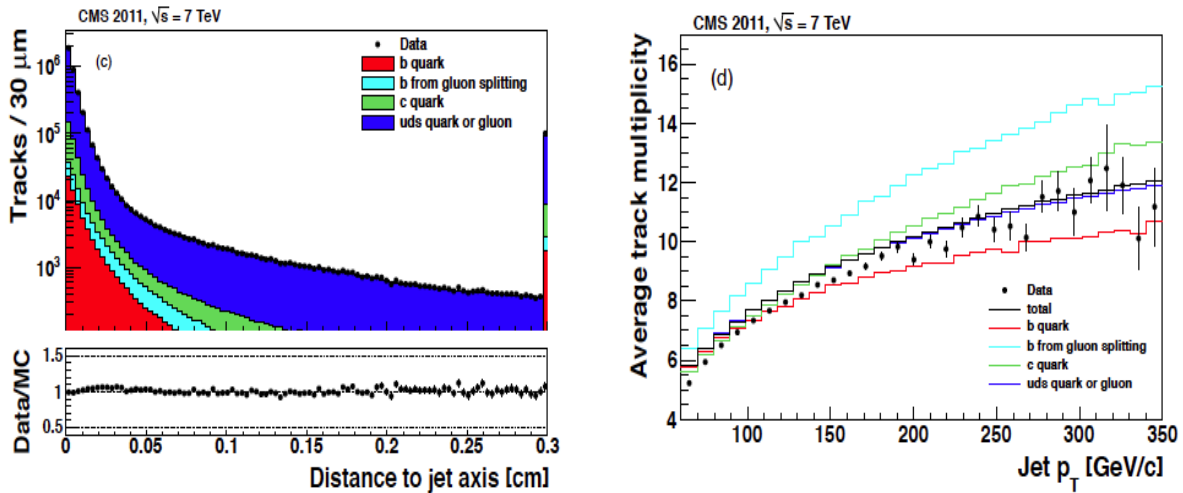


Figure 6.6: The distance to the jet axis (left) and the average number of tracks (right). The trigger selection was requiring jets with $p_T > 60$ GeV [128].

In more details, the aforementioned properties used in b -tagging are :

1. *Impact Parameters (IP) of the track*

The IP is used to distinguish the decay products of a b -hadron from prompt tracks. It is defined as the distance between the track and the PV at the point of closest approach. Taking advantage of the excellent performance of the TK, the IP is calculated in the 3D plane and carries the same sign as the scalar product of the vector pointing from the PV to the point of closest approach with the jet direction. Hence, it will be positive (negative) if the track was produced downstream (upstream) compared to the PV along the jet direction (Figure 6.7). That practically means that those tracks originating from the particles along the jet axis direction will tend to have positive values. Also, the IP is Lorentz invariant and due to the b -hadron lifetime, a typical value is $c\tau \approx 480 \mu\text{m}$. Practically, the used variable is the *Impact Parameter Significance* defined as :

$$S_{IP} = \frac{IP}{\sigma_{IP}} \quad (6.3)$$

where the denominator stands for the estimated uncertainty on the IP. Although its resolution is strongly depending on the p_T and the η of the track, all relative effects are endowed here. In Figure 6.8 the distribution of the IP values and the significance are shown [128].

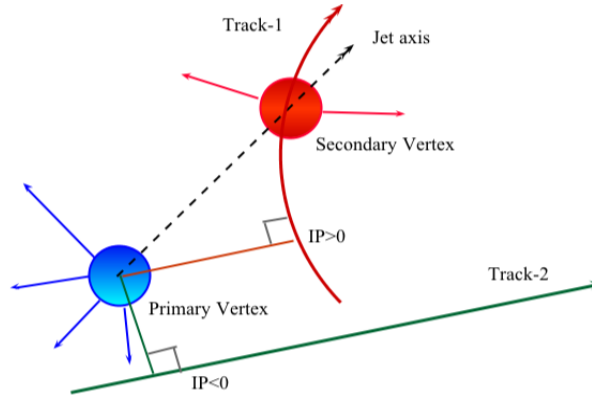


Figure 6.7: Illustration of the Impact Parameter (IP) parameter. It holds the same sign as the scalar product of the vector pointing from the PV to the point of closest approach with the jet direction.

2. *Secondary Vertex (SV)*

Because of the long lifetime of b -hadrons, their decay vertices present a completely different pattern with respect to the PV. This allows the reconstruction of the so-called *Secondary Vertex (SV)* [98]. Indeed, the presence of the SV together with its associated kinematic variables, can be very useful to properly identify b -jets. The main considered variables are the direction and the flight distance of the

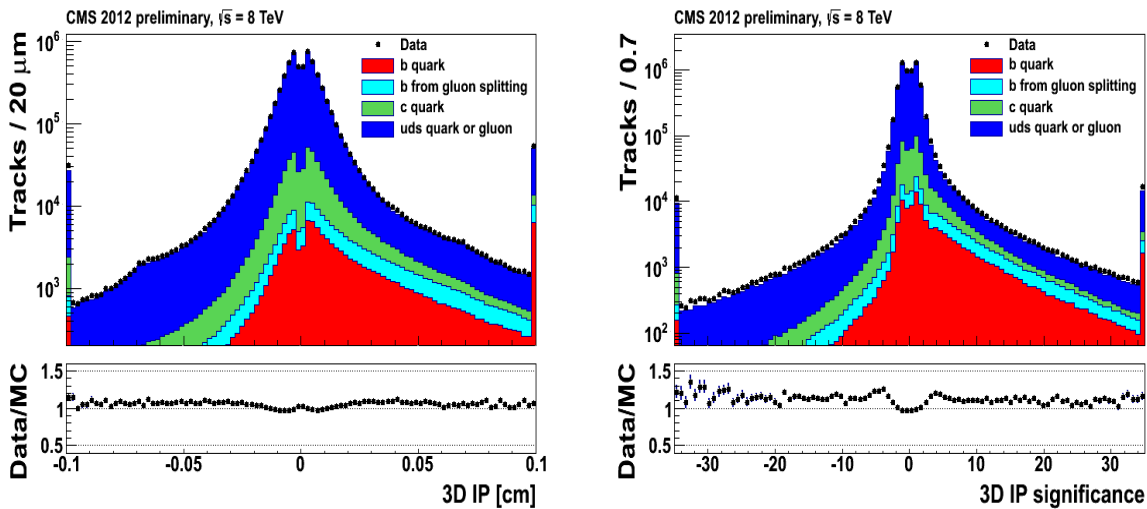


Figure 6.8: The 3D impact parameter (left) and the significance of the 3D IP (right) for all selected tracks. Underflow and overflow are added to the first and last bins, respectively [128].

SV. Other variables can incorporate the energy, the mass, or even the multiplicity of the tracks associated with the SV. The reconstruction of the SV starts from the tracks associated with a jet [129], while several additional quality cuts are applied to increase the purity of the track sample. Currently, two main algorithms based on the SV information are used in CMS. These are the *Simple Secondary Vertex* (SSV) and the *Combined Secondary Vertex* (CSV) methods.

- The SSV method exploits the significance of the flight distance, defined as the ratio of the flight distance and its estimated uncertainty but the efficiency is limited by the SV reconstruction efficiency ($\approx 65\%$). Two SSV optimised versions exist, the *Simple Secondary Vertex High Efficiency* (SSVHE) which takes into account vertices with more than one associated track present at the vertex and the *Simple Secondary Vertex High Purity* (SSVHP) which requires at least three tracks. Both the mass and the flight distance significance associated with the SV are illustrated in Figure 6.9 [128].
- The combination of the information from the displaced track with the SV gives the *Combined Secondary Vertex* (CSV) algorithm. which has an increased maximum efficiency compared to the SSV method. A "pseudo-vertex" is constructed if there are at least two tracks found $S_{IP} > 2$, something that helps evaluating a smaller class of quantities associated with SV-like objects, but without the need for an actual vertex fit. In general, there is a list of variables like the vertex mass, the ratio of the energy carried by

tracks at the PV with respect to all tracks in the jet, or even the multiplicity of tracks in the jet. These variables are fully exploited and can provide high discriminating power. At the end, a likelihood are made from all these variables and the optimum goal is to discriminate between b, c and the rest of the light parton jets. In Figure 6.10 the distribution of the CSV variable and the vertex multiplicity are shown [128].

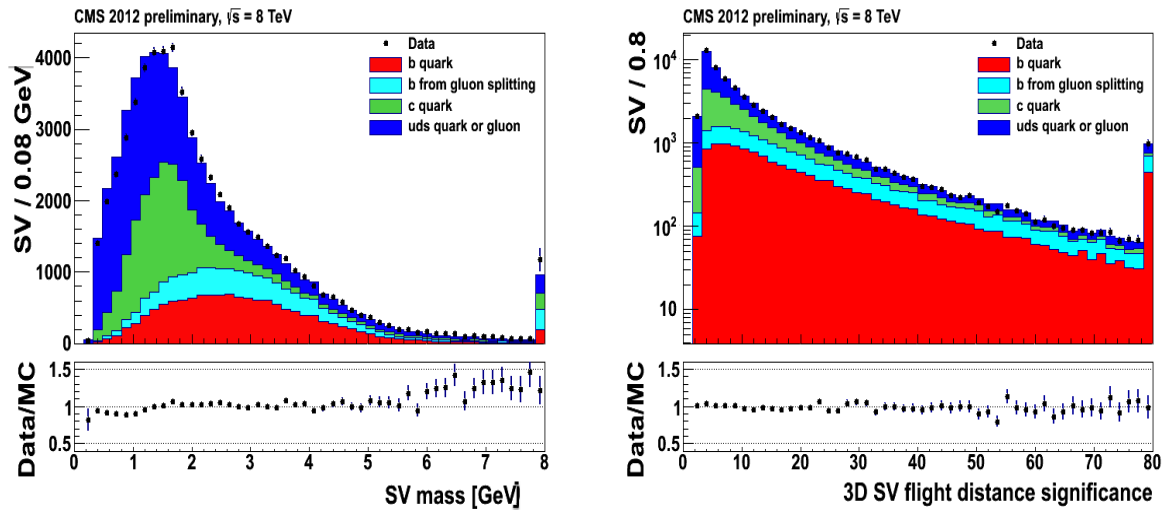


Figure 6.9: The mass (left) and the 3D significance (right) of the secondary vertex [128].

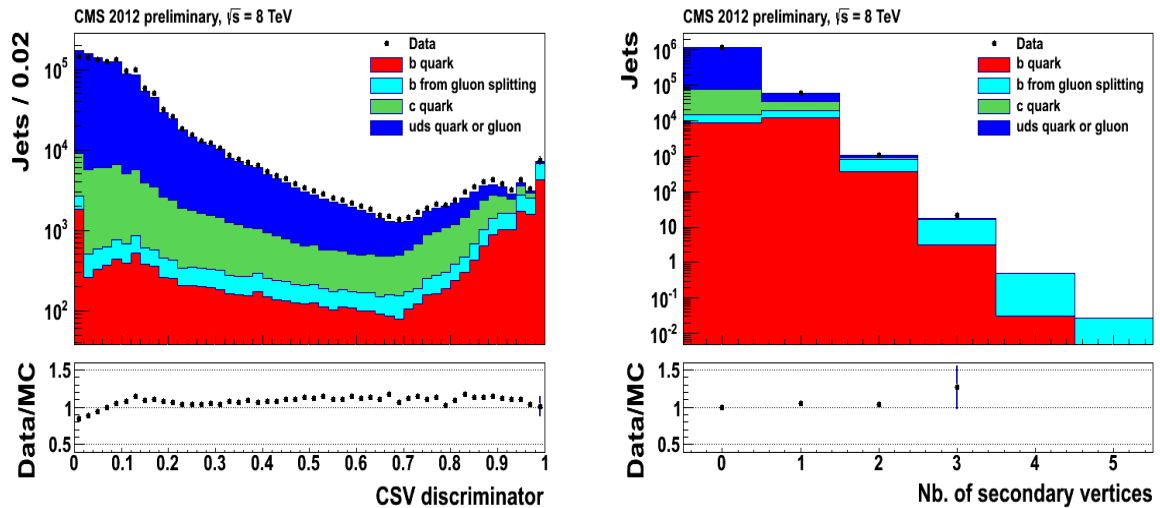


Figure 6.10: The distribution of the CSV discriminator (left) and the multiplicity of the SV vertices (right) [128].

3. Soft-Lepton

The b -tagging algorithms can also benefit from the fact that b -hadrons can decay

to final states containing muons or electrons [129]. In particular, b hadrons can decay leptonically resulting in jets with a muon (the BR reaches 20% if the $b \rightarrow c \rightarrow \ell$ is considered). That is the reason why it is useful to study the muons/electrons inside a jet, as they can help to increase the performance of the tagging algorithms that are based on the lifetime of b -hadrons. Due to the large b quark mass, the momentum of the muon/electron transverse to the jet axis has a harder spectrum for muons/electrons from the b -hadron decay chain compared to the muons associated with light-flavour jets.

6.5.4.2 Performance of the b -tagging algorithms

The efficiency of the b -tagging algorithms can be quantified by varying the cuts on the considered discriminator variable. In CMS, different "working points" have been established named *loose* (L), *medium* (M) and *tight* (T). These working points correspond to a certain value of the misidentification probability for identifying a non b -jet as a b -jet at the 10, 1 and 0.1% level respectively. In this thesis, the CSV-Medium working point has been used. Figure 6.11 [128] presents the efficiencies for various b -tagging algorithms and for all of the three working points. One can see that the CSV has the best performance for the Medium working point as it yields an efficiency of about 70% to identify b -jets.

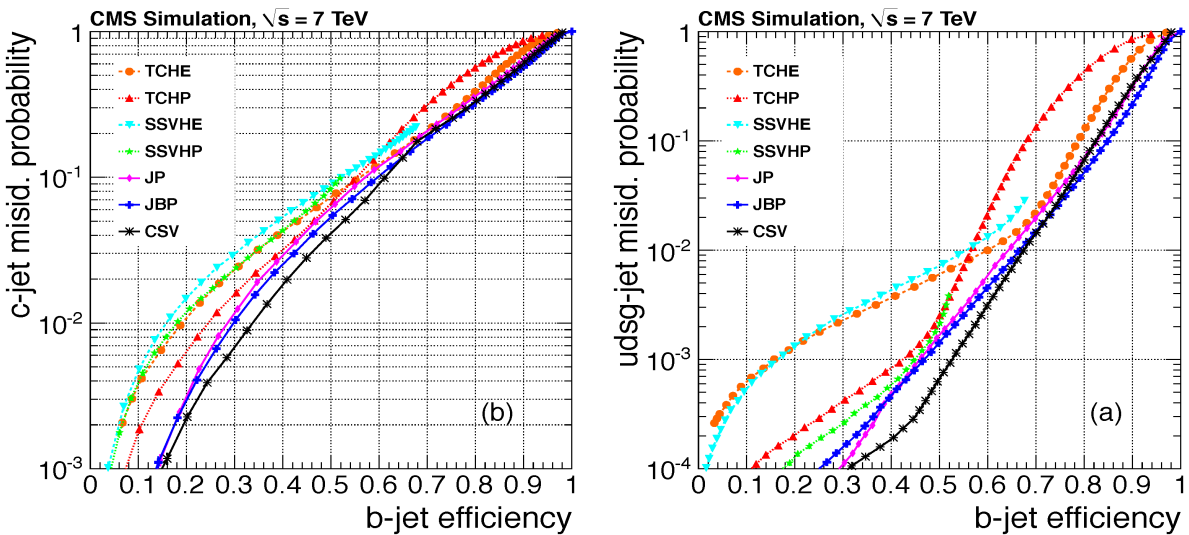


Figure 6.11: Performance curves obtained from simulation for various b -tagging algorithms for c jet (left) and light-parton (right) misidentification probabilities as a function of the b -jet efficiency [128].

6.5.5 Missing Transverse Energy (\cancel{E}_T)

Particles like the neutrinos and weakly interacting stable particles do not interact with the material of the detector and they escape direct detection. To properly account for these, the missing transverse momentum needs to be constructed. It is defined as the imbalance in the transverse momentum of all final state reconstructed (visible) particles. It can be expressed as the vector momentum imbalance in the plane perpendicular to the direction of the incoming beams along the z-axis. In particular within the PF algorithm, the missing transverse momentum is given by the negative momentum sum of all final state objects (PF candidates) in the event :

$$\mathbf{E}_T^{\text{miss}} = - \sum_i \mathbf{p}_i \quad (6.4)$$

where i runs over all final state reconstructed objects of the event. What is actually used in analyses, is its magnitude known as the *missing transverse energy* and is denoted by \cancel{E}_T [130]. The \cancel{E}_T is given by the formula :

$$\cancel{E}_T = \sqrt{(\sum_i E_x^i)^2 + (\sum_i E_y^i)^2} \quad (6.5)$$

where $E_{x(y)}^i$ is the energy of the i -th object along the x (y)-axis. In any case, the determination and robust reconstruction of \cancel{E}_T is crucial for many analyses involving measurements of W bosons, top quarks, SUSY etc as these particles are typically decaying into weakly interacting particles. Within the PF algorithm, the \cancel{E}_T is reconstructed by applying an optimal combination of the information of all subdetectors. In order to control the effects of inhomogeneous and non-linear calorimeter response [98], the \cancel{E}_T is corrected based on the corrections applied for jets with $p_T > 10$ GeV (Section 6.5.3) when for instance the jet energy scale corrections are more important than the \cancel{E}_T resolution. The threshold of the 10 GeV on the p_T is applied because the uncertainty on the jet energies for jets with lower values of p_T is so larger that it would introduce the same large uncertainty in the \cancel{E}_T value as well.

Figure 6.12 shows plots from the \cancel{E}_T distribution obtained from $W \rightarrow \mu\nu_\mu$ and $W \rightarrow e\nu_e$ processes reconstructed with the use of the PF algorithm. Here, the \cancel{E}_T is characterised as "genuine" (or "real") since real neutrinos are present in the decay chain. In most of the cases where W -bosons decay leptonically, the \cancel{E}_T distribution resembles that of the p_T of the charged lepton, but its resolution is dominated by the hadronic recoil [130].

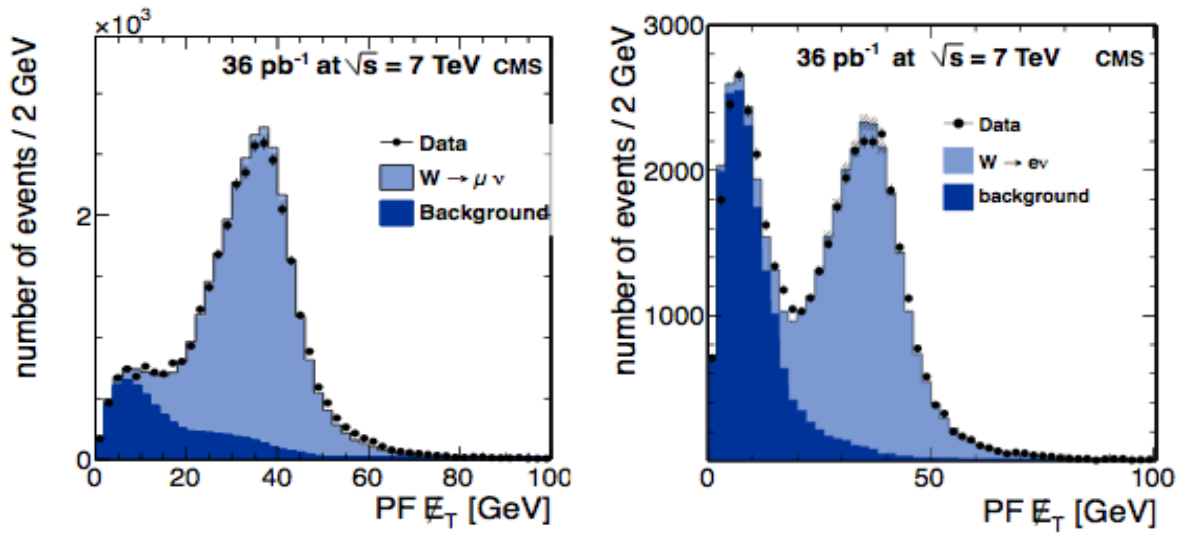


Figure 6.12: The PF E_T distribution for $W \rightarrow \mu \nu_\mu$ (left) and $W \rightarrow e \nu_e$ (right). This E_T is characterised as "genuine" as neutrinos are present in the final state. Data and simulation agree well [130].

You can know the name of a bird in all the languages of the world, but when you're finished, you'll know absolutely nothing whatever about the bird... So let's look at the bird and see what it's doing – that's what counts.

Richard Feynman

CHAPTER 7

DATASETS AND EVENT SELECTION

The generation of the simulated datasets along with the event selection applied on the final reconstructed objects is elaborated in this chapter. First, in Section 7.1 the utilised collision data samples are described, followed by Section 7.2 where the details of the generation and the production for both the background and the signal (direct stop quark pair) processes are outlined. Finally, the baseline selection is discussed in Section 7.3, including the Triggers, as well as the selection of the final state objects used in this thesis namely for the muons, the jets and the \cancel{E}_T . Finally, in Section 7.6 a comparison of the observation versus expectation is discussed including the reconstruction of the $t\bar{t}$ topology.

7.1 Recorded data

Typically in collider experiments like the LHC, data is been taken in different periods, each one having different instantaneous luminosity conditions. However, from the final delivered data, only the fraction that is validated is finally stored for further use. If all sub-detectors are operational and the trigger conditions are met, the run is then tagged as a "good" one and it is officially "certified". Next and depending if the trigger was fired by an event with specific characteristics, this event is selected by the HLT and finally it is saved in a special data stream format. Therefore, a different choice on the event's characteristics implies that a different trigger has to be used, hence resulting to a different data stream. These data streams although are nothing physical, they

practically serve as an efficient way to group triggers for processing and data access at any later time. For instance, a data stream can include events of the *Double-Electron* or *Double-Muon* or *Muon-Electron* type. For this analysis however, the *Single-Muon* data stream was used which includes events with one muon with a p_T above the trigger threshold and within a predefined $|\eta|$ acceptance, while the exact details of the trigger will be discussed in Section 7.3.1.

The aforementioned chain of certification is done centrally by a CMS dedicated team, which is also responsible to provide the official list of "good" runs. The data that the CMS experiment recorded during the 2012 data taking period corresponding to an integrated luminosity of $\sim 19 \text{ fb}^{-1}$ from p - p collisions at centre of mass energy of 8 TeV (C.M.E) is used in this thesis. Table 7.1 summarises the used collision datasets. The luminosity measurement of this dataset has an uncertainty of 4.4% [131].

Single-Muon datasets during the 2012 data-taking period
/SingleMu/Run2012A-13Jul2012-v1/AOD
/SingleMu/Run2012B-13Jul2012-v1/AOD
/SingleMu/Run2012C-PromptReco-v1/AOD
/SingleMu/Run2012C-PromptReco-v2/AOD
/SingleMu/Run2012D-PromptReco-v1/AOD

Table 7.1: Summary of Single-Muon dataset streams utilised for this analysis.

7.2 Generation of simulated datasets

For the generation of the signal simulated datasets, the MadGraph event generator was used exclusively. This was a very challenging task, both on the physics but also on the technical side. The same event generator has been also used for the bulk of the background samples, but MC@NLO and PowHeg have been occasionally used as well.

The choice to use MadGraph as the main event generator was based on its feature to include extra partons to serve as ISR at ME level. But the idea itself behind the requirement of extra ISR is motivated by the need to fully exploit the possibilities where the global jet activity can help increasing the signal selection efficiency. This is more critical the closer we get to the compressed region in the SUSY parameter space, where the already published results have difficulties reaching it [132]. However, having extra ISR is motivated yet for another reason. Assume that a PS generator like Pythia is

used explicitly for the generation of the simulated datasets. Hence, the PS is supposed to cover coherently the whole of the phase space. That means, that the PS should sufficiently describe the ISR effects and the parton splittings, both at the soft and the collinear limits equivalently well. But the PS description can easily be problematic above a certain scale and the PS approach fails where the ME is more appropriate to populate that corner of the phase space. If that scale is pushed to be high enough, this can result to altered and/or downgraded kinematic properties of the ISR-associated partons. This would underestimate the kinematical properties of the event, thus the selection efficiency and sensitivity would be reduced. The solution is to combine both the ME and PS tools while letting each one govern that part of the phase space that they are optimised for.

7.2.1 Generation of SUSY signal simulated datasets

The used workflow for the generation of the signal process according to $p-p \rightarrow \tilde{t}_1 \bar{\tilde{t}}_1$ (direct stop quark pair production) in a SMS framework was :

1. For a particular point of the considered parameter space, the only relevant parameters are the masses of the s-particles. Thus, in order to build a SMS, all squark and chargino masses except those involved in the production and decay of the model in interest, have to be set to high values. Practically, all the rest of the s-particles will have to be decoupled from the particle spectrum, so that only the diagrams relevant to our SMS get generated. In addition, we assign a 100% BR to the decay channel of our choice, that is $\tilde{t}_1 \rightarrow t \tilde{\chi}_1^0$. In this analysis, the $p-p \rightarrow \tilde{t}_1 \bar{\tilde{t}}_1$ with $\tilde{t}_1 \rightarrow t \tilde{\chi}_1^0$ is produced by setting low (accessible) masses for the \tilde{t}_1 and $\tilde{\chi}_1^0$, while all other squark and gluino masses were set to high values.
2. MadGraph was used for the generation of the matrix-element cross section covering the range where $m_{\tilde{t}_1} \in [175, 700]$ GeV and $m_{\tilde{\chi}_1^0} \in [0, m_{\tilde{t}_1} - 100]$ GeV with a step of 25 GeV. In addition, up to two extra partons (N=0,1,2) were generated for each signal sample which play the role of ISR. In our approach, the stop quark pairs were produced always on-shell. In case the stops quarks were produced off-shell, a more careful strategy would be needed, which would take into account effects due to the *narrow-resonant-widths* phenomenology [133].

In general, both the ATLAS and the CMS collaborations use a fixed value to account for the width of the stop quark, namely something like 1 GeV. However, the used value of 1 GeV is too small compared to the mass of the stop

quark ($\Gamma/M \ll 1$), thus there is no need to take into account the phase space-dependence of the width. In any case and just for consistency, we have calculated the width of the $\tilde{t}_1 \rightarrow \mu\nu_\mu\tilde{\chi}_1^0 b$ process for all of the considered points in the $(m_{\tilde{t}_1}, m_{\tilde{\chi}_1^0})$ plane and these are illustrated in Figure 7.1 (left plot). As it will be also discussed in Section 7.5, the selection efficiency of the signal is general small. Thus, we had to generate an abundant number of simulated events, typically some orders of magnitude higher compared to the integrated luminosity of the collision datasets (Figure 7.1, right plot).

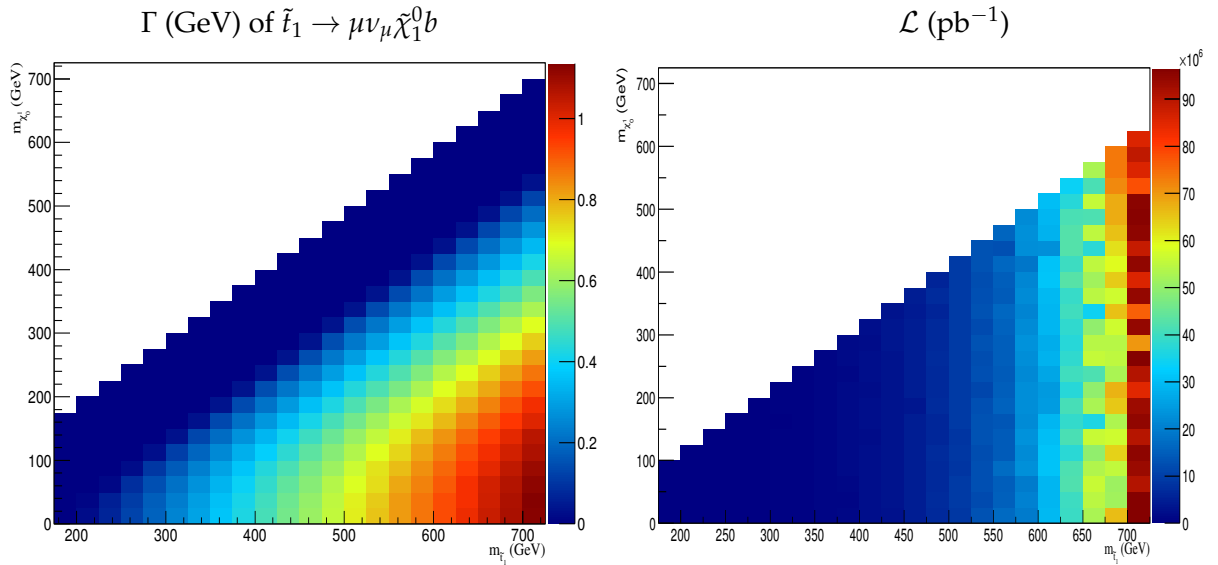


Figure 7.1: The widths (Γ) (GeV) of the $\tilde{t}_1 \rightarrow \mu\nu_\mu\tilde{\chi}_1^0 b$ process with the use of MadGraph (left) and the equivalent luminosity (pb^{-1}) of the generated simulation datasets (right).

3. The distance between the ISR partons is measured in k_T measures. This practically separates the phase space into two regions, one which will have to be described by the PS (low k_T region) and the other which will be described by the ME (high k_T region). The boundary between those regions is oriented by the $Q_{\text{ME}}^{\text{cut}}$ which is coded as xqcut in the MadGraph routine.
4. Since the ME is supposed to populate only the region above the matching scale (Q_{match}) in principle, there is no need to choose $Q_{\text{ME}}^{\text{cut}} \neq Q_{\text{match}}$. Nevertheless, within the k_T -MLM matching scheme, the exact value of Q_{match} must be decided after having taken into account also the FSR effects. Thus, some smearing in the neighbourhood of Q_{match} is expected, shifting a bit its nominal value. That practically means, that if a priori we set $Q_{\text{ME}}^{\text{cut}} = Q_{\text{match}}$, then some peculiar behaviour affecting the physics of the events located near the Q_{match} can be observed. In or-

der to quantify the above, one needs to draw the *Differential Jet Rates* (DJR). More details are discussed in Section 7.2.3.

5. To ensure the smoothest possible transition between the low and the high k_T regions, the emissions from the ME have to be treated as close as possible to the PS ones. For this, the sequence of the various steps of the PS history have to be known. Thus, each vertex has to be reweighed taking into account the corresponding value of k_T as a function of the running α_s coupling i.e. $\alpha_s(k_T)$. This helps to mimic as close as possible what the PS algorithm is doing.
6. The events are then showered with Pythia and one top quark is allowed to decay according to $t \rightarrow \mu\nu_\mu b$ while the other is decaying according to $t \rightarrow q\bar{q}b$.
7. The jet clustering algorithms take charge to cluster the showered partons to form jets.
8. For a given event, if it comes from the highest multiplicity (i.e. the +2 jet subsample), all additional jets not coming from the ME are kept and each ME parton has to be matched with one jet within a distance Q_{match} . If this condition is not satisfied, the event has to be rejected.
9. Events that do not come from the highest multiplicity have to be treated exclusively; this means that each of the jets has to be matched with exactly one parton within a distance Q_{match} .

Specifically for the detector simulation step of the SUSY datasets, the CMS Fast Simulation (FS) software [134] was used. The FS algorithm contains a more simplistic description of the detector's geometry while using parametrized models for its sub-components. For example, the Inner Tracker is simulated by a more simplified tracker geometry after scattering and ionisation effects have been taken into account. In any case, FS routines try to simulate in the most coherent way the various features of the detector. For instance, the cracks between the modules in the HCAL and ECAL, or the electronic noise are simulated as closely as possible to the Full-Simulation but without being so much time consuming. However, some characteristics are ported from studies based on the Full-Sim, for example the energy response of the calorimeters for hadrons. On the same footing, leptons are reconstructed with the help of parametrized functions; for instance, the muons reconstruction is based on a parametrized function obtained from the Full-Simulation performance but incorporated in a more simplified detector geometry. At the end, all reconstructed physics objects must be identical to those derived by the Full-Simulation, within some acceptable discrepancy range.

The use of FS for the SUSY samples was dictated by the need for such a large scale simulated events campaign as in the context of this thesis. This would have been impossible by using Full-Sim, mainly due to the required CPU resources. Indeed, in Fast-Sim, typically it takes about one second for an event to be reconstructed, while the time it needs for a Full-Simulation reconstruction is higher by several orders. Figure 7.2 illustrates a comparison of FS and Full-Sim based on the $t\bar{t}$ simulated events for the \cancel{E}_T , the H_T , the jet multiplicity, the transverse momentum and the η of the isolated muon, the $\Delta\Phi(\cancel{E}_T, \mu)$ and the $\Delta R(\mu, Jet^1)$, where no significant differences are observed.

7.2.2 Generation of background simulated datasets

For the generation of the background simulated samples, similar workflows to the one that was employed for the generation of the simulated signal datasets were used. The following physics processes have been considered for this analysis :

Top quark pair production:

1. For all of the samples of this category, the top quark mass was set to 172.5 GeV with a width of 1.5 GeV while both MC@NLO and MadGraph were used as event generators. In the latter case, up to three extra partons were generated. Also, the next-to-leading-order (NLO) parton density function (PDF) set CTEQ6.6 was used for MC@NLO [135], while the LO PDF set CTEQ6L1 [135] was used for the MadGraph sample.
2. These samples were normalised to NLO cross sections [136, 137].

At the time that this search was performed, there were no available Q^2 and matching scale variations simulated datasets with MC@NLO , thus we had to make use of the MadGraph ones to account for corresponding systematics (Chapter 9). But before mixing datasets from different event generators, we performed several tests in order to assess the level of agreement regarding their physics content to make sure that they don't present strong discrepancies. For this task, we compared the MadGraph versus a MC@NLO and for even more completeness versus a PowHeg $t\bar{t}$ simulated dataset as well, although the last one was utilised no further.

Figure 7.3 shows the comparison for some kinematic and angular variables that rely on the jets, the \cancel{E}_T and the properties of the isolated muon. Although there are some distinct differences between the shapes derived from the MadGraph and the MC@NLO, however there are no strong discrepancies. The MadGraph tends to give a harder spectrum

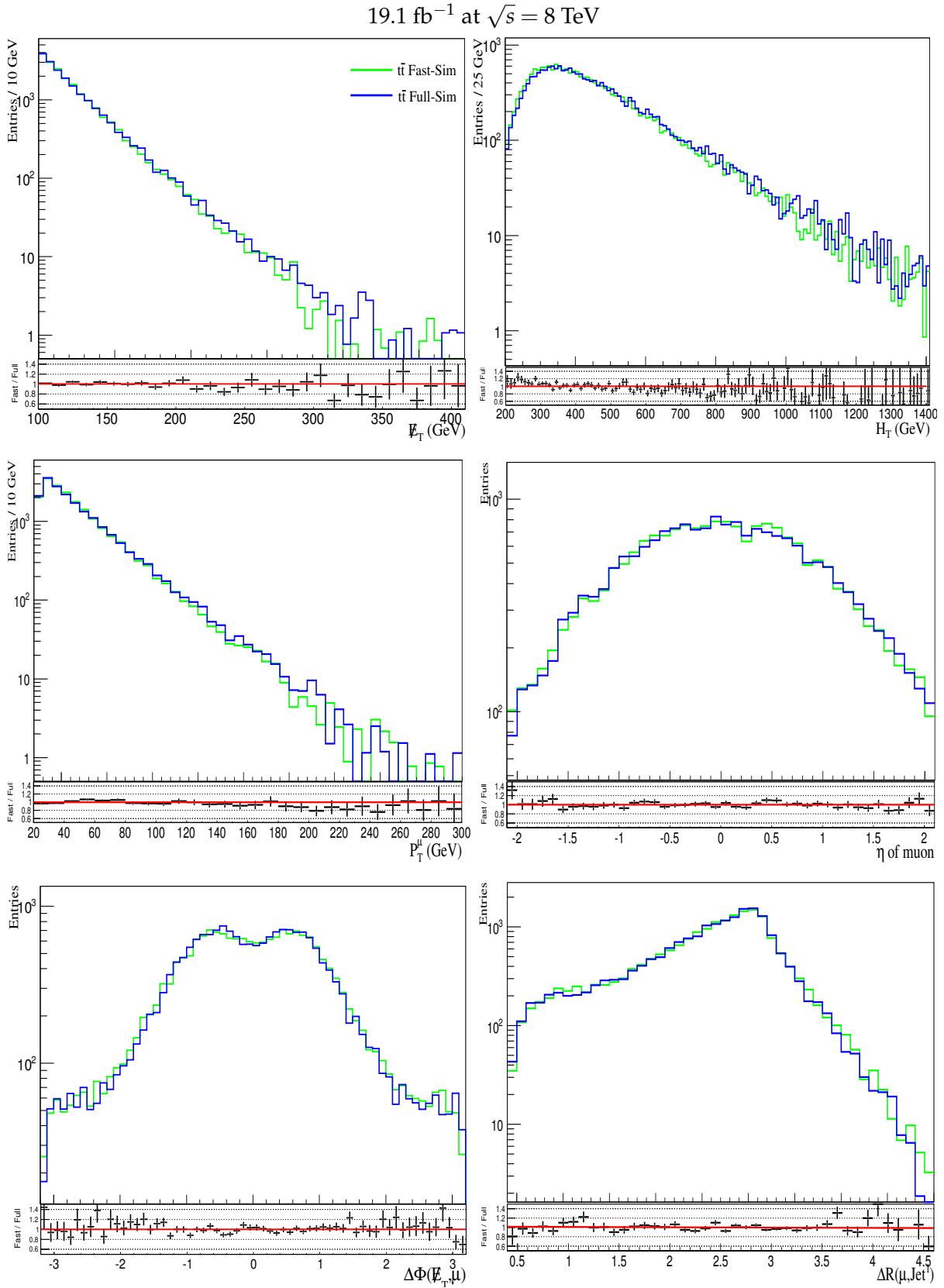


Figure 7.2: Comparison between FS and Full-Sim from the \cancel{E}_T (top row, left plot), the H_T (top row, right plot), the p_T (second row, left plot) and the η of the isolated muon (second row, right plot) the $\Delta\Phi(\cancel{E}_T, \mu)$ (bottom row, left plot) and the (μ, Jet^1) (bottom row, right plot). Two $t\bar{t}$ samples generated with *MadGraph* with up to 3 extra partons were used for this comparison, while the same event selection has been applied to both.

on both the \cancel{E}_T and the transverse momentum of the muon, but this offset is mostly present in the tails where the statistical fluctuations are dominating there, hence making a definite conclusion is hard.

Single-Top quark production:

1. The Single-Top quark datasets were generated with the use of PowHeg event generator with a top quark mass fixed at 173 GeV, while the used PDF set was the MSTW2008 [74]. These samples were normalised to NNLO cross sections [136].

Single-boson ($W, Z/\gamma^* + \text{jets}$) production:

1. This category includes the $W+\text{jets}$ and $Drell\text{-}Yan$ (Z/γ^*) processes, which were produced in association with light and heavy flavour jets with MadGraph. The $W+\text{jets}$ events were produced with up to four extra partons at ME level and only $W \rightarrow \ell\nu_\ell$ final states were considered. These samples have been normalised to NLO using the inclusive $k\text{-factor}$ where possible.
2. Exclusive in jet multiplicity samples were used for the $Z/\gamma^* \rightarrow \ell^+\ell^-$ processes with up to four extra partons. The lower threshold of the invariant mass of the dileptons was set to 50 GeV. For all the above, the used PDF set was the CTEQ6L1 [135]. The Z/γ^* samples were normalised to the next-to-next-to-leading order (NNLO) cross sections computed with FEWZ [138].

Top quark pair + X ($t\bar{t} + X$) production:

Processes like $t\bar{t} + \gamma$ and $t\bar{t} + V$ where V is a vector boson, have been included in this class. MadGraph has been used solely for the generation of these datasets, while the used PDF set was the CTEQ6L1 [135]. These processes have a tiny cross section and their NLO values were obtained with the use of MCFM [139] tool.

Di-boson and Tri-Boson production:

1. This class includes processes like WW, WZ, ZZ and WWW, WWZ, WZZ, ZZZ . All of them were generated with MadGraph (except one, where Pythia was used), while the used PDF set was the CTEQ6L1 [135]. These processes constitute a very small background, thus only those that can result in a final state similar to the one of interest are considered. The normalisation of these samples is based on cross sections determined at LO and in some cases at NLO with the use of MCFM where appropriate.

Finally, all of the background samples were interface to Pythia for the fragmentation

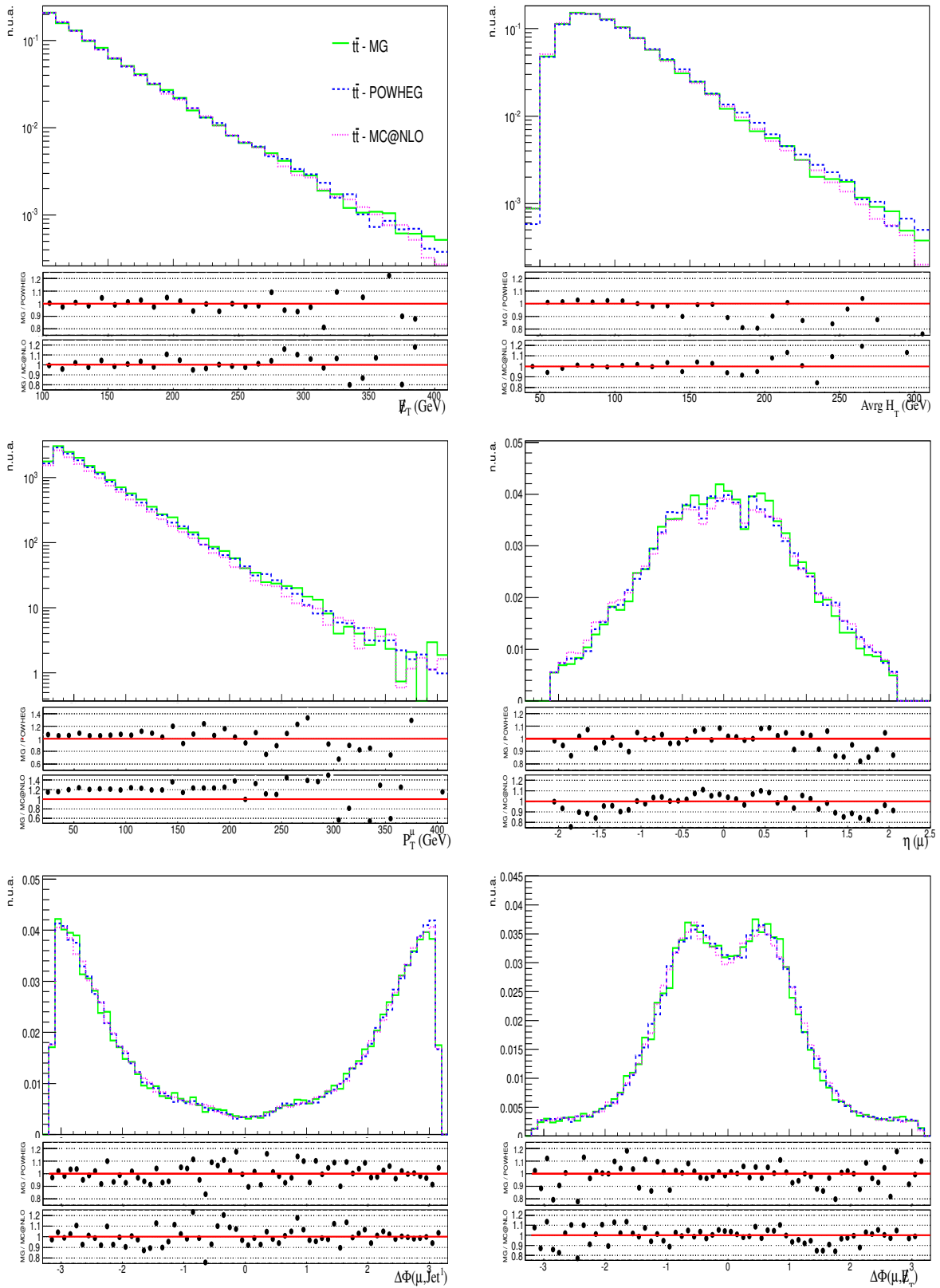
19.1 fb⁻¹ at $\sqrt{s} = 8$ TeV

Figure 7.3: The distributions of the \cancel{E}_T (top row, left plot), the average H_T (top row, right plot), the transverse momentum and the η of the muon (second row) and the $\Delta\Phi$ between the muon and the leading jet (bottom row, left plot) and between the muon and the \cancel{E}_T as well (bottom row, right plot).

and hadronisation steps. In Table 7.2 the used background simulated datasets are summarised.

Physics Process	8TeV σ (pb)	Generator
$t + \text{jets}$		
$t\bar{t} + \text{jets}(0,1,2,3)$	225.2 (NLO)	MadGraph & MC@NLO
$W, Z/\gamma^* + \text{jets}$		
$W+1 \text{ jets} \rightarrow \ell\nu$	6440.4 (NLO)	MadGraph
$W+1 \text{ jets} \rightarrow \ell\nu$	2087.2 (NLO)	MadGraph
$W+3 \text{ jets} \rightarrow \ell\nu$	619. (NLO)	MadGraph
$W+4 \text{ jets} \rightarrow \ell\nu$	255.2 (NLO)	MadGraph
$Z/\gamma^*+1 \text{ jets} \rightarrow \ell^+\ell^-$	5400 (NLO)	MadGraph
$Z/\gamma^*+2 \text{ jets} \rightarrow \ell^+\ell^-$	1750 (NLO)	MadGraph
$Z/\gamma^*+3 \text{ jets} \rightarrow \ell^+\ell^-$	519 (NLO)	MadGraph
$Z/\gamma^*+4 \text{ jets} \rightarrow \ell^+\ell^-$	214 (NLO)	MadGraph
Single-Top		
<i>Single-Top s-channel</i>	3.79 (NNLO)	PowHeg
<i>Single-Top t-channel</i>	56.4 (NNLO)	PowHeg
<i>Single-Top tW-channel</i>	11.1 (NNLO)	PowHeg
<i>Single-\bar{t} s-channel</i>	1.76 (NNLO)	PowHeg
<i>Single-\bar{t} t-channel</i>	30.7 (NNLO)	PowHeg
<i>Single-\bar{t} tW-channel</i>	11.1 (NNLO)	PowHeg
$t\bar{t} + X + \text{jets}$		
$t\bar{t}Z/\gamma^* + \text{jets}$	0.208 (NLO)	MadGraph
$t\bar{t}W + \text{jets}$	0.232 (NLO)	MadGraph
$t\bar{t}\gamma + \text{jets}$	2.166 (NLO)	MadGraph
$t\bar{t}WW + \text{jets}$	0.002037 (NLO)	MadGraph
Di-Bosons + jets		
$ZZ/\gamma^* + \text{jets} \rightarrow 2\ell 2q$	0.91 (LO)	MadGraph
$ZZ/\gamma^* + \text{jets} \rightarrow 2\ell 2\nu$	0.28 (LO)	MadGraph
$WZ/\gamma^* + \text{jets} \rightarrow 3\ell\nu$	0.8674 (LO)	MadGraph
$WZ/\gamma^* + \text{jets} \rightarrow 2\ell 2q$	1.755 (LO)	MadGraph
$WZ/\gamma^* + \text{jets} \rightarrow 2\nu 2q$	0.705 (LO)	MadGraph
$WW + \text{jets} \rightarrow 2\ell 2\nu$	5.8123 (NLO)	MadGraph
Tri-Bosons + jets		
$WWG + \text{jets}$	0.528 (LO)	MadGraph
$WWZ/\gamma^* + \text{jets}$	0.05795 (NLO)	MadGraph
Other		
W^+W^- Double-Scattering	0.5879 (LO)	Pythia

Table 7.2: Summary of the simulated datasets with the cross sections of the processes and the used event generator. Contributions from higher order QCD corrections are included where available.

7.2.3 Variation and control of the matching parameters

It is obvious from the previous discussion that although the matching procedure basically relies on just a couple of parameters, namely the $Q_{\text{ME}}^{\text{cut}}$ and the Q_{match} , one needs to carefully choose the appropriate values of these two. In general, in the context of the k_{T} -MLM algorithm, the Q_{match} is usually larger than the $Q_{\text{ME}}^{\text{cut}}$, while in some cases they can be equal provided that we can avoid or neglect any smearing effects of the PS close to the matching scale. As it has been pointed out previously, the transition between the ME and the PS has to be as smooth as possible, while at the same time the effective cross section has to be stable. But since the Q_{match} is a rather arbitrary quantity and it is not associated with any physical observable, one can easily choose either a too low or a too high value. In the former case, that would result in the ME approach to populate a corner of the phase space where it is not appropriate and thus divergencies may arise in the generation of the ME events. If on the other hand, the Q_{match} is set too high, then the PS will not be able to describe coherently this region of the phase space that should be described by the ME, thus discontinuities may appear, for example "deeps" or "bumps". That is exactly why it is not sufficient to only choose some intuitively "reasonable" values for the $Q_{\text{ME}}^{\text{cut}}$ and the Q_{match} parameters. Instead, we need to rely on some tests to find their optimal values. This can be done in two ways, either by inspecting the stability of the cross section while varying the matching scale, or by drawing the *Differential Jet Rate* (DJR) distributions.

The DJR distributions help to visualise where an event coming from a N jets configuration, passes to a $N-1$ one, while the event is been clustered by the k_{T} algorithm. All showered partons linked with the same showering have to be clustered together within a k_{T} distance, provided that this k_{T} is smaller than the used cut-off value ($Q_{\text{ME}}^{\text{cut}}$). On the other hand, the associated to a different ME parton jets are located away (always measured in k_{T} distance) from the used $Q_{\text{ME}}^{\text{cut}}$. Thus, when a N configuration passes to a $N-1$ configuration, all events with a multiplicity smaller than N are clustered together and have to be settled below the $Q_{\text{ME}}^{\text{cut}}$ value. It follows, that the events with a multiplicity equal or even greater than N will have to lay above the $Q_{\text{ME}}^{\text{cut}}$ as their k_{T} distance is larger than the $Q_{\text{ME}}^{\text{cut}}$.

However, in the used k_{T} -MLM scheme there must be a sharp and distinct border line in the DJR plot between the ME and the PS regions. This would help to quantify at which level the transition is indeed smooth. Thus, the choice of the optimal values of the $Q_{\text{ME}}^{\text{cut}}$ and of the Q_{match} scales is mostly based on the smoothness of the DJR distributions spanning across the matching scale. Since the idea of having extra ISR in

the simulated samples is to have the most correct possible description of the ISR while benefiting from the presence of hard jet spectra, it is desirable to choose the matching scale as lower as possible while the DJR remains smooth in order to ensure that we don't spoil the soft-collinear description given by the PS. That practically means that we allow the ME to populate as much as possible of the phase space as possible.

Figure 7.4 illustrates the DJR plots for the $2 \rightarrow 1$ and $1 \rightarrow 0$ cases for the direct stop quark pair production while also the contributions from the different multiplicity samples are shown separately. The higher multiplicity considered in this case was 2, as the higher order transitions down to $3 \rightarrow 2$ (included) are given from the PS. Also, we need to note that as the region below the matching scale is dominated by the PS, consequently it also edicts the shape of the curve there. As expected, above the matching scale, it is the ME that dictates the shape. Having performed this study systematically for many points, the matching scale was set to 44 (46) GeV for $m_{\tilde{t}_1} < (>) 500$ GeV. Table 7.3 summarises the $Q_{\text{ME}}^{\text{cut}}$ and Q_{match} that were chosen for the signal samples. As a comparison, we quote the $Q_{\text{ME}}^{\text{cut}}$ value for the MadGraph $t\bar{t}$ simulated datasets which was 20 GeV, while its Q_{match} value was 40 GeV.

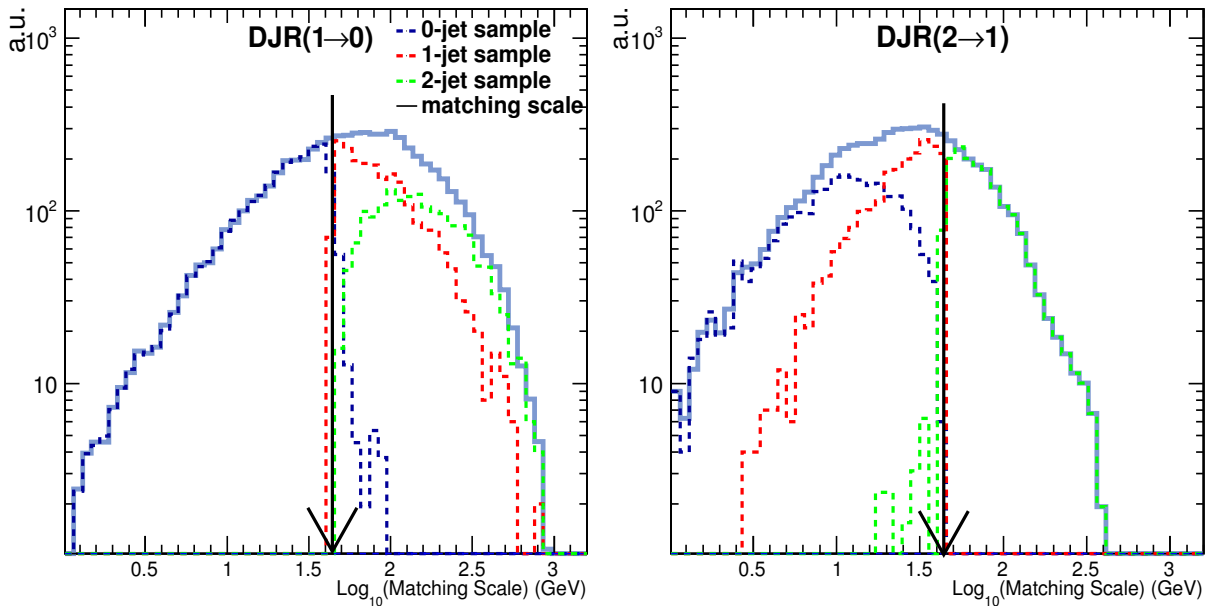


Figure 7.4: The differential jet distribution for the $2 \rightarrow 1$ and $1 \rightarrow 0$ configuration with the individual contribution from the different multiplicities for the T2tt model. Higher order transitions such as $3 \rightarrow 2$ will be given by the PS. Based on these plots, the Q_{match} was set to 44 (46) GeV for $m_{\tilde{t}_1} < (>) 500$ GeV.

$Q_{\text{ME}}^{\text{cut}}$ (GeV)	Q_{match} (GeV)	Mass range
30	44	$m_{\tilde{t}_1} < 500 \text{ GeV}$
30	46	$m_{\tilde{t}_1} > 500 \text{ GeV}$

Table 7.3: Summary of $Q_{\text{ME}}^{\text{cut}}$ and Q_{match} that were used for the signal MC datasets.

7.2.4 Parton Showering and hadronization

The generated signal samples have been interfaced to Pythia for the Parton Showering, the hadronization and the matching processes. Within Pythia the hadronization is simulated using the Lund string model [140]. The used parameters for hadronization with the use of the Z2* tune [92] are listed in Appendix A.

7.3 Selection of the event topology

In this section we discuss the selection of events. The final state considered in this analysis is a single isolated μ with the presence of jets and \cancel{E}_T .

In the case of our signal's topology, i.e. direct stop quark pair production, this final state is realised from the 2-body decay of the stop quark :

$$pp \rightarrow \tilde{t}_1 \bar{\tilde{t}}_1, \text{ with } \tilde{t}_1 \bar{\tilde{t}}_1 \rightarrow t\bar{t} + 2 \tilde{\chi}_1^0 \quad (7.1)$$

while the top quark pair can decay according to $t\bar{t} \rightarrow bW\bar{b}W \rightarrow b\bar{b} q\bar{q} \mu\nu_\ell$. Thus, at least four jets are expected in the final state with two of them being b -jets, along with an isolated muon, while \cancel{E}_T must be present due to the neutrinos and the neutralinos that escape direct detection. The most important background source is the SM $t\bar{t}$ process while following a semi-muonic decay path, thus giving a similar experimental signature like that of signal. For reasons that will be explained later on, we require the muon to have a $p_T > 25 \text{ GeV}$ while the selected event must have at least four jets with $p_T > 40 \text{ GeV}$ each, while at least one of them has to be identified as a b -jet. To suppress the background contributions, we also require the \cancel{E}_T to be above 100 GeV and the scalar sum of the p_T of all jets to be above 200 GeV.

7.3.1 Trigger

Since initially the main background comes from multi-jets plus \cancel{E}_T final states, we begin with the selection of the isolated muon in the trigger. In order to collect only the events of interest, a single isolated muon is required to be above a certain p_T threshold, so to "fire" the trigger. Furthermore and in order to ensure high efficiency of the selected events, the applied thresholds at analysis level (i.e. offline selection) must be tighter than the ones used while collecting data (i.e. online selection). In general, the trigger has to be a non pre-scaled one. As it was already mentioned, data was taken in different periods, where the conditions and the exact trigger p_T thresholds varied. For higher values of the instantaneous luminosity, the online p_T thresholds have to be raised typically by a few GeV in order to keep the output rate under control. Also, as in the beginning of each of the data taking periods the conditions and triggers are not fully optimised, a trigger path is updated regularly resulting into several different versions of the same menu for this period. The trigger path that was used is summarised in Table 7.4.

Trigger for 8 TeV - $\mu+$ jets				
Run Range	p_T (GeV)	$ \eta $	Trigger	Effective $\mathcal{L}(\text{pb}^{-1})$
190738 - 208686	≥ 24	< 2.1	HLT_IsoMu24_eta2p1	19125

Table 7.4: The trigger that was used in both collision and simulated datasets.

7.3.1.1 Turn-on curves

The performance and understanding of the online trigger is essential to ensure a high efficiency while applying certain offline selection cuts. Its performance is evaluated with the *Tag-and-Probe* method [141] which is based on the reconstruction of a resonance, like J/Ψ or $Z \rightarrow \mu^- \mu^+$. The underlying idea is that one of the muons that passes some tight isolation criteria is labeled as the "tag muon". Usually, these "tight" conditions are sufficient to ensure very small fake rates ($< 1\%$). All other muons passing some looser selection criteria form the collection of "probe muons" (N_{all_probes}). Next, the tag and probe muons are paired to reconstruct the invariant mass of the resonance. The efficiency is the number of matching probes (N_{probe}) passing the trigger selection criteria divided by the total number of all matching probes (N_{all_probes}) that were used to reconstruct the resonance :

$$\epsilon = \frac{N_{probe}}{N_{all_probes}} \quad (7.2)$$

This efficiency is evaluated for different transverse momentum of the probe muon. At the end, in order to obtain the p_T dependence, a fit is applied which has a Gaussian-like shape around the trigger threshold region and then once the maximum efficiency is reached it has a flat-shape ("plateau"). This is usually obtained from a Gaussian convoluted with a step function :

$$\epsilon_{Trig} = A + \frac{B - A}{2} \left(1 + \operatorname{erf} \left(\frac{x - \mu}{\sqrt{2}\sigma} \right) \right) \quad (7.3)$$

Where A stands for the low efficiency before reaching the threshold and B denotes the plateau i.e. the high efficiency region after having passed the threshold. Also σ stands for the width of the turn-on curve and μ stands for the turn-on threshold i.e. the value where the trigger reaches 50% of its efficiency. The measured efficiency is usually plotted as a function of the p_T or the η . The efficiency of the $HLT_IsoMu24_eta2p1$ trigger obtained from RunA and RunB periods is illustrated in Figure 7.5. On top, the official recommendations were followed to ensure that the off-line threshold is well above the L1 (online) threshold, just to secure that we are on the high efficiency region of the turn-on curve.

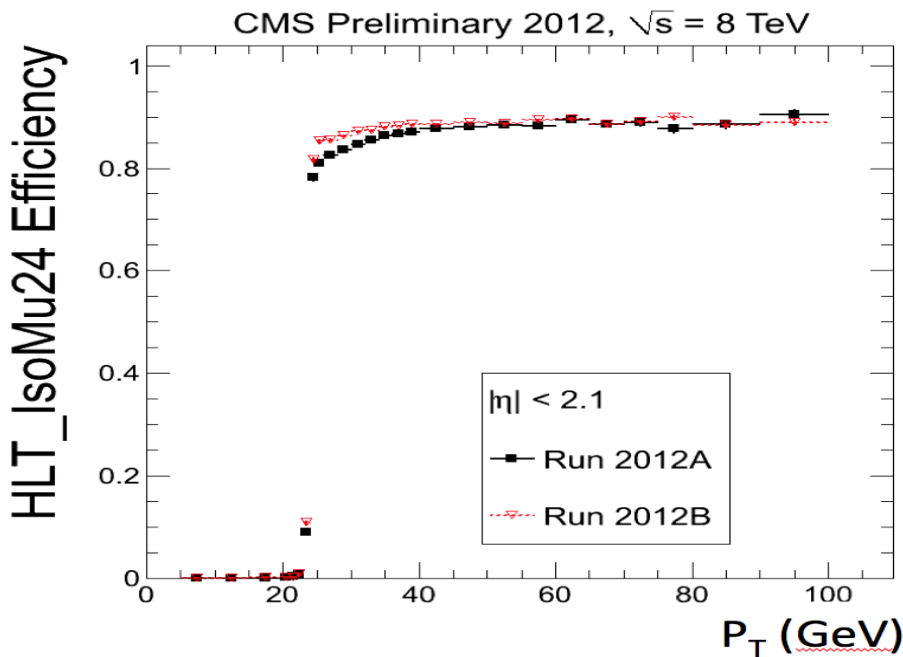


Figure 7.5: Efficiency of the $IsoMu24_eta2p1$ trigger path which was used for the $\mu+$ jets channel during the RunA and RunB data-taking periods of 2012. The curve corresponding to "RunB" shows a higher efficiency and even a sharper turn-on, due to PU corrections which were introduced for the lepton isolation.

7.3.2 Event cleaning

Only events passing the trigger selection are used, but three additional conditions serving as "cleaning" filters have to be fulfilled as well. The first filter aims to remove events that were recorded but have many reconstructed tracks with a very low purity; this is caused by the background noise from the beam (*beam scrapping events*). The second filter requires the presence of a *Primary Vertex* passing certain quality criteria. The last filter rejects events that are associated to noise from the HCAL caused by instrumentation failures.

7.3.3 Event selection criteria

In this section we discuss the selection based on all final state objects expected in events with stop quark pairs decaying according to $\tilde{t}_1\tilde{t}_1 \rightarrow b\bar{b} \mu\nu_\mu q\bar{q} \tilde{\chi}_1^0 \tilde{\chi}_1^0$.

All of the event datasets, both collision and simulation, are skimmed (preselection) by requiring at least 3 jets after having applied the L2L3 corrections with a $p_T^{\text{L2L3}} > 25$ GeV within the tracker acceptance ($|\eta| < 2.4$). In addition, at least one muon is required with $p_T > 20$ GeV and should have been reconstructed within the muon system offline acceptance ($|\eta| < 2.4$). At this point, the size of the datasets is reduced significantly becoming more manageable. All of the reconstruction objects are based on the PF event reconstruction algorithm.

More details of the selection of the final state objects are given in the corresponding sections for the muon selection (7.3.4), the jets, the E_T , the H_T selection (7.3.5) and finally the b-tagging requirement (7.3.6).

7.3.4 Muon selection

The collection of reconstructed muons is made from PF global muon candidates which must not to be clustered into a jet. A "global" muon is one that has been reconstructed using information from the Inner Tracker and the Muon System. In addition, some looser requirements were used to veto the second lepton.

1. **Trigger.** As it has been elaborated in Section 7.3.1, all muon candidates must satisfy the online trigger p_T threshold which is 24 GeV within the pseudo-rapidity region $|\eta| < 2.1$. As it can be seen in Figure 7.5, the efficiency of the trigger is

increasing radically by slightly increasing the transverse momentum threshold from 24 to 25 GeV. Hence this is our requirement for the offline selection as well.

2. *One isolated muon.* In most analyses, it is very crucial to properly isolate and identify leptons. These leptons can be associated either with the hard scattering of the event, or even with the hadronization process. Thus, and in order to ensure the robustness of the physics objects, it is important to distinguish and differentiate those isolated and interesting leptons from the rest. Furthermore, the lepton isolation has been proven powerful to discriminate against QCD background. For this, usually one has to monitor the activity in the neighbourhood of the lepton and after applying certain quality cuts that lepton can be tagged as isolated or not. However, in the case that more than one isolated muon is selected in the event, the one with the highest transverse momentum is kept.

Further and to ensure the selection of qualitative tracks, a minimal number of silicon tracker hits associated with the global muon ($N_{trkhits} > 5$) is required, while the transverse impact parameter of the muon track with respect to the beam spot ($|d_0, pv|$) has to be < 0.2 cm. In addition, in order to enhance the purity of the prompt muons, the global track fit is required to have $\chi^2/\text{n.d.o.f} < 10$ (combination of tracker and muon detector hits) with at least one hit in the muon detector. The muons that pass these quality cuts are characterised as *high-purity muons*.

Briefly, this begins by considering a cone of opening angle $\Delta R = \sqrt{(\Delta\eta)^2 + (\Delta\phi)^2}$ around the direction of the lepton starting from the PV. Then, a veto cone is built around the direction of the lepton projected at the surface of the calorimeters. Depending which sub-detector is considered, a TK/ECAL/HCAL isolation cone is constructed relative to the p_T of the muon. In order to optimise the muon isolation efficiency, all deposits from the lepton within that cone have to be removed. In other words, the relative TK/ECAL/HCAL isolation cone equals the sum of energy deposits above a certain threshold in a cone of radius ΔR and around the lepton found in the sub-detectors under question. The opening angle of the isolation cone that was used was $\Delta R < 0.4$, while the opening angle of the veto cone was taken to be $\Delta R < 0.1$. A graphical illustration of the isolation is shown in Figure 7.6.

The isolation cone could be defined by incorporating the reconstructed objects while the kinematic properties of the identified and reconstructed charged and neutral hadrons and photons are used. The isolation can be then expressed as :

$$Iso_{rel}^{\mu} = \frac{\sum p_T^{\text{photons}} + \sum p_T^{\text{neutral_hadrons}} + \sum p_T^{\text{charged_hadrons}}}{p_T^{\mu}} \quad (7.4)$$

However, this particle based isolation is sensitive to PU, as the photons and the neutral hadrons are mostly affected due to the fact that they cannot be matched to the PV, in contrast with the charged hadrons. Hence, the PU contribution has to be removed from the relative cone.

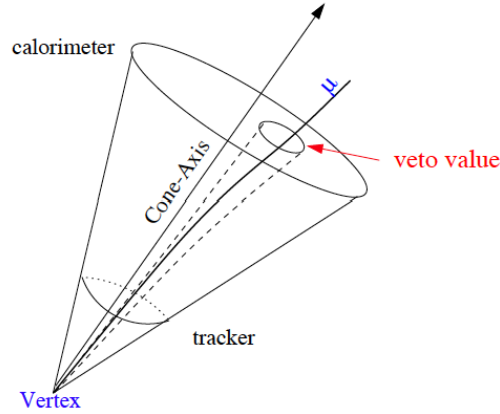


Figure 7.6: Illustration of the isolation cone around a muon and the veto cone used to subtract the contribution of the muon itself.

3. **Veto on a 2nd lepton.** A veto is applied on the presence of a second isolated lepton. This is necessary since there are some processes where more than one isolated leptons are expected, like in the case of the $(Z/\gamma^* \rightarrow \mu\mu)$, or the di-leptonic decay of a $t\bar{t}$ event. By applying this veto the number of these background processes is reduced significantly.

The requirements for the isolated muon as well as those for the veto on the second lepton requirements are summarised in Table 7.5.

7.3.5 Jets and E_T selection

Both the considered signal topology and at least the most important background sources are characterised by the presence of high jet activity which can be attributed mainly to

Observable	Isolated Muon	Loose Muon	Loose Electron
p_T (GeV)	> 25	> 24	> 20
$ \eta $	< 2.1	< 2.3	< 2.5
$\chi^2/\text{n.d.o.f.}$	< 10	-	-
$\Delta R(\ell, \text{jet})$	> 0.3	-	-
Silicon layers	> 5	-	-
Valid Hits in the Pixel	> 0	-	-
Matched muon station	> 1	-	-
$ d_{0,pv} $ (cm)	< 0.2	-	< 0.04
$ d_{z,pv} $ (cm)	< 0.5	-	< 0.2
Iso_{rel}	< 0.12	< 0.2	< 0.2
$\sigma_{i\eta i\eta}$ (Barrel/Endcap)	-	-	$< 0.01/0.03$
$\Delta\phi_{In}$ (Barrel/Endcap)	-	-	$< 0.8/0.7$
$\Delta\eta_{In}$ (Barrel/Endcap)	-	-	$< 0.007/0.01$
H/E (B/E)	-	-	< 0.15

Table 7.5: The muon selection requirements used in this analysis. The $|d_{0,pv}|$ ($|d_{z,pv}|$) refers to the transverse (longitudinal) IP of the muon with respect to the Primary Vertex (PV).

the ISR and the FSR. On top, since neutrinos and neutralinos escape direct detection, the experimental signature of the stop quark pair process includes \cancel{E}_T . Therefore, it is necessary to pose additional cuts on both the jets global activity and the \cancel{E}_T in order to suppress the background contribution.

Jets were reconstructed with the anti- k_T [142] clustering algorithm within a cone of radius $R = 0.5$. Next, they get corrected for the different energy response in pseudorapidity and transverse momentum by applying the L2L3 corrections. On top, the residual correction need to be applied in order to correct for the jet energy scale (JES) difference that is observed between the collision data and the Monte Carlo simulation. Nevertheless, there are also other factors, like the UE, the amount of PU collisions or the electronic noise that in total have a non-negligible impact on the reconstructed energy of the jets. To balance this, an offset L1FastJet correction is applied, both on collision data and simulation that is obtained using the Jet Area Method [143]. A more detailed description was discussed in Section 6.5.3 while the exact details of the jets selection are provided in Table 7.6.

But since there is the possibility that leptons can be reconstructed as PF jets, thus, it is required that the jet collection has to pass a cleaning procedure. If a jet is matched with

one of the isolated muons better than $R < 0.3$ the jet has to be removed. Furthermore, in order to reduce the fake jet rate due to detector noise, a loose identification criterion is required as well.

Also, the scalar sum of the transverse momentum of the jets in the event, denoted by H_T , must be larger than 200 GeV. Finally, the \cancel{E}_T must be above 100 GeV. These cuts are used to suppress the contributions from electroweak and QCD processes.

Observable	Value or Range
p_T	> 40 GeV
$ \eta $	< 2.4
Charged hadron fraction of the jet	> 0
Neutral hadron fraction of the jet should	< 1
Charged multiplicity of the jet	> 0
Charged electromagnetic fraction of the jet	< 1
Neutral electromagnetic fraction of the jet	< 1
Id	Loose
$\Delta R(\ell, \text{jet})$	> 0.3

Table 7.6: The applied jets selection requirements

7.3.6 Applying b-tagging in the event selection

As contributions from the background processes need to be suppressed as much as possible, b-tag requirements are also applied. In CMS several algorithms have been developed. As it was elaborated in Section 6.5.4, the idea is to exploit the intrinsic properties of b quarks and/or various kinematic properties related to its high mass. The result of these algorithms is a discriminator ("b-tag discriminator") for each jet, on which cuts are applied (looser or tighter) in order to distinguish b -jets from non b -jets. For this analysis, the *Combined Secondary Vertex* (CSV) algorithm was used at the medium working point while requiring at least 1 b-tagged jet in the event.

7.4 Corrections to simulated datasets

The simulated datasets present some discrepancies when compared to data. This happens as some effects appearing in a recorded collision dataset have not been incor-

porated within the simulation ones. For example, the number of PU events, the implementation of the trigger menus or even the JEC/JER corrections, are not always modelled in the same fashion in the simulated datasets compared to what exists in the collision samples. In order to correct for these effects, it is customary that some scale factors (SF) are applied on the simulated events. In this section, we present the different SF categories used for this analysis.

7.4.1 PU treatment

The simulated datasets used for the analysis have been generated with a distribution mimicking the real number of PU interactions expected during the data-taking. Although PU itself cannot be directly measured, however it can be linked with some other directly measurable quantities. As PU comes from additional p - p interactions, the number of PV can thus be correlated directly to the amount of PU. It follows, that the higher the PV multiplicity, the more PU attributed energy to the jets. The total offset for the event is equal to the average energy from a non-hard-scatter PV times the number of observed primary vertices (N_{PV}).

In order to properly accommodate PU in the simulated datasets, a reweighting is applied which takes into account the differences in the number of PU interactions from simulation versus data. A set of weights w_i is derived on a bin-by-bin basis:

$$w_i = \frac{N_i^{Data}}{N_i^{MC}} \quad (7.5)$$

where N_i^{Data} stands for the number of events having i PU interactions from data, while N_i^{MC} is the corresponding yield obtained from simulation. Figure 7.7 shows the distribution of the number of Primary Vertices after applying the reweighting on the simulated datasets compared to the PV distribution observed in data.

7.4.2 Jet Energy Resolution (JER)

Measurements reveal that the jet energy resolution (JER) in the collected data is worse than in the simulation in a non negligible way [143]. To correct this peculiar behaviour, SF have been obtained which are applied on the simulated events. A selected jet is matched to the GenJet collection and the difference of their p_T is multiplied by the SF and the result is propagated back to the four-vector of the PF jet. Table 7.7 quotes

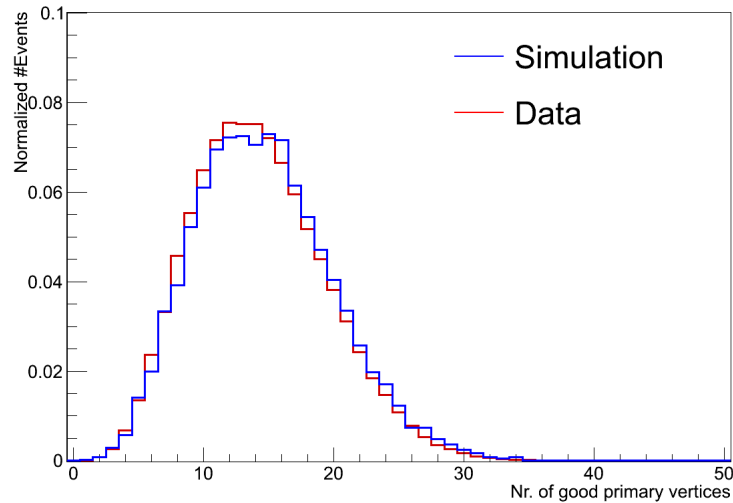


Figure 7.7: The number of Primary Vertices on simulation after applying the reweighting factors compared to the observed distribution from Single- μ datasets corresponding to 19.1 fb^{-1} of integrated luminosity.

the utilised JER scale factors, recommended by the CMS collaboration for use with the 2012 collision datasets.

$ \eta $	JER scale factor
0.0-0.5	1.052
0.5-1.1	1.057
1.1-1.7	1.096
1.7-2.3	1.134
2.3-5.0	1.288

Table 7.7: The scale factors that were utilised to account for the Jet Energy Resolution differences.

7.4.3 B-tagging scale factors

Like in the case of JER, also the b-tagging algorithms perform slightly different in simulation compared to collision datasets. To correct this, SF for the different sub-categories of the jets (i.e. b -like jets, c -like jets and light i.e. when the flavour of the jet is a u, s, c, d quark), are applied to reconstructed jets in the simulated datasets [144].

As it was explained in Chapter 6, for each b-tagging algorithm, each working point has a certain mis-tag rate. Also, the efficiency of the b-tagging algorithm accounts for

the ratio of identifying a b -jet correctly. This efficiency is determined by counting the number of b -tagged jets in a sample of true b -jets. The mis-tag rate is obtained with a similar procedure by counting the jets that were mis-identified as b -jets divided by the total number of jets. At the end, a SF is applied which corrects for this efficiency. The applied SF cover the p_T range between 20 and 800 GeV and $|\eta| < 2.4$ with some uncertainty. For values of the transverse momentum outside these boundaries i.e. when $p_T > (<)800$ (20) GeV the uncertainty is doubled. Also, for the signal simulated datasets the uncertainty was doubled independent of the p_T, η in order to have a more conservative approach to account for any possible discrepancies between FS and Full-Sim detector simulation.

7.4.4 Lepton scale factors

Since the trigger paths are not exactly the same between the collision and simulated datasets, we need to correct for the discrepancies appearing due to the different implementation of the same trigger menus in the simulation compared to data. Practically, that means that the trigger will differ while comparing the performance between simulation and data. Thus, in order to accommodate these effects, the offline isolated selected muon has to be matched to the corresponding trigger object in the offline selection. The obtained SFs are applied in bins of η . In general, those SF are not varied too much with respect to the p_T , thus binning on the p_T is not necessary. In general, this is considered to have a small effect but not negligible.

7.5 Efficiency and event yields

Table 7.8 lists the event yields and selection cut efficiencies for the used datasets. Similarly, Table 7.9 lists the relative acceptance efficiencies using always the preselected samples as the point of reference. This is why the preselected datasets start with an efficiency equal to unity.

1. The trigger requirement reduces the accepted events by around 50% for all except the QCD process where as expected the trigger efficiency is even lower (13%) relative to the preselected datasets efficiency.
2. The requirement for a *Good PV* practically leaves unchanged the event yields since all "triggered" events have well reconstructed PVs.

3. Requiring exactly one isolated muon reduces the amount of $t\bar{t}$ and Single-Top processes by 8-9% more, but it has a larger effect on the rest of the processes.
4. The requirement of events with at least four jets with $p_T > 40$ GeV further reduces the background efficiency by more than 20% for the $t\bar{t}$ and by an extra 27% for the Single-Top events. For the W+ jets the extra reduction is 28% and around 15% for the Z/γ^* + jets and the Rare processes respectively, while the QCD is further suppressed by an order of magnitude.
5. After applying the \cancel{E}_T , the H_T and the b-tag requirements, the final selection efficiency is around 3% for the $t\bar{t}$ and the Single-Top processes and 1 (0.4)% for the W (Z/γ^*)+ jets on absolute differences compared to the initial events present in the preselected datasets, whereas the QCD is practically vanished. This reveals the importance of the H_T and the \cancel{E}_T cuts for this analysis in order to control the contributions from the QCD.

The total selection efficiency for the data Single- μ stream is around 0.6%. In total, the final event yields between simulation and collision datasets agree within statistical uncertainties.

Cut/Dataset	$t\bar{t}$	Single-Top	W+ jets	Z/γ^* + jets	QCD	Other	Total Bkg	Data
triggered	233515	19853.1	341976.7	312234.1	344290	6296.4	1.258165 M	2.23324 M
Good PV	233515	19853.1	341976.7	312234.1	344290	6296.4	1.258165 M	2.23324 M
1 Isolated μ	198642	16277.6	251628.6	195965.6	9058.2	4941.8	676513.9	1.79449 M
Veto on 2nd μ	196489	16198.9	251610.3	138206.9	9052.4	4609.8	616167.3	1.71415 M
Veto on e	188217	15908.5	250966.8	136903.7	9043.9	4250.8	607485.7	1.6817 M
≥ 4 Jets ($p_T > 40$ GeV)	85469.2	5100.7	39305.2	36990.5	1310.9	2324.5	170500	156057
$H_T \geq 200$ GeV	84401.1	5037.2	38607.9	36240.5	1310.9	2312.6	167910.2	153616
$\cancel{E}_T \geq 100$ GeV	15460.3	1106.8	6913.6	2430.5	0.91	609.04	26521.2	25187
≥ 1 b-Jets (CSV-M)	13211.2 \pm 39.8	892.2 \pm 18.4	929 \pm 18.7	396 \pm 16.2	0.4 \pm 0.3	458.2 \pm 13.1	15886.8 \pm 49.4	15925

Table 7.8: Event yields for the μ + jets channel for $\mathcal{L} = 19125.2$ pb^{-1} at $\sqrt{s} = 8$ TeV.

For the signal simulated datasets, the exact same selection cuts have been applied like for the background simulated datasets. On average and when $m_{\tilde{t}_1} - m_{\tilde{\chi}_1^0} \geq m_t$ the total selection efficiency is around 7%. However, the selection efficiency is reduced the smaller the $\Delta m = m_{\tilde{t}_1} - m_{\tilde{\chi}_1^0}$ is, meaning the "deeper" we go into the compressed region which starts once the condition $m_{\tilde{t}_1} - m_{\tilde{\chi}_1^0} < m_t$ is true. The minimum efficiency is in the region where $m_{\tilde{t}_1} - m_{\tilde{\chi}_1^0} < 125$ GeV and is below 0.02%. This is a characteristic of this peculiar corner of the phase space and the selection efficiency is typically too small

Cut/Dataset	$t\bar{t}$	Single-Top	W+ jets	Z/ γ^* + jets	QCD	Other	Data
preselected	1	1	1	1	1	1	1
triggered	0.52	0.50	0.44	0.39	0.13	0.50	0.85
Good PV	0.52	0.50	0.44	0.39	0.13	0.50	0.85
1 Isolated μ	0.44	0.41	0.32	0.24	0.003	0.40	0.68
Veto on 2nd μ	0.43	0.41	0.32	0.17	0.003	0.37	0.65
Veto on e	0.42	0.40	0.32	0.17	0.003	0.34	0.65
≥ 4 jets ($p_T > 40\text{GeV}$)	0.19	0.13	0.05	0.04	0.0004	0.19	0.06
$H_T \geq 200\text{ GeV}$	0.19	0.13	0.049	0.04	0.0004	0.18	0.06
$\cancel{E}_T \geq 100\text{ GeV}$	0.03	0.03	0.009	0.003	$3.5 \cdot 10^{-7}$	0.05	0.01
≥ 1 b-jets (CSV-M)	0.03	0.02	0.001	$4 \cdot 10^{-3}$	$1.5 \cdot 10^{-7}$	0.04	0.006

Table 7.9: The cut efficiencies (relative to the preselected datasets) obtained after applying sequentially the different selection cuts, for both the background and the collision event datasets used in this analysis.

to have any sensitivity there. In our analysis however, as it will also be demonstrated later on, we have sensitivity to this region compared to other similar searches (Chapter 11) and this is partially attributed to the size of the expected signal cross section.

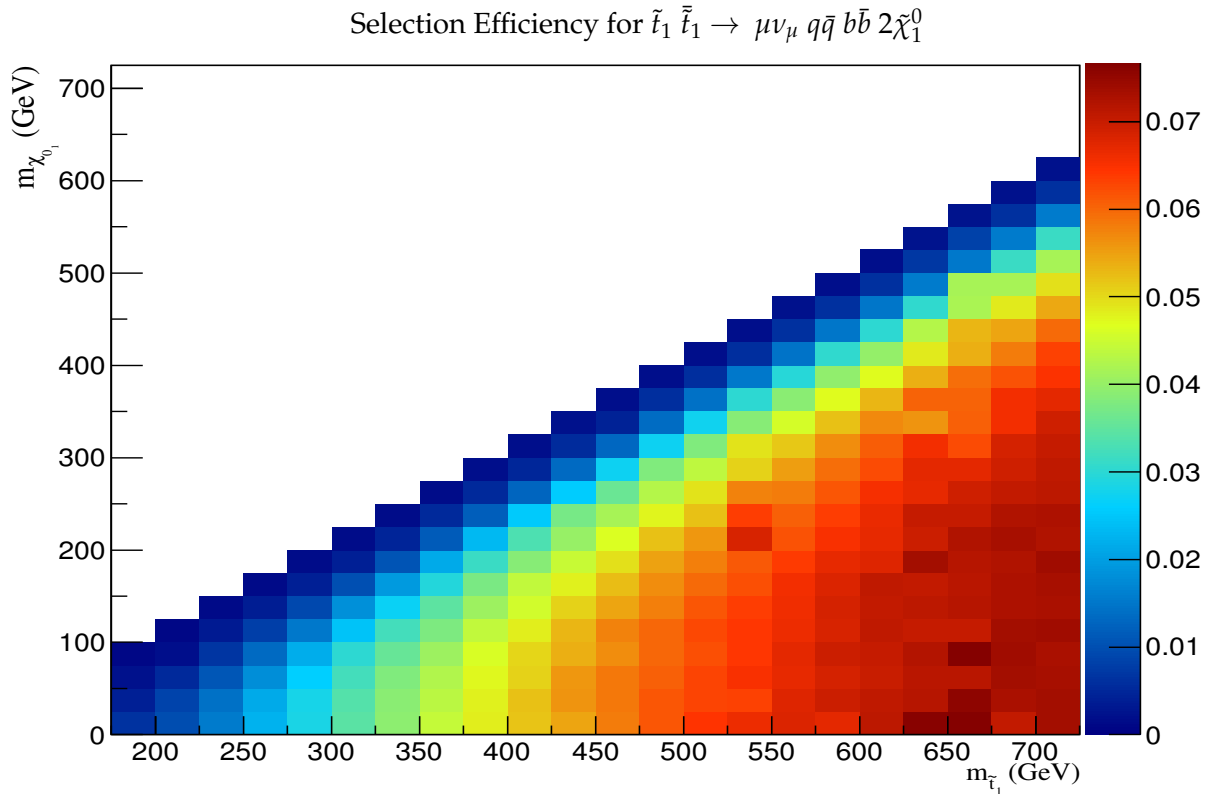


Figure 7.8: The selection efficiency of the signal for each point in the $(m_{\tilde{t}_1}, m_{\tilde{\chi}_1^0})$ plane.

7.6 Comparison of data with expectation

After applying all of the selection cuts, the number of expected events is 15886.8 ± 49.4 while we had 15925 observed events. In Figure 7.9 the comparison of data versus expectation of the transverse momentum of the isolated muon and of the $\Delta\Phi$ between the selected muon and the \cancel{E}_T is illustrated. Similarly, Figure 7.10 shows the \cancel{E}_T , the p_T of the leading jet, the multiplicity of jets, the H_T , the sum of the $\Delta\Phi(\mu, Jet^1)$ and of the $\Delta\Phi(\mu, Jet^2)$ and the transverse mass of the W-boson as well. Finally, Figure 7.11 shows the comparison of the multiplicity of the b-tagged jets and the distribution of the "W-Hadronic Decays CSV discriminator", meaning the CSV discriminator value of the b-jet from the top quark decay for which the subsequent W-boson decays into quarks.

We observe that for low values of the transverse momentum of the muon and of the H_T spectrum, data slightly overshoots simulation, but in general the agreement is good. Similarly there are small discrepancies on the multiplicity of the jets and the b-tagged jets. The same conclusion holds for the rest of the monitored variables as well.

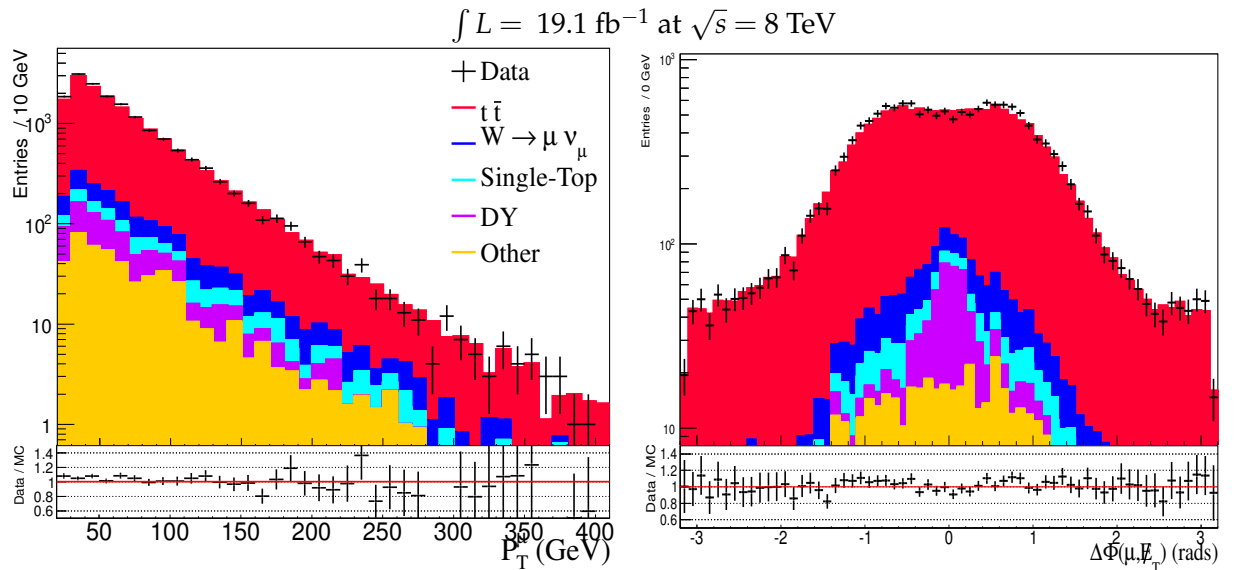


Figure 7.9: Comparison of data versus expectation of the p_T of the isolated muon (left) and the $\Delta\Phi$ between the muon and the \cancel{E}_T (right) after the baseline selection.

7.6.1 Reconstruction of the top quark pair event topology

Up to this point, we have discussed the various applied kinematic event selection criteria which have been used for the simulation, the signal and the collision datasets. The

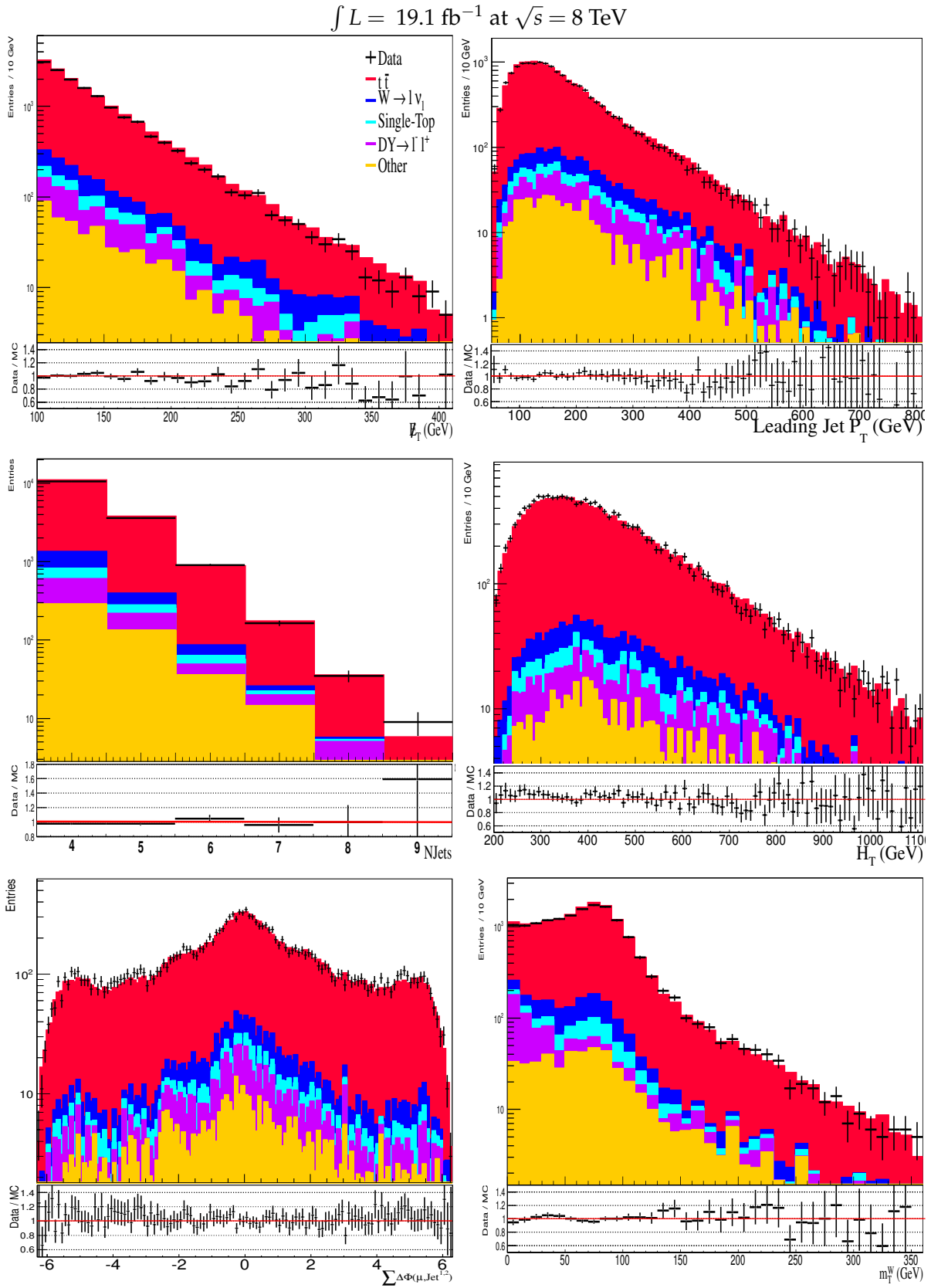


Figure 7.10: Comparison of data versus expectation for the E_T (top row, left plot), the p_T of the leading jet (top row, right let), the multiplicity of jets (second row, left plot), the sum of the p_T of the jets (H_T) (second row, right plot), the sum of $\Delta\Phi(\mu, \text{Jet}^1) + \Delta\Phi(\mu, \text{Jet}^2)$ (bottom row, left plot) and the transverse mass of the W-boson (bottom row, right plot) after the baseline selection.

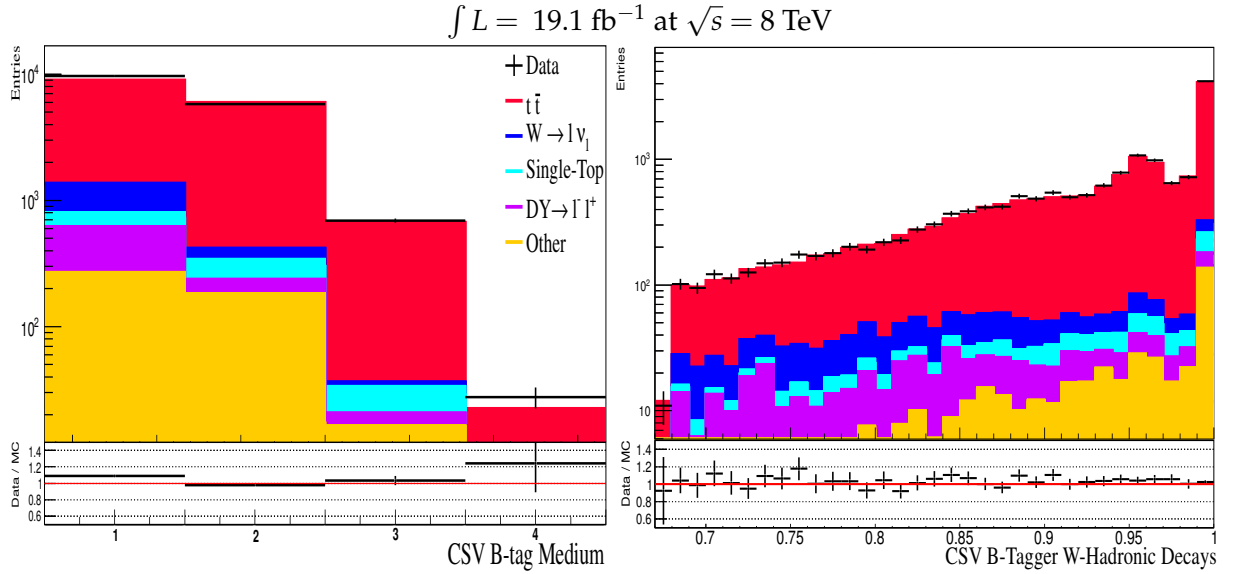


Figure 7.11: Comparison of data versus expectation after the baseline selection of the multiplicity of the b -tagged jets (left) and the distribution of discriminant used for the hadronic decays of W used by the CSV algorithm (right) based.

selected events include at least four jets, one isolated muon and \cancel{E}_T . Since some of the variables used in this analysis require the reconstruction of the $t\bar{t}$ system, it is critical to properly identify the final state particles. But the main difficulty of this task, is due to the fact that we do not know the flavours of the selected jets and the z -component of the neutrino as well while reconstructing the $t\bar{t}$ system from the semi-muonic events.

In order to reconstruct the W -boson which has decayed in hadrons, a simple χ^2 minimisation was adopted. This χ^2 was not used as a fit, but as a way to perform the matching of the selected jets to the quarks by choosing which two jets to assign to the W -boson's hadronic decay, which jet to assign to the W -boson's leptonic decay and which one to assign as the b -jet of the the top quark whose W -boson decayed hadronically. For this χ^2 we use the top quark and W -boson mass constraints and we also make use of the selected b -tagged jet information as this is known from the requirement to have at least such a jet among our selected jets. Opposite to most analyses where the four leading jets are considered, in our approach we consider all possible combinatorics from all selected jets in the event. The χ^2 formula is given by :

$$\chi^2 = \left(\frac{m_{q\bar{q}} - m_W}{\sigma_W} \right)^2 + \left(\frac{m_{bq\bar{q}} - m_t}{\sigma_t} \right)^2 \quad (7.6)$$

The masses of the top quark and of the W -boson, as well as their widths have been

determined from the $t\bar{t}$ simulated dataset. But as we do not match the reconstructed jets with the GenJets collection, we expect that the distributions of the reconstructed W-boson and that of the top quark will have long tails and although the peak around the top quark mass should be clearly distinguishable, the distribution will be "wider" with a larger width. This is happening because the presence of ISR and FSR results in more "hard" jets which can always get selected in the χ^2 procedure. These distributions are illustrated in Figure 7.12 derived from the MC@NLO $t\bar{t}$ simulated dataset. Once the minimum χ^2 for each event has been found and three jets are "assigned" with a role, we make an assumption and we pick the leading jet of the remaining jets of the event as the b -jet of the W-boson leptonic decay (i.e. in the b -jet in the $t \rightarrow b\mu\nu_\mu$ decay).

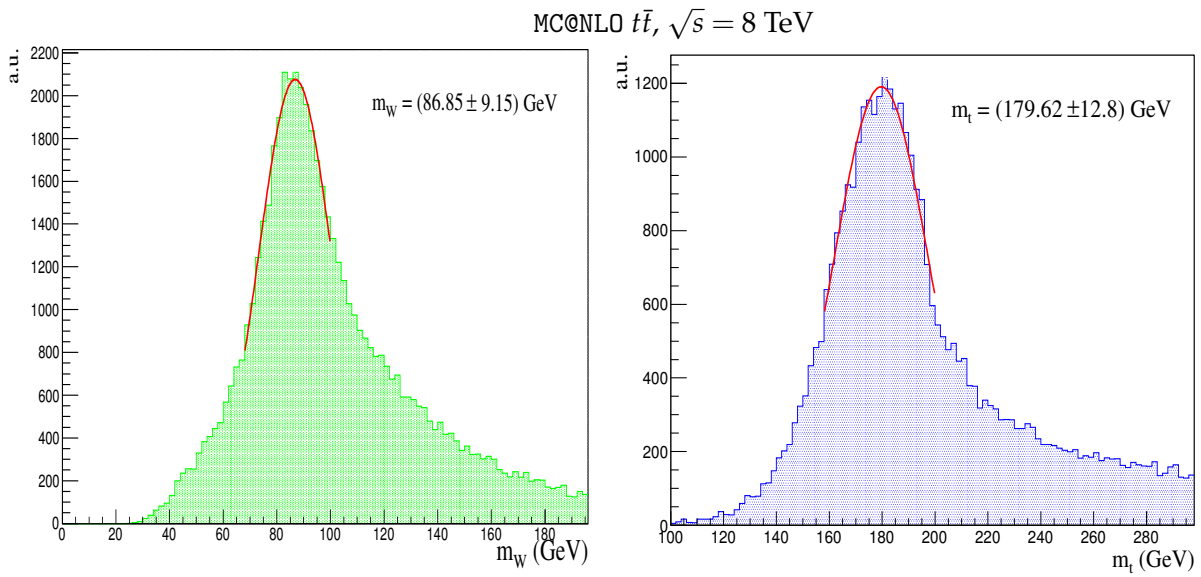


Figure 7.12: The reconstructed mass of the W-boson (left) and that of the top quark (right) from the $t \rightarrow q\bar{q}b$ with the use of a minimised χ^2 as explained in the text.

Once all these is done, the only missing piece in order to reconstruct the $t\bar{t}$ system from a semi-muonic event is the z-component of the neutrino's momentum. But due to the fact that in this analysis the mass difference between the stop and the neutralino goes down to 100 GeV, i.e. $m_{\tilde{t}_1} - m_{\tilde{\chi}_1^0} > 100$ GeV, consequently the W-boson will be on-shell. Thus the W-boson constraint is used again here and we can write :

$$m_W^2 = E_W^2 - \mathbf{p}_W^2 \quad (7.7)$$

The above can be rewritten as :

$$\begin{aligned} m_W^2 &= m_\mu^2 + 2(E_\mu, \mathbf{p}^\mu)(E_\nu, \mathbf{p}^\nu) \\ &= m_\mu^2 + 2(E_\mu E_\nu - \mathbf{p}^\mu \cdot \mathbf{p}^\nu) \end{aligned} \quad (7.8)$$

This equation is quadratic in p_z^μ and has no solution if the measured \cancel{E}_T fluctuates such that the neutrino-lepton invariant mass is above the W-boson mass. Hence we can rewrite :

$$0 = (p_{v_z})^2 - \frac{2\beta p_{\mu_z}}{E_\mu^2 - p_{\mu_z}} p_{v_z} + \frac{\beta^2 - E_\mu^2 p_{\mu_T}^2}{E_\mu^2 - p_{\mu_z}} \quad (7.9)$$

$$= (p_{v_z})^2 - K p_{v_z} - \Lambda \quad (7.10)$$

where

$$\beta \equiv \frac{1}{2}(a - p_{v_T}^2 + p_{\mu_z}^2) \quad (7.11)$$

$$a = m_W^2 + (p_{\mu_x} + p_{v_x})^2 + (p_{\mu_y} + p_{v_y})^2 - E_\mu^2 \quad (7.12)$$

$$E_\nu^2 = p_{\mu_T}^2 + p_{v_z}^2 \quad (7.13)$$

The Equation 7.10 is solvable when $\Delta = K^2 - 4\Lambda \geq 0$ and then it holds :

$$p_{v_z} = \frac{1}{2}(\pm\sqrt{\Delta}) \quad (7.14)$$

and the smallest solution is chosen. But if $\Delta < 0$, then $p_{v_z} = \frac{p_{\mu_z} p_{v_T}}{p_{\mu_T}}$. Figure 7.13 illustrates the reconstructed z-component of the neutrino derived from the MC@NLO $t\bar{t}$ simulated dataset.

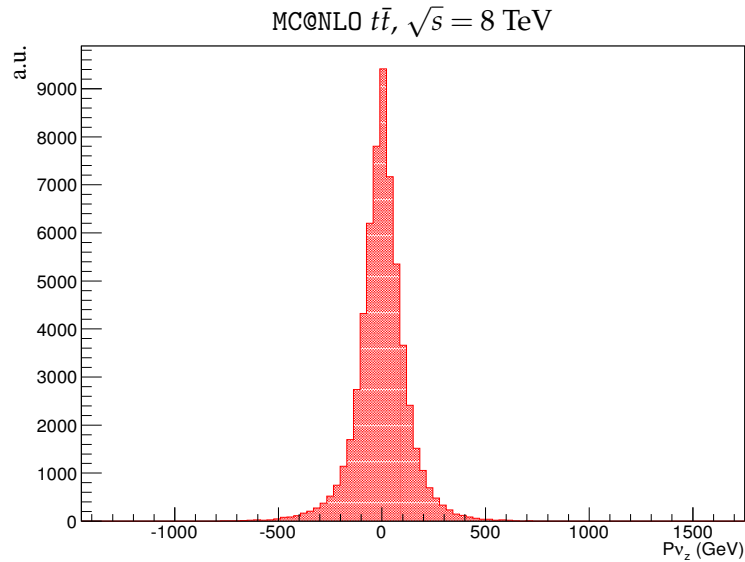


Figure 7.13: The reconstructed z-component of the neutrino's momentum.

Finally, in Figure 7.14 various distributions are shown for the reconstructed "hadronic" and the reconstructed "leptonic" top quark, as well as for the reconstructed $t\bar{t}$ system. The terms "hadronic" and "leptonic" top quark denote the reconstructed top quark that has decayed according to $t \rightarrow q\bar{q}b$ and $t \rightarrow \mu\nu_l b$ respectively.

We observe that simulation with data agree well, although for this analysis is not really crucial to put more constraints on these reconstructed quantities. What is more important is that conceptually the phenomenally of the reconstructed objects should be coherent. For instance, for the $\Delta\Phi$ distribution, the "hadronic" and the "leptonic" reconstructed top quarks are mostly back-to-back, as expected. However, there are still contributions from other processes except the $t\bar{t}$, as the only requirement is that the selected events minimise the χ^2 satisfying the W -boson and the top quark mass constraints.

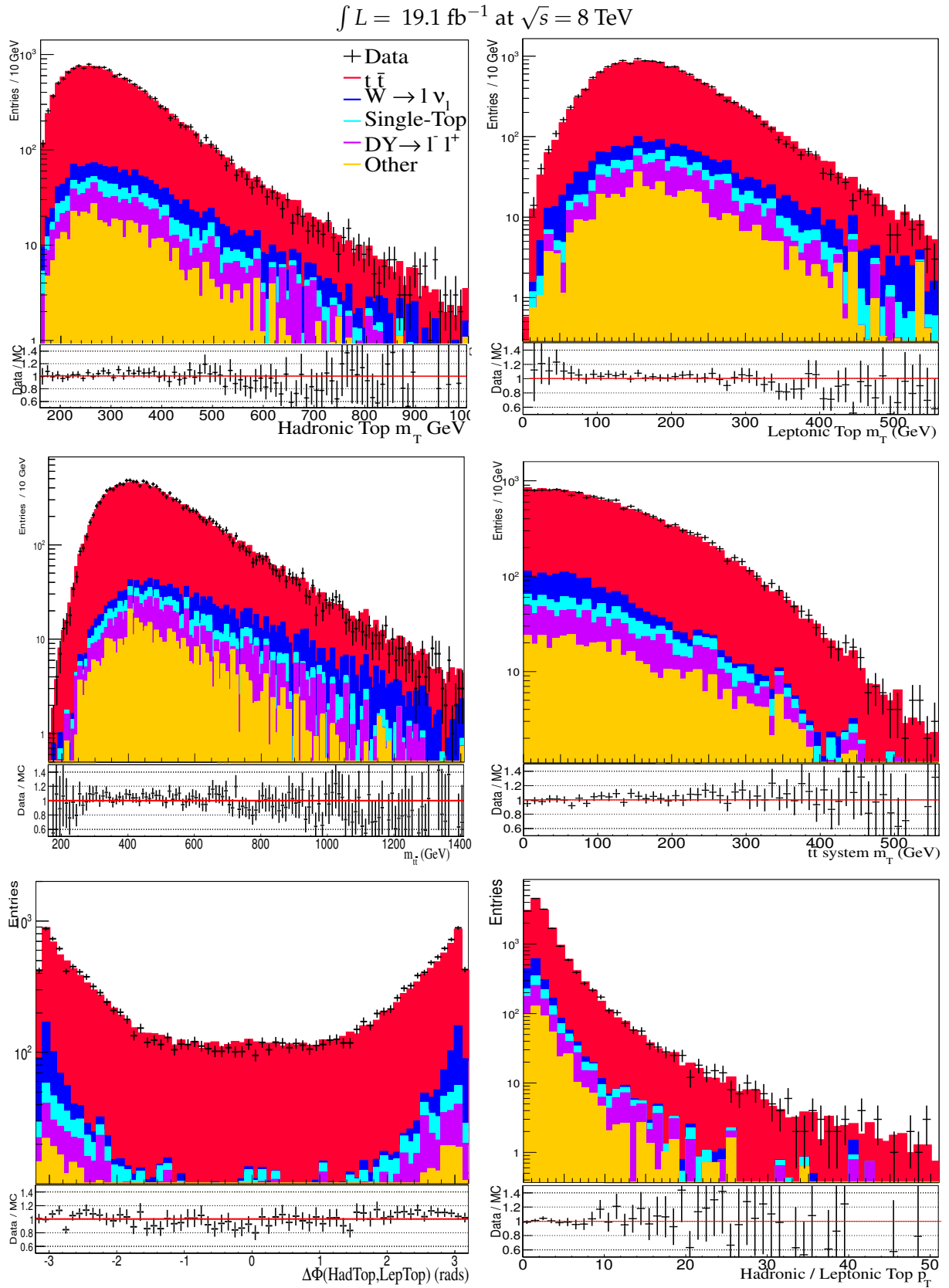


Figure 7.14: From left to right : The distributions of the transverse mass of the reconstructed "hadronic" and that of the "leptonic" top quarks (top row), the mass of the reconstructed $t\bar{t}$ system and its transverse mass (second row), the $\Delta\Phi$ and the ratio of the p_T of the "hadronic" versus that of the "leptonic" reconstructed top quarks (bottom row).

The aim of science is not to open the door to infinite wisdom, but to set a limit to infinite error.

Bertolt Brecht

CHAPTER 8

SELECTION OF OBSERVABLES AND MULTIVARIATE ANALYSIS TECHNIQUES

In this chapter we discuss the consolidation, selection and optimisation of the variables, but also the usage and determination of the optimal Multivariate Analysis Techniques (MVA) for the needs of this analysis. Section 8.1 discusses the classification of the used variables, while Section 8.2 presents how variables are ranked in order to maximise the discrimination power and how the decision is taken which of them are to be used in the MVA at the end. In Section 8.3 we briefly discuss the general characteristics of MVA tools, along with their applicability in this analysis and some sanity tests that were carried out in order to choose the optimal MVA method.

8.1 Selection of variables

Once we have decided on the baseline selection to be applied on the datasets, several observables are constructed to be used with Multivariate Analysis Techniques (MVA). The strategy is to make use and exploit those variables that provide more discriminating power and can strongly differentiate SM from possible SUSY-like signal events. Most of these variables are built from the four-momenta of the final state (reconstructed) objects.

8.1.1 Variables with discriminating power

About 45 variables have been implemented in the context of this thesis. Most of them make use of the four-momenta of the reconstructed objects in the final state, while several of them can be combined to form even more complex observables. The variables are grouped into four main different categories :

1. *Individual Object Kinematic Variables* : This class consists of variables which characterise the kinematic properties of each of the final state objects. Examples are the transverse momentum of the jets or of that of the muon, their mass, their pseudo-rapidity or the multiplicity of jets of the event.
2. *Global Event Kinematic Variables* : This class contains quantities reconstructed from two or more final state objects by using their kinematic properties. Example variables are the \cancel{E}_T , the scalar sum of all the jet's transverse momentum (H_T), or even the invariant mass of the 3 leading jets (denoted by m_3).
3. *Angular Variables* : This class contains all the angular-shaped variables, like the angular separation of the two leading jets, or the pseudo-rapidity of the i -th jet. These observables can be reconstructed from two or even more final state objects.
4. *B-Tag discriminators* : This class includes those variables that make use of the b-tag discriminators of the CSV algorithm.

The full list of variables is given in Appendix B.

8.2 Ranking of variables

One of the main goals of this analysis is to optimise the efficiency and sensitivity individually for each of the points in the $(m_{\tilde{t}_1}, m_{\tilde{\chi}_1^0})$ plane. To achieve this and since each point of the phase space can be ruled by different phenomenology, a dynamic method is implemented. That said, one of the novelties of this search is that it does not use the same predefined list of variables for each point while the phase space is surveyed; on the contrary, the variables that are finally used at each point, change according to their discriminating performance at this particular corner of the phase space. The underlying idea is that using a "frozen" list for all points would not necessarily result in a higher sensitivity compared to our approach. This is true since one variable that is not too sensitive for a given point, might become important for the differentiation of SM

versus the NP signal at another point in the $(m_{\tilde{t}_1}, m_{\tilde{\chi}_1^0})$ plane.

But beforehand and while designing the variables, one cannot know which ones have more discriminating power. Also, many of them might be highly correlated, therefore will not give any added value if they are used together. This is why it is important to *first* identify and *then* sort those variables which are more sensitive to NP and this has to be done systematically in a coherent way, throughout the $(m_{\tilde{t}_1}, m_{\tilde{\chi}_1^0})$ plane.

The method that was developed can be described in the following steps:

1. **Overlapping of distributions** : For each one of the observables which have been constructed as explained in Section 8.1.1, the PDF distributions of the signal at each point in the $(m_{\tilde{t}_1}, m_{\tilde{\chi}_1^0})$ plane and the background are compared. From this comparison, an overlapping coefficient $\epsilon_{overlap} \in [0, 1]$ is calculated, with 0 meaning that the two distributions are completely separated while 1 states that they are completely overlapped.
2. **Sorting** : Once the above step has been repeated sequentially for all observables one by one, an ascending list is then assembled according to the obtained $\epsilon_{overlap}$. A smaller value of $\epsilon_{overlap}$ means that signal is more separated from background. Consequently, a smaller overlapping value can be interpreted as an indication that this variable can give more discriminating power compared to the ones associated with higher $\epsilon_{overlap}$ values.
3. **Correlation** : The next step is to remove the highly correlated variables as they neither carry any additional information nor they provide better discrimination. To do so, a linear correlation among all variables is determined using the background simulated dataset. In case that a variable is highly correlated with another above a maximum correlation coefficient denoted by $|\rho_{max}|$, the one that has the lower overlapping fraction $\epsilon_{overlap}$ obtained from the first step is kept in the list, while the other is totally removed. At the end of this step, the variables are sorted according to both their overlapping fraction $\epsilon_{overlap}$ and their inter-correlation, from the least overlapped and least-correlated to the most-overlapped and most-correlated ones. Still, at this stage different collections are kept for different maximum correlation coefficients ($|\rho_{max}|$).

Thus, different lists for different values of the $|\rho_{max}|$ are compiled, that is for $|\rho_{max}| \in [0.5, 0.8]$ with a step of 0.1. Of course, varying the $|\rho_{max}|$ implies that for each value, different amount of variables make it to the final list. Figure 8.1 gives the number of survived variables for the two extreme $|\rho_{max}|$ values (i.e. 0.5 and

0.8) in the $(m_{\tilde{t}_1}, m_{\tilde{\chi}_1^0})$ plane. By comparing these two plots, one can see that the number of variables that make it to the final list does not change significantly. Since on average this difference is around 5-6 variables, we use the $|\rho_{max}| = 0.8$ throughout this analysis to have a more complete list. Nonetheless, we observe that for most of the point in the $(m_{\tilde{t}_1}, m_{\tilde{\chi}_1^0})$ plane for these two values of the $|\rho_{max}|$ the top 6-8 ranked variables according to $\epsilon_{overlap}$ remain the same. Practically, the MVA will be using highly-ranked variables anyway, so even with the $|\rho_{max}| = 0.8$ we do not lose any sensitivity, on the contrary, we allow more variables to enter the MVA procedure.

4. **Repeat for all points** : The above steps are repeated sequentially for each point in the $(m_{\tilde{t}_1}, m_{\tilde{\chi}_1^0})$ plane. The motivation of doing so, is that in general SUSY events are described by harder QCD radiation and higher scales. This can result in an increased jet activity and larger \cancel{E}_T in the event but subjected to the exact details of the model under consideration. Thus, obtaining a list for just one model and using it for all of the models will simply diminish the sensitivity of the analysis. To some extent, this could result to a situation where inappropriate variables are injected as "sensitive-ones" while they are not qualified as such.
5. **Performance plots** : Once all the above is done, 2D maps can be obtained giving information about the behaviour of the observables and their discriminating power throughout the $(m_{\tilde{t}_1}, m_{\tilde{\chi}_1^0})$ plane. Looking systematically at these plots, we can draw conclusions. These 2D maps can include for example the ranking of a variable throughout the $(m_{\tilde{t}_1}, m_{\tilde{\chi}_1^0})$ plane, its overlapping $\epsilon_{overlap}$ fraction, or even the ratio of the $\epsilon_{overlap}/\epsilon_{best}$ which is the ratio of the overlap value divided by the overlapping ratio of the best one (i.e. top ranked variable).

Figure 8.2 presents the above 2D maps for the \cancel{E}_T and the invariant mass of the 3 leading jets, but of course, these plots have been obtained systematically for all of the variables. In particular for the aforementioned variables, one can note that :

- \cancel{E}_T is highly ranked in most of the points, while the m_3 is better ranked in the compressed area (i.e. when $\Delta m = m_{\tilde{t}_1} - m_{\tilde{\chi}_1^0} < 175$ GeV i.e. the boundary where the top quark is off-shell).
- The \cancel{E}_T overlapping fractions in general are $\sim 0.3 - 0.6$ for the uncompressed (bulk) region while a certain pattern is revealed for the low $m_{\tilde{t}_1}$ region where the fraction is ~ 0.9 . This is a somewhat expected behaviour, since phenomenologically speaking, in this corner the stop quarks are not boosted and the produced top quark pair looks kinematically very much alike to a SM top quark pair pro-

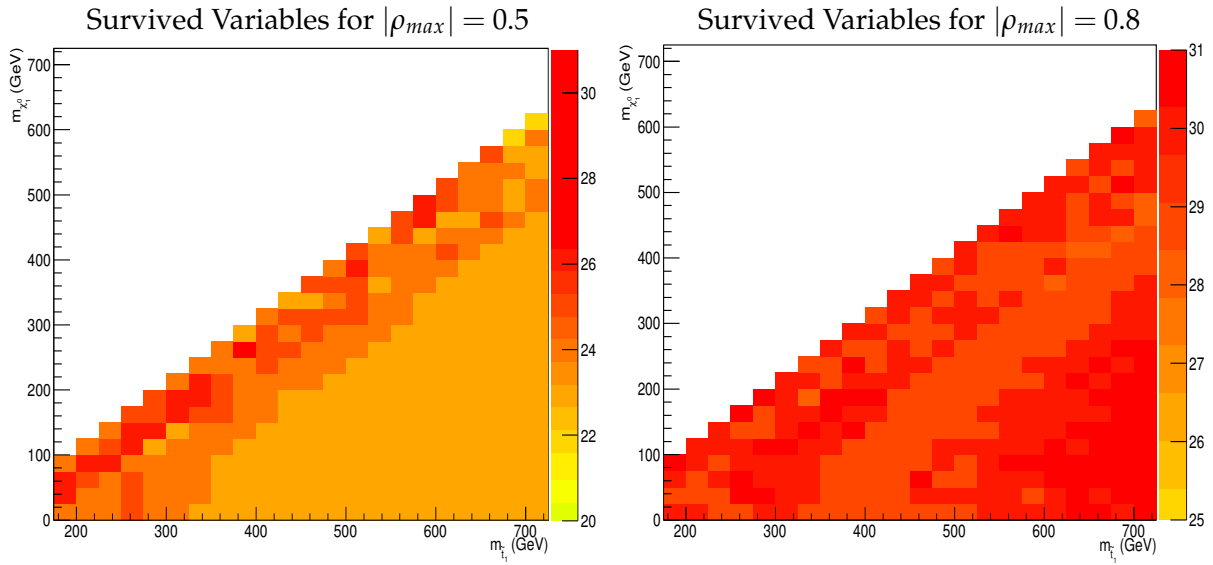


Figure 8.1: Number of survived variables for $|\rho_{max}| = 0.5$ (left) and $|\rho_{max}| = 0.8$ (right). In general the change of the $|\rho_{max}|$ does not alter radically the number of survived variables that make it to the final list.

duction, if we neglect the fact that some extra \cancel{E}_T is present in the former case due to the neutrinos. Thus, the overlapping value close to unity is expected, but the extra \cancel{E}_T differentiates a bit the SMS versus the SM model. On the other hand and for $m_{\tilde{\tau}_1} > 350$ GeV the values get smaller again.

- The $m3$ variable does not seem to be the most powerful variable as it is not very highly ranked in the bulk region. This argument is further enhanced as its overlapping values in general are bigger than 0.8 in that region. But if we look in the compressed spectrum i.e. when $\Delta m < 175$ GeV, the $m3$ is ranked higher, thus becomes more "important". That means that the $m3$ is expected to be "on average" and important variable but surely, not the most powerful one. On the other hand, since the \cancel{E}_T is ranked relatively high in most of the points, this qualifies it as a "potentially" very good/strong discriminating observable. The word "potentially" means that although the initial list covers a diverse spectrum of variables, there is always the possibility that we can come up with a new variable which could be even more sensitive. In any case, lower overlapping values result to more powerful variables.

Other tests include the monitoring of the medians of each variable distribution in the $(m_{\tilde{\tau}_1}, m_{\tilde{\chi}_1^0})$ plane. For instance, Figure 8.3 shows the median for six variables, namely that of the H_T4 Jets, the \cancel{E}_T , the H_T , the transverse momentum of the muon, the trans-

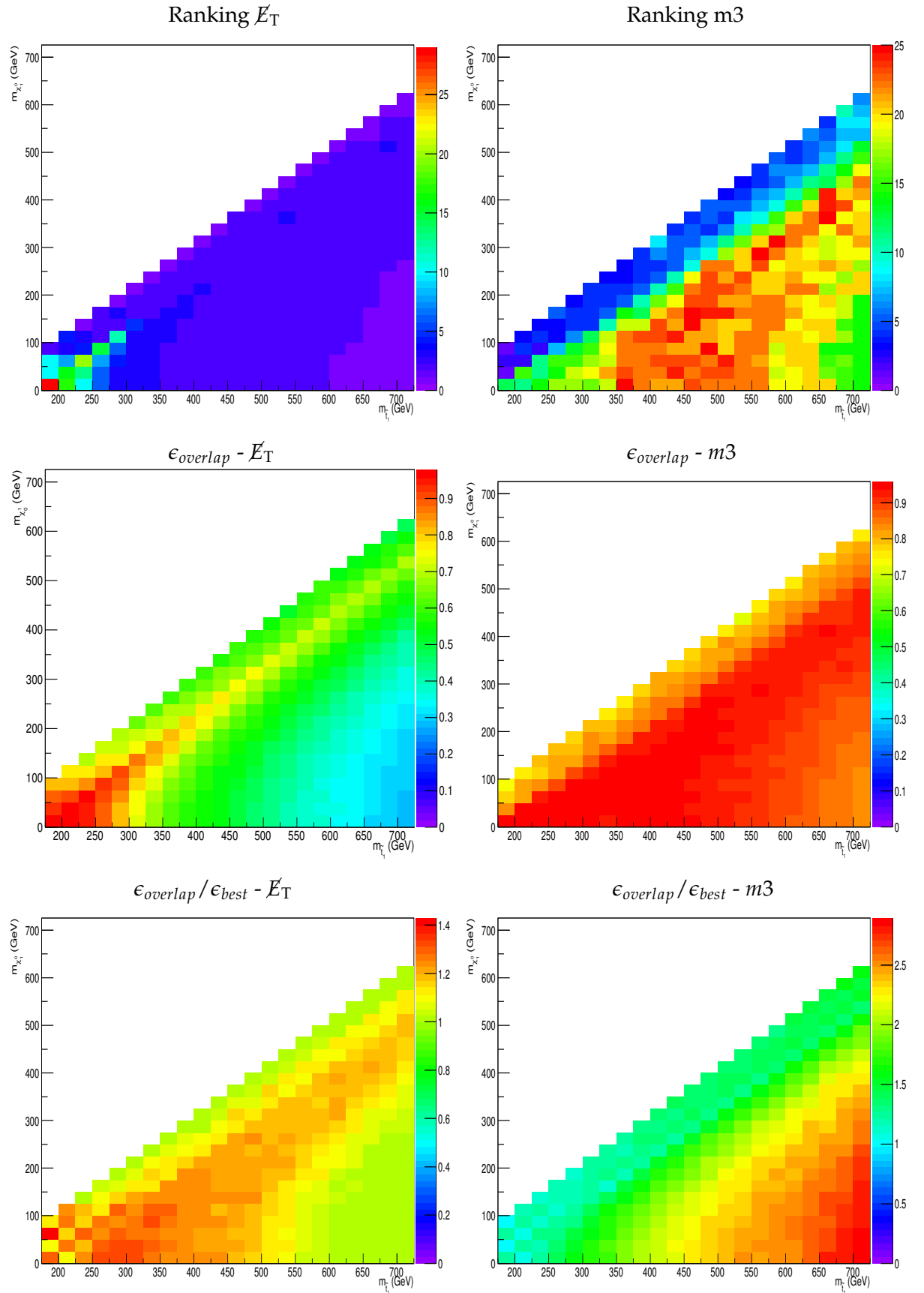


Figure 8.2: The 2D performance plots of the \mathcal{E}_T and the p_T of the muon. Top row shows the ranking, second row the $\epsilon_{\text{overlap}}$ fractions and bottom row the $\epsilon_{\text{overlap}}/\epsilon_{\text{best}}$ for $|\rho_{\text{max}}| = 0.8$.

verse mass of the W -boson and that of the m_3 .

The question after having drawn these 2D maps, is wherever one can draw any conclusions regarding the importance of the used variables by comparing against the median values of the background processes as well. For example, Table 8.1 lists the median values for the same variables that were illustrated in Figure 8.3 obtained from the MC@NLO $t\bar{t}$ simulated dataset.

Process	$H_T4\text{Jets}$ (GeV)	\cancel{E}_T (GeV)	H_T (GeV)	p_T^μ (GeV)	m_T^W (GeV)	m_3 (GeV)
$t\bar{t}$	385	130	403	58	67	254

Table 8.1: The median values of some observables obtained from the MC@NLO $t\bar{t}$ simulated dataset.

Comparing the behaviour, we can see that for example and for the $H_T4\text{Jets}$ variable, there are just 16 points in the $(m_{\tilde{t}_1}, m_{\tilde{\chi}_1^0})$ plane where the median value is below 400 GeV, while that of the $t\bar{t}$ is around 385 GeV. Therefore, we expect the $H_T4\text{Jets}$ to be a sensitive variable. Similarly, the median value for the \cancel{E}_T from the $t\bar{t}$ simulated dataset is close to 130 GeV, while there are only a few points below 140 GeV in the $(m_{\tilde{t}_1}, m_{\tilde{\chi}_1^0})$ plane and more specific on the low $(m_{\tilde{t}_1}, m_{\tilde{\chi}_1^0})$ corner. Thus, we also anticipate that the \cancel{E}_T will be an important variable, whereas the same goes also for the m_T^W and the m_3 variables. On the contrary, when it comes for the transverse momentum of the muon, we observe that the median obtained from the $t\bar{t}$ simulated dataset is close to 60 GeV, a value that is also oftenly met on the 2D map of the $(m_{\tilde{t}_1}, m_{\tilde{\chi}_1^0})$ plane. Hence, we expect that this variable should not be a very powerful one.

In any case, the above discussion cannot possible drive us to safe and finite conclusions, rather than just give us a qualitatively estimation of the performance of each observable. This is true, also because we just considered the case of the $t\bar{t}$ process for the sake of simplicity, but it is actually the interplay of all the contributing processes that really determines the final median values for any given variable.

To end this exercise, after having repeated the steps (as listed in 8.2) for all points in the $(m_{\tilde{t}_1}, m_{\tilde{\chi}_1^0})$ plane, we have counted how many times each variable appears in the list of the 4-best ones (we will refer to Section 8.3.2 why we are interested in the 4-best and not the 10-best for example). Table 8.2 lists this frequency provided that a given variable appears at least once. We observe that what was discussed in the previous paragraphs is verified and what we "naively" envisaged as good discriminates, they indeed make it to the list. On the contrary, the transverse momentum of the muon does not get selected not even once in the 4-best variables. Also, variables like the \cancel{E}_T and the H_T ,

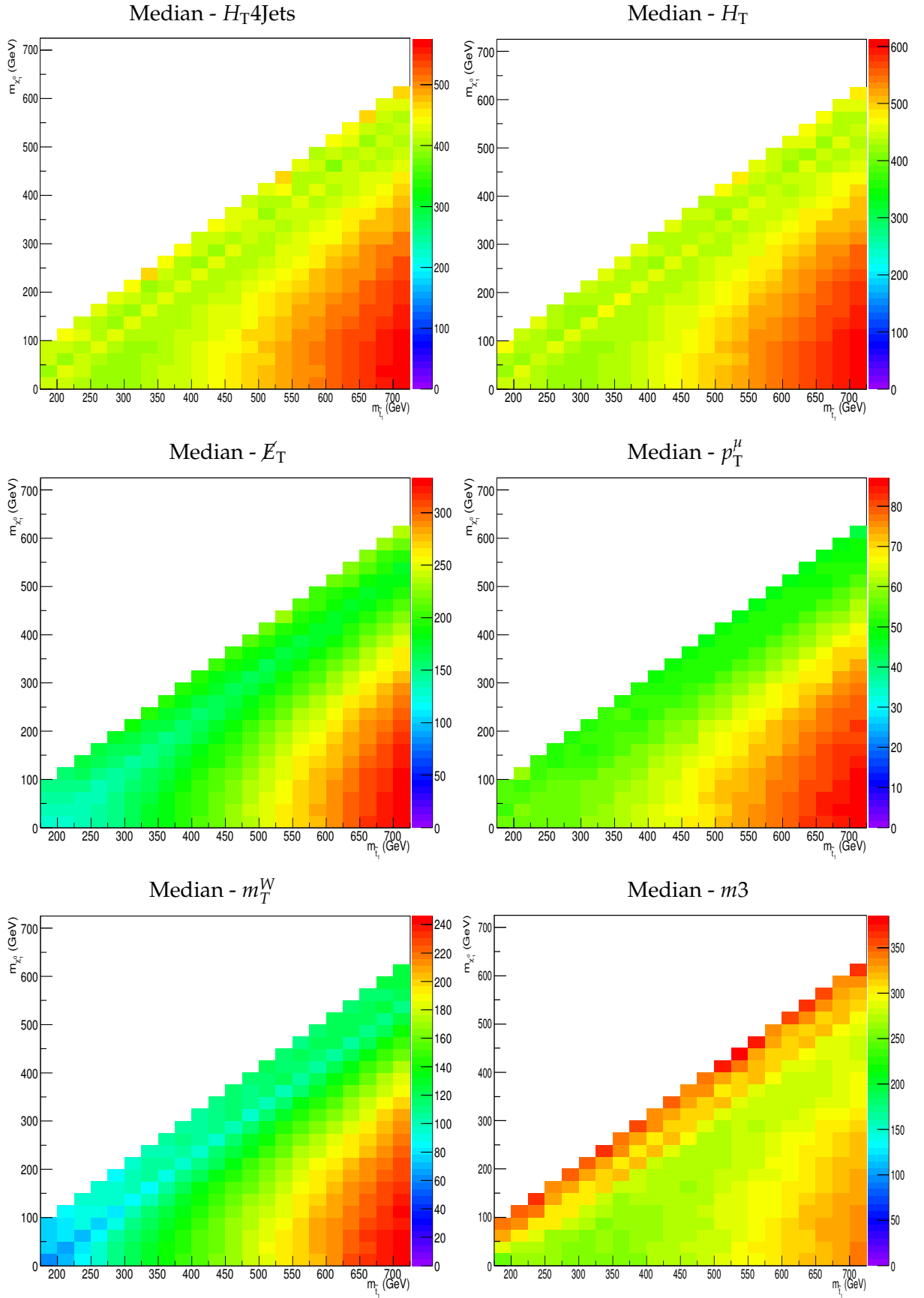


Figure 8.3: The median values in the $(m_{T1}, m_{\tilde{\chi}_1^0})$ plane of the H_{T4Jets} and of the H_T (top row), of the \cancel{E}_T and of the transverse momentum of the muon (second row) and of the reconstructed W -boson transverse mass and of the invariant mass of the three leading jets (m_3) (bottom row).

although they get repeatedly selected, are not the very best ones, contradictory to what many SUSY analysis do and treat them as key observables. As a general remark, we could say that most of the variables that make it to the list are associated either with the jet activity of the event and/or the \cancel{E}_T , while some angular variables appear as well. Although these are not many, they are ranked relatively high.

The above results drive us to believe that our chosen strategy to select "dynamically" variables rather than using a fixed and predefined one pays off, in the sense that we have found variables that appear to be even more sensitive than the "classic" ones like the H_T , the \cancel{E}_T etc. In any case, we mean not to abolish nor to underestimate the importance of these variables for inclusive SUSY searches, rather than to point out that there is always the possibility to invent new and useful variables that can offer high discrimination.

8.3 Tools for Multivariate Analysis (MVA)

In this section we review the basic concepts of *Multivariate Analysis* (MVA) (Section 8.3.1). In Section 8.3.2 the steps that were followed to assess the performance of the various available MVA methods and of the considered variables in the context of this analysis are discussed. However, we will avoid to go into many technical details on the exact machinery behind, something that is done in Appendix C.

8.3.1 MVA introduction

The Toolkit for Multivariate Analysis (TMVA) [145], is a commonly used MVA framework written in C++ and is based on ROOT. TMVA provides the platform to carry out and apply multiple advanced learning machine analysis techniques in a user friendly way. It is true that during the last years MVA tools have become very popular within the HEP community, as they can address several problems and offer an easy way to test and evaluate several various classification algorithms. In parallel they provide several visualisation tools to easily examine their qualitative outcome. That said, obtaining the separation power of the given variables turns to be a relative simplified procedure.

The motivation to use statistical MVA tools, is usually the lack of knowledge of the mathematical/phenomenological modelling and dependence of the quantity in ques-

	Observable	Frequency in 4 best variables
1	m_T^W	314
2	$\Delta\Phi(\mu, \cancel{E}_T)$	297
3	$H_T4\text{Jets}$	165
4	$H_T4\text{JetsMuon}\cancel{E}_T$	163
5	\cancel{E}_T	135
6	m_3	40
7	$\Delta R(\mu, \text{Jet}^1)$	47
8	$\Delta\Phi(\mu, \text{Jet}^1)$	34
9	BTaggerLepB	22
10	H_T	11
11	Centrality	10
12	ET1oET3	13
13	m_{eff}	7
14	$m_{t\bar{t}}$	6
15	ET1oET4	5
16	BTaggerHadB	2
17	ET1oET2	2
18	$H_T4\text{jets}\cancel{E}_T$	2
19	$m_{t\bar{t}}$	2
20	ET34	1
21	HZ4Jets	1
22	$\Sigma [\Delta\Phi(\mu, \text{Jet}^1), \Delta\Phi(\mu, \text{Jet}^2)]$	1
23	$m_T^{\text{Hadr}}(t\bar{t})$	1

Table 8.2: The frequency of the observables that appear at least once in the best 4 selected variables. The full list and their exact definition is given in Appendix B.

tion related to the observed quantities. Each of the MVA methods is implemented within a given algorithm. Furthermore, one main goal of the TMVA, is to guarantee the unbiased performance comparison between the different available methods although it seems that many of them share common features. Typically, the algorithms consist of two phases :

1. **Training** : Here the algorithm learns how to classify background from signal events. To achieve this separation, each method has to be trained and tested. For the exact process of the separation and the optimisation of "signal-like" and "background-like" events, a given set of variables has to be injected from a finite, yet representative collection of simulated events. At the end of this phase, a combined "weight" is returned (one per event) which is stored and it is used while in the Evaluation step.
2. **Evaluation** : At this step, the separation rules obtained while training the classifier(s) are now being applied to new collections of signal and background but to the collision events as well in separate phases. At the end and for each process, a combined variable is formed from the MVA which could be thought as the result of the interplay between all of the input variables incorporating the weights on the nodes that were obtained during the training phase. At this point, the classification response can be transformed to a probability of the candidate being either signal or background. At the end, the events are weighted to the target integrated luminosity.

To ensure the robustness of the results, the different collections of events that are used for the aforementioned phases have to be statistically independent. This requirement insinuates that one must make sure that enough simulated events are available.

8.3.2 Determining the optimal MVA method

Trying to choose the optimal MVA method is not always easy, as one needs to take different factors into account, like the processing time, the overall performance, the applicability and feasibility, the CPU budget etc. This Section discusses the results of several performance tests in order to determine the optimal classifier. We also determine the optimal number of variables that will be used for the training so to achieve the maximum discrimination. Indeed, following the discussion of Section 8.2, it is obvious that at the end of the Ranking step of the variables, a final list is compiled per point in the $(m_{\tilde{t}_1}, m_{\tilde{\chi}_1^0})$ plane. But it does not mean that by using all of the variables present in this

list within a MVA method the maximum discrimination is ensured. Since by definition some variables have more discriminating power than others, it is anticipated that the maximum discrimination could be in principle achieved even by using a subset of these "final" variables. Injecting more, probably will not offer neither better discriminating power nor better performance of the method itself, while the CPU time will be increased for sure.

8.3.3 The Receiver Operating Characteristics (ROC) curve

A way to judge the performance of a given method while trying to separate background over signal, is to monitor the *background rejection versus signal efficiency curve*. Statistically speaking, this curve is made by creating a likelihood ratio test which tells where a given method achieves reducing Type I (false positive) and Type II (false negative) errors at the same time. The likelihood ratio is expressed like :

$$y(x) = \frac{P(S|x)}{P(B|x)} \quad (8.1)$$

This gives the *Receiver Operating Characteristics* (ROC) curve, i.e. the fraction of true positives out of the positives versus the fraction of false positives out of the negatives while varying the discrimination threshold. This actually determines the performance of a given classifier, but one needs to take into account that since the false-positive (type I error) is equal to the $\epsilon_{\text{background}}$ the higher it is, the higher the loss of purity of the sample. On the same footing, when it comes to the false negative or equivalently the $1 - \epsilon_{\text{signal}}$, the higher it gets, the higher the loss on the efficiency.

That said, we need the $1 - \epsilon_{\text{background}}$ to be minimum while maximising the ϵ_{signal} at the same time. As an example, Figure 8.4 demonstrates the ROC curves for different classifiers and different number of injected variables starting from the higher ranked one (i.e. the 2-best, the 4-best etc) as these were drawn from the "final" list. Although we here present just the results for one particular point in the $(m_{\tilde{t}_1}, m_{\tilde{\chi}_1^0})$ plane, similar plots have been obtained and studied for many points. The choice for this analysis is to use the four best variables for each point in the $(m_{\tilde{t}_1}, m_{\tilde{\chi}_1^0})$ plane with both the MLP and the BDT classifiers.

8.3.4 Checks for overtraining

In general, the MVA methods can become overtrained (some methods more easily than others). Overtraining implies that the algorithm "learned" the statistical fluctuations from the input information. When overtraining occurs, an artificial and overestimated discrimination power is obtained, which cannot not be trusted. Practically, there are some tips to avoid this unwanted behaviour. For example, using large enough datasets for training and tweaking some parameters of the algorithm, will help limiting the size and complexity of the synopsis, hence minimise the risk of overtraining. The way to inspect that overtraining does not occur, is to use a sample for the testing and then inspect the behaviour of the method on the "test" dataset and compare it against the output obtained from the training. Figure 8.5 demonstrates exactly the result of this comparison and as it can be seen training and test output present a very similar behaviour.

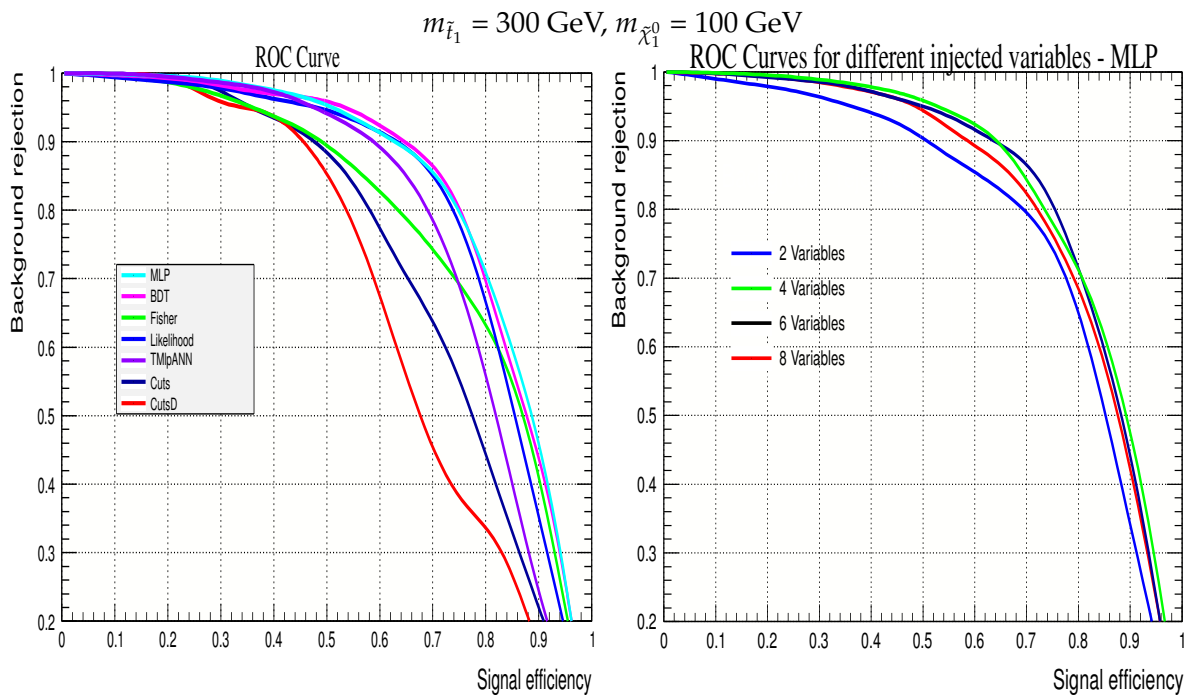


Figure 8.4: The ROC curves for several classifiers (left) and for different number of injected variables (right). One can see that using more than 4 variables practically does not improve the performance of the MVA.

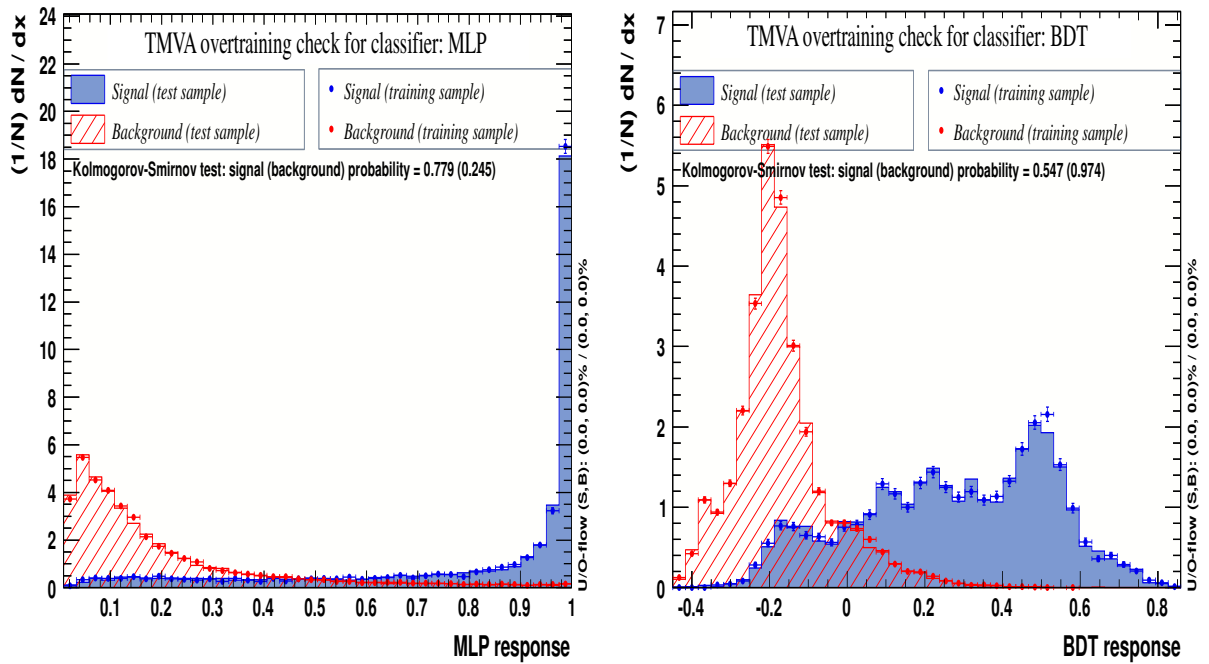


Figure 8.5: A check for overtraining for the MLP (left) and the BDT (right) classifiers. Training and testing samples present a very good convergence for both of them. Similar checks have been carried out for many different points in the $(m_{\tilde{\tau}_1}, m_{\tilde{\chi}_1^0})$ plane and no strong inconsistencies have been found.

*Measure what can be measured, and
make measurable what cannot be
measured.*

Galileo Galilei

CHAPTER 9

SYSTEMATIC UNCERTAINTIES

This chapter presents the considered systematic uncertainties for this analysis, although they will be treated as nuisance parameters in a fitting template method (Chapter 10). The systematics can be classified into experimental (Section 9.1), and theoretical ones (Section 9.2).

9.1 Experimental uncertainties

The following systematic uncertainties have been considered on both the signal and the background simulated samples.

Luminosity : The data luminosity measurement comes with an uncertainty, which in the case of the 2012 LHC run it was estimated to be 4.4% (Section 7.1). This uncertainty affects only the level and not the shape of the distributions.

Jet Energy Scale (JES) : The jets energy scale is shifted by $\pm 1\sigma$ reflecting the jet energy scale uncertainty which is parametrised as a function of the jet's p_T and η . This variation accounts also for the flavour-dependance of the jets, as well as for the uncertainty due to PU corrections in the jet calibration procedure. This uncertainty is also propagated to the \cancel{E}_T [126] and in our case is the most important source of systematic uncertainty. Figure 9.1 illustrates the distributions derived from the MC@NLO $t\bar{t}$ simulated dataset of the scalar sum of the four leading jets (denoted by $H_{T4\text{Jets}}$), the

\cancel{E}_T , the transverse mass of the reconstructed W-boson and the invariant mass of the three leading jets (m_3), for the nominal and the systematic variations $\pm 1\sigma$ of the JES as well.

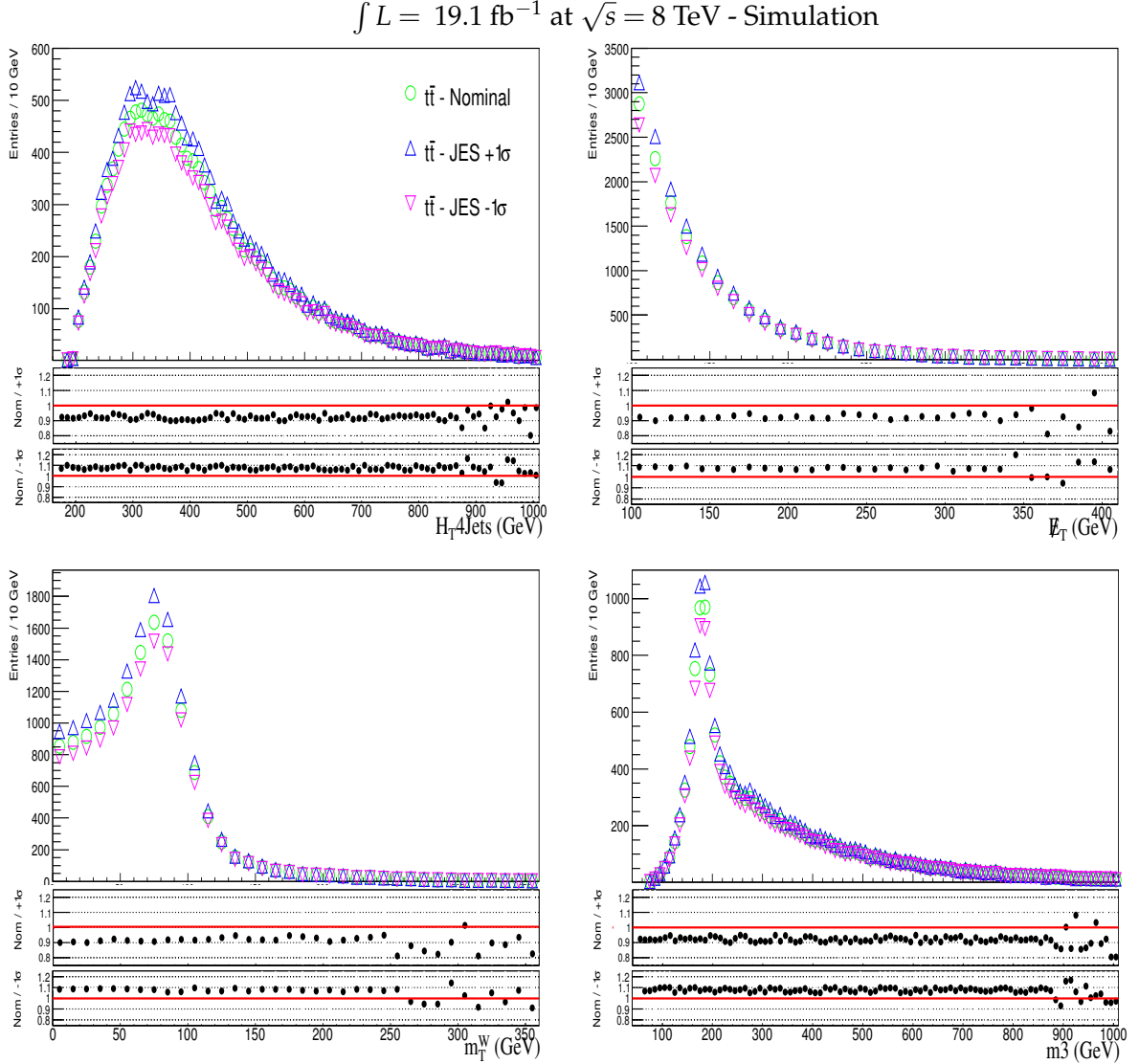


Figure 9.1: The expectation distributions for 19.1 fb^{-1} of integrated luminosity of the scalar sum of the four leading jets (denoted by $H_{T4} \text{Jets}$) (top left), the \cancel{E}_T (top right), the transverse mass of the reconstructed W-boson (bottom left) and the invariant mass of the three leading jets (denoted by m_3) (bottom right) for the nominal (open green circle) and for the $\pm 1\sigma$ variations of the JES (open triangles). The plots have been obtained from the MC@NLO $t\bar{t}$ simulated dataset after the baseline selection.

The effect of the JES systematic is of the order of 10-12% but there are higher fluctuations for the higher bins as these are less populated. Further, in general the upward variation ($+1\sigma$) results in higher event yields, while this is inverted for the down-

ward variation (-1σ). Finally, as the calorimeters have a non-linear response of the deposited energy (as a function of p_T) this uncertainty affects the shape of the distribution as well.

Jet Energy Resolution (JER) : For this systematic, the p_T of all jets are smeared by the $\pm 1\sigma$ uncertainty on the nominal jet energy resolution. This is parametrised as a function of the p_T and of the η of the jets. This variation is propagated to the \cancel{E}_T as well.

Figure 9.2 demonstrates the nominal and the $\pm 1\sigma$ JER variation distributions of the JER for the $H_T 4\text{Jets}$, the \cancel{E}_T , the transverse mass of the reconstructed W-boson and the p_T of the leading jet, all derived from the MC@NLO $t\bar{t}$ simulated dataset. As it can be seen, the effect of the JER variations is rather small at the level of few percent, but like in the case of the JES the shape is again affected.

B-tagging efficiency : The nominal b-tagging efficiency which is parametrised as a function of the p_T of the jets for $|\eta| < 2.4$ when $20 < p_T < 800$ GeV, is varied by $\pm 1\sigma$. For values of $p_T > 800$ (< 20) GeV the scale factor obtained for $p_T = 800$ (20) GeV with twice the quoted uncertainty is used.

In Figure 9.3 the nominal and the $\pm 1\sigma$ variation distributions are demonstrated for the number of b-tagged jets and the distribution of the CSV algorithm b-tagger discriminator of the b-jet associated to the top quark decay where the W-boson decays into quarks for the Medium working point. It can be seen that the effect of this systematic source is rather small, of the order of 1-3%. But in particular, the effect on the multiplicity of the b-tagged jets is $\sim \pm 5\%$ for the $\pm 1\sigma$ variation respectively. However, for more than 2 b-tag jets, the sign is flipped, and the $\pm 1\sigma$ results has an effect of $\sim \mp 5$ (10)% for the 3 (4) b-tagged jets respectively, something that can be attributed to the fact that the b-tagging efficiency depends on the event kinematics while the multiplicity of the b-jets is not such an observable.

Lepton scale factors and Muon Trigger : Due to small uncertainties associated to the lepton reconstruction and identification (Section 7.4.4) and the muon trigger efficiency for single isolated muon with $20 < p_T < 100$ GeV as well, scale factors (SF) have been applied on the selected isolated muon. These SF have been obtained centrally from CMS by using a Tag-and-Probe method on Drell-Yan di-electron and di-muon events. The overall trigger efficiency for these two event topologies was found to be 90.8 and 92.4 %, respectively [146]. In any case, these trigger efficiency uncertainties were taken into account while the lepton-SF were obtained, thus there is no need to assign an additional systematic uncertainty.

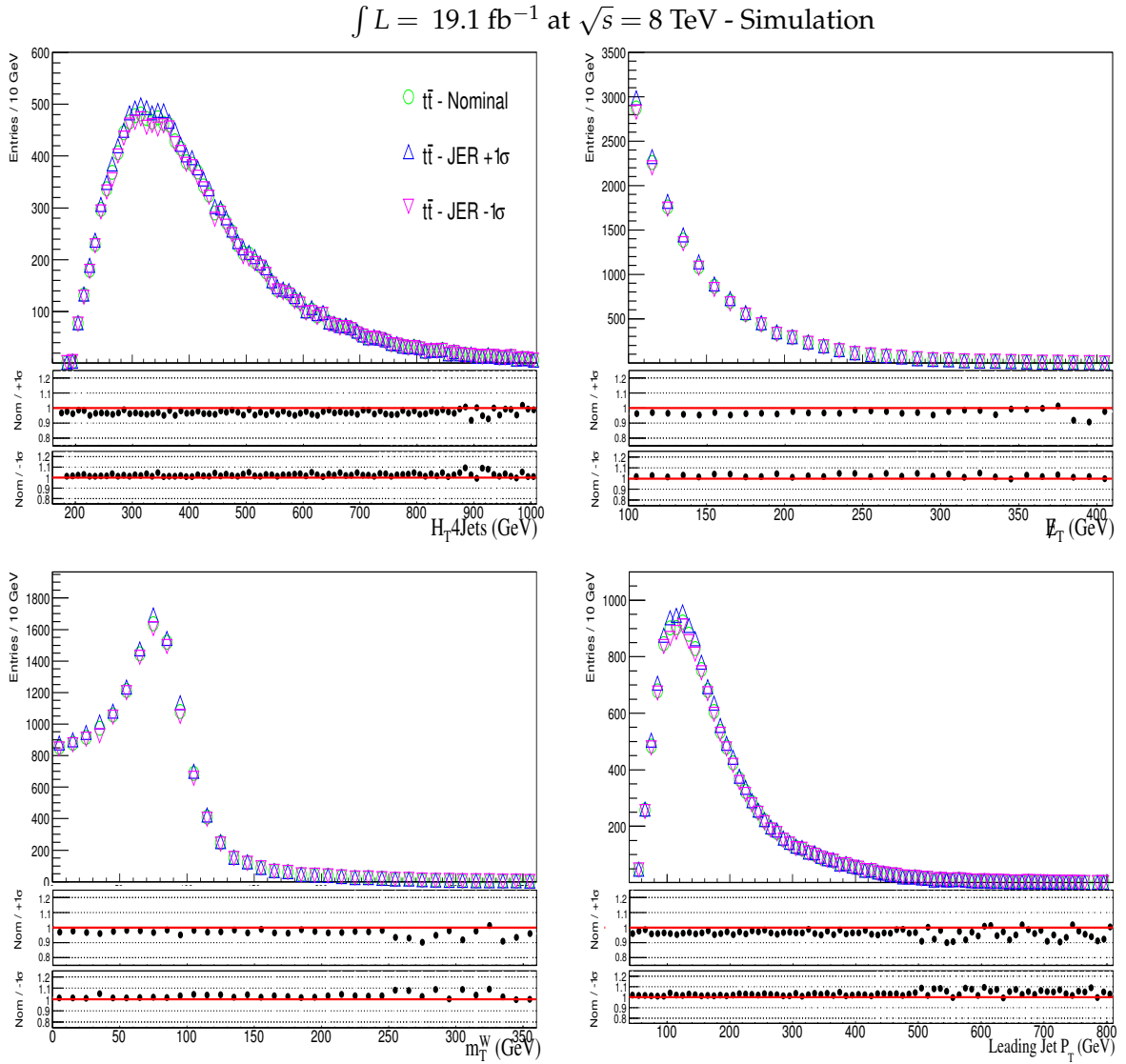


Figure 9.2: The expectation distributions for 19.1 fb^{-1} of integrated luminosity of the scalar sum of the four leading jets (denoted by $H_{T4\text{Jets}}$) (top left), the E_T (top right), the transverse mass of the reconstructed W-boson (bottom left) and the transverse momentum of the leading jet (bottom right) for the nominal (open green circle) and after having applied the $\pm 1\sigma$ variations of the JER (open triangles). The plots have been obtained from the MC@NLO $t\bar{t}$ simulated dataset after the baseline selection.

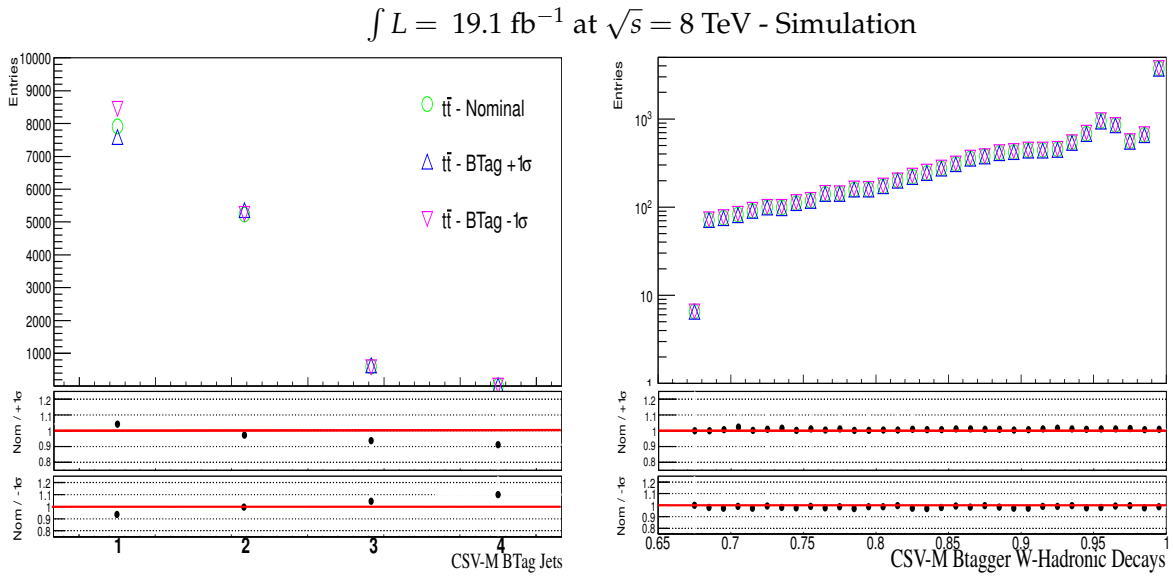


Figure 9.3: The expectation distributions for 19.1 fb^{-1} of integrated luminosity of the number of b -tagged jets (left) and the CSV-M b -tagger distribution of the $t \rightarrow b\bar{q}\bar{q}$ decays discriminant (right) for the nominal (open green circle) and after having applied $\pm 1\sigma$ variations on the b -tag efficiency (open triangles). The plots have been obtained from the $MC@NLO$ $t\bar{t}$ simulated dataset after the baseline selection.

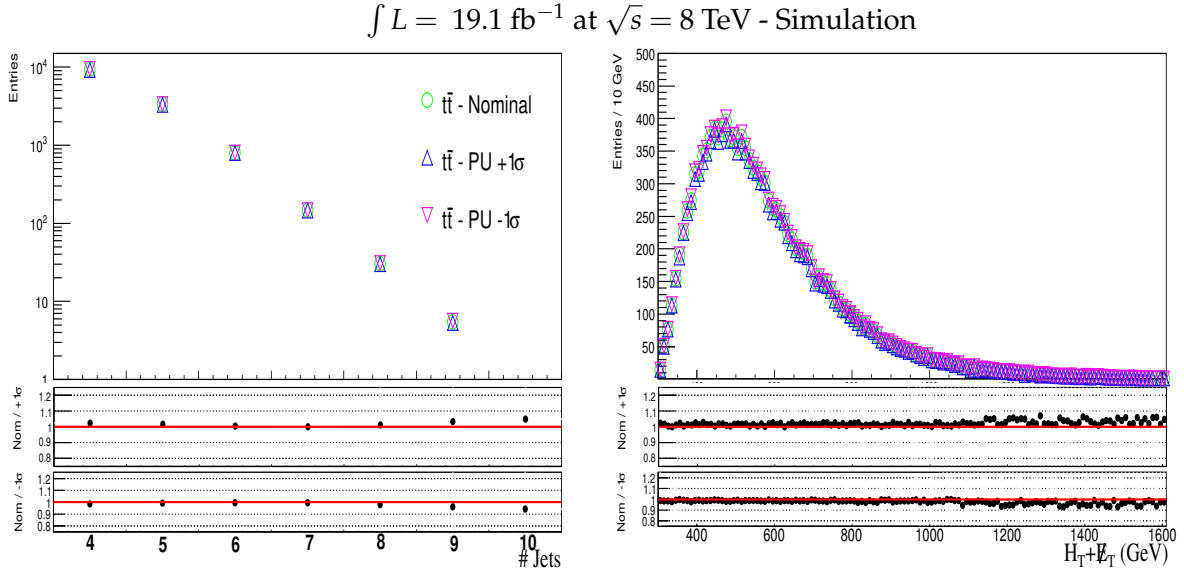


Figure 9.4: The expectation distributions for 19.1 fb^{-1} of integrated luminosity of the number of reconstructed jets (left) and the sum of H_T and E_T (right) for the nominal (open green circle) and after having applied $\pm 1\sigma$ variations on mean number of interactions to account for the PU corrections (open triangles). The plots have been obtained from the $MC@NLO$ $t\bar{t}$ simulated dataset after the baseline selection.

PU reweighting : The simulated events have to be reweighted in order to take into account the observed contributions from PU in data. Practically, each event is weighted taking into account the interplay between PU and the instantaneous luminosity. Still, the uncertainties on the modelling of the PU and that of measurement of the total inelastic cross section affect these weights as well. The mean number of interaction is varied by $\pm 6\%$ (which corresponds to $\pm 1\sigma$) to account for the systematic uncertainty due to PU effects. In Figure 9.4 these effects are demonstrated on the number of reconstructed jets and the sum of H_T and \cancel{E}_T . The effect of this systematic uncertainty is less than 5%.

9.2 Theoretical uncertainties

Cross section normalization : The cross section normalization systematic will affect the level of the distributions of the process in question. Assigning a few percent uncertainty on the nominal cross section reflecting its theoretical prediction should cover it. A more conservative approach is however adopted. We assign a 20% uncertainty on the signal, 12% on the $t\bar{t}$ process and 20% for all of the rest processes i.e. for W+Jets, DY, Single-Top and Rare/Rest processes.

Q^2 scale : In order to study the effect of the uncertainties on the QCD normalization and factorization scales, separate simulated datasets have been built corresponding to the "scale-up" and "scale-down" variations where the Q is varied by a factor 0.5 and 2 respectively. This variation has been applied on the $t\bar{t}$ and the W+jets simulated datasets.

Matching scale : The matching scale is varied in a "matching-up" and "matching-down" fashion, meaning that the nominal matching scale is multiplied by 0.5 and 2 respectively. Similarly to the normalization/factorization variations, this systematic uncertainty was considered for the $t\bar{t}$ and the W+jets simulated datasets.

Table 9.1 summarises the details of the simulated datasets that were used for the Q^2 and the matching scale variations.

Physics Process	8TeV σ (pb)	Generator
$t\bar{t}$ + (0,1,2,3) jets- Scale Up	97.7 (LO)	MadGraph
$t\bar{t}$ + (0,1,2,3) jets- Scale Down	228 (LO)	MadGraph
$t\bar{t}$ + (0,1,2,3) jets- Matching Up	138 (LO)	MadGraph
$t\bar{t}$ + (0,1,2,3) jets- Matching Down	130 (LO)	MadGraph
W + 3 jets - Scale Up	340 (LO)	MadGraph
W + 3 jets - Scale Down	1030 (LO)	MadGraph
W + 3 jets - Matching Up	198 (LO)	MadGraph
W + 3 jets - Matching Down	780 (LO)	MadGraph
W + 4 jets - Scale Up	120 (LO)	MadGraph
W + 4 jets - Scale Down	520 (LO)	MadGraph
W + 4 jets - Matching Up	57 (LO)	MadGraph
W + 4 jets - Matching Down	410 (LO)	MadGraph

Table 9.1: Summary of the SM simulated datasets that were used for the Q^2 and the matching scale variations.

9.3 Effect of systematic uncertainties on MVA distributions

The distributions derived from the systematic simulated datasets are also used in the MVA to perform a separate evaluation, just like it was done for the nominal ones. Figures 9.5 - 9.9 show the MVA discriminant distributions of the MLP classifier obtained from the $t\bar{t}$ simulated datasets for all of the used experimental and theoretical uncertainties that were presented in the previous sections and for four different points in the $(m_{\tilde{t}_1}, m_{\tilde{\chi}_1^0})$ plane. One side note for the $m_{\tilde{t}_1} = 175$ GeV, $m_{\tilde{\chi}_1^0} = 0$ GeV model in particular, is that the shape looks different from the rest of the demonstrated distributions, and we have seen that the shape is almost identical to the distribution obtained from the signal. But this comes as no surprise, as this exact point has qualitatively speaking, the phenomenology of a SM top quark pair process, thus we expect the MVA distributions to have a similar shape. But in general, the effect of these systematics on the MVA distributions is consistent with what was already discussed and demonstrated in the previous paragraphs, with JES and Q^2 scale variation to have the bigger effect from the experimental and theoretical uncertainties respectively.

However, qualitatively speaking what is more important while comparing the nominal and the systematic variation distributions, is that their shapes should resemble, but

differences will still be visible as MVA just classifies events as "background" or "signal" like. Therefore one should not expect a "stable" upward/downward offset throughout the discriminator's range. Further, as the "background-like" events should land mostly in the first-half of the MVA distribution, it then makes perfect sense that the right part of the MVA distributions have relative fewer entries coming from this class of events, hence the uncertainties will be also higher there. Another reason of the discrepancies must be the limited statistics of the systematic simulated datasets and also the fact that the training was performed by using the nominal datasets only. Finally, we should not forget that the simulated events for the systematic studies were made with the use of MadGraph , whereas the nominal with MC@NLO.

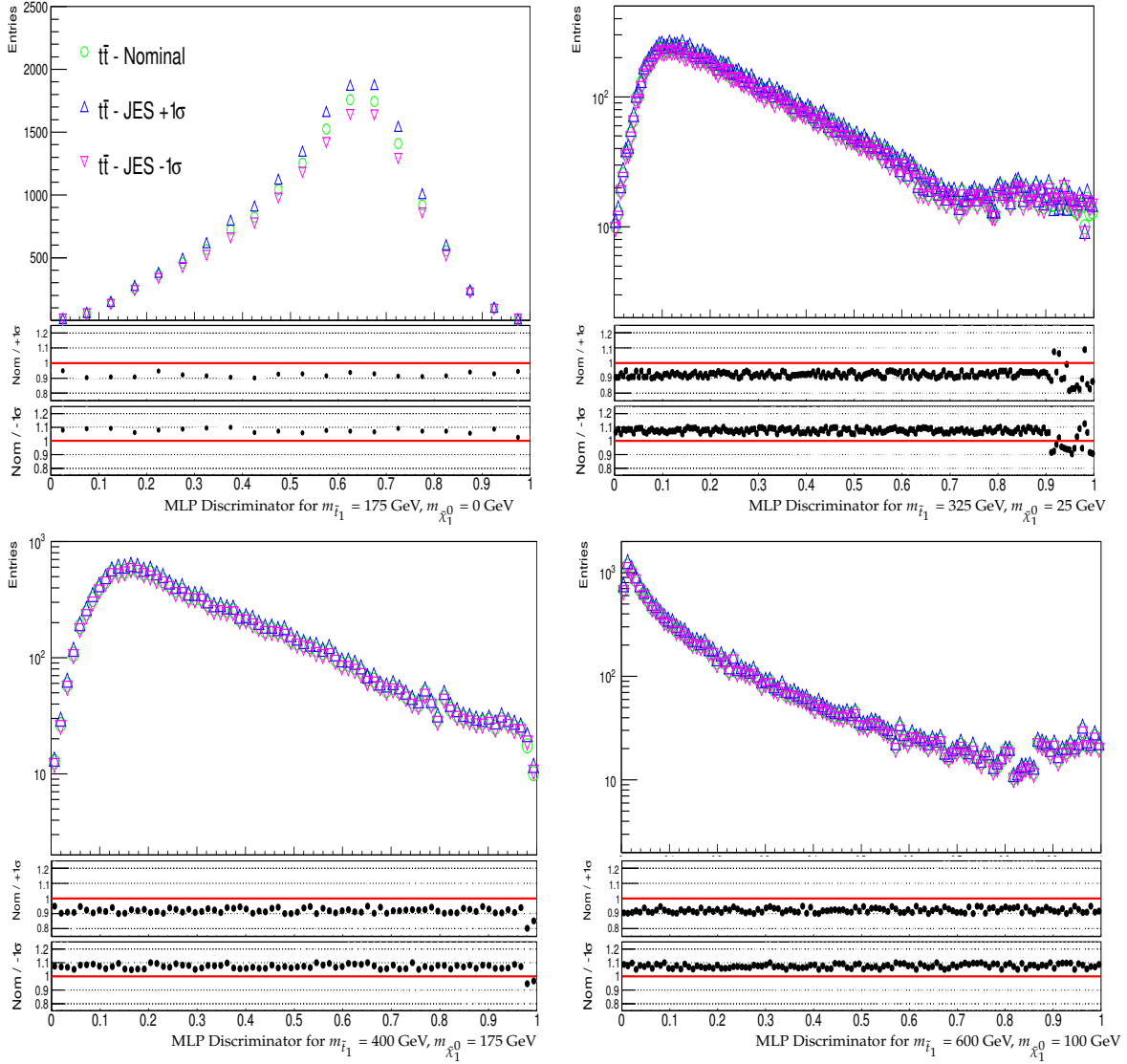
MLP / $\int L = 19.1 \text{ fb}^{-1}$ at $\sqrt{s} = 8 \text{ TeV}$ 

Figure 9.5: The distributions of the MLP classifier for the nominal (open green circle) and the $\pm 1\sigma$ variation of the JES (open triangles) for four different points in the $(m_{\tilde{t}_1}, m_{\tilde{\chi}_1^0})$ plane (indicated on the x-axis of each plot) from the $t\bar{t}$ systematic datasets.

MLP / $\int L = 19.1 \text{ fb}^{-1}$ at $\sqrt{s} = 8 \text{ TeV}$

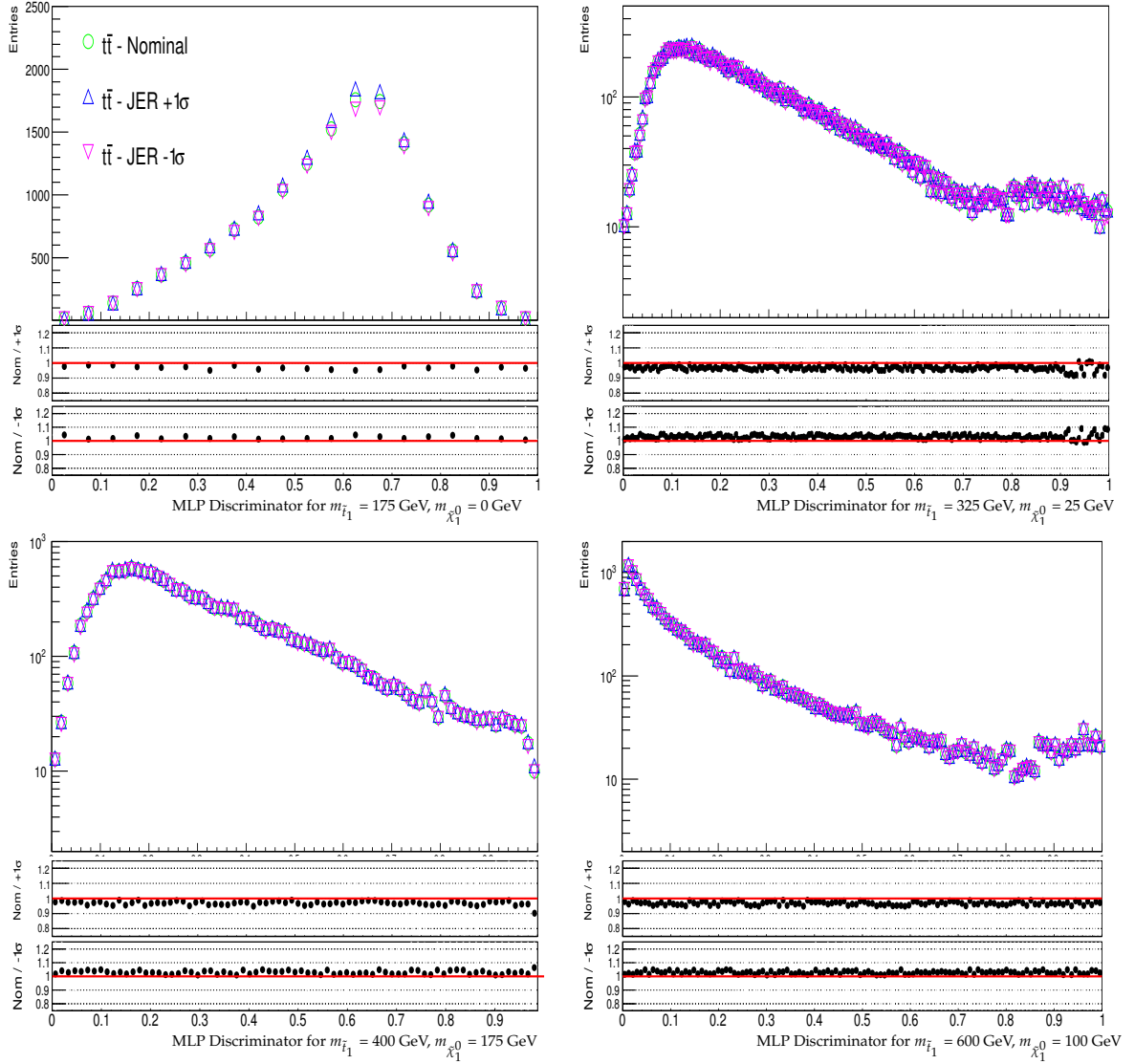


Figure 9.6: The distributions of the MLP classifier for the nominal (open green circle) and the $\pm 1\sigma$ variation of the JER (open triangles) for four different points in the $(m_{\tilde{\tau}_1}, m_{\tilde{\chi}_1^0})$ plane (indicated on the x-axis of each plot) from the $t\bar{t}$ systematic datasets.

MLP / $\int L = 19.1 \text{ fb}^{-1}$ at $\sqrt{s} = 8 \text{ TeV}$

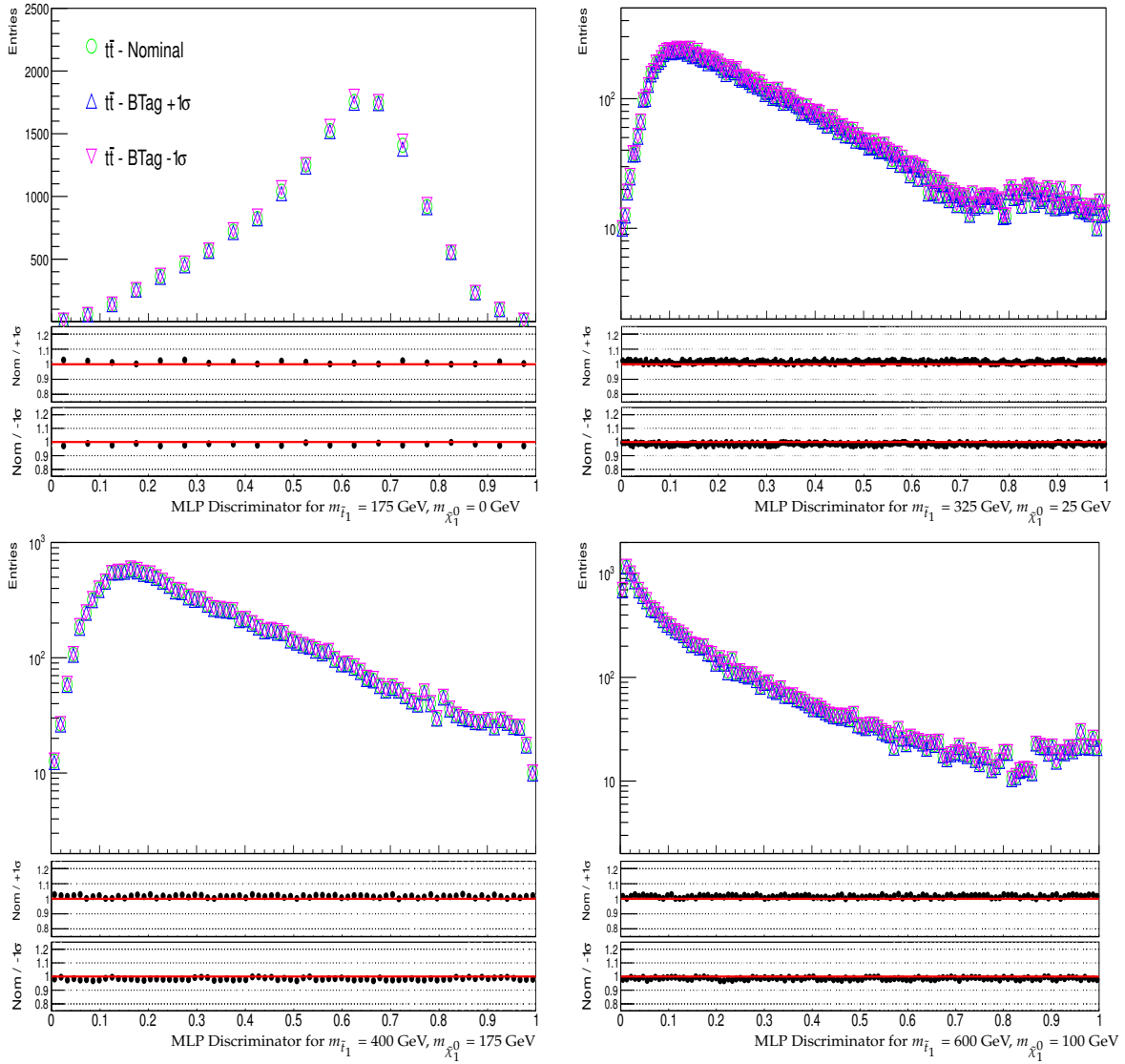


Figure 9.7: The distributions of the MLP classifier for the nominal (open green circle) and the $\pm 1\sigma$ variation of the b-tagging efficiencies (open triangles) for four different points in the $(m_{\tilde{\tau}_1}, m_{\tilde{\chi}_1^0})$ plane (indicated on the x-axis of each plot) from the $t\bar{t}$ systematic datasets.

MLP / $\int L = 19.1 \text{ fb}^{-1}$ at $\sqrt{s} = 8 \text{ TeV}$

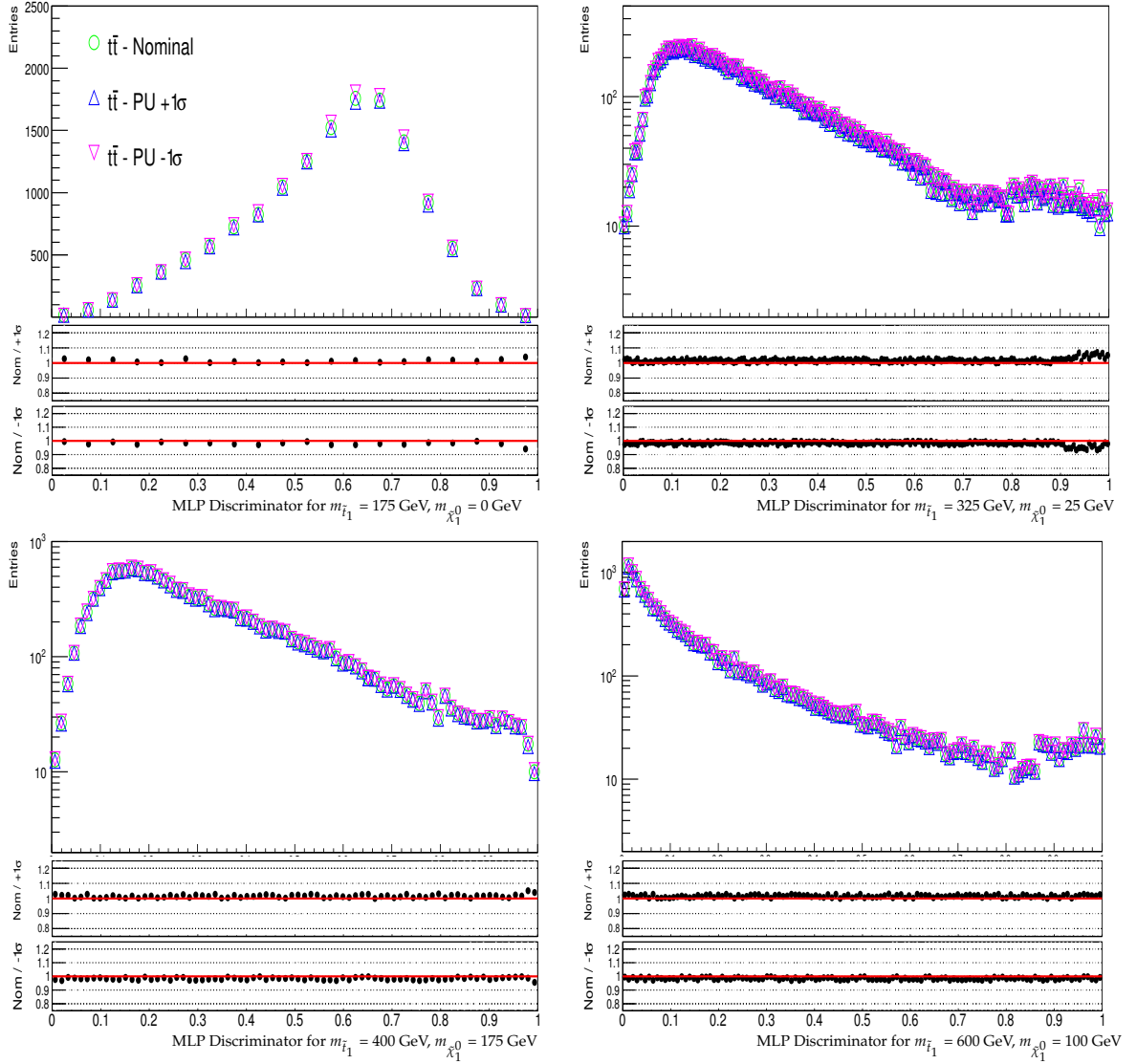


Figure 9.8: The distributions of the MLP classifier for the nominal (open green circle) and the $\pm 1\sigma$ variation of the PU (open triangles) for four different points in the $(m_{\tilde{\tau}_1}, m_{\tilde{\chi}_1^0})$ plane (indicated on the x-axis of each plot) from the $t\bar{t}$ systematic datasets.

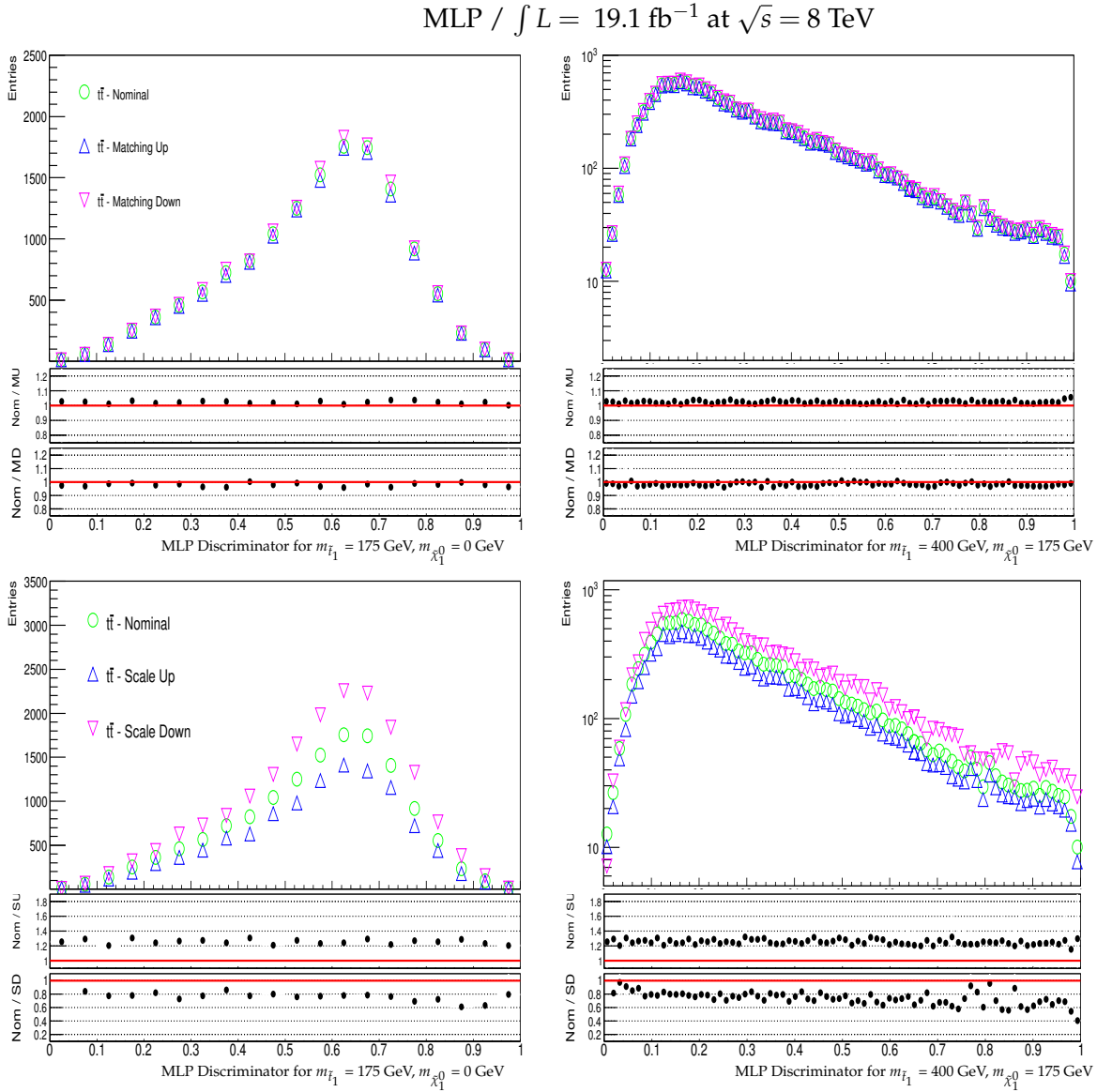


Figure 9.9: Top row : The MVA classifier discriminant distributions for the nominal (open green circle) compared to the Matching-Up (MU) and the Matching-Down (MD) (open triangles) from the $t\bar{t}$ systematic datasets for two different points in the $(m_{\tilde{t}_1}, m_{\tilde{\chi}_1^0})$ plane. Bottom row : The MVA classifier discriminant distributions for the nominal and the Scale-Up (SU) and the Scale-Down (SD) from the $t\bar{t}$ systematic datasets. The points are indicated on the x-axis of each plot.

CHAPTER 10

FITTING TEMPLATE ANALYSIS

In this chapter it is discussed how the template histograms were constructed and optimised in order to perform an analysis of the observed shape of the distribution of the MVA variable. We also present the statistical tools that were used while checking for a possible excess in the data of a SUSY signal over the SM background. Although several statistical procedures are available, here the asymptotic CLs method was used [12, 147] which is what CMS has adopted in most searches. However, in the absence of any significant excess no discovery has been made, thus an upper limit on the cross section of the T2tt model was set. The results are interpreted as an exclusion range in the $(m_{\tilde{t}_1}, m_{\tilde{\chi}_1^0})$ plane.

The chapter is organised as follows : In Section 10.1 the statistical tools that have been used are briefly discussed, while Section 10.2 discusses the optimisation of the used templates, whereas in Section 10.3 several closure tests are presented. Our final experimental results for the p - p collision data that was collected during 2012 corresponding to a total integrated luminosity of 19.1 fb^{-1} in the single- μ channel at $\sqrt{s} = 8 \text{ TeV}$ will be presented in the next chapter.

10.1 Statistical Tools

While performing measurements using the observed data one can be interested to estimate one or even more physical parameters, setting confidence intervals, or even upper/lower limits on the production cross section of the model etc. Typically, a likelihood function is required which should incorporate all information about the theoretical modelling and the actual experimental measure with their associated uncertainties, both the systematic and the statistical ones. In this search, HistFactory [148] was used, which is a tool that builds parametrized PDFs and joint likelihood functions in order to incorporate all associated systematic uncertainties. At the end, with the use of a test statistic, a confidence interval is found for a given parameter of interest. In our case, the parameter of interest is the production cross section of each point in the $(m_{\tilde{t}_1}, m_{\tilde{\chi}_1^0})$ plane.

10.1.1 Construction of the Likelihood function in HistFactory

The HistFactory package is written in C++ and uses the ROOT [149] framework. It uses libraries from the RooFit and the RooStat packages and can be interfaced via XML or python as a front end. Within HistFactory, the construction of the likelihood is done by taking a modular approach to the construction of a PDF, where several templates corresponding to different parameters are used individually or can be combined altogether to get a more complete description of the model under consideration. Furthermore, the systematics are treated as nuisance parameters and get integrated into the likelihood function.

Consider the case where a measurement is based on the distribution of a variable x , while the signal and the background are denoted by "S" and "B" respectively. Also, the normalised distribution of variable x under the signal and the background hypotheses can be expressed as $f_S(x)$ and $f_B(x)$. At this point, we introduce a *signal-strength* parameter which is denoted by μ_s . In principle, the μ_s stands for the parameter of interest and it scales with the expected number of events coming from the signal process. Consequently, $\mu_s = 0$ is consistent with a "background-only" hypothesis, whereas the $\mu_s = 1$ with the "background+signal" hypothesis. Also, a parameter \mathcal{B} is needed that scales with the expected number of background events, but for the sake of simplicity we will assume it to be known, thus fixed. The expected number events from both the

signal and background is :

$$N_{exp} = \mu_s S + B \quad (10.1)$$

For a given value of the parameter μ_s , the probability to measure values $\{x_1, x_2 \dots x_n\}$ of the x variable can be expressed from what is known as the *marked Poisson model* :

$$\mathcal{P}(\{x_1 \dots x_n\} | \mu_s) = \text{Pois}(n | N_{exp}) \left[\prod_{i=1}^n \frac{\mu_s S f_S(x_i) + B f_B(x_i)}{N_{exp}} \right] \quad (10.2)$$

The first term on the right hand side, describes the Poissonian probability to observe n events given the expectation of N_{exp} events. The second part, describes the probability for each individual event to get the value x_i . Taking the logarithm of the above equation, we derive the *extended maximum likelihood expression* :

$$\begin{aligned} -\ln L(\mu_s) &= -n \ln(N_{exp}) + N_{exp} + \ln n! - \sum_{i=1}^n \ln \left[\frac{\mu_s S f_S(x_i) + B f_B(x_i)}{N_{exp}} \right] \\ &= N_{exp} + \ln n! - \sum_{i=1}^n \ln [\mu_s S f_S(x_i) + B f_B(x_i)] \end{aligned} \quad (10.3)$$

In our case, the $f_S(x)$ and the $f_B(x)$ are distributed in N_{bins} total bins. These "template" histograms can now be denoted by h_{data}^b , h_{sgnl}^b and h_{bkg}^b standing for the observed data, the signal and the background expectation respectively, while $b = \{1, 2, \dots, N_{bins}\}$ is the bin index. Therefore, we can write :

$$\mathcal{P}(\vec{h}_{data} | \mu_s) = \prod_{b=1}^{N_{bins}} \text{Pois}(h_{data}^b | \mu_s h_{sgnl}^b + h_{bkg}^b), \quad (10.4)$$

where \vec{h}_{data} is the histogram of the observed data distributed also in N_{bins} total bins.

10.1.2 Systematics in HistFactory

While building the likelihood, it is necessary to integrate the effects of the uncertainties. The uncertainties in general can be classified to the ones that scale the overall yield of the distributions (like the cross section normalization) and those that in addition alter also the shape (like the JES/JER). In particular, for each source of systematic

uncertainty, distributions of the variable x corresponding to the $\pm 1\sigma$ envelop of the systematic effect have to be given as inputs to the HistFactory and for each background and signal process separately. In our case, the variable x is simply the MVA discriminant.

After having constructed all necessary histograms for each process and for each systematic source, HistFactory fits the expected model including the nuisance parameters to the data.

For instance, for each model parameter i and for a given bin b , the expected number of events for the total background is :

$$h_{\text{bkg}}^b(\vec{\alpha}) = \sum_{\text{bkg}} N_{\text{exp,bkg}}^b \left(1 + \sum_{i=1}^p \alpha_i \Delta N_i^b \right) \text{ with } \Delta N_i = \begin{cases} \Delta N_i^{b+}, & \alpha_i > 0 \\ \Delta N_i^{b-}, & \alpha_i < 0 \end{cases} \quad (10.5)$$

where $\vec{\alpha} = \{\alpha_1, \alpha_2, \dots, \alpha_p\}$ is the set of the considered nuisance parameters and ΔN_i^{b+} (ΔN_i^{b-}) stands for the absolute differences in $N_{\text{exp,bkg}}^b$ due to the upward (downward) changes of α_i . Also, the notation is that $\alpha_i = 0$ corresponds to the nominal value of a given parameter i , whereas $\alpha_i = \pm 1$ correspond to the upward/downward $\pm 1\sigma$ variations. Further and to accommodate the uncertainties, constraint terms have to be added to the likelihood. Each additional term describing a given source of systematic uncertainty is constrained by a Gaussian product in the likelihood. That said and without going into many details, the joint likelihood can be written as :

$$\mathcal{P}(\vec{h}_{\text{data}} | \vec{\alpha}, \mu_s, \lambda) = \prod_b \text{Pois}(n_b | \nu_b) \cdot G(L_0 | \lambda) \quad (10.6)$$

$$(10.7)$$

- ν_b : The expected events.
- n_b : The observed events.
- L_0 : The nominal integrated luminosity of the data which is 19.1 fb^{-1} in our case with its uncertainty σ_{L_0} expressed by the gaussian $G(L_0, \sigma_{L_0})$. The strength of this systematic uncertainty σ_{L_0} is scaled with a parameter λ .
- $\vec{\alpha}$: parameters associated to sources of systematic uncertainties.

Once the likelihood is built, HistFactory returns all of the α_i factors from the best fit which can be applied on the collection of the nominal histograms. One expects

that the fitted model should describe data better than the un-fitted one. In that spirit, as a closure test, we apply the fitted nuisance parameters \vec{a} to the initial collection of prediction histograms (cfr Equation 10.5), in order to check the stability and the performance of the fit. At the end, once the likelihood has been assembled it is fed to the CLs method.

10.1.3 The CLs method

In order to test the "signal+background" (H_1) and the "background only" (H_0) hypotheses optimally with the data, a test statistic has to be defined. This test statistic q_{μ_s} , typically is the likelihood ratio of the Poissonian probabilities for the H_0 and the H_1 hypotheses, while $\mu_s = 0$ is consistent with the former and $\mu_s = 1$ with the latter hypothesis.

$$q_{\mu_s} = \frac{\mathcal{P}(\text{Data}|H_1)}{\mathcal{P}(\text{Data}|H_0)} \quad (10.8)$$

with

$$\mathcal{P}(\text{Data}|H_1) = \prod_{i=1}^{N_{bins}} \frac{(s_i + b_i)^{n_i} e^{-(s_i + b_i)}}{n_i!} \quad (10.9)$$

$$\mathcal{P}(\text{Data}|H_0) = \prod_{i=1}^{N_{bins}} \frac{(b_i)^{n_i} e^{-b_i}}{n_i!} \quad (10.10)$$

where n_i , s_i , b_i stand for the number of the observed and the expected number of signal and background events in the i -th bin respectively.

Based on the expected distributions of the test statistic q_{μ_s} , the "CLs" method [147] rejects the H_1 hypothesis at a confidence level of $1 - a$ if :

$$CLs \equiv \frac{p_{s+b}}{1 - p_b} \leq a \quad (10.11)$$

where p_b stands for the p -value based on the H_0 hypothesis while p_{s+b} is the p -value corresponding to the H_1 hypothesis. In this analysis, a value $1 - a$ of 95% will be used, or equivalently the threshold of the CLs is 0.05.

10.1.4 The Asymptotic CLs method

Suppose the case where the true signal-strength parameter is μ_s , while the data happens to be distributed according to a strength parameter μ_{obs} . However, in the case of a single parameter of interest, the likelihood ratio test statistic reads [150]:

$$-2\ln q_{\mu_s} = \frac{(\mu_s - \mu)^2}{\sigma^2} + \mathcal{O}(N^{-1/2}) \quad (10.12)$$

where μ follows a Gaussian with an expected value μ_{obs} and variance equal to σ , while N stands for the size of the data sample.

Having omitted the last term, it can be proven that the above Gaussian approximation works well when the total background events $b_{total} \geq 10$ [150]. This is something that we will need to refer to later on, while optimising the output histograms of the MVA variable which are then given as an input to the HistFactory. Further, while using the asymptotic CLs method, both the theoretical and the experimental uncertainties as they were described in Chapter 9 are taken into account.

10.2 Building the template histograms

By definition, the MVA classifiers are built in such a way that their discriminator values close to zero (one) are classified as background (signal) events. Since HistFactory uses template histograms as inputs to create the likelihood and to perform a global fit, it is true that the way the histograms are constructed can affect the sensitivity on μ_s . But exactly because the signal over background separation cannot be perfect and given as typically the rate of the background is typically some orders of magnitude higher, the "background" contamination in the "signal-like" bins will be higher than the signal contamination in the "background-like" bins of the histogram. The exact level of these effects is connected not only to the MVA performance, but also to the chosen bin width of the histograms. Especially for the later, for a given histogram with a predefined range ($\in [0,1]$ for example), changing the bin width means that the number of bins will be altered as well. For what concerns the MVA workflows, just after the training and the evaluation steps in MVA, a histogram is filled for each MVA method, which is constructed with a predefined number of bins. By default the TMVA uses 25 bins, but of course this choice is a bit arbitrary.

Targeting to maximise the sensitivity in a dynamic way and for each point in the $(m_{\tilde{t}_1}, m_{\tilde{\chi}_1^0})$ plane separately, we require a minimum number of entries per bin. This determines both the final number of bins and the bin width of the histograms. However, we have to remember that since we will use the asymptotic CLs, at least 10 expected background entries per bin must be present (Section 10.1.4). In order to comply with this requirement, once we have collected the MVA discriminant's values, we fill a histogram which has the maximum number of bins provided that the requirements to have at least 10 entries per bin based on the $t\bar{t}$ dataset and that each bin has the same bin width are met. This is repeated for all points in the $(m_{\tilde{t}_1}, m_{\tilde{\chi}_1^0})$ plane. Choosing the $t\bar{t}$ process is justified since this process dominates the background. At the end of this step, a newly constructed histogram is filled which has a different number of bins compared to the initial "default" MVA histogram. This is demonstrated in Figure 10.1, where the final number of bins are shown for both the MLP and the BDT classifiers. We observe that for the MLP, in general the number of bins is around 20-30 for the low stop quark mass region, but when $m_{\tilde{t}_1} > 350$ GeV the number of the bins of the histograms is around 120 or more. On the contrary, for the BDT classifier, for the low stop quark mass region the number of bins is around 10-14, while for $m_{\tilde{t}_1} > 350$ GeV it is less than 10. These conclusions simply mean, that if we had chosen to make use of the "default" MVA histograms without performing the re-binning, for the MLP is obvious that the sensitivity would be decreased. This is true, as in general one can distribute the same information in more bins, thus expecting to increase the sensitivity especially in the last bins. On the other hand, for the BDT the "default" 25-bins configuration would simply result in histograms with empty bins, something that would be problematic for the asymptotic formula to converge.

In general, more bins in the MVA discriminant distribution will result in a better sensitivity to a NP search given as the signal (background) tends to peak for the higher (lower) values, but the sensitivity depends also on the bins content itself. An approach where the histograms have less bins is preferable to reduce the CPU time needed by the HistFactory and the CLs method. In Figures 10.2 the MLP and BDT distributions are demonstrated for the $m_{\tilde{t}_1} = 400$ GeV, $m_{\tilde{\chi}_1^0} = 100$ GeV model. We observe that for the MLP classifier, the background peaks for low values of the discriminant while the signal peaks around 1. For the BDT, the background presents the same features, but the signal presents a somehow flat behaviour. Of course, the exact behaviour of the MVA discriminant based on the signal and that of based on the background is not always the same for all points. However, as a rule of thumb we expect the signal (background) to peak for the more higher (lower) values of the discriminant. In any case, the exact de-

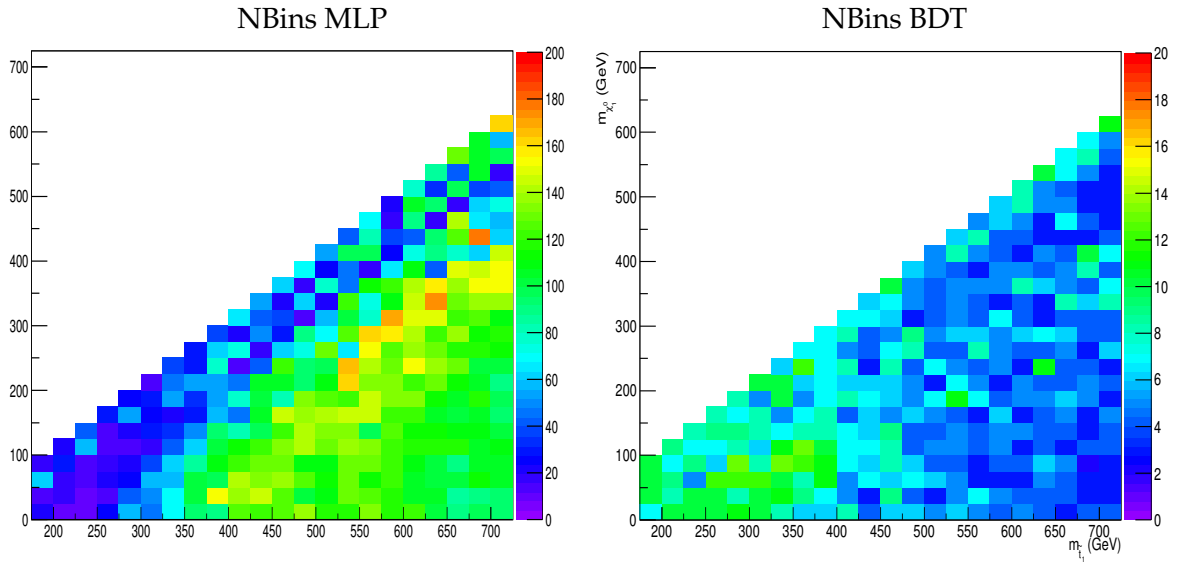


Figure 10.1: The number of bins of the MLP (left) and the BDT (right) distribution histograms after requiring at least 10 $t\bar{t}$ events in each bin.

tails are dependent on the way the different MVA classifiers work, but on the topology and the specific kinematic features of each point in the $(m_{\bar{t}_1}, m_{\tilde{\chi}_1^0})$ plane as well.

19.1 fb⁻¹ at $\sqrt{s} = 8$ TeV

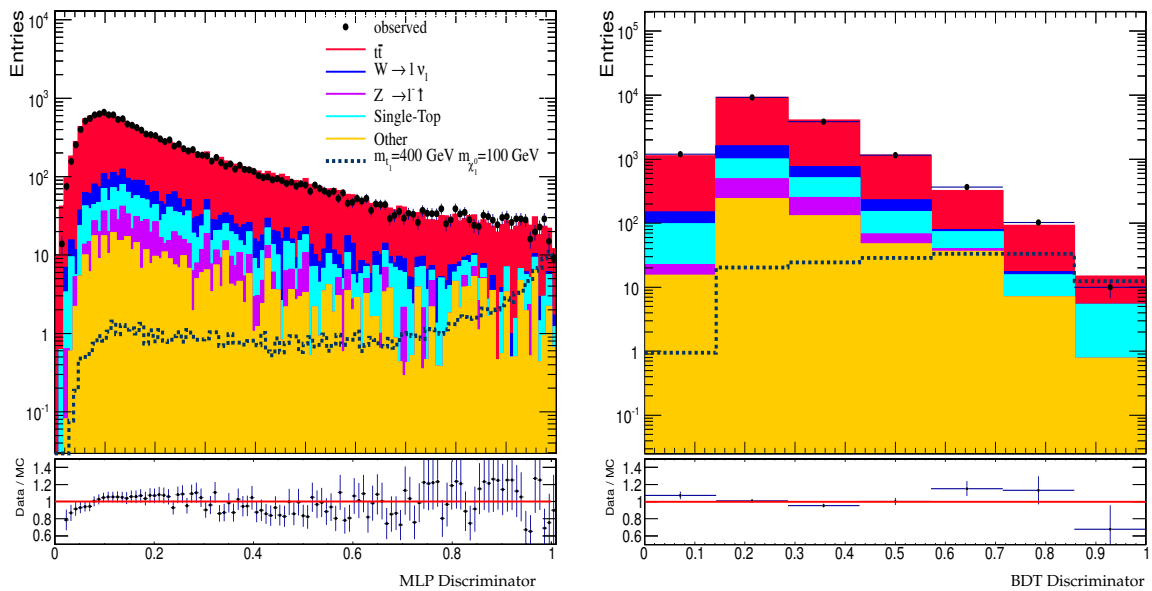


Figure 10.2: The MVA distributions of the MLP (left) and the BDT (right) classifiers after requiring at least 10 $t\bar{t}$ entries to be present at each bin for the $m_{\bar{t}_1} = 400$ GeV, $m_{\tilde{\chi}_1^0} = 100$ GeV model.

10.3 Closure Tests

In this Section, we discuss the performance of several closure tests which serve as a cross check in order to estimate the robustness and check the coherence of our results as well. Since all systematics were integrated in the likelihood as nuisance parameters, it is important to check their effect as individual sources of uncertainties. The fit is using the systematics templates and adjusts their level in such a way, so at the end, the best fit "provides" the best agreement between data and the simulated background model. In case strong discrepancies remain after the best fit has been derived, this can be an indication of either an excess of data over prediction, or that the background model cannot describe the data.

10.3.1 Interpretation of the α_i coefficients

After the HistFactory has built the likelihood and the fit is performed, the α_i factors are returned, which account for the level of a given systematic while obtaining the best fit response. These coefficients practically help to assess the effect of the used uncertainty sources. For instance, a value of $\alpha_{JES} = +0.2$ for a given point in the $(m_{\tilde{t}_1}, m_{\tilde{\chi}_1^0})$ plane should be interpreted as the level (20%) that the fit had to scale the $+1\sigma$ JES template to get the optimal fit response. In general, we should expect some stability of the α_i values throughout the $(m_{\tilde{t}_1}, m_{\tilde{\chi}_1^0})$ plane, while the returned value for each parameter should typically be in the range $[-1, 1]$. A large value of a $|\alpha_i|$ would indicate a strong discrepancy between expectation and data, which could not be accounted by the 1σ envelope of systematic uncertainties considered. In Figure 10.3 the returned α_i values from the fit are shown in the $(m_{\tilde{t}_1}, m_{\tilde{\chi}_1^0})$ plane and for each experimental systematics for the MLP classifier. Similarly, Figures 10.4 and 10.5 demonstrate the α_i coefficients for the theoretical uncertainties associated with the cross section normalization, as well as for the matching and for the Q^2 scale variation for the same classifier.

On average, the effect of the JES is $\sim 0.4 - 0.7 \times 1\sigma$ depending on the exact point, while it is $\sim -0.3 - +0.4 \times 1\sigma$ for the JER. We have to note that the JES looks to be important for most of the points when $\Delta(m_{\tilde{t}_1} - m_{\tilde{\chi}_1^0}) > 150$ GeV while JER has on "average" the same effect throughout the $(m_{\tilde{t}_1}, m_{\tilde{\chi}_1^0})$ plane. This is consistent with the fact that many variables which are highly ranked, thus are getting selected in that region of the parameter space, are constructed from objects like the E_T , or the transverse momentum of

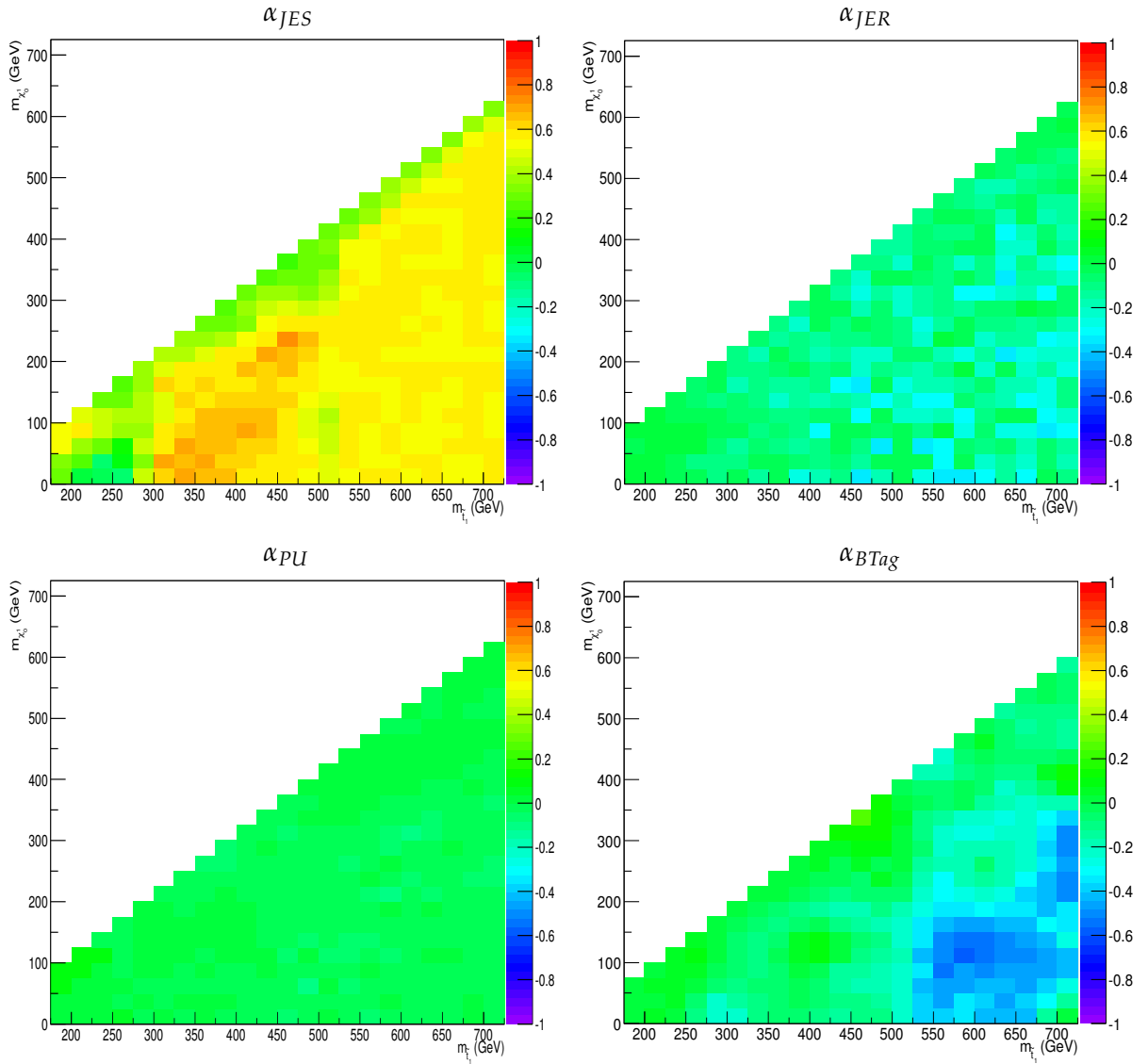


Figure 10.3: The α_i values from the fit for the experimental systematics of JES (top left), JER (top right), PU (bottom left) and BTag (bottom right).

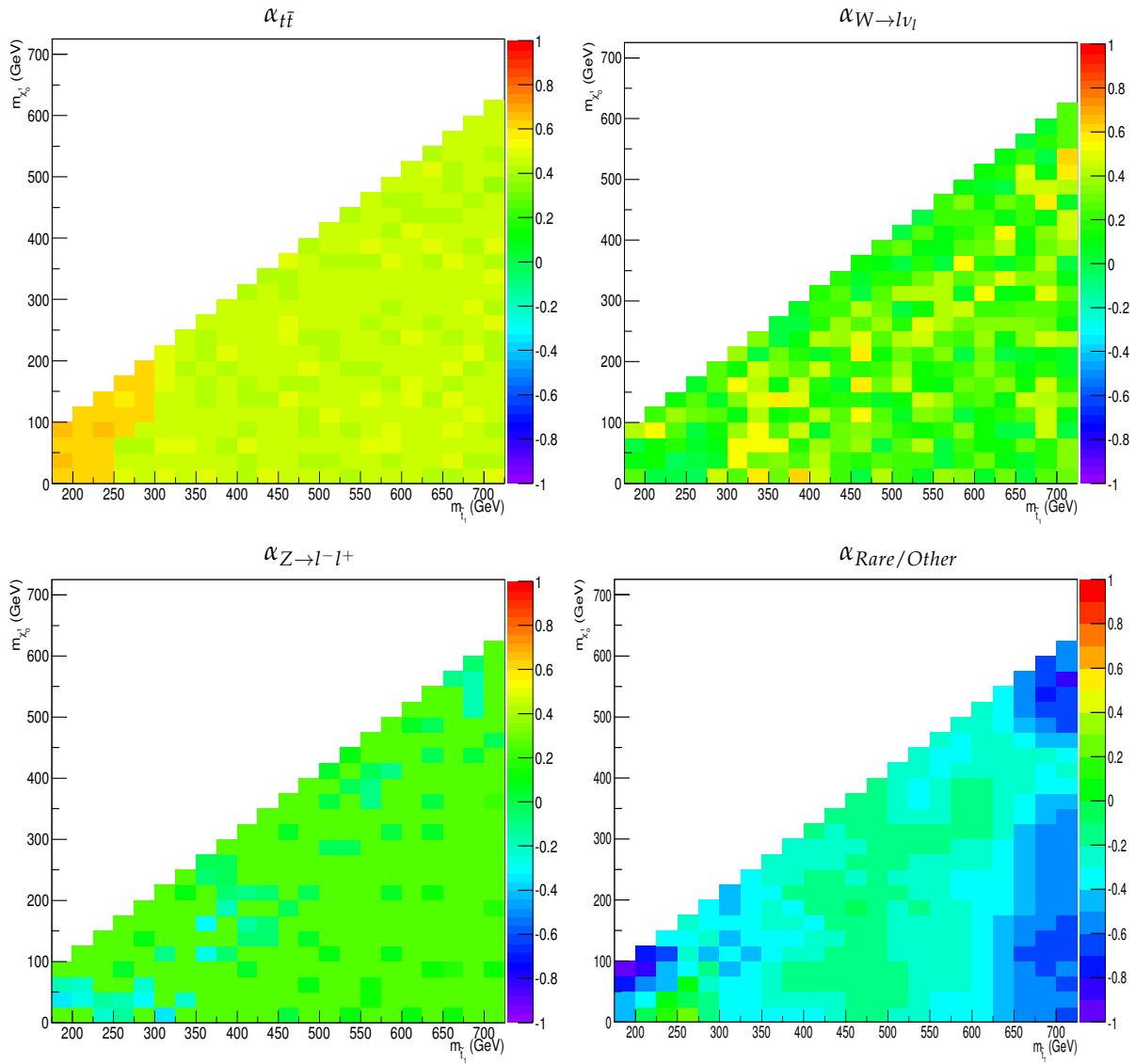


Figure 10.4: The α_i values from the theoretical systematics. These are the cross section normalization applied to the $t\bar{t}$ (top left), the $W \rightarrow l\nu_l$ (top right), the DY (bottom left) and the Rare/other (bottom right) datasets.

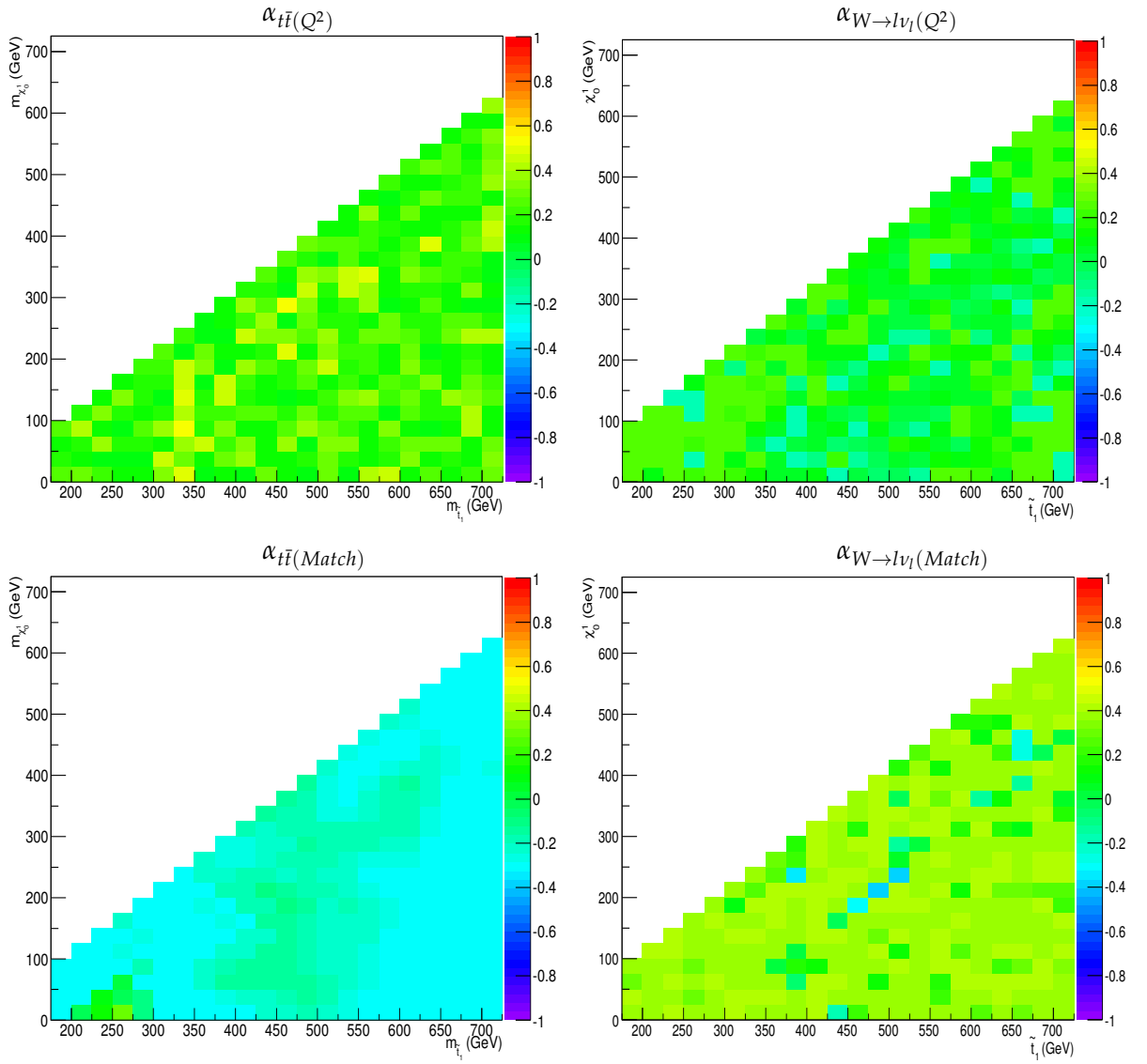


Figure 10.5: The α_i values obtained from the fit for the Q^2 (top row) and the matching scale variations (bottom row) for the $t\bar{t}$ and the $W \rightarrow l\nu_l$ processes.

the jets for instance, whose shape strongly depend on the JES and the JER as well. The effect of the PU uncertainty is smaller, namely $\sim 0.2 \times 1\sigma$, while the b-tagging systematics gives negligible contributions for the stop quark masses less than 500 GeV, but becomes more important for the higher $m_{\tilde{t}_1}$ masses and when $\Delta(m_{\tilde{t}_1} - m_{\tilde{\chi}_1^0}) > 200$ GeV, namely at the level of $\sim -0.5 \times 1\sigma$. This behaviour could be due to the fact that at this region the stop quarks are more boosted, while at the same the b-tagging efficiencies have bigger uncertainties for large values of the p_T of the jets. Hence, the JES, the JER and the b-tagging systematics appear to have the greater impact from the experimental uncertainties.

For the theoretical uncertainties the effect of the cross section normalization for the $t\bar{t}$ process is of the order of $\sim \pm 0.4 - 0.7 \times 10\% \approx 5 - 7\%$ for $m_{\tilde{t}_1} < 300$ GeV while it is $\sim 0.3 - 0.5 \times 10\% \approx 3 - 5\%$ for $m_{\tilde{t}_1} > 300$ GeV. Thus, it appears that this systematic is more important for the low region in the $(m_{\tilde{t}_1}, m_{\tilde{\chi}_1^0})$ plane. On the other hand, for the $W \rightarrow lv_l$ the effect is $\sim 0.3 \times 20\% \approx 6\%$. For the $Z \rightarrow l^-l^+$ and Single-Top (the latter is not shown here) the effect is $\sim 0.1 \times 20\% \approx 2\%$, whereas for the Rare/Other processes $\sim 0.3 \times 20\% \approx 5 - 6\%$ respectively. Negative values reveal that the expectation overshoots data, thus the fit had to scale down the nominal expectation shapes to get a better result. Specifically for the Rare processes, some of the used datasets have been normalised to NLO cross section values, while some others were know to LO only. In any case, typically these processes have small cross sections with large uncertainties and this can be the reason why the α_i has a negative sign in many of the points. For the Q^2 and matching scale variations, their effect appears to be of the level of $\sim 0.3 \times 1\sigma$ in general, indicating that the 1σ envelop for these systematics is probably too conservative.

While trying to interpret all of the above, one has to bear in mind that the different processes have different rates. Since the α_i provides just a way to estimate "how much" of a given systematic has to be used to get the best fit, thus it makes sense to check that while spanning throughout the $(m_{\tilde{t}_1}, m_{\tilde{\chi}_1^0})$ plane there are no big discontinuities between adjacent points for the same source of systematic uncertainty.

As an extra sanity check, Figures 10.6 & 10.7 show the MLP and the BDT classifier distributions respectively and for few points in the $(m_{\tilde{t}_1}, m_{\tilde{\chi}_1^0})$ plane, before and after having applied the corrections on the expectation by using each α_i for the corresponding systematic. In the same plots, the ratio between data and expectation before (denoted by Data/MC) and after having applied the corrections (denoted by Data/MC $_{\alpha_p}$) are given. From the MVA systematics distributions assuming no correlation between the

systematic sources, the absolute uncertainty per bin for the systematic i is :

$$\Delta S^{bin} = \sqrt{\sum_{i \in Systematics} \left(\frac{\Delta N_i}{2}\right)^2} \quad (10.13)$$

where $\Delta N_i = N^+ - N^-$ is the absolute difference between the expected number of events from the upward and the downward effects. Dividing the ΔS^{bin} value with the expected bin content, we also obtain the relative uncertainty per bin. At the end, we fit the relative uncertainty as a function of the discriminator and this provides a content and a shape parameter as can be seen in Figures 10.6 & 10.7 (bottom right plots). Further, Figure 10.8 illustrates the constant and the slope terms obtained from this linear fit for each point in the $(m_{\tilde{t}_1}, m_{\tilde{\chi}_1^0})$ plane which helps us to assess the trend of the relative uncertainty bin by bin, which is at the level of $\sim 10 - 14\%$ corresponding to the 1σ systematic envelope and is shown in the plots as light green bands around each expected bin content. In general, we observe that the agreement between expectation and data improves after the corrections and the "corrected" bins are within the ΔS boundaries.

Finally, we have checked the effect of the fitted nuisance parameters in control samples on the variables that were used for the MVA training for several different points in the $(m_{\tilde{t}_1}, m_{\tilde{\chi}_1^0})$ plane and no strong discrepancies have been observed.

10.3.2 χ^2 tests

We also performed two χ^2 goodness-of-fit tests. One in order to test how well data agrees with expectation *after* having corrected the latter for the α_i factor and another by using the "individual" α_i coefficients we obtained from the fit for each systematic uncertainty source in the following definition :

$$\chi^2 = \sum_{i \in Systematics} \alpha_i^2 \quad (10.14)$$

To assess the significance of the possible data to expectation agreement, we calculate the $\chi^2/(n - 1)$ where n stands for the number of degrees of freedom. In the data versus expectation χ^2 , n is the number of bins of the histogram, while for the second χ^2 , n equals to the total number of the used systematics, but in both cases $n > 10$. Finally, from tables we read the critical value χ_{crit}^2 corresponding to a significance level of $a = 0.05$ and we should reject the null hypothesis if the $\chi^2 > \chi_{crit}^2$. In general, no χ^2

$$\text{MLP} / \int L = 19.1 \text{ fb}^{-1} \text{ at } \sqrt{s} = 8 \text{ TeV}$$

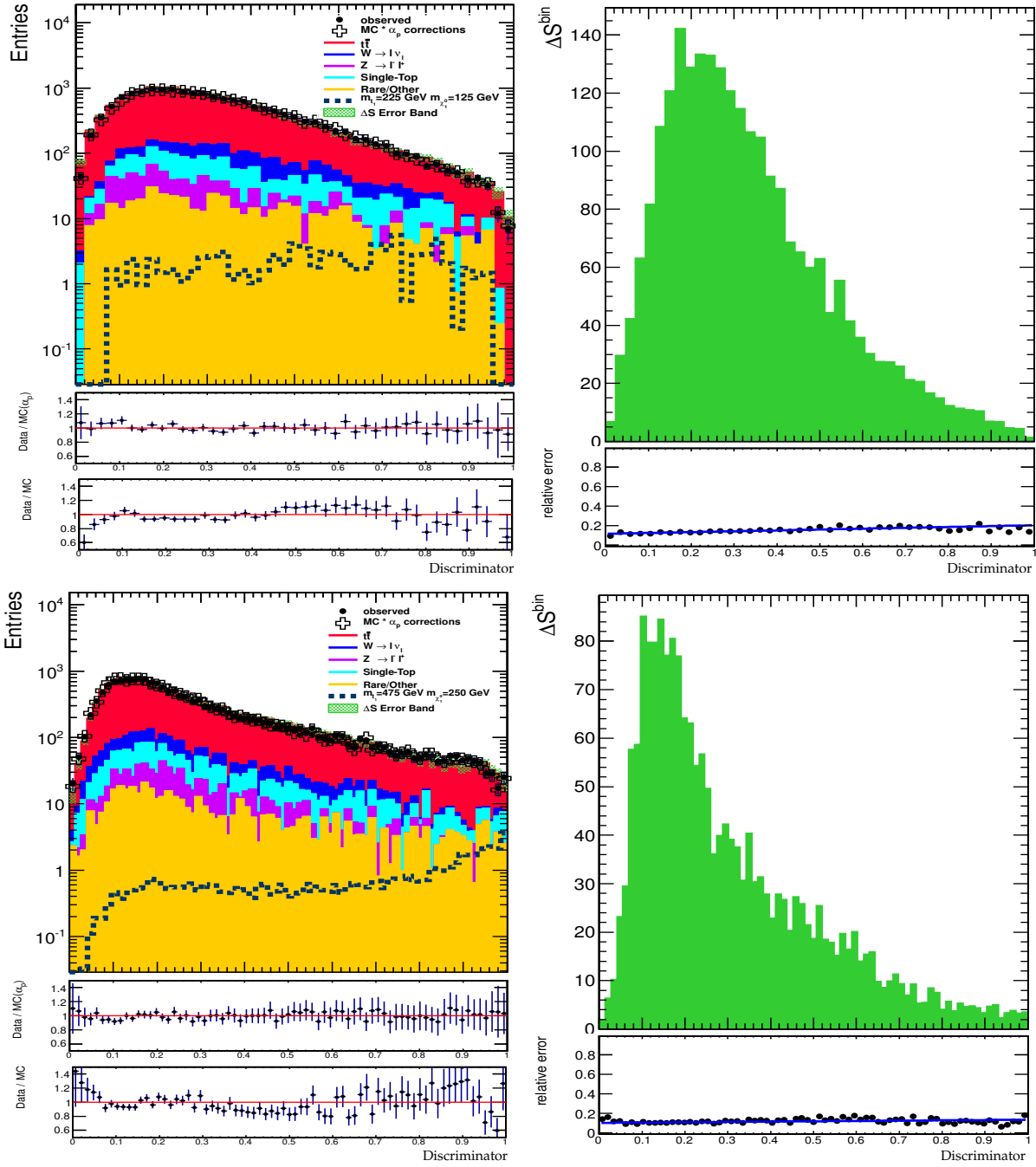


Figure 10.6: The MLP classifier distributions (left column) for two different points in the $(m_{\tilde{t}_1}, m_{\tilde{\chi}_1^0})$ plane (noted on the histograms) before (solid colours and bottom ratio plot) and after having applied the corrections obtained from the fit response for all of the α_i factors associated with the systematics (open cross and top ratio plot). Also the absolute and relative uncertainties are given (right column), whereas for the latter we perform a linear fit to estimate the trend.

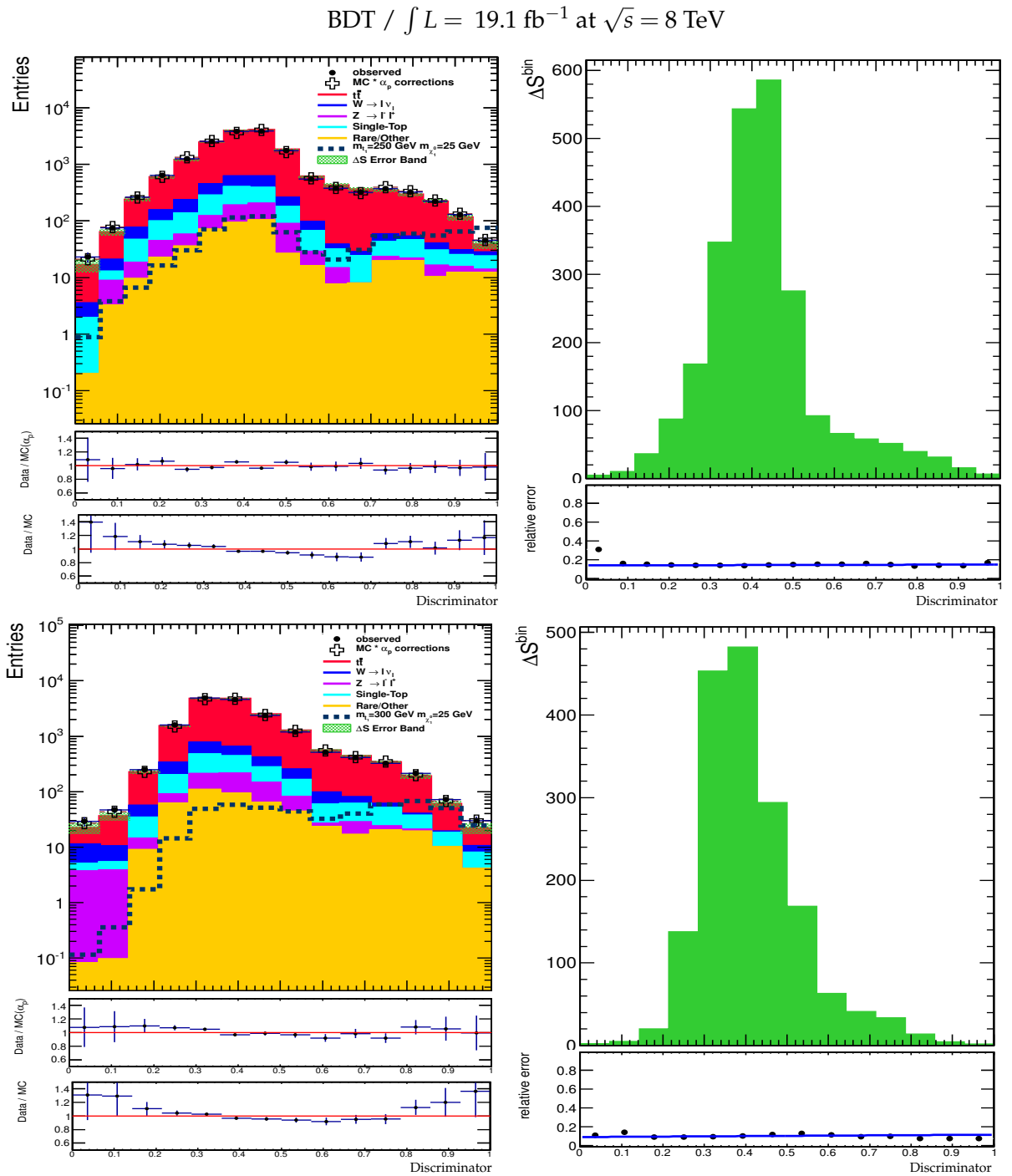


Figure 10.7: The BDT classifier distributions (left column) for two different points in the $(m_{\tilde{t}_1}, m_{\tilde{\chi}_1^0})$ plane (noted on the histograms) before (solid colours and bottom ratio plot) and after having applied the corrections obtained from the fit response for all of the α_i factors associated with the systematics (open cross and top ratio plot). Also the absolute and relative uncertainties are given (right column), whereas for the latter we perform a linear fit to estimate the trend.

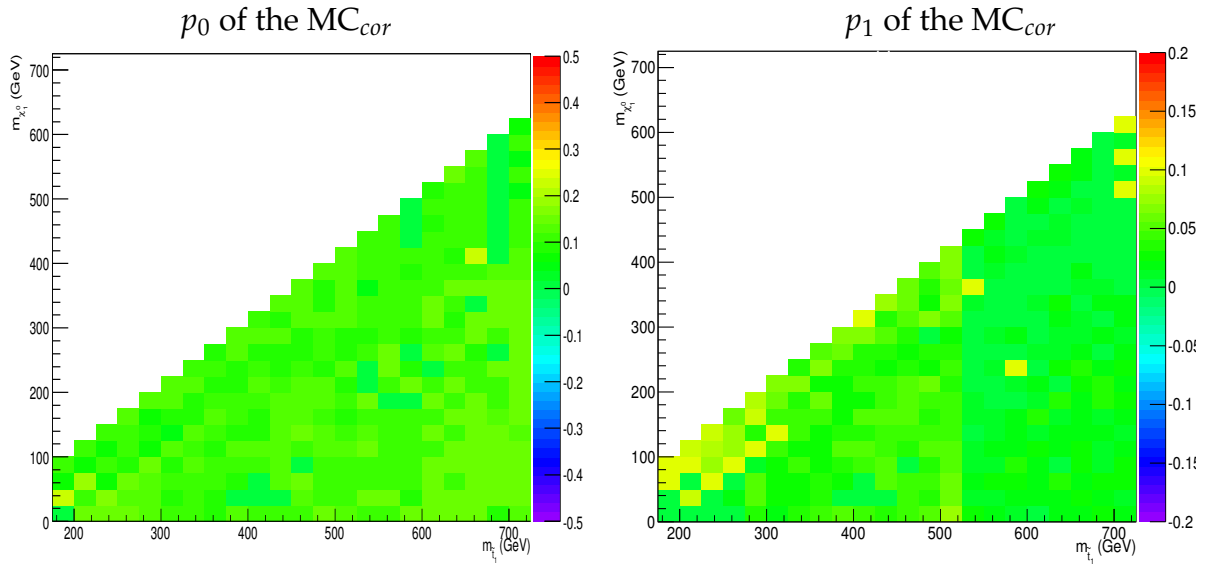


Figure 10.8: The constant (p_0) (left) and the slope (p_1) (right) terms from the linear fit performed on the MVA MLP MC_{cor} distributions, i.e. after having corrected for the α_i coefficients in order to assess the trend of relative uncertainty bin by bin.

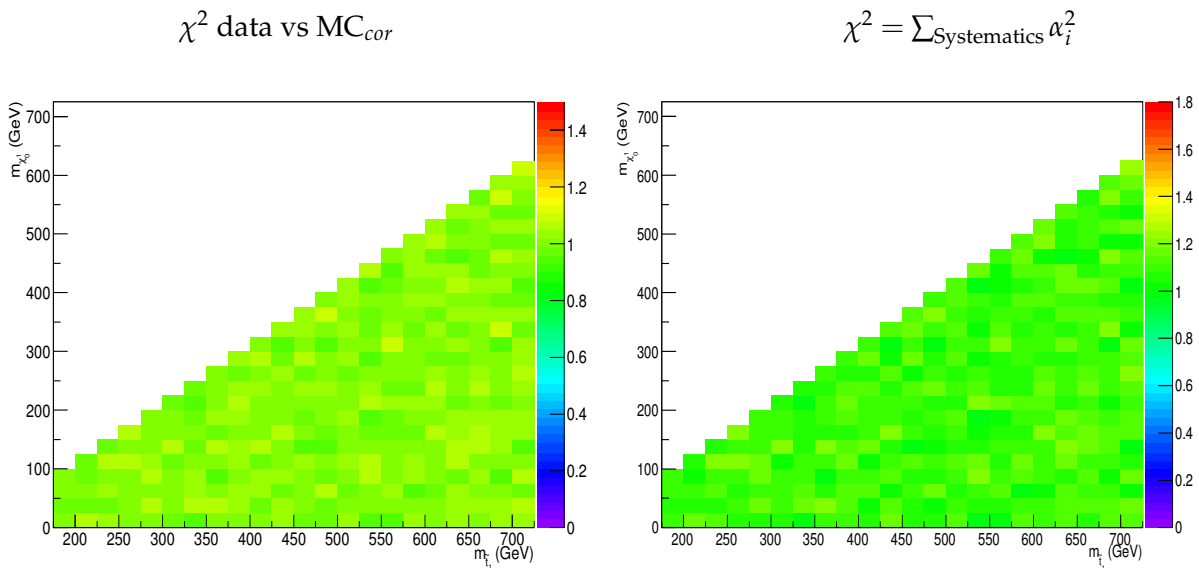


Figure 10.9: The normalised χ^2 of data vs expectation comparison (left) and that defined as $\chi^2 = \sum_i (\alpha_i)^2$ (right). In the former case, the values are below the critical values [151], while for the latter we observe that in general the χ^2 is $\mathcal{O}(1)$.

values were found above the critical ones, hence the null hypothesis is not rejected and we can state that the data agrees well with the corrected expectation from simulation. In Figure 10.9, the normalised χ^2 where the values are $\mathcal{O}(1)$, as well as the χ^2 formed using Equation 10.14 are shown.

10.3.3 Signal injection test

A signal injection test was performed as well. To do this, we inject as "data" the sum of the background and the signal prediction for the a given signal model point corresponding to $m_{\tilde{t}_1} = 500$ GeV, $m_{\tilde{\chi}_1^0} = 75$ GeV. The signal cross section corresponds to the parameter of interest and was set to a "dummy" value of unity, i.e. $\mu_s = 1$. Hence, while fitting the signal strength μ_s , the fit will return the best fitted value $\hat{\mu}_s$. The fit response was $\hat{\mu}_s = 0.995 \pm 0.168$, thus qualitatively speaking, in the signal injection test, "we got back what we have put in". We have to note however, that although we performed a signal injection test at one point, it is expected that the conclusion should be valid in the full $(m_{\tilde{t}_1}, m_{\tilde{\chi}_1^0})$ plane as we make use of the same method.

You can know the name of a bird in all the languages of the world, but when you're finished, you'll know absolutely nothing whatever about the bird... So let's look at the bird and see what it's doing – that's what counts.

Richard Feynman

CHAPTER 11

RESULTS, CONCLUSIONS AND PERSPECTIVES

11.1 Experimental Results

After the baseline event selection, a MVA event classifier is calculated for each signal hypothesis in the $(m_{\tilde{t}_1}, m_{\tilde{\chi}_1^0})$ plane. The distribution obtained from data is compared with the expected distribution in the "background" and the "background+signal" hypothesis with the CLs criterion, while also both experimental and theoretical systematics are taken into account. The last step is to obtain the upper limits in the $(m_{\tilde{t}_1}, m_{\tilde{\chi}_1^0})$ plane for each signal model cross section obtained from the fitted signal strength. If the CLs response is below the model's cross section, this point is excluded. In the direction of $m_{\tilde{\chi}_1^0}$ a linear interpolation was used to obtain the cross section upper limit at random points in the $(m_{\tilde{t}_1}, m_{\tilde{\chi}_1^0})$ plane. In Figure 11.1 the final limit on the $(m_{\tilde{t}_1}, m_{\tilde{\chi}_1^0})$ plane with the cross section values obtained from the asymptotic CLs method is demonstrated along with a zoom into for the region where $m_{\tilde{t}_1} \leq 350$ GeV. As it has been elaborated in the previous chapters, the histograms have been built while requiring at least 10 entries per bin based on the $t\bar{t}$ process from simulation for both the MLP and BDT classifiers. The obtained final results are shown in Figure 11.2.

Briefly, we observe that the MLP classifier yields stronger expected and observed upper limits compared to the BDT classifier. Therefore and at 95% CL, the excluded region in the $(m_{\tilde{t}_1}, m_{\tilde{\chi}_1^0})$ plane is between 175 GeV and 675 GeV for massless $\tilde{\chi}_1^0$, while stop

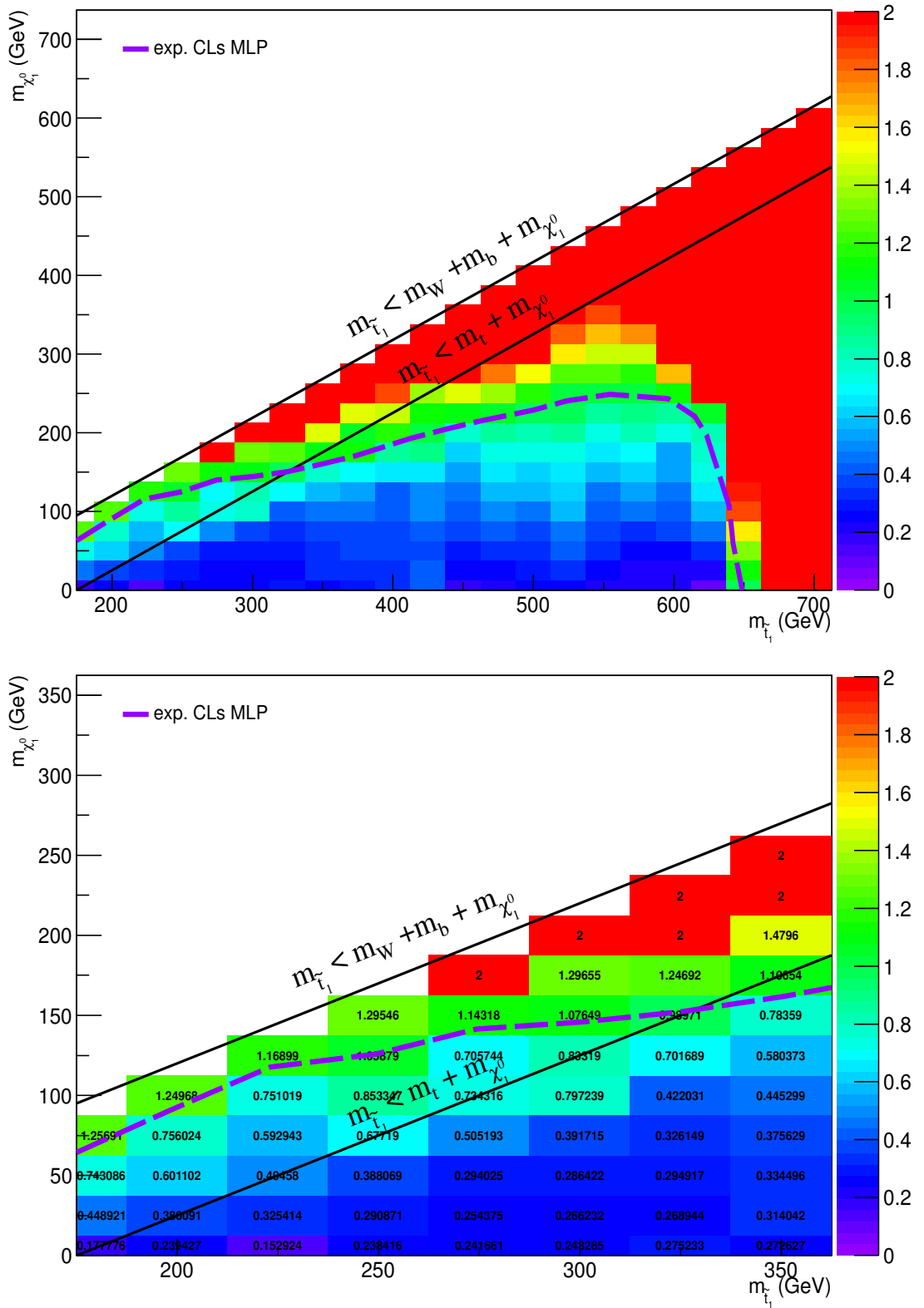


Figure 11.1: The expected limit on stop quark versus neutralino masses for the $\tilde{t}_1 \rightarrow \tilde{\chi}_1^0 + t$ SMS model for the MLP classifier (top plot) and a zoom-in for $m_{\tilde{t}_1} \leq 350$ GeV (bottom plot), along with the $\hat{\mu}_s$ values obtained from the asymptotic CLs. The zoomed-in plot is demonstrating how the linear interpolation was done in order to draw the exclusion line as it is explained in the text.

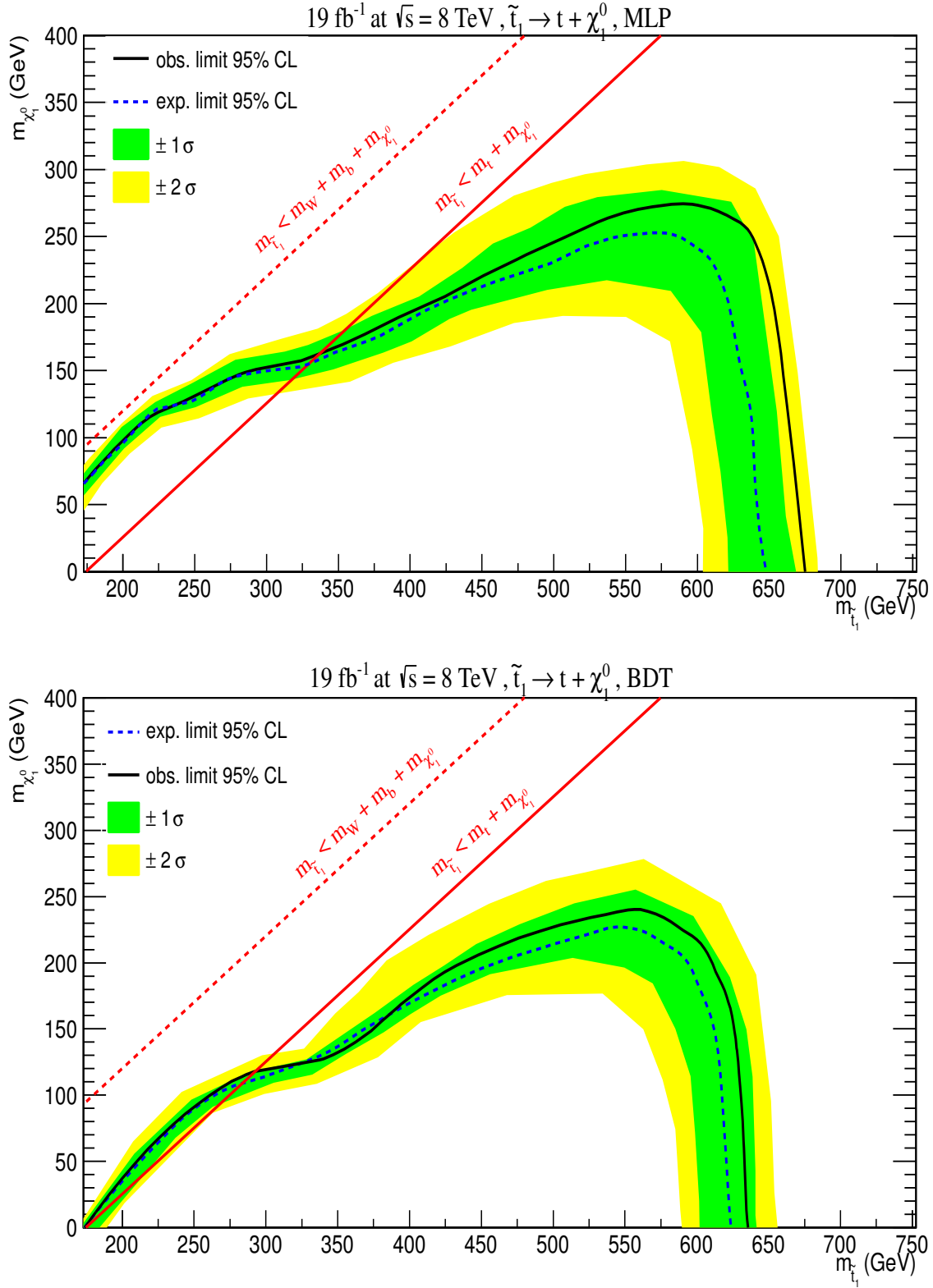


Figure 11.2: The limit on stop quark versus neutralino masses for the $\tilde{t}_1 \rightarrow \tilde{\chi}_1^0 + t$ SMS model, both for the MLP (top) and BDT (bottom) classifiers. The MLP classifier gives stronger expected and observed limits compared to the BDT which can be attributed to the fact that the template histograms have more bins in the former case as was discussed in Section 10.2. We also have to note the sensitivity in the compressed region for $m_{\tilde{t}_1} < 350$ GeV for the MLP classifier.

quark masses up to ~ 625 GeV are excluded for $\tilde{\chi}_1^0$ masses up to ~ 275 GeV. For the BDT, the excluded region for massless LSP are between 175 GeV and ~ 640 GeV, while stop quark masses up to ~ 575 GeV are excluded for $\tilde{\chi}_1^0$ masses up to ~ 230 GeV. We also observe that for the MLP classifier there is sensitivity in the compressed region where it holds $\Delta m = m_{\tilde{t}_1} - m_{\tilde{\chi}_1^0} < m_t$ and for $m_{\tilde{t}_1} < 350$ GeV. Finally, the expected and the observed limits agree within 2σ uncertainty for both the MLP and the BDT classifiers, thus no strong deviation that could indicate the existence of new physics has been observed.

11.2 Conclusions and comparison with other searches

In this Section we compare and discuss our experimental results with already published ones from other similar searches, but also against a cut-and-count approach.

11.2.1 Comparison with other published results

The ATLAS collaboration has recently published results based on $\sim 21 \text{ fb}^{-1}$ of data at the EPS-2013 conference [52]. The same event topology was used, along with a very similar event selection. Similarly, the CMS collaboration has published results from two analyses, one with the use of the BDT NN classifier for $\sim 19.5 \text{ fb}^{-1}$ of data [53] and another with the use of the "razor" variable for $\sim 19.3 \text{ fb}^{-1}$ of data [54]. The final upper limit in the $(m_{\tilde{t}_1}, m_{\tilde{\chi}_1^0})$ plane for both analyses can be seen in Figure 11.3 [45].

However, to make a fair comparison, we remind that our search considered only the single-muon final state, while both the ATLAS and the CMS results considered both single-electron and single-muon final states. Further, both the ATLAS and the CMS analyses considered the area between $m_{\tilde{t}_1} \in [100, 800]$ GeV while at the time we performed this analysis, the available simulated datasets were covering only the $m_{\tilde{t}_1} \in [175, 700]$ GeV region (i.e. always $m_{\tilde{t}_1} \geq m_t$ in our case) of the parameter space.

For the region where the stop quark is heavier than the top quark ($m_{\tilde{t}_1} \geq m_t$) based on the observed limit, the ATLAS search excludes the region of stop quark and LSP masses between 200 GeV and 610 GeV for massless LSP at 95% CL, while for massive LSP, the limit is close to 500 GeV for the stop quark mass, while the LSP mass is 250 GeV. For the CMS 1-lepton analysis, again based on their observed limit and for the single lepton analysis, the region of the excluded stop quark masses 95% CL are between 200 GeV

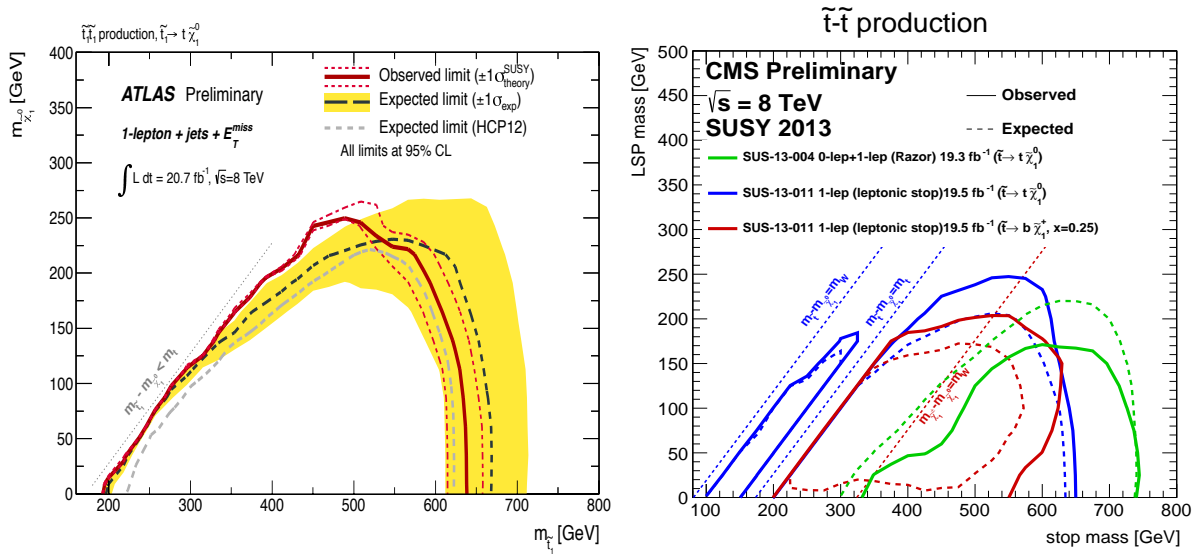


Figure 11.3: The public result from the ATLAS [52] (left) and the CMS collaboration [45, 53, 54] (right) for the $\tilde{t}_1 \rightarrow t + \tilde{\chi}_1^0$ topology in 1-lepton final state assuming the BR ($\tilde{t}_1 \rightarrow t + \tilde{\chi}_1^0$) to be 100%.

and 650 GeV for massless LSP. The limit is around 600 GeV for stop quark masses when the LSP is up to 240 GeV. The CMS "razor" analysis has no sensitivity for $m_{\tilde{t}_1} < 350$ GeV, while it excludes stop quark masses up to 710 GeV for massless LSP and it also excludes stop quarks of 670 GeV for a LSP mass of 150 GeV. Table 11.1 lists both the expected and the observed limits of this search and the currently published results from the CMS and the ATLAS collaborations. It can be seen that the MLP analysis yields better results compared to the BDT, both for the expected and the observed limits.

Further, our results have sensitivity in the compressed spectrum. This region starts when the top quark is off-shell i.e. when the condition $m_{\tilde{t}_1} < m_t + m_{\tilde{\chi}_1^0}$ holds. The ATLAS analysis is not sensitive at all to this region of the parameter space, while the CMS single-lepton analysis puts also limits there, but for $m_{\tilde{t}_1} \leq m_t$. Our search excludes well the region for stop quark masses up to 325 GeV and for a neutralino of ~ 150 GeV for the MLP classifier. Given all the above, our experimental results pose to date one of the most stringent upper limits on the T2tt model decaying to single-muon final state and in some regions the most stringent limits. Even more, both CMS and ATLAS analysis have considered polarised top quarks as well while we have not. More particular, in the ATLAS case an optimised polarisation treatment was employed where the stop quark and neutralino left-right mixing in the coupling is such that top quarks are produced mostly right handed and this affects the leptons acceptance as

they preferentially "fly" parallel to the top quark boost. Further, the CMS collaboration result [53] also investigated both right and left handed top quark scenarios and it was demonstrated that in the case of right handed top quarks the size of this effect can improve the sensitivity by 20-30 GeV. Hence, we believe that if we were able to also use polarised top quarks, our results would have probably more sensitivity. We attribute the behaviour of our results to the fact that we have optimised both the selection and the training of a separate MVA of the more discriminating variables at each point of the $(m_{\tilde{t}_1}, m_{\tilde{\chi}_1^0})$ plane, to the $t\bar{t}$ cross section constraint (especially in the low stop mass region, i.e. where $m_{\tilde{t}_1} < 350$ GeV), but also to the multiplicity of bins of the template histograms so that the asymptotic CLs to work in the most efficient way.

At this point we have to note that not all possible systematics have been considered in this analysis, like that on the lepton veto or even uncertainties on the ISR. In such a case a lot more CPU time would be needed which we did not have at our disposal at the time, although would be certainly beneficial to include them in the future. Also, other considerations could rise from a possibly different treatment of the b-tagging signal systematic (FastSim versus FullSim bias correction and thus additional uncertainty), but both the CMS collaboration published results have been used FastSim (FullSim) for the simulation of the signal (background) simulated datasets like we did.

Search	$m_{\tilde{t}_1}$ range (GeV) for $m_{\tilde{\chi}_1^0} = 0$		$m_{\tilde{t}_1}$ (GeV) for $m_{\tilde{\chi}_1^0} > 0$ (GeV)	
	Observed $m_{\tilde{t}_1}$	Expected $m_{\tilde{t}_1}$	Observed $m_{\tilde{t}_1} / m_{\tilde{\chi}_1^0}$	Expected $m_{\tilde{t}_1} / m_{\tilde{\chi}_1^0}$
This search single- μ / MLP	175-675	175-650	625 / 275	590 / 250
This search single- μ / BDT	175-635	175-625	575 / 230	550 / 220
ATLAS 1- ℓ [52]	200-610	200 - 660	500 / 250	600 / 225
CMS 1- ℓ [53]	200-650	200 -630	600 / 240	560 / 200
CMS 0+1- ℓ "razor" [54]	350-710	300 - 710	670 / 150	670 / 220

Table 11.1: Comparison of expected and observed limits for the massless as well as for the massive $\tilde{\chi}_1^0$ case between this search (for both used classifiers MLP and BDT) and the public ones from both the CMS and the ATLAS collaborations when $m_{\tilde{t}_1} \geq m_t$.

11.2.2 Comparison with a cut-and-count method

As a final check, we compare our results against a *cut-and-count* method. The first step to accomplish this, is to identify from the *cut-value versus significance* (S/\sqrt{B}) curves the

optimal-cut-point, meaning where the maximum significance is reached. Essentially, the significance should be maximised in the region where signal is mostly present. For the MLP classifier we expect this to be close to unity, in contrast with the BDT, where the maximum significance should reside in a region characterised by more intermediate values. This is due to the fact that the BDT algorithm works in a way where sequential cuts are applied to achieve maximum discrimination rather than by using a NN node-network, which is the case for the MLP.

For instance, Figure 11.4 illustrates the curves just for one point ($m_{\tilde{t}_1} = 325$ GeV, $m_{\tilde{\chi}_1^0} = 100$ GeV) and the optimal-cut-point values throughout the $(m_{\tilde{t}_1}, m_{\tilde{\chi}_1^0})$ plane for both the MLP and the BDT have been obtained from the ROC curves. Furthermore and for the optimal-cut-point of each model, it is possible to read the efficiencies for both the signal and the background (Figure 11.5) and the numerical value of the maximum significance (Figure 11.6) as well.

The last step of this exercise is to set upper limits in the $(m_{\tilde{t}_1}, m_{\tilde{\chi}_1^0})$ plane by using the events remaining after having applied the optimal selection cut on the MVA discriminator. The cut-and-count limits for the MLP are shown in Figure 11.7. The cut-and-count result is compatible to the ATLAS and CMS ones, but still inferior to the ones from our main method obtained from the MLP classifier. On the contrary, the cut-and-count results are comparable to the results obtained from the BDT classifier especially for $m_{\tilde{t}_1} > 350$ GeV. For $m_{\tilde{t}_1} < 350$ GeV, the BDT still gives better results, but as has been shown in Figure 10.1 the number of bins in this region is in general more than 10. This provides a somewhat increased sensitivity compared to the one-bin histogram of the cut-and-count but still smaller compared to the result based on the MLP classifier. On the contrary, in the region where $m_{\tilde{t}_1} > 350$ GeV, the BDT template histograms have in general less than 10 bins, hence the sensitivity is closer to that of the cut-and-count method.

The sensitivity obtained with the MLP in the region where $m_{\tilde{t}_1} < m_t + m_{\tilde{\chi}_1^0}$ and for $m_{\tilde{t}_1} < 300$ GeV could be explained by looking at the Figure 10.4 and keeping in mind that the fit while fitting the MVA shape, it also fits the nuisance parameter scaling the $t\bar{t}$ cross section. Therefore, in that region and since the effect of the $t\bar{t}$ cross section systematic uncertainty is larger compared to the rest of the points in the $(m_{\tilde{t}_1}, m_{\tilde{\chi}_1^0})$ plane, it could be also true that this systematic is probably the main one in that region and hence "responsible" for that sensitivity. On the contrary, for the cut-and-count method, this does not happen as the considered systematics merely scale the level of the one-bin content. The last argument has to be combined with the fact that the effect of the

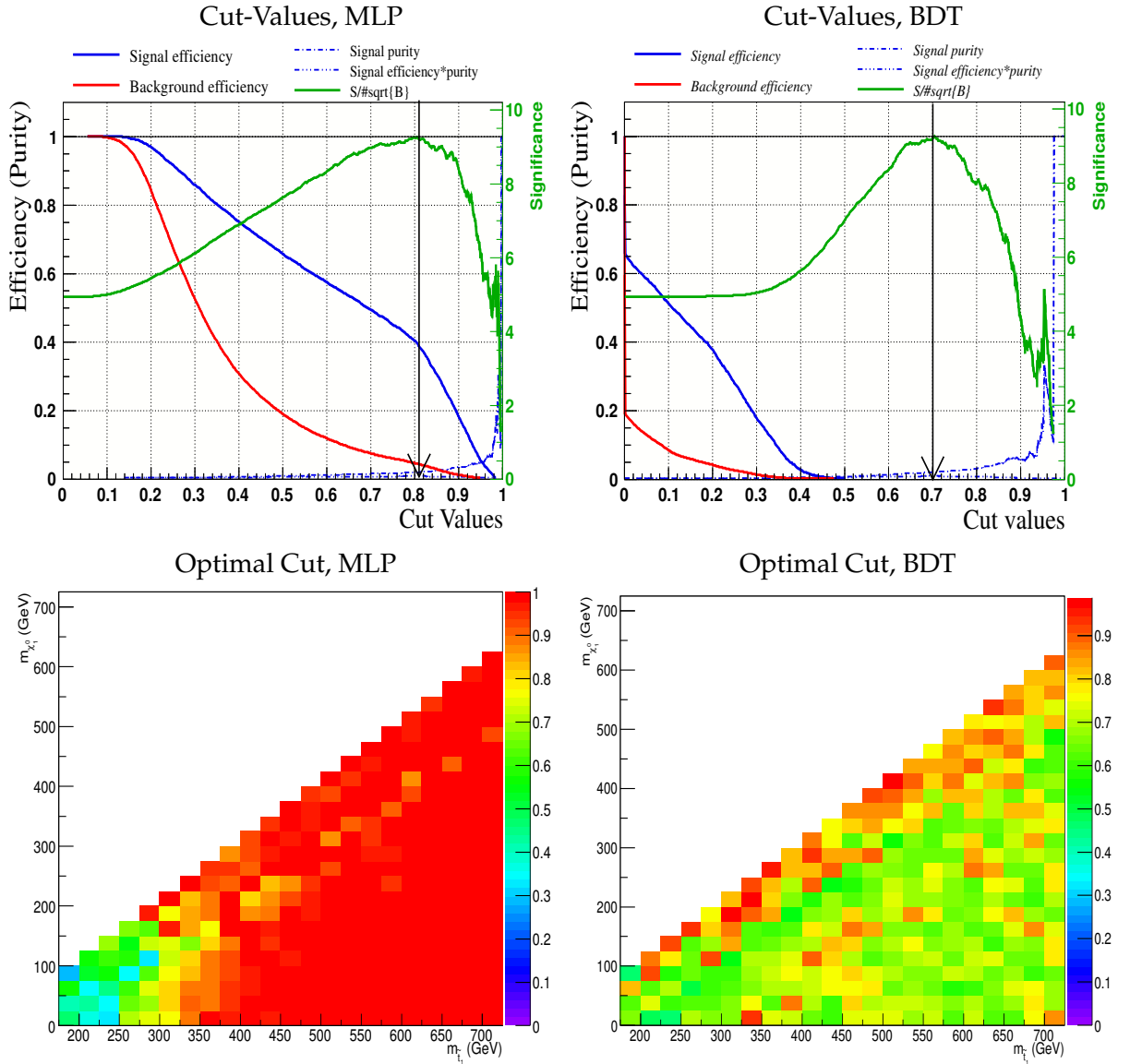


Figure 11.4: Top row : The cut-value distributions for $m_{\tilde{\tau}_1} = 325$ GeV, $m_{\tilde{\chi}_1^0} = 100$ GeV for both the MLP (left plot) and the BDT (right plot) classifiers. Bottom row : The Optimal Cut Point where the significance is maximised for the MLP (left) and the BDT (right) classifiers.

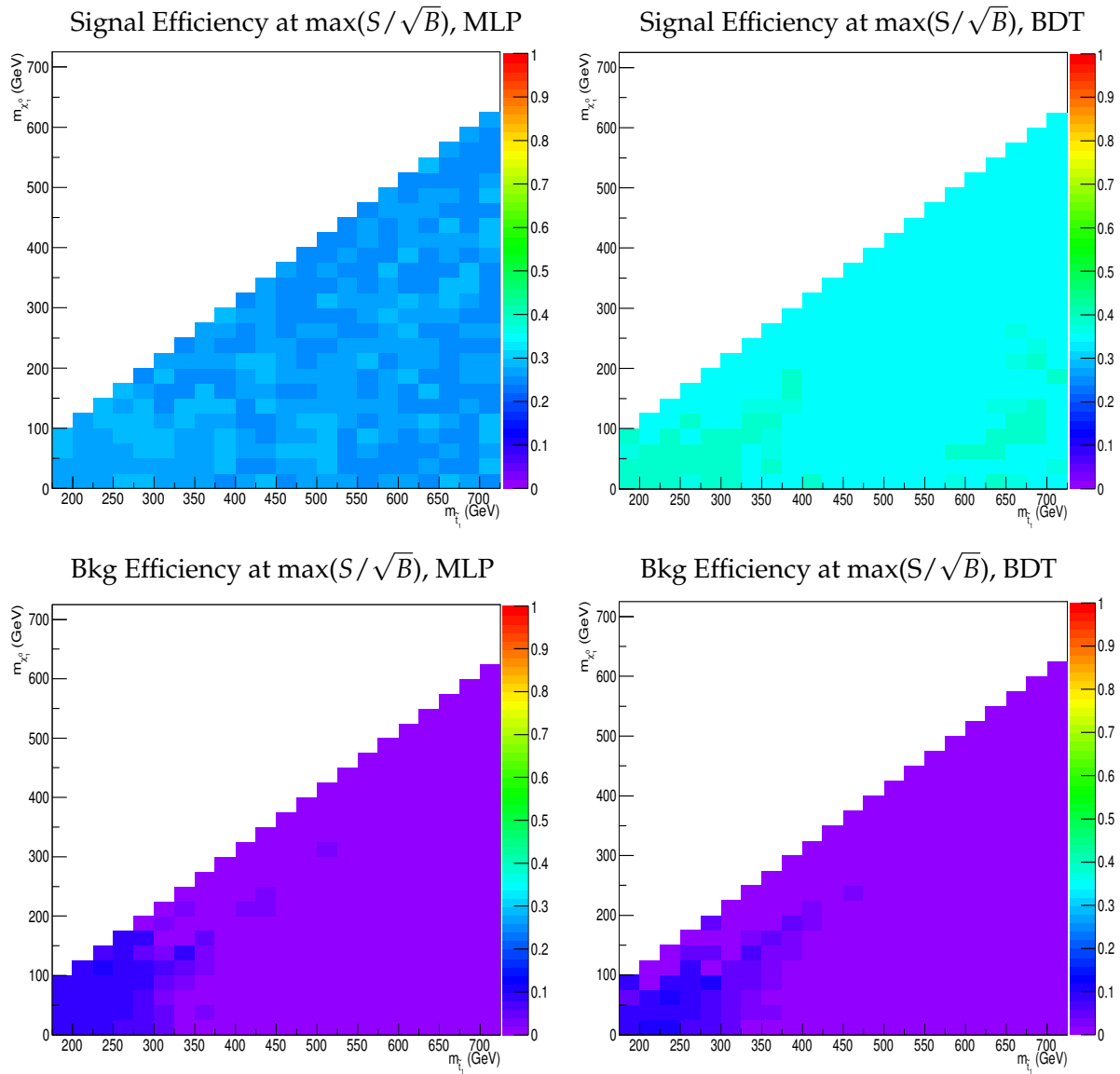


Figure 11.5: The efficiency obtained at the Optimal Cut point for signal (left row) and background (bottom row) for both the MLP (left column) and the BDT (right column) classifiers.

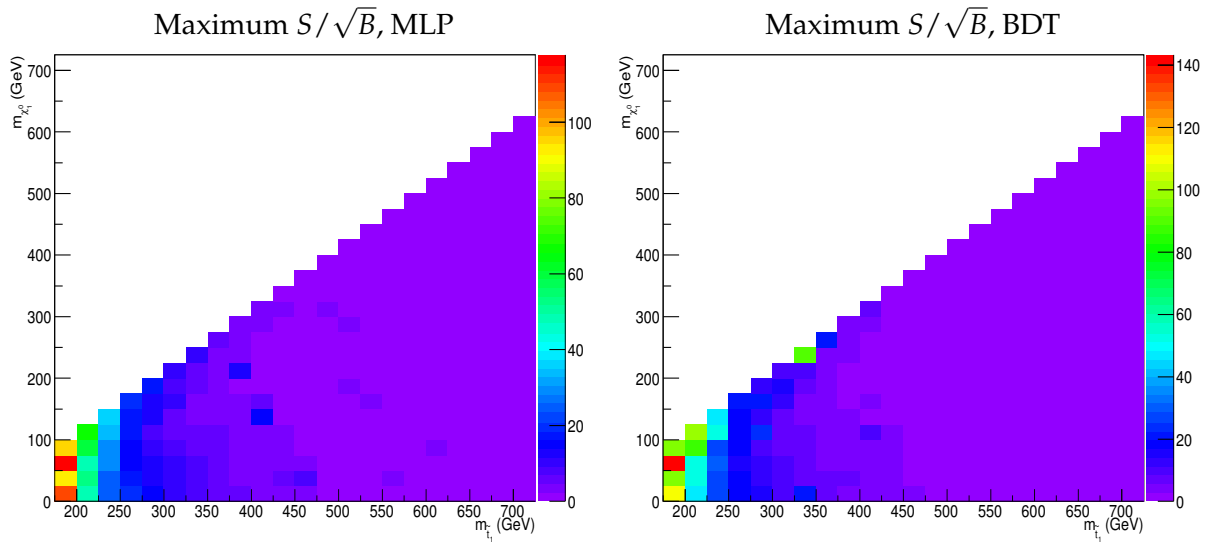


Figure 11.6: The maximum significance (S/\sqrt{B}) at the optimal cut point for the MLP and the BDT classifiers.

$t\bar{t}$ cross section as a source of systematic uncertainty is mostly "thrown" away after cutting at the optimum point. Hence, sensitivity is diminished and the total effect of the systematic uncertainties affects the limit.

Further, Figure 11.8 illustrates the MVA MLP distribution while Table 11.2 lists the event yields for the cut-and-count method for the $m_{\tilde{t}_1} = 225$ GeV, $m_{\tilde{\chi}_1^0} = 75$ GeV point. This point is excluded with our main method, but the cut-and-count cannot do so. The reason why this happens is twofold. On one hand, the systematic uncertainties are larger than the expected signal strength, hence the cut-and-count method does not have sensitivity for this point. On the other hand, similar to what was explained before, in the cut-and-count the systematics have only an effect on the level, but not on the shape, whereas the fit-method is sensitive both to the shape and the level effects of the systematics as by definition the whole range of the MVA distribution is used to perform the fit and obtain the best one. Finally, we have to stress out that although this cut-and-count approach does not take into account the effect of the systematics in the calculation of the significance for each point, one has to think this sanity check as just a way to construct a comparison test keeping in mind that the underlying idea of this analysis was not to use mainly a cut-and-count method in order to produce final results.

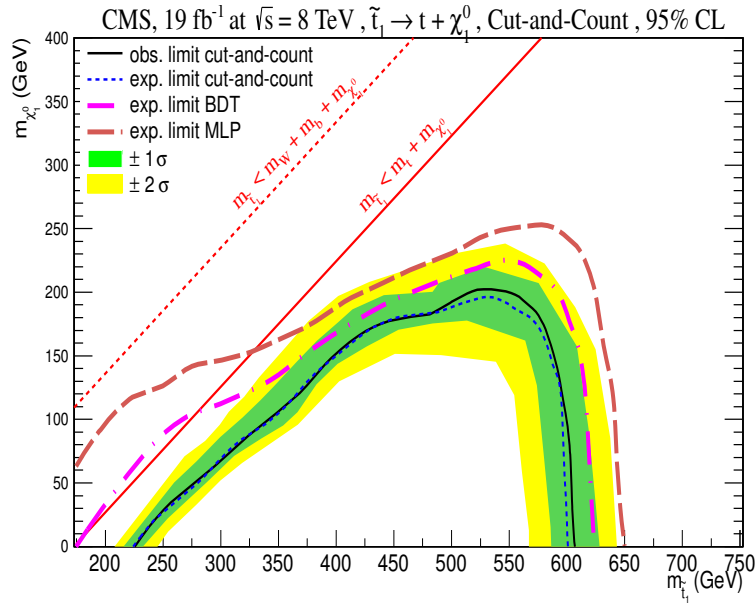


Figure 11.7: The upper limits from the MLP classifier as a counting experiment. For comparison, the expected limit from the main method for both the BDT and the MLP classifiers are superimposed.

Cut-and-Count MLP

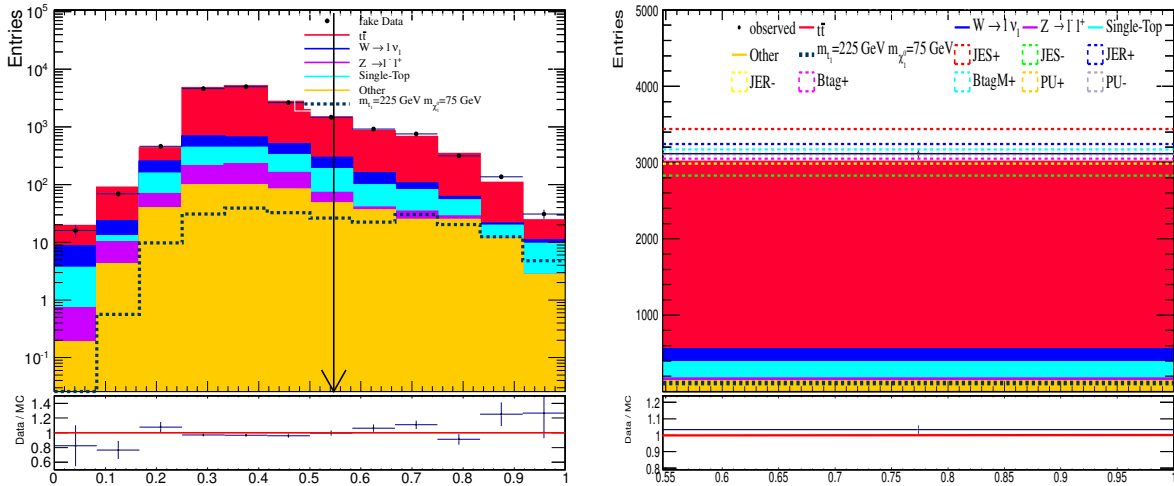


Figure 11.8: Left : The MLP distribution for the for $m_{\tilde{t}_1} = 225 \text{ GeV}$, $m_{\tilde{\chi}_1^0} = 75 \text{ GeV}$ point which is excluded with our method but not with the cut-and-count. Also, the optimal cut point is noted with an arrow. Right : The one-bin distribution which is used by the cut-and-count, along with the considered systematics which cover well the small discrepancy between expectation and data.

Event Yields , Cut-and-Count							
$t\bar{t}$	$W \rightarrow \ell\nu_\ell$	SingleTop	$Z \rightarrow \ell^- \ell^+$	Other	All Bkg	Observed	Signal
2457	173	217	32	132	3011	3114	110

Table 11.2: The event yields for the point $m_{\tilde{t}_1} = 225$ GeV, $m_{\tilde{\chi}_1^0} = 75$ GeV and for a cut-and-count method.

11.3 Overview and future perspectives

Currently the LHC is not taking data due to the scheduled Long Shutdown (LS) for upgrades and maintenance in order to prepare for the Run II. Both the ATLAS and the CMS collaborations have been investing a lot of human and computing resources during the last two decades designing and carrying out analyses, which span from SM precision measurements to searches for new phenomena. Considering the unprecedented success of Run I which established the discovery of the BEH-boson and the still unexploited potential of the LHC, it is more that certain than the restart of the LHC in 2015 will mark the beginning of a fascinating era which will propel us to uncharted regions of particle physics.

However, one of the long-standing bets for the LHC is the discovery of SUSY. Unfortunately and given the fact that we still lack any direct or indirect hint of its existence, it is therefore safe to conclude that SUSY is not the "low hanging fruit" after all, in opposite to what many physicists tended to believe until recently. But as in the near future the available phase space accessible to the LHC will be increased, new scenarios will be plausible to explore. Therefore, we should be ready to either have a discovery, or in the "worst" case scenario to have the "final word" on certain models.

In our search, we considered a SUSY model where the stop quark is considered to be the lightest squark of all, while they are produced in pairs decaying to a top quark and the lightest neutralino. Although we adopted a SMS approach, the phenomenology of this particular model is very similar to the *natural SUSY* scenario [152]. Within this framework, the 3rd generation squarks are predicted to be the lighter of all squarks with a mass below 600-700 GeV, while the higgsinos can also be light, whereas the gluinos as the rest of squarks/charginos can be above the TeV threshold with no further implications for the phenomenology of the stop quarks. That means that if SUSY is realised in nature this way, then the 3rd generation squarks have to be accessible to the LHC, hence our search is very well motivated.

The method that was developed to perform this analysis, poses several advantages

but comes with some difficulties as well. Its backbone is the way it treats a set of input variables aiming to optimise the sensitivity separately at each point of the considered parameter space. In parallel, MVA methods were used in order to get the optimal separation between signal and background. The derived template histograms from these steps were used as input for a shape-fitting analysis, where the signal strength was checked with the use of dedicated statistical tools.

At the end, we obtained very competitive results compared to similar searches performed both by the ATLAS and the CMS collaborations; we have excluded the \tilde{t}_1 masses up to 675 GeV for massless $\tilde{\chi}_1^0$, whereas for massive ones, we excluded the \tilde{t}_1 masses up to ~ 625 GeV for $\tilde{\chi}_1^0$ masses up to ~ 275 GeV. Furthermore, an important feature of this analysis is its ability to "reach" the compressed region, where typically the efficiency is very low and as a direct consequence, the sensitivity (if any) is also very small. For this peculiar corner of the phase space, we have excluded the region for \tilde{t}_1 masses up to 325 GeV and for $\tilde{\chi}_1^0$ mass up to ~ 150 GeV.

However, this search was very demanding in terms of resources that had to be put at work and also with respect to the framework that had to be built to support this analysis. Indeed, optimising the selection of the variables, studying and evaluating the performance of the MVA methods but also performing the training, the testing and the evaluation steps for each point in the $(m_{\tilde{t}_1}, m_{\tilde{\chi}_1^0})$ plane, took the larger part of the time devoted to this analysis. One more limitation, is the relative small size of the simulated datasets that we had at our disposal used to assess the effects of the systematics. Further, we also had to carry out a whole "private" production in order to build the signal datasets, something that was proven to be a very big (technical) challenge.

We think that where this analysis could be further improved, is mostly related to the input set of variables. In principle, there is no way to say that for a given variable which is quantified as a "sensitive" one, there is not a better one, but we just have not thought yet about it. This alludes that the method can get better and produce even finer results. But every time a new variable has to be injected, all sequential steps have to be executed from the beginning, something that is not that trivial nor fast. The ultimate would be to calculate the full limit each time a new variable is added, but this is computationally not possible. Hence a choice of variables has to be made on the basis of some simpler criteria like the distribution overlap we have developed. In any case, this criteria can be further improved and optimised in the future.

In a nutshell, analyses that follow a bottom-up approach and use more refined tools like this one, typically tend to yield better sensitivity. But usually this approach is

not favourable, exactly because of their complexity and the number of parameters one has to control. However, we accredit the performance of this analysis to the co-action and interplay between all the intermediate involved steps that have been individually optimised. Therefore and given our experimental results, it would be very interesting to repeat the same analysis with even more data from higher luminosities. At higher energies, we believe that conceptually, we could either make a discovery, or exclude more of the parameter space, given the fact that the cross section of direct stop quark pair production at $\sqrt{s} = 14$ TeV is about an order of magnitude higher compared to the $\sqrt{s} = 8$ TeV one. Figure 11.9 [153] shows the projected 5σ discovery reaches for two scenarios, a "pessimistic" (marked as Scenario A) and a more "optimistic" (marked by Scenario B) for $\sqrt{s} = 14$ TeV. One can clearly see that indeed in the near future even with the "pessimistic" approach, we should be able to have a more complete picture on this specific model.

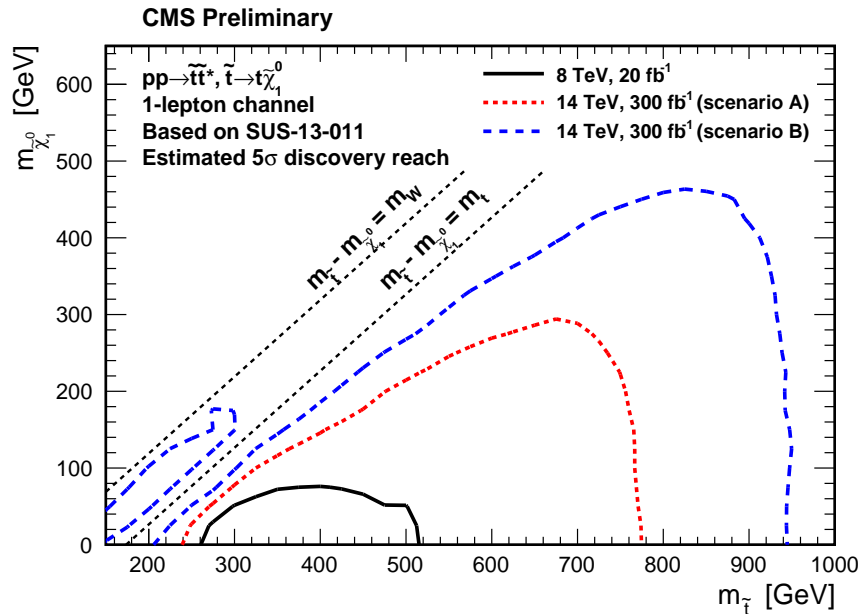


Figure 11.9: The 5σ projected discovery reaches for two scenarios, a "pessimistic" (Scenario A) and a more "optimistic" one (Scenario B) for $\sqrt{s} = 14$ TeV and for $\mathcal{L} = 300 \text{ fb}^{-1}$ [153].

Finally, we have also to point out that the exact same strategy and methodology we developed, could be used even with any other model or topology, since it does not depend on the exact details of the model itself. Hence, although this analysis consists out of many smaller pieces that have to be carefully tweaked, it presents a large potential for future uses due to its dynamic character while handling the input information and employs state-of-the-art tools to produce the final result.

Part V

Appendices

The Tune Z2* [92] parameters for the Underlying Event.

parameter	Pythia	value
$\sigma(k_T)$	PARP(91)	2.1 GeV/c
k_T^{max}	PARP(93)	10 GeV/c
β	PARP(83)	0.356
a_2/a_1	PARP(84)	0.651
p_T^{min}	PARP(81)	1.9 GeV/c
p_T^0	PARP(82)	2.7 GeV/c
\sqrt{s}^{ref}	PARP(89)	1.96 TeV
x_{scale}	PARP(90)	0.227

Table A.1: The values used with Pythia6.426 and the Tune Z2 [92] for the treatment of the UE.*

The Tune Z2* [92] parameters for the Hadronization

parameter	Pythia	value
$p_{x,h}$ and $p_{y,h}$ widths	PARJ(21)	0.36 GeV/c
Lund a	PARJ(41)	0.3
Lund b	PARJ(42)	0.58 GeV ⁻² c ²
Peterson ϵ_c	PARJ(54)	-0.05
Peterson ϵ_b	PARJ(55)	-0.005

Table A.2: The values used with *Pythia*6.426 and the Tune Z2* [92] for the hadronization.

APPENDIX B

LIST OF VARIABLES

In this Appendix, we describe all the implemented variables used for this analysis.

Individual Object Kinematics

This class includes the following variables.

1. \cancel{E}_T : The Missing Transverse Energy of the event..
2. *NofJets* : The multiplicity of Jets in the event.
3. *JetsPt¹* : The p_T of the leading Jet.
4. *JetsPt²* : The p_T of next-to-leading Jet.
5. *JetsPt³* : The p_T of the 3rd hardest Jet.
6. *JetsPt⁴* : The p_T of the 4rth hardest Jet.
7. *PtMuon* : The p_T of the selected Muon.
8. *EtaMuon* : The η of the selected Muon.

Global event. Kinematics

This class includes the following variables.

1. H_T4Jets : The scalar sum of the p_T of the four hardest jets of the event.
2. $HZ4jets$: The scalar sum of the p_Z of the four hardest jets of the event.
3. $H_T4JetsE_T$: The scalar sum of the four hardest jets of the event. plus the E_T
4. $H_T4JetsMuonE_T$: The scalar sum of the four hardest jets of the event, plus the E_T and the of the selected Muon.
5. H_T : The scalar sum of the p_T of all Jets of the event.
6. $AvgH_T$: The scalar sum of the p_T of the Jets divided by their number.
7. M_{eff} : The effective mass, which is the scalar sum of the p_T of all Jets of the events plus the E_T .
8. $ET12$: The scalar sum of the E_T of the two leading Jets.
9. $ET23$: The scalar sum of the E_T of the 2nd and 3rd leading Jets.
10. $ET34$: The scalar sum of the E_T of the 3rd and 4th leading Jets.
11. $ET1oET2$: The E_T of the leading Jet divided by the E_T of 2nd hardest Jet.
12. $ET1oET3$: The E_T of the leading Jet divided by the E_T of the 3rd hardest Jet.
13. $ET1oET4$: The E_T of the leading Jet divided by the E_T of the 4th hardest Jet.
14. $ET2oET3$: The E_T of the 2nd hardest Jet divided by the E_T of the 3rd hardest Jet.
15. $m_T^{Hadr}(t\bar{t})$: The transverse mass of the reconstructed $t\bar{t}$.
16. $m_{t\bar{t}}$: The Invariant mass of the reconstructed $t\bar{t}$.
17. W_T : The W transverse mass.
18. $m_T^{Hadr}(t)$: The Transverse mass of the reconstructed Hadronic top-quark.
19. m_T^W : The Transverse mass of the reconstructed W -boson.
20. $m^{Hadr}(t)$: The Invariant mass of the reconstructed Hadronic top-quark.
21. $m_{boost}^{Hadr}(t)$: The Lorentz-boosted Invariant mass of the reconstructed Hadronic top-quark-quark.

22. $m3$: The Invariant mass of the three hardest Jets of the event.
23. *Centrality* : The Centrality of the event, defined as the ratio of the sum of the p_T of the vectorial sum of the jets and the muon, divided by their total momentum.

$$Centrality = \frac{\sum(Jets + muon).p_T}{\sum(Jets + muon).\mathbf{p}}$$

where

$$\mathbf{P} = \begin{pmatrix} E \\ P_x \\ P_y \\ P_z \end{pmatrix}$$

In general for SUSY events which typically present an increased jet activity, one would expect that the sum of the Jets p_T plus the muon's p_T will be higher compared to SM background events, thus the Centrality will be shifted towards higher values since the four-momentum must be conserved all times.

Angular Kinematics

This class includes the following variables.

1. $\Delta\Phi(\cancel{E}_T, \mu)$: The $\Delta\Phi$ between the \cancel{E}_T and the selected Muon.
2. $\Delta\Phi(\cancel{E}_T, Jet^1)$: The $\Delta\Phi$ between the \cancel{E}_T and the leading Jet.
3. $\Delta\Phi(\cancel{E}_T, Jet^2)$: The $\Delta\Phi$ between the \cancel{E}_T and the next-to leading Jet.
4. $\Delta\Phi(Jet^1, Jet^2)$: The $\Delta\Phi$ between the fist two leading jets.
5. $\Delta\Phi(Jet^1, Jet^3)$: The $\Delta\Phi$ between the fist and the third two leading jets.
6. $\Delta R(\mu, Jet^1)$: The ΔR between the muon and the leading Jet.
7. $\Delta R(\mu, Jet^2)$: The ΔR between the muon and the next-to leading Jet.
8. $\Delta R(Jet^1, Jet^2)$: The ΔR between the fist two leading jets.
9. $\Delta R(Jet^1, Jet^3)$: The ΔR between the fist and the third two leading jets.

10. $\Delta R(\cancel{E}_T, Jet^1)$: The ΔR between the \cancel{E}_T and the leading Jet.
11. $\Delta R(\cancel{E}_T, Jet^2)$: The ΔR between the \cancel{E}_T and the next-to leading Jet.
12. $\sum [\Delta\Phi(\mu, Jet^1), \Delta\Phi(\mu, Jet^2)]$: The sum of the $\Delta\Phi(\mu, Jet^1)$ and $\Delta\Phi(\mu, Jet^2)$.

B-tag discriminators

This class includes the following variables.

1. *BTaggerHadB* : The CSV algorithm discriminator value of the b-jet from the top-quark decay for which the subsequent W-boson decays into quarks.
2. *BTaggerLepB* : The CSV algorithm discriminator value of the b-jet from the top-quark decay for which the subsequent W-boson decays into leptons.

In this Appendix, we present the basic concepts of the Artificial Neural Network techniques that were used for this analysis.

C.0.1 Artificial Neural Networks (ANN)

The concept of the Neural Networks (NN) originates from biology in order to describe the interconnection of cells in the brain which are called *neurons*, and are responsible to receive and transit electric signal to other cells. Likewise, an *Artificial Neural Network* (NN) has similar clusters of nodes, (neurones) which are capable of receiving and sending signal (information) to the nodes they are linked with. All of the currently NN algorithms implemented currently in the TMVA package, typically consist of a set of nodes with layered neurons, which are connected towards only one direction. These are formally known as *Feed-Forward MultiLayer Perceptron Networks* [145]. In this kind of NN, the transfer from input to the output within a neuron is performed with the use of a so-called *activation function*.

C.0.2 The MultiLayer Perceptron (MLP) method

In order to minimize the computational time the processing time of each point, a reduced layout was used, the so-called *Multi-Layer Perceptron* (MLP). MLP reduces significantly the complexity of the network by just ordering the neurons into several

multi-layers, and by allowing only forward (thus one-direction) connections between consecutive layers. The last layer has only one node, and its response is the combined variable of the entire network. Although a given number of n input variables can result to n^2 possible neurons, each connection has its own weight. Between the input and the output layer there is an arbitrary number of hidden layers, k . While at the learning phase, the set of weights is chosen in a fashion so that a given error function gets minimised. This error function determines the total number of hidden layers.

The problem with hidden layers, is that is not clear in advance how many of these are needed to obtain the most discriminating power of the signal, so, is like optimizing a black box. On the other hand, this can offer unbiased results.

Figure C.1 presents an example of what a MLP NN looks like. The response of a node to a given input (which is the output of the previous nodes), strongly depends on the weight i of the interconnection between two adjacent nodes and the activation function of the node as well. The output of a node j in layer n is obtained after the completion of the following steps :

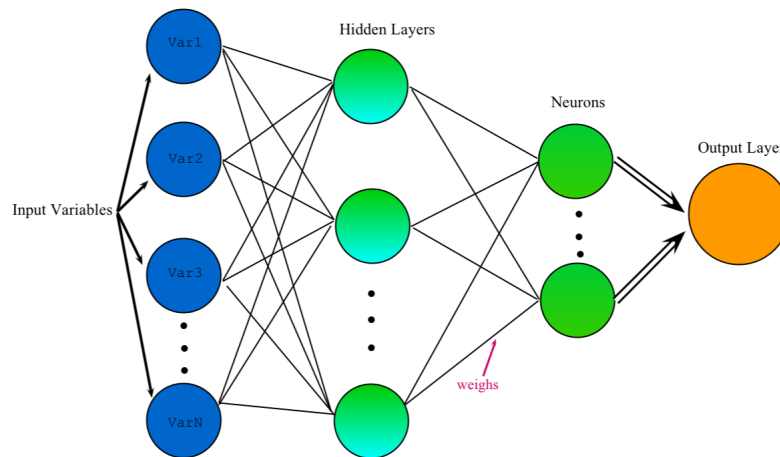


Figure C.1: Schematic diagram of a MLP NN with one hidden layers. At each layer, a weight scales its output while connecting to the next one.

1. The weighted sum of outputs in layer n is calculated :

$$x_j^{(n)} = \sum_i w_{i,j}^{(n)} x_i^{(n-1)} \quad (\text{C.1})$$

Where $w_{i,j}^{(n)}$ is the associated weight of the $n - th$ node.

2. Next, a transfer function $f(x)$ is applied at the output of each node, which can be

linear, sigmoid, or event of hyperbolic form - In this thesis, the hyperbolic tangent form has been used, namely :

$$f(x) = \frac{e^x - e^{-x}}{e^x + e^{-x}} \quad (\text{C.2})$$

At the beginning, the weights, $w_{i,j}^{(n)}$ get random values while the input variables are fed in. After successive training cycles, the output should be $\in [0,1]$. Values close to 0(1) should have come from background (signal)-like events.

3. Next, the what so-called *back propagation* is applied in order to minimise an error function E , which depends on the weights and response function from the previous steps.
 - (a) After the training phase of N_{events} total events, an indicator value O is obtained. This is usually set to 1(0) in case of a signal (background) event.
 - (b) This value is compared against the O' which is the output from each node and for each event. The overall error is then :

$$E(v_1, v_2, \dots, v_{nvar})|w = \sum_{i=1}^N E_l(\text{obs}_i|w) = \sum_{i=1}^N \frac{1}{2} (O - O')^2 \quad (\text{C.3})$$

This carries information from the individual weights of each node, and is minimised using an iterative method, formally known as *epochs*. The result of a NN trained for too many epochs is known as *over-training*. Over-training can be prevented if the error function is calculated for a completely independent sample of events and its output is then compared against the training sample. This procedure is known as *testing*. If the calculated errors diverge, the network is considered to be over-trained.

- (c) To prevent over-training, the weight factors have to be transformed to :

$$w^{m+1} = w^m - \eta \nabla_w E \quad (\text{C.4})$$

where m stands for the iterations that have to be completed in order to minimise the error and η is the *learning rate* which is normally a small number so that no big jumps on the w occur.

C.0.3 Boosted Decision Trees (BDT)

The second classifier that has been used for this analysis is the Boosted Decision Trees (BDT) method. BDT uses the so-called *Separation Class* which builds a decision tree. It starts from a single node using the variable that provides the maximum discrimination between background and signal. BDT looks very much like the traditional cut-based techniques where rectangular cuts are applied. Hence, a given variable's output has to be compared against the primary node's response to be classified as signal or background. The algorithm evaluates a number of cuts for each of the input variables, and the best cut which discriminates signal from background is obtained. A root node is constructed from several more branches which contain several cut-values for the most powerful variables. Each event from the input collection is tested against the cut at each node, and is sent to the left or to the right, depending on the answer. At the end, an event should end up in the farest/lowest node, known as *leafs* of the tree where is finally classified as a "background" or "signal-like" event.

The tree-structure approach has the advantage over cut-based analysis, that a signal event is still possible to be picked-up, even in the case that it does not pass one or more cuts. However, their disadvantage is that they lack sensitivity to statistical fluctuations when it comes to train samples. That means that the separation class can make some very bad decisions when it comes to create the nodes which have certain cut values. To treat this, a *forest* has to grow, i.e. more trees are created by using the same training sample. Then, a comparison is performed among the trees and the ones that present a poor discrimination are replaced. All of the trees are assigned with a weight factor according to their discriminating power, and all those weight are combined to get the final BDT output. The modification of the weights in order to optimise the performance and achieve the maximum discrimination is called boosting.

The workflow of a BDT is as follows :

1. First, the **purity** of the signal sample is calculated as:

$$p = \frac{n_s}{n_s + n_b} = 1 - \frac{n_b}{n_s + n_b} \quad (\text{C.5})$$

where n_s , n_b denote the signal and background events scaled in such a way so that $n_s + n_b = 1$.

2. Next, a *separation criterion* is calculated. Although, in the BDT several different implementations exist, for this thesis the *Gini* index was used :

$$S = p(1 - p) \tag{C.6}$$

The *Gini* index increases when $n_s < n_b$ and vice versa. As it can be seen, when *Gini* index is equal to 0.5, it corresponds to the case where signal and background are the same.

3. Each variable's range is surveyed with a certain (predefined) step while the separation index is calculated every time. On each iteration, the variable's numerical value and the separation index are stored and compared. Once the optimal variable and the corresponding value have been found, the sample is split into more subsets resulting in new children nodes.
4. The above step is repeated, until the *Gini* index is below a certain threshold, so no further splitting is necessary. The final nodes now form the leaves which are tagged as "signal" or "background" leaves, exactly if the signal purity is above or below 0.5.

A schematic diagram of a BDT tree is shown in Fig. C.2.

C.0.4 Comparison of ANN vs BDT

Both presented methods have its strong and weak points. If we like to outline their advantages and disadvantages, we could outline them as follows. The BDT provides a very good performance, even with low statistics, and even if some of the input variables have small discriminating power. On the other hand, BDT trees are easier to get over-trained something that could give an artificial "fake" separation of 100%. This can happen when all events, both signal and background end up in the leaf nodes. This is why is very important to use statistically independent datasets for the training and the testing, so to avoid this effect. Luckily, a "self-protection" algorithm exists, known as *pruning*, which "chops" down branches if a tree starts to grow too big.

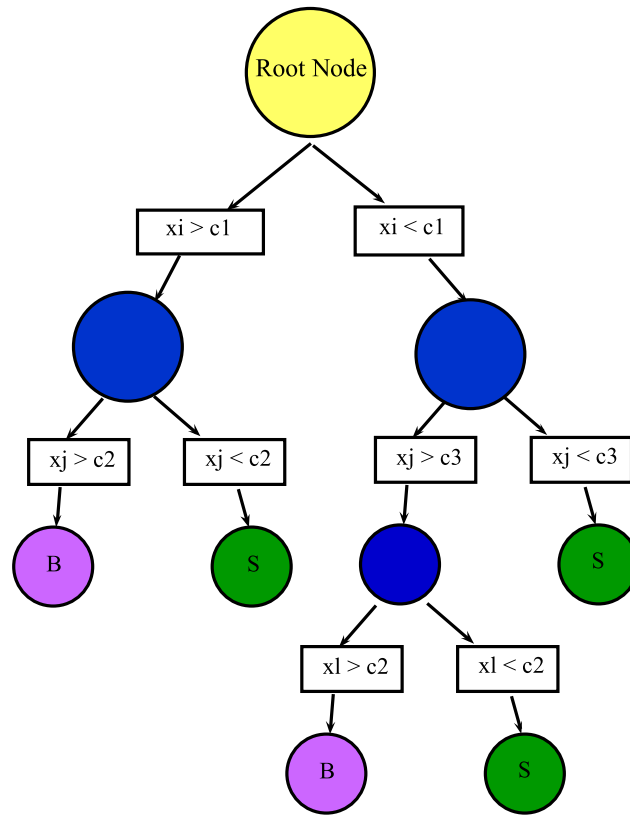


Figure C.2: Illustration of a BDT decision tree. An event starts from the Root node and goes all the way down, until it is classified as "background" or "signal"-like after reaching the corresponding leaf.

C.0.5 Other MVA methods

The ANN and BDT method are used for this analysis, since are the best performers among other available methods, something that will be demonstrated in Section 8.3.2. But before that and for completeness, we briefly present other available methods as well that we tested against the BDT & the MLP.

1. **Rectangular cut optimization (Cuts)** : For each input variable, a rectangular cut is used, which maximises the background rejection, namely the $r_b = 1 - \epsilon_b$, for a given signal efficiency ϵ_s . This can be achieved from either a direct comparison to the full input collection of the events, or by just parametrizing the PDFs. The response is a 0/1 answer, meaning that is either signal or background in contrast with other methods where a probability is returned.
2. **Projective likelihood estimation (Likelihood Ratio)** : As the name of the method suggest, the likelihood ratio is returned for each event.

3. *Fisher Discriminant* : Fisher is a linear discriminator method, and as such, linear transformations are used in order to map the input phase space. Next, a decorrelated space is formed such that events belonging to the same class are positioned "close by", while events from different classes are put away from each other. Practically, the method returns this exact distance between the classes by using a covariance matrix of the discriminating variable space. This matrix is known as *Fisher Discriminant*.

BIBLIOGRAPHY

- [1] CMS Collaboration Collaboration, “Measurement of the $B_s^0 \rightarrow \mu^+ \mu^-$ branching fraction and search for $B^0 \rightarrow \mu^+ \mu^-$ with the CMS Experiment”, [arXiv:1307.5025](#).
- [2] LHCb collaboration Collaboration, “Measurement of the $B_s^0 \rightarrow \mu^+ \mu^-$ branching fraction and search for $B^0 \rightarrow \mu^+ \mu^-$ decays at the LHCb experiment”, [arXiv:1307.5024](#).
- [3] DELPHI Collaboration Collaboration, “Measurement of the triple gluon vertex from four - jet events at LEP”, *Z.Phys.* **C59** (1993) 357–368, [doi:10.1007/BF01498617](#).
- [4] A. Czarnecki and W. J. Marciano, “The Muon anomalous magnetic moment: Standard model theory and beyond”, [arXiv:hep-ph/0010194](#).
- [5] J. Prades, “Standard Model Prediction of the Muon Anomalous Magnetic Moment”, *Acta Phys.Polon.Supp.* **3** (2010) 75–86, [arXiv:0909.2546](#).
- [6] CMS Collaboration Collaboration, “Observation of a new boson at a mass of 125 GeV with the CMS experiment at the LHC”, *Phys.Lett.* **B716** (2012) 30–61, [doi:10.1016/j.physletb.2012.08.021](#), [arXiv:1207.7235](#).
- [7] ATLAS Collaboration Collaboration, “Observation of a new particle in the search for the Standard Model Higgs boson with the ATLAS detector at the LHC”, *Phys.Lett.* **B716** (2012) 1–29, [doi:10.1016/j.physletb.2012.08.020](#), [arXiv:1207.7214](#).

- [8] F. Englert and R. Brout, "Broken Symmetry and the Mass of Gauge Vector Mesons", *Phys. Rev. Lett.* **13** (Aug, 1964) 321–323, [doi:10.1103/PhysRevLett.13.321](https://doi.org/10.1103/PhysRevLett.13.321).
- [9] P. W. Higgs, "Broken Symmetries and the Masses of Gauge Bosons", *Phys. Rev. Lett.* **13** (Oct, 1964) 508–509, [doi:10.1103/PhysRevLett.13.508](https://doi.org/10.1103/PhysRevLett.13.508).
- [10] D. Griffiths, "Introduction to Elementary Particles",.
- [11] C. Weinheimer and K. Zuber, "Neutrino Masses", [arXiv:1307.3518](https://arxiv.org/abs/1307.3518).
- [12] P. D. Group, "Review of Particle Physics", *J.Phys* **G37** (2010). 075021.[doi:10.1088/0954-3899/37/7A/075021](https://doi.org/10.1088/0954-3899/37/7A/075021).
- [13] ATLAS Collaboration Collaboration, "Evidence for the spin-0 nature of the Higgs boson using ATLAS data", [arXiv:1307.1432](https://arxiv.org/abs/1307.1432).
- [14] "Properties of the Higgs-like boson in the decay H to ZZ to $4l$ in pp collisions at $\sqrt{s}=7$ and 8 TeV", Technical Report CMS-PAS-HIG-13-002, CERN, Geneva, (2013).
- [15] "Properties of the observed Higgs-like resonance using the diphoton channel", Technical Report CMS-PAS-HIG-13-016, CERN, Geneva, (2013).
- [16] ATLAS Collaboration Collaboration, "Measurements of Higgs boson production and couplings in diboson final states with the ATLAS detector at the LHC", [arXiv:1307.1427](https://arxiv.org/abs/1307.1427).
- [17] "Combination of standard model Higgs boson searches and measurements of the properties of the new boson with a mass near 125 GeV", Technical Report CMS-PAS-HIG-13-005, CERN, Geneva, (2013).
- [18] E. Fermi, "An attempt of a theory of beta radiation. 1.", *Z.Phys.* **88** (1934) 161–177, [doi:10.1007/BF01351864](https://doi.org/10.1007/BF01351864).
- [19] S. Glashow, "Partial Symmetries of Weak Interactions", *Nucl.Phys.* **22** (1961) 579–588, [doi:10.1016/0029-5582\(61\)90469-2](https://doi.org/10.1016/0029-5582(61)90469-2).
- [20] A. Salam and J. C. Ward, "Electromagnetic and weak interactions", *Phys.Lett.* **13** (1964) 168–171, [doi:10.1016/0031-9163\(64\)90711-5](https://doi.org/10.1016/0031-9163(64)90711-5).
- [21] S. Weinberg, "A Model of Leptons", *Phys.Rev.Lett.* **19** (1967) 1264–1266, [doi:10.1103/PhysRevLett.19.1264](https://doi.org/10.1103/PhysRevLett.19.1264).

- [22] UA1 Collaboration Collaboration, “Experimental Observation of Lepton Pairs of Invariant Mass Around $95\text{-GeV}/c^2$ at the CERN SPS Collider”, *Phys.Lett. B* **126** (1983) 398–410, [doi:10.1016/0370-2693\(83\)90188-0](https://doi.org/10.1016/0370-2693(83)90188-0).
- [23] G. Arnison et al., “Experimental observation of isolated large transverse energy electrons with associated missing energy at $\sqrt{s} = 540\text{GeV}$ ”, *Phys. Lett. B* **122** (Jan, 1983) 103–116. 31 p.
- [24] S. Bethke, “Experimental tests of asymptotic freedom”, *Prog.Part.Nucl.Phys.* **58** (2007) 351–386, [doi:10.1016/j.pnpnp.2006.06.001](https://doi.org/10.1016/j.pnpnp.2006.06.001), [arXiv:hep-ex/0606035](https://arxiv.org/abs/hep-ex/0606035).
- [25] C. Balázs, M. Carena, and C. E. M. Wagner, “Dark matter, light top squarks, and electroweak baryogenesis”, *Phys. Rev. D* **70** (Jul, 2004) 015007, [doi:10.1103/PhysRevD.70.015007](https://doi.org/10.1103/PhysRevD.70.015007).
- [26] G. 't Hooft, “Renormalization of Massless Yang-Mills Fields”, *Nucl.Phys.* **B33** (1971) 173–199, [doi:10.1016/0550-3213\(71\)90395-6](https://doi.org/10.1016/0550-3213(71)90395-6).
- [27] C. Froggatt and H. Nielsen, “Trying to understand the standard model parameters”, *Surveys High Energ.Phys.* **18** (2003) 55–75, [doi:10.1080/0142241032000156559](https://doi.org/10.1080/0142241032000156559), [arXiv:hep-ph/0308144](https://arxiv.org/abs/hep-ph/0308144).
- [28] S. P. Martin, “A Supersymmetry primer”, [arXiv:hep-ph/9709356](https://arxiv.org/abs/hep-ph/9709356).
- [29] G. Bertone, D. Hooper, and J. Silk, “Particle dark matter: Evidence, candidates and constraints”, *Phys.Rept.* **405** (2005) 279–390, [doi:10.1016/j.physrep.2004.08.031](https://doi.org/10.1016/j.physrep.2004.08.031), [arXiv:hep-ph/0404175](https://arxiv.org/abs/hep-ph/0404175).
- [30] P. J. E. Peebles and B. Ratra, “The cosmological constant and dark energy”, *Rev. Mod. Phys.* **75** (Apr, 2003) 559–606, [doi:10.1103/RevModPhys.75.559](https://doi.org/10.1103/RevModPhys.75.559).
- [31] H. P. Nilles, “Supersymmetry, Supergravity and Particle Physics”, *Phys.Rept.* **110** (1984) 1–162, [doi:10.1016/0370-1573\(84\)90008-5](https://doi.org/10.1016/0370-1573(84)90008-5).
- [32] H. E. Haber and G. L. Kane, “The Search for Supersymmetry: Probing Physics Beyond the Standard Model”, *Phys.Rept.* **117** (1985) 75–263, [doi:10.1016/0370-1573\(85\)90051-1](https://doi.org/10.1016/0370-1573(85)90051-1).
- [33] L. Susskind, “The gauge hierarchy problem, technicolor, supersymmetry, and all that”, *Physics Reports* **104** (1984), no. 2–4, 181 – 193, [doi:http://dx.doi.org/10.1016/0370-1573\(84\)90208-4](https://doi.org/http://dx.doi.org/10.1016/0370-1573(84)90208-4).

- [34] D. Hooper, “TASI 2008 Lectures on Dark Matter”, [arXiv:0901.4090](#).
- [35] G. Jungman, M. Kamionkowski, and K. Griest, “Supersymmetric dark matter”, *Phys.Rept.* **267** (1996) 195–373, [doi:10.1016/0370-1573\(95\)00058-5](#), [arXiv:hep-ph/9506380](#).
- [36] P. Fayet, “A Gauge Theory of Weak and Electromagnetic Interactions with Spontaneous Parity Breaking”, *Nucl.Phys.* **B78** (1974) 14, [doi:10.1016/0550-3213\(74\)90113-8](#).
- [37] K. Inoue et al., “Low-Energy Parameters and Particle Masses in a Supersymmetric Grand Unified Model”, *Prog.Theor.Phys.* **67** (1982) 1889, [doi:10.1143/PTP.67.1889](#).
- [38] P. Van Nieuwenhuizen, “Supergravity”, *Phys.Rept.* **68** (1981) 189–398, [doi:10.1016/0370-1573\(81\)90157-5](#).
- [39] J. L. Feng, “Supersymmetry and cosmology”, *eConf* **C0307282** (2003) L11, [arXiv:hep-ph/0405215](#).
- [40] P. Nath, R. L. Arnowitt, and A. H. Chamseddine, “APPLIED N=1 SUPERGRAVITY”.
- [41] L. Hall, J. Lykken, and S. Weinberg, “Supergravity as the messenger of supersymmetry breaking”, *Phys. Rev. D* **27** (May, 1983) 2359–2378, [doi:10.1103/PhysRevD.27.2359](#).
- [42] S. K. Soni and H. A. Weldon, “Analysis of the Supersymmetry Breaking Induced by N=1 Supergravity Theories”, *Phys.Lett.* **B126** (1983) 215, [doi:10.1016/0370-2693\(83\)90593-2](#).
- [43] T. C. Collaboration, “Public CMS 7 TeV Approved Plots”, October, 2012.
- [44] ATLAS Collaborations, CMS Collaborations Collaboration, “Supersymmetry searches at the LHC”, [arXiv:1211.3887](#).
- [45] T. C. Collaboration, “Public CMS Approved Plots”, October, 2012.
- [46] W. Beenakker et al., “Stop production at hadron colliders”, *Nucl.Phys.* **B515** (1998) 3–14, [doi:10.1016/S0550-3213\(98\)00014-5](#), [arXiv:hep-ph/9710451](#).
- [47] M. Kramer et al., “Supersymmetry production cross sections in pp collisions at $\sqrt{s} = 7$ TeV”, [arXiv:1206.2892](#).

- [48] T. C. Collaboration, “CMS Physics Technical Design Report, Volume II: Physics Performance”, *Journal of Physics G: Nuclear and Particle Physics* **34** (2007), no. 6, 995.
- [49] J. Alwall, P. Schuster, and N. Toro, “Simplified Models for a First Characterization of New Physics at the LHC”, *Phys.Rev.* **D79** (2009) 075020, [doi:10.1103/PhysRevD.79.075020](https://doi.org/10.1103/PhysRevD.79.075020), [arXiv:0810.3921](https://arxiv.org/abs/0810.3921).
- [50] LHC New Physics Working Group Collaboration, “Simplified Models for LHC New Physics Searches”, *J.Phys.* **G39** (2012) 105005, [doi:10.1088/0954-3899/39/10/105005](https://doi.org/10.1088/0954-3899/39/10/105005), [arXiv:1105.2838](https://arxiv.org/abs/1105.2838).
- [51] “LHC SUSY Cross Section Working Group”,
<https://twiki.cern.ch/twiki/bin/view/LHCPhysics/SUSYCrossSections>.
- [52] “Search for direct top squark pair production in final states with one isolated lepton, jets, and missing transverse momentum in $\sqrt{s} = 8, \text{TeV}$ pp collisions using 21 fb^{-1} of ATLAS data”, Technical Report ATLAS-CONF-2013-037, CERN, Geneva, (Mar, 2013).
- [53] “Search for top-squark pair production in the single lepton final state in pp collisions at 8 TeV”, Technical Report CMS-PAS-SUS-13-011, CERN, Geneva, (2013).
- [54] “Search for supersymmetry using razor variables in events with b-jets in pp collisions at 8 TeV”, Technical Report CMS-PAS-SUS-13-004, CERN, Geneva, (2013).
- [55] F. James, “Monte Carlo theory and practice”, *Reports on Progress in Physics* **43** (1980), no. 9, 1145.
- [56] A. Buckley et al., “General-purpose event generators for LHC physics”, *Phys.Rept.* **504** (2011) 145–233, [doi:10.1016/j.physrep.2011.03.005](https://doi.org/10.1016/j.physrep.2011.03.005), [arXiv:1101.2599](https://arxiv.org/abs/1101.2599).
- [57] C. G et al., “HERWIG 6.5 -An event generator for Hadron Emission Reactions With Interfering Gluons”, *JHEP* **01** (2001) 010, [arXiv:arXiv:hep-ph/0011363](https://arxiv.org/abs/hep-ph/0011363).
- [58] T. Sjöstrand, S. Mrenna, and P. Skands, “PYTHIA 6.4 physics and manual”, *JHEP* **05** (2006) 026, [arXiv:arXiv:hep-ph/0603175](https://arxiv.org/abs/hep-ph/0603175).
- [59] The GEANT4 Collaboration *Nucl. Instrum. Meth.* **A506** (2003) 250–303.

- [60] J. de Favereau et al., “DELPHES 3, A modular framework for fast simulation of a generic collider experiment”, [arXiv:1307.6346](#).
- [61] T. Sjostrand, “Monte Carlo Generators”, [arXiv:hep-ph/0611247](#).
- [62] T. Kinoshita and A. Ukawa, “New Approach to the Singularities of Feynman Amplitudes in the Zero Mass Limit”, *Phys.Rev.* **D13** (1976) 1573, [doi:10.1103/PhysRevD.13.1573](#).
- [63] T. D. Lee and M. Nauenberg, “Degenerate Systems and Mass Singularities”, *Phys. Rev.* **133** (Mar, 1964) B1549–B1562, [doi:10.1103/PhysRev.133.B1549](#).
- [64] P. Nason, “A New method for combining NLO QCD with shower Monte Carlo algorithms”, *JHEP* **0411** (2004) 040, [doi:10.1088/1126-6708/2004/11/040](#), [arXiv:hep-ph/0409146](#).
- [65] S. Frixione, P. Nason, and C. Oleari, “Matching NLO QCD computations with Parton Shower simulations: the POWHEG method”, *JHEP* **0711** (2007) 070, [doi:10.1088/1126-6708/2007/11/070](#), [arXiv:0709.2092](#).
- [66] S. Alioli et al., “A general framework for implementing NLO calculations in shower Monte Carlo programs: the POWHEG BOX”, *JHEP* **1006** (2010) 043, [doi:10.1007/JHEP06\(2010\)043](#), [arXiv:1002.2581](#).
- [67] S. Mandelstam, “Determination of the Pion-Nucleon Scattering Amplitude from Dispersion Relations and Unitarity. General Theory”, *Physical Review* **112** (November, 1958) 1344–1360, [doi:10.1103/PhysRev.112.1344](#).
- [68] W. J. S. Ellis, R. K. and B. R. Webber., “. Cambridge University Press, 1996.
- [69] Y. L. Dokshitzer *Sov. J. Phys. JETP* **46** (1977) 641.
- [70] V. N. Gribov and L. N. Lipatov *Sov. J. Nucl. Phys.* **15** (1972) 438.
- [71] G. Altarelli and P. G *Nucl. Phys.* **B126** (1977) 298.
- [72] V. Gribov and L. Lipatov, “Deep inelastic e p scattering in perturbation theory”, *Sov.J.Nucl.Phys.* **15** (1972) 438–450.
- [73] G. Altarelli and G. Parisi, “Asymptotic Freedom in Parton Language”, *Nucl.Phys.* **B126** (1977) 298, [doi:10.1016/0550-3213\(77\)90384-4](#).

- [74] A. Martin et al., “Parton distributions for the LHC”, *Eur.Phys.J.* **C63** (2009) 189–285, doi:10.1140/epjc/s10052-009-1072-5, arXiv:0901.0002.
- [75] “Combined measurement and QCD analysis of the inclusive ep scattering cross sections at HERA”, *Journal of High Energy Physics* **2010** (2010), no. 1, doi:10.1007/JHEP01(2010)109.
- [76] D. Stump et al., “Inclusive Jet Production, Parton Distributions, and the Search for New Physics”, *JHEP* **0310** (2003) 046, arXiv:arXiv:hep-ph/0303013.
- [77] J. Pumplin et al., “New generation of parton distributions with uncertainties from global QCD analysis”, *JHEP* **0207** (2002) 012, arXiv:hep-ph/0201195.
- [78] V. Sudakov, “Vertex parts at very high-energies in quantum electrodynamics”, *Sov.Phys.JETP* **3** (1956) 65–71.
- [79] J. C. Collins, “Sudakov form-factors”, *Adv.Ser.Direct.High Energy Phys.* **5** (1989) 573–614, arXiv:hep-ph/0312336.
- [80] S. Frixione and B. R. Webber, “Matching NLO QCD computations and parton shower simulations”, *JHEP* **0206** (2002) 029, arXiv:arXiv:hep-ph/0204244.
- [81] S. Catani et al. *JHEP* **0111** (2001) 063, arXiv:arXiv:hep-ph/0109231.
- [82] L. Lonnblad, “Correcting the color dipole cascade model with fixed order matrix elements”, *JHEP* **0205** (2002) 046, arXiv:hep-ph/0112284.
- [83] S. Hoche et al., “Matching Parton Showers and Matrix Elements”, arXiv:arXiv:hep-ph/0602031.
- [84] M. Mangano et al., “Matching matrix elements and shower evolution for top-quark production in hadronic collisions”, arXiv:arXiv:hep-ph/0611129.
- [85] W. Kilian, T. Ohl, and J. Reuter, “WHIZARD: Simulating Multi-Particle Processes at LHC and ILC”, *Eur.Phys.J.* **C71** (2011) 1742, doi:10.1140/epjc/s10052-011-1742-y, arXiv:0708.4233.
- [86] M. Moretti, T. Ohl, and J. Reuter, “O’Mega: An Optimizing matrix element generator”, arXiv:hep-ph/0102195.
- [87] Z. Was, “TAUOLA for simulation of tau decay and production: perspectives for precision low energy and LHC applications”, *Nucl.Phys.Proc.Suppl.* **218** (2011) 249–255, doi:10.1016/j.nuclphysbps.2011.06.040, arXiv:1101.1652.

- [88] CDF Collaboration Collaboration, "Measurement of double parton scattering in $\bar{p}p$ collisions at $\sqrt{s} = 1.8$ TeV", *Phys.Rev.Lett.* **79** (1997) 584–589, [doi:10.1103/PhysRevLett.79.584](https://doi.org/10.1103/PhysRevLett.79.584).
- [89] Axial Field Spectrometer Collaboration Collaboration, "DOUBLE PARTON SCATTERING IN $p p$ COLLISIONS AT $S^{*(1/2)} = 63$ -GeV", *Z.Phys.* **C34** (1987) 163, [doi:10.1007/BF01566757](https://doi.org/10.1007/BF01566757).
- [90] UA5 Collaboration Collaboration, "The UA5 High-Energy anti- $p p$ Simulation Program", *Nucl.Phys.* **B291** (1987) 445, [doi:10.1016/0550-3213\(87\)90481-0](https://doi.org/10.1016/0550-3213(87)90481-0).
- [91] J. Butterworth, J. R. Forshaw, and M. Seymour, "Multiparton interactions in photoproduction at HERA", *Z.Phys.* **C72** (1996) 637–646, [doi:10.1007/s002880050286](https://doi.org/10.1007/s002880050286), [arXiv:hep-ph/9601371](https://arxiv.org/abs/hep-ph/9601371).
- [92] CMS Collaboration Collaboration, "Charged particle multiplicities in pp interactions at $\sqrt{s} = 0.9, 2.36,$ and 7 TeV", *JHEP* **1101** (2011) 079, [doi:10.1007/JHEP01\(2011\)079](https://doi.org/10.1007/JHEP01(2011)079), [arXiv:1011.5531](https://arxiv.org/abs/1011.5531).
- [93] O. S. Bruning et al., "LHC Design Report. 1. The LHC Main Ring", *CERN-2004-003-V-1*, *CERN-2004-003* (2004).
- [94] O. Bruning et al., "LHC Design Report. 2. The LHC infrastructure and general services", *CERN-2004-003-V-2*, *CERN-2004-003* (2004).
- [95] M. Benedikt et al., "LHC Design Report. 3. The LHC injector chain", *CERN-2004-003-V-3*, *CERN-2004-003* (2004).
- [96] W. J. Stirling, "Progress in Parton Distribution Functions and implications for LHC", [doi:10.3204/DESY-PROC-2009-01/41](https://doi.org/10.3204/DESY-PROC-2009-01/41), [10.3360/dis.2008.4](https://doi.org/10.3360/dis.2008.4), [arXiv:0812.2341](https://arxiv.org/abs/0812.2341).
- [97] CERN, "LHC sets new records".
- [98] The CMS Collaboration, "CMS Physics Technical Design Report Volume I: Detector Performance and Software", *CERN-LHCC-2006-001* (2006).
- [99] The CMS Collaboration, "Measurement of Tracking Efficiency", *CMS PAS TRK-10-002* (Oct, 2010).
- [100] The CMS Collaboration, "The CMS experiment at the CERN LHC", *Journal of Instrumentation* **3** (2008), no. 08, S08004.

- [101] R. Frühwirth, "Application of Kalman filtering to track and vertex fitting", *Nuclear Instruments and Methods in Physics Research A* **262** (1987) 444.
- [102] The CMS Collaboration, "Alignment of the CMS silicon tracker during commissioning with cosmic rays", *Journal of Instrumentation* **5** (2010), no. 03, T03009.
- [103] The CMS Collaboration, "Tracking and Primary Vertex Results in First 7 TeV Collisions", *CMS-PAS-TRK-10-005* (2010).
- [104] The CMS Collaboration, "The HCAL Project, Technical Design Report", *CERN-LHCC 31* (1997).
- [105] C. Collaboration, "Performance of the CMS hadron calorimeter with cosmic ray muons and LHC beam data", *Journal of Instrumentation* **5** (2010), no. 03, T03012.
- [106] T. C. Collaboration, "Performance of the CMS Drift Tube Chambers with Cosmic Rays", doi:[10.1088/1748-0221/5/03/T03015](https://doi.org/10.1088/1748-0221/5/03/T03015), arXiv:[arXiv/0911.4855](https://arxiv.org/abs/0911.4855).
- [107] C. Collaboration, "Performance of the CMS cathode strip chambers with cosmic rays", *Journal of Instrumentation* **5** (2010), no. 03, T03018.
- [108] L. Tuura, G. Eulisse, and A. Meyer, "CMS data quality monitoring web service", *Journal of Physics: Conference Series* **219** (2010), no. 7, 072055.
- [109] D. Bonacorsi and the Cms Computing project, "Experience with the CMS Computing Model from commissioning to collisions", *Journal of Physics: Conference Series* **331** (2011), no. 7, 072005.
- [110] CERN, "The Worldwide LHC Computing Grid", October, 2001.
- [111] D. Spiga et al., "CRAB: The CMS distributed analysis tool development and design", *Nucl.Phys.Proc.Suppl.* **177-178** (2008) 267–268, doi:[10.1016/j.nuclphysbps.2007.11.124](https://doi.org/10.1016/j.nuclphysbps.2007.11.124).
- [112] The CMS Collaboration, "Particle Flow Event Reconstruction in CMS and Performance for Jets, Taus and MET", *CMS PAS PFT-09-001* (2009).
- [113] The CMS Collaboration, "Jet Performance in pp Collisions at $\sqrt{s} = 7$ TeV", *CMS-PAS-JME-10-003* (2010).

- [114] The CMS Collaboration, "Missing Transverse Energy Performance in Minimum-Bias and Jet Events from p-p Collisions at $\sqrt{s}=7$ TeV", *CMS-PAS-JME-10-004* (2010).
- [115] The CMS Collaboration, "Tracking and Vertexing Results from First Collisions", *CMS PAS TRK-10-001* (2010).
- [116] R. F. W. Waltenberger and P. Vanlaer, "Adaptive vertexing", *J.Phys* **G34** (2007). N343. doi:10.1088/0954-3899/34/12/N01.
- [117] Chabanat and N. Estre, "Performance of muon identification in pp collisions at $\sqrt{s} = 7$ TeV", *CMS-PAS-MUO-10-002*.
- [118] The CMS Collaboration, "Measurement of the inclusive W and Z production cross sections in pp collisions at $\sqrt{s} = 7$ TeV", *JHEP* **10** (2011) 132, doi:10.1007/JHEP10(2011)132, arXiv:1107.4789.
- [119] The UA1 Collaboration, "Hadronic Jet Production at the CERN Proton - Anti-Proton Collider", *Phys. Lett* **B132** (1983) 214, doi:doi:10.1016/0370-2693(83)90254-X.
- [120] M. Cacciari, G. P. Salam, and G. Soyez, "The Anti-k(t) jet clustering algorithm", *JHEP* **0804** (2008) 063, doi:10.1088/1126-6708/2008/04/063, arXiv:0802.1189.
- [121] "FastJet", <http://www.lpthe.jussieu.fr/~salam/fastjet>.
- [122] M. Cacciari and G. P. Salam, "Pileup subtraction using jet areas", *Phys.Lett.* **B659** (2008) 119–126, doi:10.1016/j.physletb.2007.09.077, arXiv:0707.1378.
- [123] M. Cacciari, G. P. Salam, and G. Soyez, "The Catchment Area of Jets", *JHEP* **0804** (2008) 005, doi:10.1088/1126-6708/2008/04/005, arXiv:0802.1188.
- [124] The CMS Collaboration, "Jet Energy Corrections and Uncertainties. Detector Performance Plots for 2012", *CMS DP-2012/012*.
- [125] The CMS Collaboration, "Pileup measurement and mitigation techniques in CMS", *CMS CR-2012-190*.
- [126] The CMS Collaboration, "Status of the 8 TeV Jet Energy Corrections and Uncertainties based on 11 fb-1 of data in CMS", *CMS DP -2013-011*.

- [127] S. Esen and G. Landsberg, “MC Truth L4 EMF-Based Factorized Jet Corrections in CMS”, CMS AN-2009-013.
- [128] CMS Collaboration Collaboration, “Identification of b-quark jets with the CMS experiment”, *JINST* **8** (2013) P04013, doi:[10.1088/1748-0221/8/04/P04013](https://doi.org/10.1088/1748-0221/8/04/P04013), arXiv:[1211.4462](https://arxiv.org/abs/1211.4462).
- [129] The CMS Collaboration, “Status of b-tagging tools for 2011 data analysis”, CMS-PAS-BTV-11-002.
- [130] The CMS Collaboration, “Missing transverse energy performance of the CMS detector”, *JINST* **6** (2011) 09001, doi:[10.1088/1748-0221/8/04/P04013](https://doi.org/10.1088/1748-0221/8/04/P04013), arXiv:[1106.5048](https://arxiv.org/abs/1106.5048).
- [131] The CMS Collaboration, “CMS Luminosity Based on Pixel Cluster Counting - Summer 2012 Update”, CMS-PAS-LUM-12-001.
- [132] H. K. Dreiner, M. Kramer, and T. Jamie, “How low can SUSY go? Matching, monojets and compressed spectra”, *Europhys.Lett.* **99** (2012) 61001, doi:[10.1209/0295-5075/99/61001](https://doi.org/10.1209/0295-5075/99/61001), arXiv:[1207.1613](https://arxiv.org/abs/1207.1613).
- [133] N. Kauer, “A Threshold-improved narrow-width approximation for BSM physics”, *JHEP* **0804** (2008) 055, doi:[10.1088/1126-6708/2008/04/055](https://doi.org/10.1088/1126-6708/2008/04/055), arXiv:[0708.1161](https://arxiv.org/abs/0708.1161).
- [134] R. et al, “The Fast Simulation of The CMS Experiment”, *J. Phys.* **396** (2012) 06–2016, doi:[10.1088/1742-6596/396/6/062016](https://doi.org/10.1088/1742-6596/396/6/062016).
- [135] P. M. Nadolsky et al., “Implications of CTEQ global analysis for collider observables”, *Phys.Rev.* **D78** (2008) 013004, doi:[10.1103/PhysRevD.78.013004](https://doi.org/10.1103/PhysRevD.78.013004), arXiv:[0802.0007](https://arxiv.org/abs/0802.0007).
- [136] N. Kidonakis, “Differential and total cross sections for top pair and single top production”, doi:[10.3204/DESY-PROC-2012-02/251](https://doi.org/10.3204/DESY-PROC-2012-02/251), arXiv:[1205.3453](https://arxiv.org/abs/1205.3453).
- [137] N. Kidonakis and R. Vogt, “The Theoretical top quark cross section at the Tevatron and the LHC”, *Phys.Rev.* **D78** (2008) 074005, doi:[10.1103/PhysRevD.78.074005](https://doi.org/10.1103/PhysRevD.78.074005), arXiv:[0805.3844](https://arxiv.org/abs/0805.3844).
- [138] R. Gavin et al., “FEWZ 2.0: A code for hadronic Z production at next-to-next-to-leading order”, *Comput.Phys.Commun.* **182** (2011) 2388–2403, doi:[10.1016/j.cpc.2011.06.008](https://doi.org/10.1016/j.cpc.2011.06.008), arXiv:[1011.3540](https://arxiv.org/abs/1011.3540).

- [139] J. M. Campbell and R. Ellis, “MCFM for the Tevatron and the LHC”, *Nucl.Phys.Proc.Suppl.* **205-206** (2010) 10–15, [doi:10.1016/j.nuclphysbps.2010.08.011](https://doi.org/10.1016/j.nuclphysbps.2010.08.011), [arXiv:1007.3492](https://arxiv.org/abs/1007.3492).
- [140] B. Andersson, “The Lund fragmentation of a multigluon string state”, *Acta Phys. Polon.* **B32** (2001) 3993–4011.
- [141] The CMS Collaboration, “Generic Tag and Probe Tool for Measuring Efficiency at CMS with Early Data”, CMS AN -2009/111.
- [142] M. Cacciari, G. Salam, and G. Soyez, “The anti- jet clustering algorithm”, *JHEP* **04,063** (2008) [doi:10.1088/1126-6708/2008/04/063](https://doi.org/10.1088/1126-6708/2008/04/063).
- [143] The CMS Collaboration, “Determination of jet energy calibration and transverse momentum resolution in CMS”, *Journal of Instrumentation* **6** (November, 2011) 11002, [doi:10.1088/1748-0221/6/11/P11002](https://doi.org/10.1088/1748-0221/6/11/P11002), [arXiv:1107.4277](https://arxiv.org/abs/1107.4277).
- [144] The CMS Collaboration, “Combination of b-tagging efficiency measurements in 2012 data at 8 TeV pp collision”, CMS-AN-AN-12-470.
- [145] A. Hoecker et al., “TMVA: Toolkit for Multivariate Data Analysis”, *PoS ACAT* (2007) 040, [arXiv:physics/0703039](https://arxiv.org/abs/physics/0703039).
- [146] The CMS Collaboration, “Performance of Muon Reconstruction and Identification in pp Collisions at 7 TeV pp collision”, CMS-PAS-MUO-10-004.
- [147] A. L. Read, “Presentation of search results: the CL_s technique”, *Journal of Physics G: Nuclear and Particle Physics* **28** (2002), no. 10, 2693.
- [148] K. Cranmer et al., “HistFactory: A tool for creating statistical models for use with RooFit and RooStats”, Technical Report CERN-OPEN-2012-016, New York U., New York, (Jan, 2012).
- [149] R. Brun and F. Rademakers, “{ROOT} object oriented data analysis framework”, *Nuclear Instruments and Methods in Physics Research Section A: Accelerators, Spectrometers, Detectors and Associated Equipment* **389** (1997), no. 1–2, 81 – 86, [doi:http://dx.doi.org/10.1016/S0168-9002\(97\)00048-X](https://doi.org/http://dx.doi.org/10.1016/S0168-9002(97)00048-X).
<ce:title>New Computing Techniques in Physics Research V</ce:title>.

- [150] A. Wald, "Tests of Statistical Hypothesis Concerning Several Parameters When the Number of Observation is Large", *Transactions of the American Mathematical Society* **54** (1943) 426–482.
- [151] K. Pearson, "On the Criterion that a given System of Deviations from the Probable in the Case of a Correlated System of Variables is such that can be reasonably supposed to have arisen from Random Sampling", *Philosophical Magazine* **50** (1900) 157–175.
- [152] M. Papucci, J. T. Ruderman, and A. Weiler, "Natural SUSY Endures", *JHEP* **1209** (2012) 035, [doi:10.1007/JHEP09\(2012\)035](https://doi.org/10.1007/JHEP09(2012)035), [arXiv:1110.6926](https://arxiv.org/abs/1110.6926).
- [153] "Projected Performance of an Upgraded CMS Detector at the LHC and HL-LHC: Contribution to the Snowmass Process", Technical Report CMS-NOTE-2013-002. CERN-CMS-NOTE-2013-002, CERN, Geneva, (Jun, 2013).
Comments: to be included in the Snowmass 2013 report.

LIST OF FIGURES

2.1	Summary of various measurements of α_S as a function of the energy scale Q . Open symbols denote (resummed) NLO, and filled symbols stand for NNLO QCD calculations . The curves stand for the QCD predictions for the combined world average value of $\alpha_S(M_{Z^0})$ [24].	16
2.2	The potential of the BEH mechanism for $\mu^2 > 0, \lambda > 0$ (left) and $\mu^2 < 0, \lambda > 0$ (right) where is minimised at $-\mu^2/(2\lambda)$	18
3.1	The running gauge couplings in the SM (left) and their unification in the context of its minimal SUSY extension (right), assuming s-particle masses at the electroweak scale.	24
3.2	The evolution of the renormalization group equations (RGE) of the $m_0, m_{1/2}$ mass parameters in the MSSM in mSUGRA with inspired boundary conditions imposed at $Q_0 = 2.5 \times 10^{16} GeV$. The parameter $\mu^2 + m^2 H_u$ gets negative, provoking electroweak symmetry breaking [28].	31
3.3	The CMSSM exclusion limits in the $(m_0, m_{1/2})$ plane by the CMS collaboration obtained by using data corresponding to an integrated luminosity of $4.98 fb^{-1}$ at $\sqrt{s} = 7$ TeV Center of Mass Energy (C.M.E)[43, 44].	31
3.4	First order Feynman diagrams of stop quark pair production via $q\bar{q}$ annihilation (top) and gluon fusion (down).	36

3.5	The NLO+NLL production cross section of the $\tilde{t}_1 - \tilde{\bar{t}}_1$ as a function of the stop quark mass at $\sqrt{s} = 7$ TeV for different ranges. The black (red) lines correspond to the cross section and scale uncertainties by using the CTEQ (MSTW) PDF set. The yellow (dashed black) band corresponds to the total CTEQ (MSTW) uncertainty. The green lines show the total cross section and uncertainty [47].	37
3.6	The NLO+NLL direct stop quark pair production cross section at $\sqrt{s} = 8$ TeV (blue line) with the theoretical uncertainties (green band). The values have been obtained from [51].	44
3.7	Left : The leading order Feynman diagram of the T2tt SMS model (direct stop quark pair production) that will be considered for this analysis, along with the decay according to $pp \rightarrow \tilde{t}_1 \tilde{\bar{t}}_1 \rightarrow b\mu^+ \nu_\mu \tilde{\chi}_1^0 \bar{b} q\bar{q} \tilde{\chi}_1^0$, where also the charge conjugate diagrams are considered as well for this analysis. Right : The T2tt mass spectrum. Except the stop quark and the lightest neutralino, the rest of squarks and the gluino are considered to be much heavier, therefore decoupled and not participating in the production mechanism at all.	46
4.1	The general structure of an event generation starting from the hard interaction and the resulting fragmentation, hadronization, and decay. . .	51
4.2	The kinematic x - Q^2 plane probed in the production for an object of mass M and rapidity y for the LHC nominal $\sqrt{s} = 14$ TeV.	53
4.3	MSTW NLO PDFs for $Q^2 = 10 GeV^2$ (left) and $Q^2 = 10^4 GeV^2$ (right) [74, 75].	54
5.1	The Standard Model cross section predictions for the Tevatron and the LHC [96].	70
5.2	The CERN accelerator complex	73
5.3	The cross section of a LHC dipole magnet	74
5.4	The delivered luminosity to CMS versus time for years 2010 (green), 2011 (red) and 2012 (blue) during stable beams and data taking periods. . . .	76
5.5	Schematic view of the Compact Muon Solenoid (CMS) detector.	77
5.6	A view in $r - z$ of the CMS tracker structure.	80
5.7	A schematic illustration of the CM Pixel Detector.	81
5.8	A schematic view of one quadrant of the CMS ECAL layout.	83
5.9	A schematic view of the one quadrant of the CMS HCAL layout.	85
5.10	A quadrant of the CMS muon system.	87

6.1	Muon efficiency results from $J/\psi \rightarrow \mu\mu$ for muons with $p_T < 20$ GeV and $Z \rightarrow \mu\mu$ for muons with $p_T > 20$ GeV using PF-Muons in the barrel and overlap regions (left) and in the end-caps (right) [117].	99
6.2	Sketch of the factorized approach to apply the jet-energy corrections. . .	102
6.3	The PU measured in PF jets for the AO and JA methods. Both methods present a good linear behaviour of the p_T of the PU as a function of the number of Primary vertices in the event [124].	103
6.4	The PF jet response versus the p_T of GenJet. On the left (middle), before (after) applying any L1 correction and on the right after having applied the required MC correction chain [125].	104
6.5	Relative uncertainties of the jet energy scale correction as a function of p_T (left) and of η (right) for various sources [126].	105
6.6	The distance to the jet axis (left) and the average number of tracks (right). The trigger selection was requiring jets with $p_T > 60$ GeV [128].	107
6.7	Illustration of the Impact Parameter (IP) parameter. It holds the same sign as the scalar product of the vector pointing from the PV to the point of closest approach with the jet direction.	108
6.8	The 3D impact parameter (left) and the significance of the 3D IP (right) for all selected tracks. Underflow and overflow are added to the first and last bins, respectively [128].	109
6.9	The mass (left) and the 3D significance (right) of the secondary vertex [128].	110
6.10	The distribution of the CSV discriminator (left) and the multiplicity of the SV vertices (right) [128].	110
6.11	Performance curves obtained from simulation for various b -tagging algorithms for c jet (left) and light-parton (right) misidentification probabilities as a function of the b -jet efficiency [128].	111
6.12	The PF \cancel{E}_T distribution for $W \rightarrow \mu\nu_\mu$ (left) and $W \rightarrow e\nu_e$ (right). This \cancel{E}_T is characterised as "genuine" as neutrinos are present in the final state. Data and simulation agree well [130].	113
7.1	The widths (Γ) (GeV) of the $\tilde{t}_1 \rightarrow \mu\nu_\mu\tilde{\chi}_1^0 b$ process with the use of MadGraph (left) and the equivalent luminosity (pb^{-1}) of the generated simulation signal datasets (right).	118

- 7.2 Comparison between FS and Full-Sim from the \cancel{E}_T (top row, left plot), the H_T (top row, right plot), the p_T (second row, left plot) and the η of the isolated muon (second row, right plot) the $\Delta\Phi(\cancel{E}_T, \mu)$ (bottom row, left plot) and the (μ, Jet^1) (bottom row, right plot). Two $t\bar{t}$ samples generated with MadGraph with up to 3 extra partons were used for this comparison, while the same event selection has been applied to both. 121
- 7.3 The distributions of the \cancel{E}_T (top row, left plot), the average H_T (top row, right plot), the transverse momentum and the η of the muon (second row) and the $\Delta\Phi$ between the muon and the leading jet (bottom row, left plot) and between the muon and the \cancel{E}_T as well (bottom row, right plot). 123
- 7.4 The differential jet distribution for the $2 \rightarrow 1$ and $1 \rightarrow 0$ configuration with the individual contribution from the different multiplicities for the T2tt model. Higher order transitions such as $3 \rightarrow 2$ will be given by the PS. Based on these plots, the Q_{match} was set to 44 (46) GeV for $m_{\tilde{t}_1} < (>)$ 500 GeV. 126
- 7.5 Efficiency of the IsoMu24_eta2p1 trigger path which was used for the μ + jets channel during the RunA and RunB data-taking periods of 2012. The curve corresponding to "RunB" shows a higher efficiency and even a sharper turn-on, due to PU corrections which were introduced for the lepton isolation. 129
- 7.6 Illustration of the isolation cone around a muon and the veto cone used to subtract the contribution of the muon itself. 132
- 7.7 The number of Primary Vertices on simulation after applying the reweighting factors compared to the observed distribution from Single- μ datasets corresponding to 19.1 fb^{-1} of integrated luminosity. 136
- 7.8 The selection efficiency of the signal for each point in the $(m_{\tilde{t}_1}, m_{\tilde{\chi}_1^0})$ plane. 139
- 7.9 Comparison of data versus expectation of the p_T of the isolated muon (left) and the $\Delta\Phi$ between the muon and the \cancel{E}_T (right) after the baseline selection. 140
- 7.10 Comparison of data versus expectation for the \cancel{E}_T (top row, left plot), the p_T of the leading jet (top row, right plot), the multiplicity of jets (second row, left plot), the sum of the p_T of the jets (H_T) (second row, right plot), the sum of $\Delta\Phi(\mu, Jet^1) + \Delta\Phi(\mu, Jet^2)$ (bottom row, left plot) and the transverse mass of the W-boson (bottom row, right plot) after the baseline selection. 141

- 7.11 Comparison of data versus expectation after the baseline selection of the multiplicity of the b-tagged jets (left) and the distribution of discriminant used for the hadronic decays of W used by the CSV algorithm (right) based. 142
- 7.12 The reconstructed mass of the W-boson (left) and that of the top quark (right) from the $t \rightarrow q\bar{q}b$ with the use of a minimised χ^2 as explained in the text. 143
- 7.13 The reconstructed z-component of the neutrino's momentum. 144
- 7.14 From left to right : The distributions of the transverse mass of the reconstructed "hadronic" and that of the "leptonic" top quarks (top row), the mass of the reconstructed $t\bar{t}$ system and its transverse mass (second row), the $\Delta\Phi$ and the ratio of the p_T of the "hadronic" versus that of the "leptonic" reconstructed top quarks (bottom row). 146
- 8.1 Number of survived variables for $|\rho_{max}| = 0.5$ (left) and $|\rho_{max}| = 0.8$ (right). In general the change of the $|\rho_{max}|$ does not alter radically the number of survived variables that make it to the final list. 151
- 8.2 The 2D performance plots of the \cancel{E}_T and the p_T of the muon. Top row shows the ranking, second row the $\epsilon_{overlap}$ fractions and bottom row the $\epsilon_{overlap}/\epsilon_{best}$ for $|\rho_{max}| = 0.8$ 152
- 8.3 The median values in the $(m_{\tilde{t}_1}, m_{\tilde{\chi}_1^0})$ plane of the H_T4 Jets and of the H_T (top row), of the \cancel{E}_T and of the transverse momentum of the muon (second row) and of the reconstructed W-boson transverse mass and of the invariant mass of the three leading jets ($m3$) (bottom row). 154
- 8.4 The ROC curves for several classifiers (left) and for different number of injected variables (right). One can see that using more than 4 variables practically does not improve the performance of the MVA. 159
- 8.5 A check for overtraining for the MLP (left) and the BDT (right) classifiers. Training and testing samples present a very good convergence for both of them. Similar checks have been carried out for many different points in the $(m_{\tilde{t}_1}, m_{\tilde{\chi}_1^0})$ plane and no strong inconsistencies have been found. 160

- 9.1 The expectation distributions for 19.1 fb^1 of integrated luminosity of the scalar sum of the four leading jets (denoted by $H_T4\text{Jets}$) (top left), the \cancel{E}_T (top right), the transverse mass of the reconstructed W -boson (bottom left) and the invariant mass of the three leading jets (denoted by m_3) (bottom right) for the nominal (open green circle) and for the $\pm 1\sigma$ variations of the JES (open triangles). The plots have been obtained from the MC@NLO $t\bar{t}$ simulated dataset after the baseline selection. 162
- 9.2 The expectation distributions for 19.1 fb^1 of integrated luminosity of the scalar sum of the four leading jets (denoted by $H_T4\text{Jets}$) (top left), the \cancel{E}_T (top right), the transverse mass of the reconstructed W -boson (bottom left) and the transverse momentum of the leading jet (bottom right) for the nominal (open green circle) and after having applied the $\pm 1\sigma$ variations of the JER (open triangles). The plots have been obtained from the MC@NLO $t\bar{t}$ simulated dataset after the baseline selection. 164
- 9.3 The expectation distributions for 19.1 fb^1 of integrated luminosity of the number of b-tagged jets (left) and the CSV-M b-tagger distribution of the $t \rightarrow bq\bar{q}$ decays discriminant (right) for the nominal (open green circle) and after having applied $\pm 1\sigma$ variations on the b-tag efficiency (open triangles). The plots have been obtained from the MC@NLO $t\bar{t}$ simulated dataset after the baseline selection. 165
- 9.4 The expectation distributions for 19.1 fb^1 of integrated luminosity of the number of reconstructed jets (left) and the sum of H_T and \cancel{E}_T (right) for the nominal (open green circle) and after having applied $\pm 1\sigma$ variations on mean number of interactions to account for the PU corrections (open triangles). The plots have been obtained from the MC@NLO $t\bar{t}$ simulated dataset after the baseline selection. 165
- 9.5 The distributions of the MLP classifier for the nominal (open green circle) and the $\pm 1\sigma$ variation of the JES (open triangles) for four different points in the $(m_{\tilde{t}_1}, m_{\tilde{\chi}_1^0})$ plane (indicated on the x-axis of each plot) from the $t\bar{t}$ systematic datasets. 169
- 9.6 The distributions of the MLP classifier for the nominal (open green circle) and the $\pm 1\sigma$ variation of the JER (open triangles) for four different points in the $(m_{\tilde{t}_1}, m_{\tilde{\chi}_1^0})$ plane (indicated on the x-axis of each plot) from the $t\bar{t}$ systematic datasets. 170

- 9.7 The distributions of the MLP classifier for the nominal (open green circle) and the $\pm 1\sigma$ variation of the b-tagging efficiencies (open triangles) for four different points in the $(m_{\tilde{t}_1}, m_{\tilde{\chi}_1^0})$ plane (indicated on the x-axis of each plot) from the $t\bar{t}$ systematic datasets. 171
- 9.8 The distributions of the MLP classifier for the nominal (open green circle) and the $\pm 1\sigma$ variation of the PU (open triangles) for four different points in the $(m_{\tilde{t}_1}, m_{\tilde{\chi}_1^0})$ plane (indicated on the x-axis of each plot) from the $t\bar{t}$ systematic datasets. 172
- 9.9 Top row : The MVA classifier discriminant distributions for the nominal (open green circle) compared to the Matching-Up (MU) and the Matching-Down (MD) (open triangles) from the $t\bar{t}$ systematic datasets for two different points in the $(m_{\tilde{t}_1}, m_{\tilde{\chi}_1^0})$ plane. Bottom row : The MVA classifier discriminant distributions for the nominal and the Scale-Up (SU) and the Scale-Down (SD) from the $t\bar{t}$ systematic datasets. The points are indicated on the x-axis of each plot. 173
- 10.1 The number of bins of the MLP (left) and the BDT (right) distribution histograms after requiring at least 10 $t\bar{t}$ events in each bin. 182
- 10.2 The MVA distributions of the MLP (left) and the BDT (right) classifiers after requiring at least 10 $t\bar{t}$ entries to be present at each bin for the $m_{\tilde{t}_1} = 400$ GeV, $m_{\tilde{\chi}_1^0} = 100$ GeV model. 182
- 10.3 The α_i values from the fit for the experimental systematics of JES (top left), JER (top right), PU (bottom left) and BTag (bottom right). 184
- 10.4 The α_i values from the theoretical systematics. These are the cross section normalization applied to the $t\bar{t}$ (top left), the $W \rightarrow l\nu_l$ (top right), the DY (bottom left) and the Rare/other (bottom right) datasets. 185
- 10.5 The α_i values obtained from the fit for the Q^2 (top row) and the matching scale variations (bottom row) for the $t\bar{t}$ and the $W \rightarrow l\nu_l$ processes. 186
- 10.6 The MLP classifier distributions (left column) for two different points in the $(m_{\tilde{t}_1}, m_{\tilde{\chi}_1^0})$ plane (noted on the histograms) before (solid colours and bottom ratio plot) and after having applied the corrections obtained from the fit response for all of the α_i factors associated with the systematics (open cross and top ratio plot). Also the absolute and relative uncertainties are given (right column), whereas for the latter we perform a linear fit to estimate the trend. 189

- 10.7 The BDT classifier distributions (left column) for two different points in the $(m_{\tilde{t}_1}, m_{\tilde{\chi}_1^0})$ plane (noted on the histograms) before (solid colours and bottom ratio plot) and after having applied the corrections obtained from the fit response for all of the α_i factors associated with the systematics (open cross and top ratio plot). Also the absolute and relative uncertainties are given (right column), whereas for the latter we perform a linear fit to estimate the trend. 190
- 10.8 The constant (p_0) (left) and the slope (p_1) (right) terms from the linear fit performed on the MVA MLP MC_{cor} distributions, i.e. after having corrected for the α_i coefficients in order to assess the trend of relative uncertainty bin by bin. 191
- 10.9 The normalised χ^2 of data vs expectation comparison (left) and that defined as $\chi^2 = \sum_i (\alpha_i)^2$ (right). In the former case, the values are below the critical values [151], while for the latter we observe that in general the χ^2 is $\mathcal{O}(1)$ 191
- 11.1 The expected limit on stop quark versus neutralino masses for the $\tilde{t}_1 \rightarrow \tilde{\chi}_1^0 + t$ SMS model for the MLP classifier (top plot) and a zoom-in for $m_{\tilde{t}_1} \leq 350$ GeV (bottom plot), along with the $\hat{\mu}_s$ values obtained from the asymptotic CLs. The zoomed-in plot is demonstrating how the linear interpolation was done in order to draw the exclusion line as it is explained in the text. 194
- 11.2 The limit on stop quark versus neutralino masses for the $\tilde{t}_1 \rightarrow \tilde{\chi}_1^0 + t$ SMS model, both for the MLP (top) and BDT (bottom) classifiers. The MLP classifier gives stronger expected and observed limits compared to the BDT which can be attributed to the fact that the template histograms have more bins in the former case as was discussed in Section 10.2. We also have to note the sensitivity in the compressed region for $m_{\tilde{t}_1} < 350$ GeV for the MLP classifier. 195
- 11.3 The public result from the ATLAS [52] (left) and the CMS collaboration [45, 53, 54] (right) for the $\tilde{t}_1 \rightarrow t + \chi_1^0$ topology in 1-lepton final state assuming the BR ($\tilde{t}_1 \rightarrow t + \tilde{\chi}_1^0$) to be 100%. 197
- 11.4 Top row : The cut-value distributions for $m_{\tilde{t}_1} = 325$ GeV, $m_{\tilde{\chi}_1^0} = 100$ GeV for both the MLP (left plot) and the BDT (right plot) classifiers. Bottom row : The Optimal Cut Point where the significance is maximised for the MLP (left) and the BDT (right) classifiers. 200

11.5	The efficiency obtained at the Optimal Cut point for signal (left row) and background (bottom row) for both the MLP (left column) and the BDT (right column) classifiers.	201
11.6	The maximum significance (S/\sqrt{B}) at the optimal cut point for the MLP and the BDT classifiers.	202
11.7	The upper limits from the MLP classifier as a counting experiment. For comparison, the expected limit from the main method for both the BDT and the MLP classifiers are superimposed.	203
11.8	Left : The MLP distribution for the for $m_{\tilde{t}_1} = 225$ GeV, $m_{\tilde{\chi}_1^0} = 75$ GeV point which is excluded with our method but not with the cut-and-count. Also, the optimal cut point is noted with an arrow. Right : The one-bin distribution which is used by the cut-and-count, along with the considered systematics which cover well the small discrepancy between expectation and data.	203
11.9	The 5σ projected discovery reaches for two scenarios, a "pessimistic" (Scenario A) and a more "optimistic" one (Scenario B) for $\sqrt{s} = 14$ TeV and for $\mathcal{L} = 300 \text{ fb}^{-1}$ [153].	206
C.1	Schematic diagram of a MLP NN with one hidden layers. At each layer, a weight scales its output while connecting to the next one.	216
C.2	Illustration of a BDT decision tree. An event starts from the Root node and goes all the way down, until it is classified as "background" or "signal"-like after reaching the corresponding leaf.	220

LIST OF TABLES

2.1	Summary of the fundamental forces and its properties	9
2.2	The three generations of fermions in the context of the SM with their electric charge (Q), mass (M) and the forces they "feel" [12].	11
3.1	The chiral supermultiplets in the MSSM along with their $SU(3)_C \times SU(2)_L \times U(1)_Y$ quantum numbers. For simplicity, only one generation of quarks and leptons is listed. However, for each of the quarks, leptons or BEH supermultiplet, there exists a corresponding anti-particle multiplet including the charge conjugate fermions with their associated scalar partners.	27
3.2	The gauge supermultiplets in the MSSM along with their $SU(3)_C \times SU(2)_L \times U(1)_Y$ quantum numbers.	28
3.3	The kinematical conditions that have to be satisfied for the specific decay modes of the \tilde{t}_1	39
4.1	Some of the $2 \rightarrow 2$ QCD parton scatterings at tree-level along with the expression for the $ \mathcal{M} ^2$ using the Mandelstam variables.	56
7.1	Summary of <i>Single-Muon</i> dataset streams utilised for this analysis. . . .	116
7.2	Summary of the simulated datasets with the cross sections of the processes and the used event generator. Contributions from higher order QCD corrections are included where available.	124
7.3	Summary of Q_{ME}^{cut} and Q_{match} that were used for the signal MC datasets.	127
7.4	The trigger that was used in both collision and simulated datasets. . . .	128

7.5	The muon selection requirements used in this analysis. The $ d_{0,pv} $ ($ d_{z,pv} $) refers to the transverse (longitudinal) IP of the muon with respect to the Primary Vertex (PV).	133
7.6	The applied jets selection requirements	134
7.7	The scale factors that were utilised to account for the Jet Energy Resolution differences.	136
7.8	Event yields for the $\mu+$ jets channel for $\mathcal{L} = 19125.2 \text{ pb}^{-1}$ at $\sqrt{s} = 8 \text{ TeV}$. .	138
7.9	The cut efficiencies (relative to the preselected datasets) obtained after applying sequentially the different selection cuts, for both the background and the collision event datasets used in this analysis.	139
8.1	The median values of some observables obtained from the MC@NLO $t\bar{t}$ simulated dataset.	153
8.2	The frequency of the observables that appear at least once in the best 4 selected variables. The full list and their exact definition is given in Appendix B.	156
9.1	Summary of the SM simulated datasets that were used for the Q^2 and the matching scale variations.	167
11.1	Comparison of expected and observed limits for the massless as well as for the massive $\tilde{\chi}_1^0$ case between this search (for both used classifiers MLP and BDT) and the public ones from both the CMS and the ATLAS collaborations when $m_{\tilde{t}_1} \geq m_t$	198
11.2	The event yields for the point $m_{\tilde{t}_1} = 225 \text{ GeV}$, $m_{\tilde{\chi}_1^0} = 75 \text{ GeV}$ and for a cut-and-count method.	204
A.1	The values used with Pythia6.426 and the Tune Z2* [92] for the treatment of the UE.	209
A.2	The values used with Pythia6.426 and the Tune Z2* [92] for the hadronization.	210

Part VI

Epilogue

The unprecedented high center of mass energy at 8 TeV that the Large Hadron Collider (LHC) reached during the 2012 data taking period has marked the beginning of a new era in particle physics for the study and discovery of new phenomena at the TeV scale. Although the discovery of the Higgs-boson is a tremendous milestone, there are still many unanswered questions that seek an answer right after the restart of the LHC in 2015. Physicists have been struggling for years to track down any experimental evidence for the existence of the Supersymmetry, one very appealing theory that can help to get a more complete picture of how nature works.

Some more simplified theories like *natural SUSY* probe the existence of light 3rd generation top supersymmetric particles that must be accessible to the LHC provided they exist. This analysis searches for evidence of such particles produced in pairs via a direct production mode while they decay according to $pp \rightarrow \tilde{t}_1 \bar{\tilde{t}}_1 \rightarrow b\mu\nu_\mu \tilde{\chi}_1^0 \bar{b} q\bar{q} \tilde{\chi}_1^0$. Further and in order to reduce the CPU time while building the simulated datasets but also to be able to have an easier interpretation of the final result, *Simplified Model Spectrum* (SMS) have been employed. The SMS practically allows us to build a more simplistic model while the physics of the topology of interest is not affected. That practically boils down to the fact that the free parameters can be minimised. In our case, the free parameters are the masses of the top squark ($m_{\tilde{t}_1}$) and of the lightest neutralino ($m_{\tilde{\chi}_1^0}$). The covered parameter space considered in the analysis is $m_{\tilde{t}_1} \in [175, 700]$ GeV and $m_{\tilde{\chi}_1^0} \in [0, m_{\tilde{t}_1} - 100]$ GeV resulting in 319 signal simulated datasets which have been privately produced.

Furthermore, dedicated event selection criteria have been deployed, in particular criteria based on the isolation of the muon in the final state while posing several other cuts

in order to efficiently suppress the background contributions. Next, an initial diverse list of input observables is optimised for each considered signal model which is used in conjunction with Multivariate Analysis Tools in order to construct a combined final variable which serves to discriminate signal versus background events. The next step includes the building of optimised template histograms which are then used in order to build a test statistic. This test statistics is a negative log likelihood ratio formed from the H_0 and the H_1 hypotheses. The final step includes the calculation of the upper limits on the signal production cross section by using the asymptotic CLs method while the systematic uncertainties are taken into account.

The final result is interpreted as an exclusion range in the $(m_{\tilde{t}_1}, m_{\tilde{\chi}_1^0})$ plane where we have excluded \tilde{t}_1 masses up to 675 GeV for massless $\tilde{\chi}_1^0$. Similarly and for the case of a massive neutrino, we excluded the \tilde{t}_1 masses up to ~ 625 GeV for $\tilde{\chi}_1^0$ masses up to ~ 275 GeV. Furthermore, this analysis manages to put limits in the compressed region (i.e. when the condition $m_{\tilde{t}_1} - m_{\tilde{\chi}_1^0} < m_t$ is met), where usually the efficiency is very low and as a direct consequence the sensitivity (if any) is also very small. For this peculiar corner of the phase space, the region for \tilde{t}_1 masses up to 325 GeV and for $\tilde{\chi}_1^0$ mass up to ~ 150 GeV has been excluded. These results are directly comparable and very competitive to what the ATLAS and the CMS collaborations have already published at the time.

imuleerde datasets die geproduceerd werden in het kader van deze thesis.

Om de relevante proton botsingen te selecteren werden specifieke selectie criteria ontwikkeld. In het bijzonder zijn er criteria die vragen dat de activiteit rond het muon minimaal is (geïsoleerd muon), hetgeen verwacht wordt voor het signaal proces. Samen met een aantal andere selectiesneden worden de contributies van achtergrond processen gereduceerd terwijl de criteria efficiënt zijn voor het signaal proces. Met de geselecteerde gebeurtenissen wordt een lange lijst waarneembare grootheden opgesteld waarvoor de distributies in min- of meerdere mate verschillend (discriminerend) zijn voor het signaal en de achtergrond processen. Voor elk signaal model in de beschouwde parameter ruimte worden de meest discriminerende grootheden gecombineerd met een zogeheten multivariate analyse, waarna de bekomen distributie van de gecombineerde variabele gebruikt wordt om een teststatistiek op te stellen. De teststatistiek is de negatieve waarde van het logaritme van de likelihood ratio gevormd door de H_0 en H_1 hypothesen. Met deze teststatistiek en rekening houdend met de systematische onzekerheden wordt de bovengrens bepaald op de werkzame doorsnede van de productie van het signaal proces aan de hand van de CL_s voorwaarde, waarbij een asymptotische benadering gebruikt werd.

Het eindresultaat kan geïnterpreteerd worden als een regio in de parameter ruimte $(m_{\tilde{t}_1}, m_{\tilde{\chi}_1^0})$ plane waar het signaal model uitgesloten kan worden. Indien het neutralino massaloos is, worden top squarks met een massa tot 675 GeV uitgesloten. Voor een neutralino met een massa van ongeveer 275 GeV, worden top squarks met massa's lager dan ongeveer 625 GeV uitgesloten. Deze analyse slaagt er daarenboven in om een bovengrens te bekomen op de werkzame doorsnede van de productie van het signaal proces in de regio waar $m_{\tilde{t}_1} - m_{\tilde{\chi}_1^0} < m_t$. In deze regio van de parameter ruimte is de efficiëntie om het signaal proces van de achtergrond processen te onderscheiden waardoor de gevoeligheid typisch klein is. In deze specifieke regio van de parameter ruimte worden top squarks met een massa tot 325 GeV uitgesloten voor neutralino massa's tot ongeveer 150 GeV. Deze resultaten kunnen rechtstreeks vergeleken worden met de resultaten die de ATLAS en CMS collaboraties reeds gepubliceerd hebben en zijn zeer competitief.

ACKNOWLEDGEMENTS

Although many people contributed in different ways for this thesis to become reality, I would like to express my sincere gratitude to my advisor Prof. Jorgen D' Hondt. From 2009 when I joined IIHE, he has been an ideal supervisor, a source of real inspiration and continuous support to me, always highly motivated and enthusiastic with great insightful comments. I have been enjoying our (usually) long discussions, and at the end of the day he was always coming with some great suggestions and this is how we managed to produce such a competitive result as it is sketched in this manuscript.

Besides my advisor, I would like to thank the rest of my lab mates which have been creating an incredibly inspiring and pleasant working environment : Petra helped me through many fruitful discussions we had during the last 4 years. James helped deepen my understanding on statistics something that proved to be very useful at the end. Annik, Gerrit, Michael and Stijn tolerated me as their office mate and they have been always very supportive even if that meant that they had to spend time for questions trivial to them but new to me. I also want to wish good luck to the newest members of our group, which I am confident that they will do great things. Finally, a special thanks to the IT and the support team of the IIHE whose help has been of vital importance for the success of this project.

My special thanks to my very best friend John Vasilakos for his unconditional moral support and help. John, I am really lucky to have made such a true friend like you and I wish you the best of luck for whatever you choose to do in the future.

Last but certainly not least, I would like to thank my family and especially my mother and my wife for their support to whatever I have been trying to accomplish throughout my life time.